

FINAL TECHNICAL REPORT

Award Number G17AP00021

Ground Motion Characterization and Site-Specific IMASW Vs-depth Measurements at CEUS Seismic Stations: The 2011 Prague, OK Earthquake

Principal Investigators:

Carlos Mendoza¹, Jamey Turner², Daniel O'Connell³

Affiliation:

Fugro Consultants, Inc.

1726 Cole Blvd. Ste. 230 Lakewood, CO 80401

¹ Current Affiliation: Centro de Geociencias
Universidad Nacional Autonoma de Mexico
Campus Juriquilla
Queretaro, Qro. MEXICO, cmdozer@gmail.com

² Current Affiliation: Tetra Tech, 350 Indiana St., Suite 500, Golden,
CO 80401, jamey.turner@tetrattech.com

³ Current Affiliation: Tetra Tech, 350 Indiana St., Suite 500, Golden,
CO 80401, dan.oconnell@tetrattech.com

Term: February 15, 2017 to February 15, 2018

Keywords:

IMASW, NEHRP Site Classification, Vs30, Amplification,
Site Response, Ground Motions

Program Element I

**Ground Motion Characterization and
Site-Specific IMASW Vs-depth
Measurements at CEUS Seismic
Stations: The 2011 Prague, OK
Earthquake**

U. S. Geological Survey
National Earthquake Hazards Reduction Program
Award Number G17AP00021

November 7, 2017

Research supported by the U.S. Geological Survey (USGS), Department of the Interior, under USGS award number G17AP00021. The views and conclusions contained in this document are those of the authors and should not be interpreted as necessarily representing the official policies, either expressed or implied, of the U.S. Government

0	Final submittal	JT	CM	DO	7 November 2017
Issue	Final Technical Report Status	Prepared	Checked	Approved	Date

AWARD G17AP00021
Ground Motion Characterization and Site-Specific IMASW Vs-depth Measurements at CEUS Seismic Stations: The 2011 Prague, OK Earthquake

Principal Investigators:
Carlos Mendoza, Jamey Turner, Daniel O'Connell

ABSTRACT

This study has two components: 1) a seismological site response investigation using existing ground motion data recorded for the 6 November 2011 Mw 5.6 Prague, Oklahoma earthquake at seismic monitoring stations located within a 2° radius surrounding the Oklahoma City region, and 2) field surveys that acquired new active source shallow 3-component seismic (shear-wave) measurements at the seismic monitoring station locations to measure site effects, horizontal to vertical spectral ratios (HVSr), Vs30, Vs-depth structure and develop NEHRP Site Classification and calculate empirical ground motion amplification functions. The site response investigation used spectral inversion methodology to simultaneously identify source, site, and path effects from the inversion of observed ground motions (Hartzell and Mendoza, 2011). The procedure allows a systematic identification of resonance peaks in the site response that can be attributed to weakly consolidated sediments at depth. These resonant frequencies have generally been found to be comparable to spectral ratios of horizontal to vertical motions of micro-tremor. The site response functions have also shown higher frequency resonance peaks likely caused by a combination of higher order harmonics and shallower structure. Although more robust determinations of site amplification might be obtained using multiple sources at different distances and azimuths, amplification factors derived using data from the single 2011 Prague, Oklahoma earthquake are of great value both in identifying points of anomalous site amplification and also reconciling independent observations of site response.

The field-based Vs survey used 15 Sigma4 three-component seismographs with varying array geometries and active sourcing to obtain new site Vs structure profiles and HVSr at eleven seismic monitoring stations across Oklahoma that recorded ground motions from the 6 November 2011 Mw 5.6 Prague, Oklahoma earthquake. In addition, the three component seismic data were processed and analyzed to develop NEHRP Soil Site Classifications, and calculate site-specific ground motion amplification functions. Local soil classes and/or velocity profiles are generally not available for CEUS stations, and obtaining site measurements helps calibrate, or otherwise verify amplification factors identified using the Hartzell and Mendoza (2011) waveform-analysis approach. The surface-wave dispersion data provide site-specific 1D shear-wave velocity measurements that are compared directly with the inversion results to evaluate the performance of the estimated site amplification.

CONTENTS

Page

1.	INTRODUCTION	1
1.1	Background	1
1.2	Project Objectives	1
2.	SITE VS-DEPTH AND H/V INVESTIGATION	3
2.1	Data Acquisition	3
2.1.1	Testing of 2D Array Shapes	3
2.1.2	Supplementary Source Type Testing	4
2.2	Data Processing	10
2.2.1	H/V Processing	10
2.2.2	Ambient-Noise Interferometry: Tensor Green's Function Processing	10
2.2.3	Joint Inversion of Rayleigh-Wave Dispersion and H/V for Vs-Depth	13
2.3	Vs-Depth and H/V Data	13
2.3.1	FNO	13
2.3.2	OK-001	14
2.3.3	OK-002	15
2.3.4	OK-005	15
2.3.5	OK-009	16
2.3.6	TUL-1	17
2.3.7	V35A	17
2.3.8	W35A	18
2.3.9	W36A	19
2.3.10	WMOK	19
2.3.11	X34A	20
2.4	Site Geology, Vs, and H/V Results	20
3.	SEISMOLOGICAL SITE RESPONSE	22
3.1	Spectral Analysis	22
3.2	Inversion Results and Site Response	24
4.	SUMMARY	26
5.	ACKNOWLEDGEMENTS	27
6.	DISSEMINATION OF RESULTS	28
7.	REFERENCES	29

LIST OF FIGURES

- Figure 1.1. Regional Location Map
Figure 1.2 Geologic Map and Station Locations
Figure 1.3 Explanation of Geologic Units
- Figure 2.1a FNO Geologic Map and Site Location
Figure 2.1b FNO Station Dispersion Pathways and Source Positions
Figure 2.1c. FNO Multimodal p-f Dispersion Images and Picks
Figure 2.1d. FNO Vertical Component Dispersion Green's Function
Figure 2.1e. FNO Vs-Depth, Vs30, and Nearfield H/V Model
Figure 2.1f. FNO All Stations H/V
Figure 2.1g. FNO Site Average H/V
Figure 2.2a. OK-001 Geologic Map and Site Location
Figure 2.2b. OK-001 Station Dispersion Pathways and Source Positions
Figure 2.2c. OK-001 Multimodal p-f Dispersion Images and Picks
Figure 2.2d. OK-001 Additional Multimodal p-f Dispersion Images and Picks
Figure 2.2e. OK-001 Radial Component Dispersion Green's Function
Figure 2.2f. OK-001 Vs-Depth, Vs30, and Nearfield H/V Model
Figure 2.2g. OK-001 All Stations H/V
Figure 2.2h. OK-001 Site Average H/V
Figure 2.3a. OK-002 Geologic Map and Site Location
Figure 2.3b. OK-002 Station Dispersion Pathways and Source Positions
Figure 2.3c. OK-002 Dispersion Green's Function ZZ and ZR Multimodal p-f Dispersion Images and Picks
Figure 2.3d. OK-002 Dispersion Green's Function TT Component Multimodal p-f Dispersion Images and Picks
Figure 2.3e. OK-002 TT Component Dispersion Green's Function
Figure 2.3f. OK-002 ZZ Component Dispersion Green's Function
Figure 2.3g. OK-002 Love Wave Vs-Depth, Vs30, and H/V Model
Figure 2.3h. OK-002 Rayleigh Wave Vs-Depth, Vs30, and H/V Model
Figure 2.3i. OK-002 All Stations H/V
Figure 2.3j. OK-002 Site Average H/V
Figure 2.4a. OK-005 Geologic Map and Site Location
Figure 2.4b OK-005 Station Dispersion Pathways and Source Positions
Figure 2.4c. OK-005 Multimodal p-f Dispersion Images and Picks
Figure 2.4d. OK-005 Vertical Component Dispersion Green's Function
Figure 2.4e. OK-005 Vs-Depth, Vs30, and Nearfield H/V Model
Figure 2.4f. OK-005 All Stations H/V
Figure 2.4g. OK-005 Site Average H/V
Figure 2.5a. OK-009 Geologic Map and Site Location
Figure 2.5b OK-009 Station Dispersion Pathways and Source Positions
Figure 2.5c. OK-009 Multimodal p-f Dispersion Images and Picks
Figure 2.5d. OK-009 Radial Component Dispersion Green's Function
Figure 2.5e. OK-009 Vs-Depth, Vs30, and Nearfield H/V Model
Figure 2.5f. OK-009 Map View Slow Thickness Variations and Maximum H/V
Figure 2.5g. OK-009 All Stations H/V
Figure 2.5h. OK-009 Site Average H/V
Figure 2.6a. TUL-1 Geologic Map and Site Location
Figure 2.6b. TUL-1 Station Dispersion Pathways and Source Positions
Figure 2.6c. TUL-1 R-, RZ-, and Z-Component Multimodal p-f Dispersion Images and Picks

Figure 2.6d. TUL-1 TT- and T-Component Multimodal p-f Dispersion Images and Picks

Figure 2.6e. TUL-1 TT Component Dispersion Green's Function

Figure 2.6f. TUL-1 RZ Component Dispersion Green's Function

Figure 2.6g. TUL-1 Love Wave Vs-Depth, Vs30, and H/V Model

Figure 2.6h. TUL-1 Rayleigh Wave Vs-Depth, Vs30, and H/V Model

Figure 2.6i. TUL-1 Rayleigh and Love Wave Vs-Depth Model Comparison

Figure 2.6j. TUL-1 All Stations H/V

Figure 2.6k. TUL-1 Site Average H/V

Figure 2.7a. V35A Geologic Map and Site Location

Figure 2.7b. V35A Station Dispersion Pathways and Source Positions

Figure 2.7c. V35A Multimodal p-f Dispersion Images and Picks

Figure 2.7d. V35A Vertical Component Dispersion Green's Function

Figure 2.7e. V35A Vs-Depth, Vs30, and Nearfield H/V Model

Figure 2.7f. V35A All Stations H/V

Figure 2.7g. V35A Site Average H/V

Figure 2.8a. W35A Geologic Map and Site Location

Figure 2.8b. W35A Station Dispersion Pathways and Source Positions

Figure 2.8c. W35A Multi-Component Multimodal p-f Dispersion Images and Picks

Figure 2.8d. W35A Vertical Component Dispersion Green's Function

Figure 2.8e. W35A Vs-Depth, Vs30, and Nearfield H/V Model

Figure 2.8f. W35A All Stations H/V

Figure 2.8g. W35A Site Average H/V

Figure 2.9a. W36A Geologic Map and Site Location

Figure 2.9b. W36A Station Dispersion Pathways and Source Positions

Figure 2.9c. W36A Multi-Component Multimodal p-f Dispersion Images and Picks

Figure 2.9d. W36A Vertical Component Dispersion Green's Function

Figure 2.9e. W36A Vs-Depth, Vs30, and Nearfield H/V Model

Figure 2.9f. W36A All Stations H/V

Figure 2.9g. W36A Site Average H/V

Figure 2.10a. WMOK Geologic Map and Site Location

Figure 2.10b. WMOK Station Dispersion Pathways and Source Positions

Figure 2.10c. WMOK Multi-Component Multimodal p-f Dispersion Images and Picks

Figure 2.10d. WMOK Vertical Component Dispersion Green's Function

Figure 2.10e. WMOK Vs-Depth, Vs30, and Nearfield H/V Model

Figure 2.10f. WMOK All Stations H/V

Figure 2.10g. WMOK Site Average H/V

Figure 2.11a. X34A Geologic Map and Site Location

Figure 2.11b. X34A Station Dispersion Pathways and Source Positions

Figure 2.11c. X34A Multi-Component Multimodal p-f Dispersion Images and Picks

Figure 2.11d. X34A Radial Component Dispersion Green's Function

Figure 2.11e. X34A Vs-Depth, Vs30, and Nearfield H/V Model

Figure 2.11f. X34A All Stations H/V

Figure 2.11g. X34A Site Average H/V

Figure 2.11h. X34A Average H/V at the Vault

Figure 3.1. TUL1 observed horizontal displacement spectra.

Figure 3.2. OK001 observed and predicted horizontal displacement spectra.

Figure 3.3. OK002 observed and predicted horizontal displacement spectra.

Figure 3.4. OK005 observed and predicted horizontal displacement spectra.

Figure 3.5. OK009 observed and predicted horizontal displacement spectra.
Figure 3.6. T34A observed and predicted horizontal displacement spectra.
Figure 3.7. U32A observed and predicted horizontal displacement spectra.
Figure 3.8. U35A observed and predicted horizontal displacement spectra.
Figure 3.9. V35A observed and predicted horizontal displacement spectra.
Figure 3.10. W35A observed and predicted horizontal displacement spectra.
Figure 3.11. W36A observed and predicted horizontal displacement spectra.
Figure 3.12. W37B observed and predicted horizontal displacement spectra.
Figure 3.13. W38A observed and predicted horizontal displacement spectra.
Figure 3.14. X35A observed and predicted horizontal displacement spectra.
Figure 3.15. X36A observed and predicted horizontal displacement spectra.
Figure 3.16. X37A observed and predicted horizontal displacement spectra.
Figure 3.17. X38A observed and predicted horizontal displacement spectra.
Figure 3.18. Y35A observed and predicted horizontal displacement spectra.
Figure 3.19. Y36A observed and predicted horizontal displacement spectra.
Figure 3.20. Y37A observed and predicted horizontal displacement spectra.
Figure 3.21. WMOK observed and predicted horizontal displacement spectra.
Figure 3.22. Response spectra for OK001, OK002, OK005, OK009, V35A, W35A, W36A, and WMOK compared with HVSR
Figure 3.23. Response spectra for T34A, U32A, U35A, W37B, W38A, X35A, X36A, and X37A compared with HVSR
Figure 3.24. Response spectra for X38A, Y35A, Y36A, and Y37A compared with HVSR

LIST OF TABLES

Table 2-1. Site-Specific Survey Data.....21
Table 3-1. Station Coordinates and Distance from Epicenter23
Table 3-2. Source and Attenuation Parameters24

1. INTRODUCTION

This study analyzes site effects associated with the Mw 5.6, 6 November 2011 Prague, Oklahoma earthquake, and provides new data from a targeted field-based investigation using active-source and three-component low frequency seismograph sensors to obtain surface geophysical data at strong motion sites across Oklahoma.

1.1 Background

In 2016-2017, the USGS initiated a similar effort to measure approximately 13 strong motion sites around the Fairview area and 15 sites in the vicinity of Cushing (Pers. Comm., Bill Stephenson, 2017). Some of these seismic monitoring stations are located in areas of high population densities in and around Oklahoma City, but most are spread across rural Oklahoma.

The work funded by this grant (award G17AP000021) directly addresses the priority topics for research outlined for Central Eastern United States (CEUS) in the FY2017 USGS Earthquake Hazards Program (EHP) External Research Support program announcement. This investigation directly addresses the priority topics for research outlined for the Central and Eastern U.S. (CEUS) in the FY2016 USGS Earthquake Hazards Program (EHP) External Research Support program announcement. These priority topics specifically state *“Another priority is an improved understanding of seismic wave propagation at local and regional distances using a combination of field observations, analysis of monitoring data and modeling approaches. Research activities that utilize monitoring data from the regional seismic and geodetic networks are strongly encouraged.”* In particular, the investigation seeks to characterize wave propagation and attenuation in the CEUS and also to improve estimates of site response using instrumental recordings and site-specific geophysical field measurements to characterize shallow geologic properties and velocity structure at existing and temporary seismic stations, directly in line with the CEUS **Element 1 (Regional earthquake hazards assessments)** priority specifically stipulated in the FY2016 EHP program announcement that states *“Constrain ground motions at seismograph stations through site characterization studies of existing ANSS and Transportable Array (TA) stations). Use of seismic data from ANSS and EarthScope TA or flexible array stations is encouraged.”* This work was performed using a methodology developed in collaboration with Dr. Steve Hartzell of the USGS.

Additionally, this work partially addresses a priority task identified in **Element 2, Research on Earthquake Effects**, by providing calculated amplification functions for the stations near Oklahoma City, which would provide new data for efforts to address the need to *“develop sedimentary basin amplification terms and regional amplification factors for deep soil sites that could be included in future building codes.”*

1.2 Project Objectives

Primary objectives of the field investigation were to determine the most efficient data acquisition and processing approaches to obtain robust estimates of seismometer site Vs-depth to at least 30 m depth, and to directly constrain site responses and site response variability by also collecting broadband three-component data to estimate H/V over an area around seismometer sites.

Primary objectives of the seismological site response investigation were to apply the Hartzell and Mendoza (2011) generalized inversion method to estimate site terms using earthquake ground motion data and compare site terms to site-survey estimates of Vs-depth and H/V to understand the most effective methods to acquire data to estimate ground motions for future earthquakes.

Secondary project objectives were to test various distributed 2D seismometer array distributions to acquire data and to test if sledgehammer-based vertical seismic sourcing was sufficient to obtain broadband constraints on surface-wave dispersion active-source surface-wave dispersion processing combined with a deconvolution approach to seismic interferometry.

2. SITE VS-DEPTH AND H/V INVESTIGATION

2.1 Data Acquisition

The authors worked with the USGS and the Oklahoma Geologic Survey to develop a list of target sites and gain property access. Geophysical surveys were obtained at eleven sites ([Figure 1.1](#)). We attempted to re-survey sites that Stephenson had surveyed in 2016-2017 to obtain overlapping data between the different field campaigns, but encountered access issues and were not successful.

For this investigation, Vs data were acquired at seismic monitoring stations area using varying 3D geometries deploying 15 Sigma4 3-component (3C) 2 Hz seismograph sensors using a hammer and strike plate active source approach outside the dimensions of each 3D array. Ideally, the array was centered about the seismograph station in a nominal “Y” or “K” shaped array. In some cases, site accessibility logistics required other array geometries. The 15 3C Sigma4 units each contain a vertical and two horizontal sensors, ultimately providing 45 channels. The Interferometric Multichannel Analysis of Surface Waves (IMASW) approach of O’Connell and Turner (2011) was used to calculate multi-component Rayleigh wave dispersion curves (e.g., vertical-vertical, vertical-radial, radial-radial, and all combinations therein). Site-specific subsurface velocity data were obtained to provide constraints on site ground conditions for calibration of seismic instrumentation and recorded ground motions.

The seismic data collected were used to develop multi-component Rayleigh wave dispersion, in some cases Love wave dispersion, dispersion Green’s Functions (DGFs), Sigma4 station pair pathway plots, best-fit Vs-depth and Vs30 site models, Horizontal to Vertical (H/V) ratios for each station, and a site-averaged H/V ratio. IMASW data collected for this study reduces uncertainty related to site response estimates, provides additional inputs for Next Generation Attenuation models (i.e., NGA3), and support development of single-station sigma models.

2.1.1 Testing of 2D Array Shapes

Permanent seismographic stations are typically located near property lines or amongst buildings, often limiting or preventing the ability to deploy seismometer arrays surrounding a permanent station with ideal shapes like a series of concentric circles or embedded triangles to employ processing techniques such as spatial autocorrelation or 2D slowness frequency analyses. The field project tested several 2D seismic array shapes that could be rapidly deployed using a measuring tape within single properties including Y-, K-, and truncated-star-shaped arrays.

Distributed 2D seismic arrays are more robust than linear seismic arrays because the point-spread (smearing) function for multiple dimension deconvolution (MDD) are better conditioned (are not singular) when inverted to obtain MDD estimates of Green’s functions between pairs of seismometers from seismometer arrays (Wapenaar et al., 2011). Distributed arrays also provided lateral averages over an area instead of a line which is better suited for modeling earthquake ground motions since seismic energy from multiple earthquakes may arrive at a site from many different azimuths. The distributed arrays used variable station spacing to ensure adequate spatial sampling close to seismometer vault locations to avoid spatial aliasing at high frequency while having sufficiently-wide array aperture to constrain low-frequency long-

wavelength dispersion. Distributed 2D array shapes ensure that estimated surface-wave dispersion is obtained from lateral spatial averages appropriate to estimate Vs-depth for earthquake ground motion modeling purposes.

2.1.2 Supplementary Source Type Testing

Ambient noise rarely contains sufficient high-frequency energy distributed over a range of azimuths to reliably estimate high-frequency dispersion. This field investigation began with conducting field testing to find an efficient zero-impact supplementary seismic sourcing approach to obtain high-frequency constraints on surface-wave dispersion and H/V. The complete surface-wave Green's function expressions from Haney and Nakahara (2016) shown in equations (1-5) below provide a means to investigate how different orientations of seismic sources as moment tensor components will excite surface waves as a function of frequency and surface-wave mode number. The displacement expressions in equations (1-5) are implicitly a function of wavenumber and source-receiver distance.

Let r be the distance between source and receiver, c be phase velocity (Love-wave for equations 1-2 and Rayleigh-wave for equations 3-5), U be group velocity (Love-wave for equations 1-2 and Rayleigh-wave for equations 3-5), $k_r = \omega/c$ be wavenumber where ω is angular frequency, h be the depth of the source, and z be the depth of the receiver, I_1 be the Love-wave eigenfunction as a function of depth, r_1 be the Rayleigh-wave horizontal eigenfunction as a function of depth, r_2 be the Rayleigh-wave vertical eigenfunction as a function of depth, ϕ be the azimuth in radians clockwise from north for a coordinate system where for $\phi = 0$ x is oriented north, y is oriented east, and z is oriented positive down. The seismic moment tensor source components are the set $[M_{xx}, M_{xy}, M_{xz}, M_{yx}, M_{yz}, M_{yy}, M_{zx}, M_{zy}, M_{zz}]$; including all nine moment tensors terms which independently allow for single couples like a transverse shear surface at the surface (M_{xy}). $H_m^{(1)}$ are Hankel functions of the first kind of integer order m . Love-wave displacement expressions as a summation over modes numbers n are shown in equations (1-2):

$$\begin{aligned}
u_x^{\text{LOVE}} = \sum_n \frac{il_1(z)}{8cUI_1} \times & \left[\frac{l_1(h)k_n}{2} \left((M_{xx} \cos \phi + M_{xy} \sin \phi) \right. \right. \\
& \left[H_1^{(1)}(k_n r) - \frac{\cos 2\phi}{2} [H_1^{(1)}(k_n r) - H_3^{(1)}(k_n r)] \right] \\
& - (M_{yx} \cos \phi + M_{yy} \sin \phi) [H_1^{(1)}(k_n r) \\
& - H_3^{(1)}(k_n r)] \frac{\sin 2\phi}{2} + 2 \frac{H_2^{(1)}(k_n r)}{k_n r} (M_{yx} \sin \phi \cos 2\phi \\
& + M_{xy} \cos \phi \sin 2\phi - M_{xx} \sin \phi \sin 2\phi \\
& - M_{yy} \cos \phi \cos 2\phi) \Big) + \frac{dl_1}{dz} \Big|_h \left(\frac{M_{xz}}{2} [H_0^{(1)}(k_n r) \right. \\
& \left. + H_2^{(1)}(k_n r) \cos 2\phi] + M_{yz} H_2^{(1)}(k_n r) \sin \phi \cos \phi \right) \Big], \tag{1}
\end{aligned}$$

$$\begin{aligned}
u_y^{\text{LOVE}} = \sum_n \frac{il_1(z)}{8cUI_1} \times & \left[\frac{l_1(h)k_n}{2} \left((M_{yx} \cos \phi + M_{yy} \sin \phi) \right. \right. \\
& \left[H_1^{(1)}(k_n r) + \frac{\cos 2\phi}{2} [H_1^{(1)}(k_n r) - H_3^{(1)}(k_n r)] \right] \\
& - (M_{xx} \cos \phi + M_{xy} \sin \phi) [H_1^{(1)}(k_n r) - H_3^{(1)}(k_n r)] \\
& \times \frac{\sin 2\phi}{2} + 2 \frac{H_2^{(1)}(k_n r)}{k_n r} (M_{xx} \sin \phi \cos 2\phi \\
& - M_{yy} \cos \phi \sin 2\phi + M_{yx} \sin \phi \sin 2\phi - M_{xy} \cos \phi \cos 2\phi) \Big) \\
& + \frac{dl_1}{dz} \Big|_h \left(\frac{M_{yz}}{2} [H_0^{(1)}(k_n r) - H_2^{(1)}(k_n r) \cos 2\phi] \right. \\
& \left. + M_{xz} H_2^{(1)}(k_n r) \sin \phi \cos \phi \right) \Big]. \tag{2}
\end{aligned}$$

For Rayleigh-waves the displacement expressions are:

$$\begin{aligned}
 u_z^{\text{RAYLEIGH}} = \sum_n \frac{ir_2(z)}{8cUI_1} \times & \left[\frac{r_1(h)k_n}{2} \left([H_0^{(1)}(k_n r) - H_2^{(1)}(k_n r)] \right. \right. \\
 & \times [M_{xx} \cos^2 \phi + (M_{xy} + M_{yx}) \sin \phi \cos \phi + M_{yy} \sin^2 \phi] \\
 & + 2 \frac{H_1^{(1)}(k_n r)}{k_n r} [M_{yy} \cos^2 \phi - (M_{xy} + M_{yx}) \sin \phi \cos \phi \\
 & \left. + M_{xx} \sin^2 \phi] \right) - \frac{dr_1}{dz} |_h H_1^{(1)}(k_n r) (M_{xz} \cos \phi \\
 & + M_{yz} \sin \phi) + r_2(h) k_n H_1^{(1)}(k_n r) (M_{zx} \cos \phi \\
 & \left. + M_{zy} \sin \phi) + \frac{dr_2}{dz} |_h H_0^{(1)}(k_n r) M_{zz} \right], \quad (3)
 \end{aligned}$$

$$\begin{aligned}
u_x^{\text{RAYLEIGH}} = & \sum_n \frac{ir_1(z)}{8cUI_1} \times \left[\frac{r_1(h)k_n}{2} \left((M_{xx}\cos\phi + M_{xy}\sin\phi) \right. \right. \\
& \times \left[H_1^{(1)}(k_nr) + \frac{\cos 2\phi}{2} [H_1^{(1)}(k_nr) - H_3^{(1)}(k_nr)] \right] \\
& + (M_{yx}\cos\phi + M_{yy}\sin\phi) [H_1^{(1)}(k_nr) - H_3^{(1)}(k_nr)] \\
& \times \frac{\sin 2\phi}{2} - 2 \frac{H_2^{(1)}(k_nr)}{k_nr} (M_{yx}\sin\phi \cos 2\phi \\
& + M_{xy}\cos\phi \sin 2\phi - M_{xx}\sin\phi \sin 2\phi \\
& - M_{yy}\cos\phi \cos 2\phi) \Big) + \frac{dr_1}{dz} \Big|_h \left(\frac{M_{xz}}{2} [H_0^{(1)}(k_nr) \right. \\
& - H_2^{(1)}(k_nr)\cos 2\phi] - M_{yz}H_2^{(1)}(k_nr)\sin\phi \cos\phi \Big) \\
& - r_2(h)k_n [H_0^{(1)}(k_nr) - H_2^{(1)}(k_nr)] (M_{zx}\cos\phi \\
& + M_{zy}\sin\phi) \frac{\cos\phi}{2} + r_2(h) \frac{H_1^{(1)}(k_nr)}{r} \\
& \times (M_{zy}\cos\phi - M_{zx}\sin\phi) \sin\phi \\
& \left. + \frac{dr_2}{dz} \Big|_h H_1^{(1)}(k_nr) M_{zz} \cos\phi \right], \tag{4}
\end{aligned}$$

$$\begin{aligned}
u_y^{\text{RAYLEIGH}} = & \sum_n \frac{ir_1(z)}{8cUI_1} \times \left[\frac{r_1(h)k_n}{2} \left((M_{yx} \cos \phi + M_{yy} \sin \phi) \right. \right. \\
& \times \left[H_1^{(1)}(k_n r) - \frac{\cos 2\phi}{2} [H_1^{(1)}(k_n r) - H_3^{(1)}(k_n r)] \right] \\
& + (M_{xx} \cos \phi + M_{xy} \sin \phi) [H_1^{(1)}(k_n r) \\
& - H_3^{(1)}(k_n r)] \frac{\sin 2\phi}{2} - 2 \frac{H_2^{(1)}(k_n r)}{k_n r} (M_{xx} \sin \phi \cos 2\phi \\
& - M_{yy} \cos \phi \sin 2\phi + M_{yx} \sin \phi \sin 2\phi \\
& - M_{xy} \cos \phi \cos 2\phi) \left. \right) + \frac{dr_1}{dz} \Big|_h \left(\frac{M_{yz}}{2} [H_0^{(1)}(k_n r) \right. \\
& + H_2^{(1)}(k_n r) \cos 2\phi] - M_{xz} H_2^{(1)}(k_n r) \sin \phi \cos \phi \left. \right) \\
& - r_2(h)k_n [H_0^{(1)}(k_n r) - H_2^{(1)}(k_n r)] (M_{zx} \cos \phi \\
& + M_{zy} \sin \phi) \frac{\sin \phi}{2} - r_2(h) \frac{H_1^{(1)}(k_n r)}{r} \\
& \times (M_{zy} \cos \phi - M_{zx} \sin \phi) \cos \phi \\
& \left. + \frac{dr_2}{dz} \Big|_h H_1^{(1)}(k_n r) M_{zz} \sin \phi \right]. \tag{5}
\end{aligned}$$

For surface-wave dispersion processing, it is best to not combine Love-wave and Rayleigh-wave energy on horizontal components of ground motion measurement because they have different but similar fundamental-mode phase-velocities. It is often necessary to estimate Rayleigh-wave phase velocities from radial-components over frequency bands where H/V becomes large and Rayleigh-wave energy on vertical components becomes small. Consequently, the best strategy is to find a seismic source configuration that does not produce Love-waves on radial-component ground motions because Love-wave energy could bias estimates of Rayleigh-wave phase velocities. For simplicity of discussion let $\phi=0$ so that the x component is the radial horizontal component and the y component is the transverse horizontal component. For a vertical source directed downward such as a hammer impact, only the M_{zz} component is nonzero to first order and only Rayleigh-wave displacements are nonzero on the vertical (z) and radial (x) components; the transverse component is zero because $\sin(\phi)=0$ in equation (5).

Compaction of soil can produce nonzero M_{xz} and M_{yz} shear components in the zone between zero compaction and maximum compaction.

Differential compaction during vertical seismic sources will produce vertical shearing of soil along the edges of a baseplate if the area of the baseplate is not sufficient. Examples of seismic sources that can produce significant excitation of M_{xz} and M_{yz} include soil compaction devices like slide hammers and some Vibroseis vehicles that have large hold-down weights relative to baseplate areas. Vibroseis vehicles with vertical vibrator masses can reduce M_{xz} and M_{yz} excitation by reducing drive levels in soft soil areas. Consequently, use of a baseplate of sufficient diameter to avoid significant concentrated soil compaction minimizes the M_{xz} and M_{yz} source shear terms that produce nonzero Love-wave horizontal displacements as well as transverse-component Rayleigh-wave displacements. The project used a steel plate with a vertically directed sledgehammer to reduce ground deformation to avoid leaving any marks on property which also minimized the M_{xz} and M_{yz} source shear terms to minimize excitation of Love-waves on the radial horizontal components so that unbiased estimates of Rayleigh-wave phase velocities could be obtained from radial-component ground motions at high frequencies; Love-wave phase velocities tend to be about 10% faster than Rayleigh-wave phase velocities.

For shear-wave refraction and Love-wave dispersion data acquisition excitation of the M_{xy} component will produce some Rayleigh-wave energy on the transverse horizontal component as shown in equation (4). Setting all the moment components to zero except the M_{xy} component and placing sources and receivers at the surface ($z=h=0$), the ratio of transverse Rayleigh-wave displacement to transverse Love-wave displacement for each mode is (equation 6):

$$\frac{u_y^{RAYLEIGH}}{u_y^{LOVE}} = \frac{r_1^2(0) c_L U_L}{l_1^2(0) c_R U_R}$$

(6)

Where c_L and U_L are Love-wave phase- and group-velocities respectively, c_R and U_R are Rayleigh-wave phase- and group-velocities respectively, $r_1(0)$ is the Rayleigh-wave horizontal displacement eigenfunction value at the free surface, and $l_1(0)$ is the Love-wave horizontal displacement eigenfunction value at the free surface. Thus, adding transverse horizontal shear source energy (M_{xy} shear component) to produce shear-waves and Love-waves produces transverse ground motions that are a superposition of Rayleigh- and Love-wave displacements. In contrast, using exclusively vertical excitation (M_{zz}) produces only Rayleigh-wave surface displacements since there is no M_{zz} term in the Love-wave displacements in equations (1-2). Consequently, the project exclusively used a vertically oriented sledgehammer striking a steel plate to maximize M_{zz} source-excitation and to minimize soil compaction to minimize M_{xz} and M_{yz} source excitation.

Anelastic attenuation limits observation of high-frequency fundamental-mode dispersion when there are low-Vs ($V_s < 300$ m/s) surficial deposits. Most of the fundamental mode energy is confined to depths of a third wavelength. So at high frequencies when $V_s < 300$ m/s and frequencies are > 30 Hz half-wavelengths will be < 3 m where Qs will generally be < 10 (Brocher, 2005). Consequently, at higher frequencies higher modes will dominate recorded ground motions because higher-mode eigenfunctions have significant

displacement below the shallow low Qs layer and allow higher-modes to “tunnel” beneath the shallow low Qs layer. Sigma4 51020 suffered some sort of sensor malfunction during the OK-005 deployment that produced spurious H/V responses, particularly at low frequencies. Sigma4 51020 appears to exhibit the sensor malfunctions that corrupted low-frequency H/V up to survey W35A (bad for surveys OK-005, V35A, WMOK, and X34A) and then seems fine for survey W36A and the two later surveys that used it (FNO and TUL1).

2.2 Data Processing

All processing methods require that all components have the same amplitude and phase responses. The Sigma4 seismographs have nominal 2 Hz sensors, but actual individual component sensor natural periods vary from 2.0 Hz to 2.25 Hz, damping varies up to nearly 9%, and generator constants vary up to nearly 7%. Consequently, the calibration data for each component of the 15 Sigma4 seismographs (natural frequency, damping, and generator constant), were used to create a transfer function so that each component had the response of the average response of all the components (natural frequency of 2.125 Hz, damping of 0.522, and generator constant of 27.40 V/in/s). Since the data are recorded in one-minute blocks each one-minute block from each component was corrected to the common instrument response as the initial processing step.

Subsequent processing consists of these three steps, detailed in subsections 2.2.1, 2.2.2, and 2.2.3

1. H/V analyses
2. Generate tensor Green’s functions using deconvolution interferometry with all station pairs
3. Jointly invert Rayleigh-wave dispersion and H/V for Vs-depth.

2.2.1 H/V Processing

Multi-taper Fourier spectra were calculated using five orthogonal 3π Slepian tapers applied to two overlapping 32.768-second-long records spanning each one-minute data block. Individual time-window H/V ratios were calculated for each horizontal component from the log-averages of the multi-taper orthogonal estimates of Fourier spectra of each component. Each station’s horizontal component H/V was calculated from an alpha-trimmed log-mean of all the time-windows with H/V estimates; the data in the upper and lower 20% tails were excluded from the log-means. The station-average H/V was calculated as the log-mean of all horizontal components’ H/V at each frequency.

2.2.2 Ambient-Noise Interferometry: Tensor Green’s Function Processing

The most widely used application of ambient-noise interferometry is the retrieval of seismic surface waves between seismometers from continuous recordings of Earth noise. Wapenaar et al. (2011) provides a summary discussion and references (Section 6.1 therein). Earth noise tends to be deficient in high frequencies so additional high-frequency energy is often imparted around seismometer arrays to provide high-frequency energy to better resolve shallow velocity structure. We used a sledge-hammer and impact plate to provide supplemental high-frequency seismic excitation at varying distances and azimuths outside the edges of the seismic receiver arrays.

Processing of all nine component combinations of three-component motions from receiver pairs yields a tensor Green's function. The tensor Green's function is essential to resolve fundamental mode dispersion when Rayleigh-wave polarization becomes almost exclusively horizontal at site resonant frequencies. In the frequency-bands of site resonance the radial-radial (RR) Green's function component provides good signal-to-noise to measure fundamental-mode phase velocities whereas the vertical-vertical (ZZ) Green's function has too little motion to measure fundamental-mode phase velocities in the neighborhood of site resonant frequencies. Haney et al. (2012) present analyses showing that the radial-vertical (ZR-RZ) Green's function components can provide valuable constraints on Rayleigh-wave dispersion even when effective source excitation has poor azimuthal coverage.

Wapenaar et al. (2011) show that multidimensional deconvolution (MDD) is most likely to produce the best estimates of tensor Green's functions. In particular, if tensor Green's function amplitudes are needed MDD processing is really the only approach that has the potential to recover realistic amplitudes over wide frequency bands since MDD is the most effective method when source excitation is irregular in space and frequency. Wapenaar et al. (2011) note that MDD requires matrix inversion which can be unstable. The stability of MDD matrix inversion depends on the number of available sources, source aperture, source bandwidth and, for multicomponent data, on the number of independent source components. Thus, MDD requires spectral analyses of the point-spread function to determine what spatial and temporal frequencies can be resolved with matrix inversion (van der Neut et al., 2011). Consequently, MDD is not well-suited for semi-automated processing.

We use phase-stacking (O'Connell and Turner, 2011), which does not require rigorous recovery of Green's function amplitudes, to estimate Rayleigh-wave phase-velocities from offset gathers of station-pair Green's function. The priority for phase-stack processing is to obtain Green's function responses over as wide a frequency bandwidth as possible. Only first-order relative amplitude responses are needed within single Green's function components from single station pairs to successfully estimate slowness-frequency using phase stacking. Thus, we seek an ambient-noise interferometry processing approach that maximizes Green's function frequency bandwidth and is robust when implemented as a semi-automated processing sequence.

Vasconcelos and Snieder (2008) demonstrated that scalar deconvolution interferometry successfully recovers elastic impulse response between two receivers without the need for an independent estimate of the source function. Deconvolution interferometry provides wave arrivals with correct kinematics but distorted amplitudes (Draganov et al., 2006; Vasconcelos and Snieder, 2008) which makes deconvolution interferometry well suited for our phase-stack approach to estimate phase velocities. Also scalar deconvolution produces the maximum frequency bandwidth that can be achieved relative to cross correlation (Vasconcelos and Snieder, 2008). Thus, scalar deconvolution ensures that correct wave kinematics are recovered over the maximum frequency bandwidth that is possible. For these reasons we adapted the scalar deconvolution approach from Vasconcelos and Snieder (2008) to estimate each component of the tensor Green's function from each pair of three-component seismometers.

After correction to common instrument response, the three-component motions are rotated into radial and transverse horizontal components relative to the azimuth joining the receiver pairs to start the interferometric processing. We use relatively short time windows that are long enough to contain all surface-wave arrivals for the maximum receiver-pair offsets after deconvolution. We use a prewhitening scheme similar to Bensen et al. (2007) to produce independent prewhitening data for each component for each time window. The short time windows are overlapped by half the window length which allows subsets of data to be deconvolved with time-variation whitening to obtain more deconvolution estimates of Green's functions for the relatively short fixed recording durations at each site of about one hour. Each short time window of each component of ground motion is whitened using three successive operations. First amplitudes are regularized in the time domain with an automatic gain control (AGC) operator with an operator length of 0.12 s. Second, the frequency response is whitened by dividing the Fourier transform of the AGC output by the mean of its multitaper estimate of the Fourier amplitude response using five 3π Slepian tapers and the data is returned to the time domain via inverse Fourier transform. Third, the same AGC operator used in the first preprocessing step is applied to the time-domain data output of the second preprocessing step and then transformed to frequency with a forward Fourier transform in preparation for frequency-domain deconvolution.

The numerical implementation of deconvolution from Vasconcelos and Snieder (2008) is based on water-level deconvolution (Clayton and Wiggins, 1976) given by (equation 7):

$$D_{AB} = \frac{u(\mathbf{r}_A, \mathbf{s})}{u(\mathbf{r}_B, \mathbf{s})} \approx \frac{u(\mathbf{r}_A, \mathbf{s})u^*(\mathbf{r}_B, \mathbf{s})}{|u(\mathbf{r}_B, \mathbf{s})|^2 + \varepsilon \langle |u(\mathbf{r}_B, \mathbf{s})|^2 \rangle} \quad (7)$$

where \mathbf{s} is the vector of source positions, $\langle |u(\mathbf{r}_B, \mathbf{s})|^2 \rangle$ is the average of the power spectrum of data measured at receiver \mathbf{r}_B , $\langle |u(\mathbf{r}_A, \mathbf{s})|^2 \rangle$ is the average of the power spectrum of data measured at receiver \mathbf{r}_A . The water-level damping parameter ε is selected to stabilize the deconvolution. In the absence of our three-step amplitude and spectral whitening processing when ε is too small the deconvolution becomes unstable. When ε is too large the deconvolution approaches the result of cross-correlation eliminating the advantages of deconvolution.

One advantage of our three-stage prewhitening process for each short time window prior to deconvolution is that a relatively small value of ε ensures the stability of deconvolution while retaining the advantages of deconvolution over cross correlation because ε is small; we use $\varepsilon = 1\%$ of the mean of $\langle |u(\mathbf{r}_B, \mathbf{s})|^2 \rangle$ below a maximum frequency of interest. The second advantage of our prewhitening process prior to deconvolution is that a second deconvolution can be produced by interchanging $\langle |u(\mathbf{r}_A, \mathbf{s})|^2 \rangle$ and $\langle |u(\mathbf{r}_B, \mathbf{s})|^2 \rangle$ in equation (7) so that there are two deconvolution estimates of the forward and reverse-time Green's functions for the station pair to average to further reduce the influence of ε and obtain more robust estimate of Green's functions. All the individual time window estimates of Green's function components are summed to produce the final estimates of tensor Greens' functions for each station pair.

2.2.3 Joint Inversion of Rayleigh-Wave Dispersion and H/V for Vs-Depth

Halliday and Curtis (2008) and Kimman and Trampert (2010) show that, when primary seismic sources are confined to the free surface, cross-correlation gives rise to spurious interferences between higher-order modes and the fundamental mode, whereas the presence of seismic sources at depth enables the correct recovery of all modes independently (Wapenaar & Fokkema 2006). In an urban environment there may be some seismic sources at depth due to pumps and other subterranean infrastructure but most seismic noise sources are usually located at the free surface consisting primarily of traffic noise. Consequently, we only use fundamental-mode dispersion data from ambient-noise interferometry and active-source stacks of slowness-frequency estimates in the objective functions for joint inversion of dispersion data and H/V data for Vs-depth. Sledge hammer sourcing in stationary phase regions outside the seismic receiver arrays often produces seismic records with sufficient signal-to-noise to constrain higher-mode dispersion, and higher-mode phase velocity can be used as additional constraints on Vs-depth.

Tuan (2009) showed that H/V responses are essentially the same in cases of large shallow impedance contrasts whether H/V is modelled as surface waves or vertically-propagating body waves. In typical soil-cover site conditions, it is appropriate to model H/V responses as vertically propagating shear-waves instead of fundamental-mode surface waves. Thus, model H/V is calculated as the low-strain amplification of the *nrattle* SH-viscoelastic propagator (Boore, 2015) with seismic energy vertically-incident from seismic basement located at the bottom of the velocity models.

Downhill simplex joint-inversion fundamental-mode phase velocities and H/V used a starting model produced using the linearized initial dispersion inversion approach of O'Connell and Turner (2011). The key characteristic to match from H/V observations is the frequency of maximum H/V. Since the wave-type composition contributing to produce H/V is in general not known, it is not realistic to expect to fit absolute amplitudes of H/V with amplification estimates from an SH propagator. However, it is instructive to search for models that reproduce the first order shape of H/V as a function of frequency while simultaneously fitting available phase velocity data. It was necessary to adjust the relative misfit weights of H/V misfit and phase-velocity misfit during iterative inversion for Vs-depth to avoid having H/V dominate the inversion. Models that reproduced H/V shape were always required to reproduce observed phase dispersion within measurement uncertainties.

2.3 Vs-Depth and H/V Data

Site descriptions and data summaries for each of the eleven seismic stations are presented below. Station locations are shown in Figure 1.1. Each subsection includes a review of the geology at the station and the results of the Vs-Depth and H/V analysis. Results are presented for each station in Figure 2.1 through 2.11. A discussion of the relationship of these results to bedrock geology is presented in section 2.4.

2.3.1 FNO

FNO station is located on early Permian shale and siltstone, Pfa, (Heran, et al., 2003; USGS, 2005) (Figures 1.2, 2.1a), in a forested area bounded by a fence north of the vault resulted in an irregular 2D array geometry. Active sourcing was limited to the north, and more azimuthal coverage and offset emanated from the southern quadrants. Figure 2.1b shows the station pair raypaths used to generate dispersion images,

nominal hammer source positions and offsets, and omitted Sigma4 station that had a faulty GPS. [Figure 2.1c](#) provides three dispersion plots with multimodal picks; all picks derived from all three images are combined on each image: from top to bottom: top) Hammer-blow R-component phase stack, mid) Dispersion Green's Function (DGF) vertical-vertical component phase stack, and bottom) DGF radial-radial component phase stack ([Figure 2.1c](#)). Fundamental mode picks on the R- and ZZ- plots are constrained from 5 to 40 Hz and higher mode picks on the R- and RR- plots from 13 to 67 Hz ([Figure 2.1c](#)). [Figure 2.1d](#) shows the DGF for the ZZ-component with first arrival fit line.

The [Figure 2.1e](#) upper plot provides the Vs-depth plot with 1/3 wavelength depth resolution limit; Vs30 is 548 m/s, Vs-depth at FNO is constrained to approximately 50 meters depth, and we interpret the station to be placed on soil approximately 2m thick with Vs ~300-400 m/s, weathered/saprolitic bedrock from 2-14 m depth with velocities around 400-650 m/s, and underlying bedrock velocity of 900 m/s to the 50-meter resolution limit. The middle plot shows model vs. picked fundamental and higher modes. The lower plot shows the H/V ratios for the five Sigma4 stations nearest the FNO vault, which peaks at H/V=2.3 at 7.5 Hz, with a broadband secondary peak H/V= 1.5-1.8 from 22 to 39 Hz ([Figure 2.1e](#)).

[Figure 2.1f](#) provides H/V for each of the 15 Sigma4 stations from 0.1 to 100 Hz, and the site mean maximum H/V of 3.0. [Figure 2.1g](#) provides the average H/V curve from all 15 Sigma4 Stations combined as an Ln mean, smooth mean, and 1 σ uncertainty bounds.

2.3.2 OK-001

OK-001 station is located inside a school building approximately 93 meters north-northeast of the survey array, which was collected on an adjacent football field ([Figure 2.2a](#)); and the school grounds are located on a Pleistocene sand and gravel (Qt) inset into Paleozoic bedrock ([Figure 1.2](#)) (Heran, et al., 2003; USGS, 2005). [Figure 2.2b](#) shows the 3-pronged array geometry, the station pair raypaths used to generate dispersion images, nominal hammer source positions and offsets, and omitted Sigma4 location that had a faulty GPS. [Figures 2.2c and 2.2d](#) each provide three dispersion plots with multimodal picks; all picks derived from all six dispersion images are combined and plotted on each dispersion image: from top to bottom on [Figure 2.2c](#): top) Hammer-blow Z-component phase stack, mid) DGF vertical-vertical component phase stack, and bottom) DGF radial-radial component phase stack. From top to bottom on [Figure 2.2d](#): top) R-component phase stack, mid) DGF vertical-radial phase stack, bottom) DGF radial-radial phase stack. Fundamental mode picks on the DGF RR image are constrained from 5 to 18 Hz and higher mode picks on remaining dispersion plots from 6 to 80 Hz ([Figures 2.2c, 2.2d](#)). [Figure 2.2e](#) shows the DGF for the RR-component with first arrival fit line, which is better constrained at near offset (2-30 m) and less so from 30 to 65 m.

The upper plot on [Figure 2.2f](#) provides the Vs-depth curve with 1/3 wavelength depth resolution limit; Vs30 is 542 m/s, Vs-depth at OK-001 is constrained to approximately 32 meters depth, and we interpret the station to be placed on weathered/saprolitic bedrock from 0-6 m depth with velocities around 300-400 m/s, and underlying bedrock velocity of 600-700 m/s to the 32 m depth resolution limit. The middle plot shows model vs. picked fundamental and higher modes. The lower plot shows the H/V ratios for four Sigma4

stations near the center of the three-pronged array, with H/V peaks at ~ 1.8 at 13 Hz, ~ 1.7 at 38-42 Hz (Figure 2.2f).

Figure 2.2g provides H/V for each of the 15 Sigma4 stations from 0.1 to 100 Hz, and the site mean maximum H/V of 6.5. Figure 2.2h provides the average H/V curve from all 15 Sigma4 Stations combined as an Ln mean, smooth mean, and 1σ uncertainty bounds.

2.3.3 OK-002

OK-002 is located on private property approximately 150 meters south-southeast of the survey array (Figure 2.3a). Due to access limitations, OK-002 was a linear array collected along the nearest accessible right of way (Figure 2.3a). Bedrock is composed of Permian sandstone and conglomerate (Heran, et al., 2003; USGS, 2005) (Figure 1.2); bedrock outcrops were observed along the road cut adjacent to the seismic survey, but ground conditions at the seismograph vault were unable to be assessed. Figure 2.3b shows the six-station linear array geometry, the station pair raypaths used to generate dispersion images which are limited to nominal E-W azimuthal coverage with limited offset, and nominal hammer source positions and offsets. Figures 2.3c and 2.3d provide three and two dispersion plots, respectively, with multimodal picks; all picks derived from all five dispersion images are combined and plotted on each dispersion image: from top to bottom on Figure 2.3c: top) DGF ZZ-component phase stack, mid) DGF ZR component phase stack, and bottom) hammer blow Z-component phase stack, and on Figure 2.2d: top) DGF TT-component phase stack, and bottom) hammer blow T-component phase stack. Fundamental mode picks are composited from the DGF ZZ stack (1.5-14 Hz), ZR stack (24-30 Hz), and TT stack (17-25 and 42-46 Hz). Higher mode picks are based on compositing portions of all five dispersion plots from 8 to 45 Hz (Figures 2.3c, 2.3d). Figure 2.3e shows the DGF for the TT-component, and Figure 2.3f shows the DGF ZZ-component with first arrival fit lines spanning the ~ 87 m array total offset.

Two dispersion models for OK-002 are presented, a Love wave and a Rayleigh wave model. The upper plot on Figure 2.3g presents the Love wave model; the Vs-depth curve with 1/3 wavelength depth resolution limit; Vs30 is 567 m/s, Vs-depth at OK-002 is constrained to approximately 72 meters depth. The Rayleigh wave model is shown in Figure 2.3h. We interpret the station to be placed on saprolite from 0-6 m depth with velocities around 300-400 m/s, with an underlying bedrock weathering profile from ~ 6 to 30 m depth. The Love wave model 1/3 wavelength resolution limit is 72 m depth, and the Rayleigh wave model resolution limit is? 100 m depth (Figures 2.3g, 2.3h). Unweathered bedrock velocity is ~ 980 m/s from 45 m depth to the resolution limit. The middle plot shows model vs. picked fundamental and higher modes. The lower plot shows the modeled H/V ratio at the survey site, with H/V peak at ~ 2 at 10 Hz (Figure 2.3h).

Figure 2.3i provides H/V for each of the 6 Sigma4 stations from 0.1 to 100 Hz, and the site mean maximum H/V of 1.9. Figure 2.3j provides the average H/V curve from six Sigma4 Stations combined as an Ln mean, smooth mean, and 1σ uncertainty bounds.

2.3.4 OK-005

OK-005 is located inside a school building approximately 93 meters east north-east of the survey array, which was collected on an adjacent football field (Figure 2.4a); and the school grounds are located on a

Pleistocene sand and gravel (Qt) inset into Paleozoic bedrock (Figure 1.2) (Heran, et al., 2003; USGS, 2005). Figure 2.4b shows the 3-pronged array geometry, the station pair raypaths used to generate dispersion images, nominal hammer source positions and offsets, and omitted Sigma4 location that had a faulty GPS. Figures 2.4c and 2.4d each provide three dispersion plots with multimodal picks; all picks derived from all six dispersion images are combined and plotted on each dispersion image: from top to bottom on Figure 2.4c: top) Hammer-blow Z-component phase stack, mid) DGF vertical-vertical component phase stack, and bottom) DGF radial-radial component phase stack. From top to bottom on Figure 2.4d: top) R-component phase stack, mid) DGF vertical-radial phase stack, bottom) DGF radial-radial phase stack. Fundamental mode picks on the DGF RR image are constrained from 5 to 18 Hz and higher mode picks on remaining dispersion plots from 6 to 80 Hz (Figures 2.4c, 2.4d). Figure 2.4e shows the DGF for the RR-component with first arrival fit line, which is better constrained at near offset (2-30 m) and less so from 30 to 65 m.

The upper plot on Figure 2.4f provides the Vs-depth curve with 1/3 wavelength depth resolution limit; Vs30 is 542 m/s, Vs-depth at OK-005 is constrained to approximately 32 meters depth, and we interpret the station to be placed on weathered/saprolitic bedrock from 0-6 m depth with velocities around 300-400 m/s, and underlying bedrock velocity of 600-700 m/s to the 32 m depth resolution limit. The middle plot shows model vs. picked fundamental and higher modes. The lower plot shows the H/V ratios for five Sigma4 stations near the center of the three-pronged array, with H/V peaks at ~1.8 at 13 Hz, ~1.7 at 38-42 Hz (Figure 2.4f).

Figure 2.4g provides H/V for each of the 15 Sigma4 stations from 0.1 to 100 Hz, and the site mean maximum H/V of 6.5. Figure 2.4h provides the average H/V curve from all 15 Sigma4 Stations combined as an Ln mean, smooth mean, and 1 σ uncertainty bounds.

2.3.5 OK-009

OK-009 station is located inside a school building approximately 170-180 m west northwest of the survey array, which was collected on an adjacent open field (Figure 2.5a); and the school grounds are located on early Permian sandstone (Pg) (Figure 1.2) (Heran, et al., 2003; USGS, 2005). Figure 2.5b shows the 3-pronged array geometry, the station pair raypaths used to generate dispersion images, nominal hammer source positions and offsets, and omitted Sigma4 location that had a faulty GPS. Figure 2.5c provides three dispersion plots with multimodal picks; all picks derived from all three dispersion images are combined and plotted on each dispersion image: top) DCG radial-radial component phase stack, mid) DGF vertical-vertical component phase stack, and bottom) DGF vertical-radial component phase stack. Fundamental mode picks on the DGF RR image are constrained from 4 to 38 Hz and higher mode picks on remaining dispersion plots from 21 to 40 Hz. Figure 2.5d shows the DGF for the RR-component with first arrival fit line.

The lower plot on Figure 2.5e provides the Vs-depth curve; Vs30 is 355 m/s, Vs-depth at OK-009 is constrained to approximately 32 meters depth, and we interpret the station to be placed on weathered/saprolitic bedrock from 0-6 m depth with velocities < 200 m/s, and underlying bedrock velocities ranging from 400-700 m/s to the 32m depth resolution limit. The middle plot shows model vs. picked

fundamental and higher modes. The upper plot shows the observed vs. modeled H/V ratios, with H/V peaking at 2.7 at 6-7 Hz (Figure 2.5e).

Figure 2.5f provides a plot of each Sigma4 location symbolized as functions of peak H/V by color and Slow Thickness in meters by size to demonstrate the high lateral variability measured at the OK-009 site. Figure 2.5g provides H/V for each of the 15 Sigma4 stations from 0.1 to 100 Hz, and the site mean maximum H/V of 5.4. Figure 2.5h provides the site average H/V curve from all 15 Sigma4 Stations combined as an Ln mean, smooth mean, and 1σ uncertainty bounds.

2.3.6 TUL-1

TUL-1 station location is on OSU property, inside a fence which constrained the array geometry, and is positioned adjacent to an open steel cased well (which could potentially provide a good location for a downhole log for future studies) (Figure 2.6a); the site is (regionally) mapped as Middle Pennsylvanian shale (lpw), but we observed weathered/oxidized sandstone boulders and in-place outcrops across the ridge top, so more detailed mapping may be warranted (Figure 1.2) (Heran, et al., 2003; USGS, 2005). Figure 2.6b shows the irregular array geometry, the station pair raypaths used to generate dispersion images, and nominal hammer source positions and offsets. Figure 2.6c provides three dispersion plots and Figure 2.6d shows two additional plots with multimodal picks: Figure 2.6c top) hammer blow radial component phase stack, mid) DGF radial-vertical component phase stack, and bottom) hammer blow vertical component phase stack, and Figure 2.6d top) DGR T-T component phase stack and bottom) hammer-blow T-component. Fundamental mode picks on the DGF TT image are constrained from 5 to 23 Hz and higher mode picks on remaining dispersion plots are constrained from 4 to 70 Hz. Figure 2.6e shows the DGF for the TT-component, and Figure 2.6g for the RZ-component with first arrival fit line.

The upper plot on Figure 2.6g provides the Love-wave derived Vs-depth curve and 1/3 wavelength depth resolution limit; Vs30 is 741 m/s, Vs-depth at OK-009 is constrained to approximately 93 meters depth, and we interpret the station to be placed on weathered/saprolitic bedrock from 0-8 m depth with velocities from 300-400 m/s, and underlying bedrock velocities ranging from 1.2 to 1.4 km/s from 8 to 40 m, and >1.6 km/s below to the resolution limit. The middle plot shows model vs. picked fundamental and higher modes. The lower plot shows the site-average and modeled H/V ratios for all Sigma4, with site average H/V peaking at 4.3 at 15 Hz (Figure 2.6g). For comparison, Figure 2.6h shows the Rayleigh wave-derived Vs- and Vp-depth curves; this method estimates Vs30 of 694 m/s and comparable Vs-depth structure. Figure 2.6i compares the Love- and Rayleigh wave-derived Vs-depth plots directly.

Figure 2.6j provides H/V for each of the 15 Sigma4 stations from 0.1 to 100 Hz, and the site mean maximum H/V of 7.2. Figure 2.6k provides the site average H/V curve from all 15 Sigma4 Stations combined as an Ln mean, smooth mean, and 1σ uncertainty bounds.

2.3.7 V35A

V35A is located in a field on an adjacent property approximately 200-210 m southeast of the survey array (Figure 2.7a); and this survey and the seismograph are located on Late Pennsylvanian shale (Figure 1.2) (Heran, et al., 2003; USGS, 2005). Figure 2.7b shows the 3-pronged array geometry, the station pair

raypaths used to generate dispersion images, nominal hammer source positions and offsets, and omitted Sigma4 location that had a faulty GPS. [Figure 2.7c](#) provides three dispersion plots with multimodal picks; all picks derived from all three dispersion images are combined and plotted on each dispersion image: top) hammer-blow radial component phase stack, mid) DGF vertical-vertical component phase stack, and bottom) hammer-blow vertical component phase stack. Fundamental mode picks on the hammer blow vertical image are constrained from 11 to 33 Hz and higher mode picks on remaining dispersion plots are constrained? from 7 to 69 Hz. [Figure 2.7d](#) shows the DGF for the RR-component with first arrival fit line.

The upper plot on [Figure 2.7e](#) provides the Vs-depth curve; Vs30 is 580 m/s, Vs-depth at V35A is constrained to approximately 36 meters depth, and we interpret the station to be placed on weathered/saprolitic bedrock to 7-10m depth with velocities < 350 m/s, and underlying bedrock velocities ranging from 600-800 m/s to the 32 m depth resolution limit. The middle plot shows model vs. picked fundamental and higher modes. The lower plot shows the modeled H/V ratios vs. those measured by the central two stations, with H/V peaking at 2.5 at 11 Hz ([Figure 2.7e](#)).

[Figure 2.7f](#) provides H/V for each of the 15 Sigma4 stations from 0.1 to 100 Hz, and the site mean maximum H/V of 4.0. [Figure 2.7g](#) provides the site average H/V curve from all 15 Sigma4 Stations combined as an Ln mean, smooth mean, and 1 σ uncertainty bounds.

2.3.8 W35A

W35A station is located in a pasture near a fence. The survey array is centered about the vault with four array legs ([Figure 2.8a](#)). The strong motion station is located on early Permian shale (Pw) ([Figure 1.2](#)) (Heran, et al., 2003; USGS, 2005). [Figure 2.8b](#) shows the 4-pronged array geometry, the station pair raypaths used to generate dispersion images, nominal hammer source positions and offsets, and omitted Sigma4 location that had a faulty GPS. [Figure 2.8c](#) provides three dispersion plots with multimodal picks; all picks derived from all three dispersion images are combined and plotted on each dispersion image: top) DGF vertical-vertical component phase stack, mid) hammer-blow vertical component phase stack, and bottom) DGF vertical-radial component phase stack. Fundamental mode picks on the DGF vertical-vertical image are constrained from 5 to 50 Hz and higher mode picks on remaining dispersion plots from 30 to 75 Hz. [Figure 2.8d](#) shows the DGF for the ZZ-component with first arrival fit line.

The upper plot on [Figure 2.8e](#) provides the Vs-depth curve; Vs30 is 494 m/s, Vs-depth at W35A is constrained to approximately 31 meters depth, and we interpret the station to be placed on weathered/saprolitic bedrock to 10 m depth with velocities < 380 m/s, and underlying bedrock velocities ranging from 500-640 m/s to the 31 m depth resolution limit. The middle plot shows model vs. picked fundamental and higher modes. The lower plot shows the modeled H/V ratios vs. measured by the central (nearest to the vault) five stations, with H/V peaking at 2.3 at 43 Hz on Sigma4 51006 ([Figure 2.8e](#)).

[Figure 2.8f](#) provides H/V for each of the 15 Sigma4 stations from 0.1 to 100 Hz, and the site mean maximum H/V of 2.0. [Figure 2.8g](#) provides the site average H/V curve from all 15 Sigma4 Stations combined as an Ln mean, smooth mean, and 1 σ uncertainty bounds.

2.3.9 W36A

W36A station is located on private property approximately 620 meters south of the survey array ([Figure 2.9a](#)). Due to access limitations, W36A was a linear array collected along the nearest accessible right of way ([Figure 2.9a](#)). Bedrock is composed of middle Pennsylvanian sandstone (IPca) (Heran, et al., 2003; USGS, 2005) ([Figure 1.2](#)); bedrock outcrops were observed along the roadcut adjacent to the seismic survey, but ground conditions at the strong motion vault were unable to be assessed. [Figure 2.9b](#) shows the six-station linear array geometry, the station pair raypaths used to generate dispersion images limited to nominal E-W azimuthal coverage with limited offset, and nominal hammer source positions and offsets. [Figures 2.9c](#) provides three dispersion plots with multimodal picks; all picks derived from all three dispersion images are combined and plotted on each dispersion image: from top to bottom: top) hammer blow Z-component phase stack, mid) DGF ZZ component phase stack, and bottom) hammer blow R-component phase stack. Fundamental mode picks are constrained from 5 to 22 Hz by the DGF ZZ-component stack. Higher mode picks are based on compositing portions of the three dispersion plots from 15 to 60 Hz ([Figure 2.9c](#)). [Figure 2.9d](#) shows the DGF for the ZZ-component.

The upper plot on [Figure 2.9e](#) provides the Vs-depth curve with 1/3 wavelength depth resolution limit; Vs30 is 670 m/s, Vs-depth at W36A is constrained to approximately 72 meters depth. We interpret the station to be placed on saprolite/weathered bedrock from 0-5 m depth with velocities around 330-500 m/s, and underlying unweathered bedrock velocity of 800 m/s to resolution depth ([Figure 2.9e](#)). The middle plot shows model vs. picked fundamental and higher modes. The lower plot shows the modeled and measured H/V ratio from 5 Sigma4s ([Figure 2.9e](#)).

[Figure 2.9f](#) provides H/V for each of the 6 Sigma4 stations from 0.1 to 100 Hz, and the site mean maximum H/V of 3.7. [Figure 2.9g](#) provides the average H/V curve from six Sigma4 Stations combined as an Ln mean, smooth mean, and 1 σ uncertainty bounds.

2.3.10 WMOK

WMOK station is a granitic bedrock site, and is the furthest station from the Prague event that was measured for this study. The survey array was limited by outcrop to the east and west, so we centered a ring of sensors about the vault with two array legs extending north-south ([Figure 2.10a](#)). The strong motion station is located on middle Cambrian granite of the Wichita Mountains (Cwg) ([Figure 1.2](#)) (Heran, et al., 2003; USGS, 2005). [Figure 2.10b](#) shows the 2-pronged and ring array geometry, the station pair raypaths used to generate dispersion images, nominal hammer source positions and offsets, and omitted Sigma4 location that had a faulty GPS. [Figure 2.10c](#) provides three dispersion plots with multimodal picks; all picks derived from all three dispersion images are combined and plotted on each dispersion image: top) hammer blow vertical component phase stack, mid) hammer-blow radial component phase stack, and bottom) DGF vertical-vertical component phase stack. Fundamental mode picks on the hammer blow vertical image are constrained from 16 to 53 Hz and higher mode picks on remaining dispersion plots from 30 to 79 Hz. [Figure 2.10d](#) shows the DGF for the ZZ-component with first arrival fit line.

The upper plot on [Figure 2.10e](#) provides the Vs-depth curve; Vs30 is 1821 m/s, Vs-depth at WMOK is constrained to approximately 36 meters depth, and we interpret the station to be placed directly into granitic

bedrock with a thin weathered zone in the upper 5 meters with $V_s > 1100$ m/s, and > 2100 m/s below. The middle plot shows model vs. picked fundamental and higher modes. The lower plot shows the modeled H/V ratios vs. those measured by the central (nearest to the fault) Sigma4 station, with H/V peaking at 2.3 at 43 Hz on Sigma4 51002 ([Figure 2.10e](#)).

[Figure 2.10f](#) provides H/V for each of the 15 Sigma4 stations from 0.1 to 100 Hz, and the site mean maximum H/V of 4.2. [Figure 2.10g](#) provides the site average H/V curve from all 15 Sigma4 Stations combined as an Ln mean, smooth mean, and 1σ uncertainty bounds.

2.3.11 X34A

X34A station is located in a field, and the Sigma4 survey array is 3-pronged and centered about the vault ([Figure 2.11a](#)), which is located on alluvial floodplain deposits overlying early Permian conglomeratic bedrock (Pc) ([Figure 1.2](#)) (Heran, et al., 2003; USGS, 2005). [Figure 2.11b](#) shows the 3-pronged array geometry, the station pair raypaths used to generate dispersion images, nominal hammer source positions and offsets, and omitted Sigma4 location that had a faulty GPS. [Figure 2.11c](#) provides three dispersion plots with multimodal picks; all picks derived from all three dispersion images are combined and plotted on each dispersion image: top) hammer-blow vertical component phase stack, mid) hammer blow radial component phase stack, and bottom) DGF radial-radial component phase stack. Fundamental mode picks on the hammer blow vertical image are constrained from 5 to 14 Hz and higher mode picks on remaining dispersion plots from 15 to 48 Hz. [Figure 2.11d](#) shows the DGF for the RR-component with first arrival fit line.

The upper plot on [Figure 2.11e](#) provides the V_s -depth curve; V_{s30} is 461 m/s, V_s -depth at X34A is constrained to approximately 40 meters depth, and we interpret the station to be placed on alluvium 10 m thick with velocities ranging from 200-400 m/s, and underlying Permian bedrock velocities ranging from 500-1000 m/s, probably due to a paleo-weathering profile to the 40 m depth resolution limit. The middle plot shows model vs. picked fundamental and higher modes. The lower plot shows the modeled H/V ratios vs. those measured by the central five stations, with H/V peaking at 2.6 at 15 Hz on Sigma4 station 510002 ([Figure 2.11e](#)).

[Figure 2.11f](#) provides H/V for each of the 15 Sigma4 stations from 0.1 to 100 Hz, and the site mean maximum H/V of 3.4. [Figure 2.11g](#) provides the site average H/V curve from all 15 Sigma4 Stations combined as an Ln mean, smooth mean, and 1σ uncertainty bounds. [Figure 2.11h](#) provides the H/V curve from Sigma4 station 510002 nearest the X34A vault.

2.4 Site Geology, V_s , and H/V Results

Table 2-1 summarizes the strong motion station data obtained for this study. For each site, Lat-Long coordinates, location name, geologic map symbol, unit age, and (regionally mapped) rock type are provided.

Results from this study tabulated here include V_{s30} (m/s), NEHRP modified site classification, depth in meters to 1.0 Km/s ($Z_{1.0}$), and site mean maximum horizontal:vertical ratio. Most sites are NEHRP Class C. Weathering profile thickness varies across the sites, which is a controlling factor on the V_{s30} value but generally appears to be ≤ 10 meters. Beneath the saprolitic/weathered profile, generally the unweathered

sedimentary Paleozoic rock units are approximately 800 m/s. H/V values are variable across the sites, and within the Sigma4 arrays.

Table 2-1. Site-Specific Survey Data

STA	LAT	LON	LOCATION	MAP SYMBOL	UNIT_AGE	ROCK	Vs30 (m/s)	NEHRP Class	Z1.0 (m)	Site Mean Max H/V
FNO	35.257380	-97.401150	Franklin, Norman	Pfa	Early Permian	shale	548	C2	-	3.0
OK001	35.561090	-97.289490	Jones High School, Jones	Qt	Pleistocene	sand	542	C2	-	6.5
OK002	35.549340	-97.196630	Harrah	Pg	Early Permian	sandstone	567	C2	-	1.9
OK005	35.654860	-97.191100	Luther Middle School, Luther	Pw	Early Permian	shale	596	C2	-	3.2
OK009	35.581310	-97.422920	Oakdale School, Edmond	Pg	Early Permian	sandstone	355	D3	-	5.4
TUL1	35.910473	-95.791695	Leonard	IPw	Middle Pennsylvanian	shale	694	C3	16	7.2
V35A	35.762600	-96.837800	Meyer Ranch Chandler	IPv	Late Pennsylvanian	shale	580	C2	-	4.0
W35A	35.152729	-96.874534	Tecumseh	Pw	Early Permian	shale	494	C2	-	2.0
W36A	35.139300	-96.226400	Wetumka	IPca	Middle Pennsylvanian	sandstone	670	C3	-	3.7
WMOK	34.737841	-98.780711	Wichita Mountains	Cwg	Middle Cambrian	granite	1821	A	0.5	4.2
X34A	34.601020	-97.832560	Smith Ranch	Pc	Early Permian	conglomerate	461	C1	-	3.4

3. SEISMOLOGICAL SITE RESPONSE

3.1 Spectral Analysis

A spectral inversion methodology is used to independently derive the site response at seismograph stations that recorded the Mw 5.6 Prague, Oklahoma earthquake of 6 November 2011. The methodology has been previously applied in the simultaneous identification of source, path, and site effects from an inversion of recorded ground motions (Hartzell and Mendoza, 2011). The procedure allows for identification of resonance peaks in the site response that can be attributed to weakly consolidated sediments at depth or other velocity discontinuities, and the results can be compared to those obtained from theoretical calculations and/or empirical measurements. Although a more robust determination of the site amplification may be obtained using multiple sources at different distances and azimuths, the factors derived here using data from a single earthquake allow the identification of sites with anomalous amplification, providing important insight into the characterization of ground motion in the Oklahoma City region.

The inversion method follows the procedure used by Hartzell and Mendoza (2011), where the ground motions at the recording sites are fit with a Brune (1970; 1971) model that expresses the shear-wave ground displacement spectra $U(f)$ as a function of earthquake seismic moment M_0 , source spectral corner frequency f_c , anelastic attenuation $Q(f)$, geometrical spreading r^{-b} and site response $S(f)$ and is given by (equation 8)

$$U(f) = \frac{R_{\theta\phi} \theta\phi FV}{4\pi\rho\beta^3} M_0 \frac{1}{1 + \left(\frac{f}{f_c}\right)^2} \exp\left(\frac{-\pi f r}{\beta Q(f)}\right) r^{-b} S(f) \quad (8)$$

where $R_{\theta\phi}$ is the shear-wave radiation pattern, F is the free-surface effect set to 2.0, and V is set to 1.0 to partition energy equally onto horizontal components. The density ρ is set to 2.75 g/cm³, and the shear-wave velocity β is set to 3.7 km/s. We initially tried using several values for the geometrical spreading factor b and found that a factor of 0.94 provided source parameters most consistent with the known size of the earthquake.

The observed spectra $U_{\text{obs}}(f)$ are inverted for best-fitting values of M_0 , f_c , $Q(f)$, and $S(f)$, where $Q(f)$ is parameterized as $Q_0 f^\alpha$ such that f^α allows for frequency dependence. To prevent trade-offs between seismic moment and long-period noise, $S(f)$ is set at 1.0 for frequencies below 0.15 Hz since site amplification should be minimal at lower frequencies. Raw seismic velocity waveforms recorded at local and regional distances for the Prague earthquake were collected from the IRIS Data Management Center (<http://www.iris.edu/hq/>). The data were then reviewed for quality and deconvolved to ground displacement between 0.04 and 10.0 Hz, although each record was individually examined to determine the appropriate band for analysis within this frequency range.

The analysis requires selecting observation stations with displacement spectra that have flat, low-frequency levels (~0.1 to 1.0 Hz) consistent with a Brune (1970; 1971) spectrum. The recorded time series are first corrected for the instrument response and then windowed to a fixed record length (within 100 sec of the S arrival) to include direct, refracted and coda S waves. The horizontal-component records are independently

Fourier-transformed and then vector-summed to obtain a displacement spectrum for each station. This observed spectrum is smoothed using a 1/3-octave smoothing function and then sampled at designated frequencies to identify the spectral values to be used in the inversion. These depend on the quality of the data, which varies with the instrument type and the noise level. In the case of the Prague records, horizontal displacement spectra for stations to the northeast of the epicenter show a strong dip between about 0.5 and 1 Hz that reflects strong azimuthal effects. An example of this feature is shown in Figure 3.1 for station TUL1. These path effects would be mapped into anomalous site effects in our inversion, and we restrict our analysis only to those records consistent with a Brune model. We consider stations within 2° of the earthquake epicenter. This distance range includes the 11 locations where on-site field measurements were performed as described in Section 2 of this report. Of these 11 sites, station TUL1 is excluded due to the strong observed path effects. Stations FNO and X34A are also excluded since the horizontal components are clipped at both of these sites and do not allow a proper reconstruction of the S-wave spectra. Table 3-1 gives the stations included in our seismological site analysis.

Table 3-1. Station Coordinates and Distance from Epicenter

STATION	LATITUDE, °N	LONGITUDE, °W	DISTANCE, °
V35A	35.76	96.84	0.22
OK002	35.55	97.20	0.33
OK005	35.65	97.19	0.35
W35A	35.15	96.87	0.37
OK001	35.56	97.29	0.40
OK009	35.58	97.42	0.51
W36A	35.14	96.23	0.60
U35A	36.37	96.73	0.82
X36A	34.57	96.35	1.03
W37B	35.14	95.43	1.16
X35A	34.40	96.97	1.16
X37A	34.59	95.37	1.49
T34A	37.02	97.19	1.51
Y35A	33.91	97.04	1.66
Y36A	33.90	96.28	1.68
X38A	34.67	94.83	1.81
Y37A	33.98	95.62	1.83
WMOK	34.74	98.78	1.84
W38A	35.07	94.52	1.89
U32A	36.38	99.00	2.00

The inversion applies the nonlinear hybrid global search algorithm of Liu et al. (1995) that uses a combination of simulated annealing and downhill simplex methods to fully explore the solution space. Squared differences between the logarithms of observed and model spectra are minimized over all spectral frequencies and observation stations, averaged over the total number of frequencies used for all stations. Our approach here has been to first set prescribed ranges for each of the M_0 , f_c , and $Q(f)$ parameters based

on known or published CEUS attenuation relationships and to solve for $S(f)$ using these intervals. For M_0 , we set the limits between 1.0 and 10.0×10^{24} dyne-cm based on the expected size of the earthquake, with the corner frequency f_c limited to values between 0.15 and 0.35. For the frequency dependence of Q ($Q(f) = Q_0 f^\alpha$), we use a range of 600 to 1200 for Q_0 and a range of 0.1 to 0.4 for α based on results obtained by Atkinson (2004), Erickson et al. (2004), Hartzell and Mendoza (2011), and McNamara et al. (2014) from the analysis of frequencies above 1 Hz for CEUS earthquakes. We first invert the spectra from stations located within 1° of the earthquake using these prescribed intervals and up to 45 predefined frequencies in the range of 0.05 to 10 Hz. This provides initial values for M_0 , f_c , α and Q_0 that we then use to further restrict each parameter in a second inversion for site response at all distances. Table 3-2 gives the source and attenuation parameters obtained both from the initial inversion of the spectra using stations within 1° and from the final inversion for all stations at distances up to 2° . The fits between observed and predicted displacement spectra for the final inversion are shown in Figures 3.2 to 3.21 for stations within 2° of the earthquake epicenter.

Table 3-2. Source and Attenuation Parameters

Inversion	M_0 (dyne-cm)	f_c (Hz)	α	Q_0
Initial, stations within 1°	3.5×10^{24}	0.252	0.394	1100
Final, stations within 2°	4.3×10^{24}	0.247	0.386	1101

3.2 Inversion Results and Site Response

The seismic moment and corner frequency obtained in the final inversion (Table 3-2) suggest an M_w magnitude of 5.7 and a radial source dimension of 4-5 km for the 2011 Prague earthquake, consistent with the rupture extent inferred by Sun and Hartzell (2014) from a finite-fault analysis using regionally-recorded seismic waveforms. For the attenuation, we obtain the relation $Q(f) = 1100f^{0.386}$, within the bounds of attenuation parameters previously measured in the CEUS. The inversion also recovers the frequency-dependent site response at each site. These are shown as black curves in Figures 3.22 to 3.24 for the 20 stations located within 2° of the earthquake epicenter. The plots show strong amplification (more than a factor of 2) at several sites that include stations OK001, OK002, OK005, OK009, W35A, T34A, U32A, U35A, W37B, W38A, X35A and X36A. We have examined the validity of the site response spectra obtained from the spectral inversion by comparing against horizontal-to-vertical spectral ratios (HVSr) derived from the horizontal and vertical components recorded for the 2011 Prague earthquake. The ratios are calculated from the S-wave power spectral densities observed at each site using the Kawase *et al.* (2011) relation (equation 9).

$$\frac{H(\omega)}{V(\omega)} = \sqrt{\frac{H_1^2(\omega) + H_2^2(\omega)}{V^2(\omega)}} \quad (9)$$

for earthquake ground motion, where H_1 and H_2 are the two horizontal components, V is the vertical component, and ω is the angular frequency. These ratios are shown in blue in Figures 3.22 to 3.24. Although

the HVSR approach cannot reliably identify the absolute amplification, it provides an estimate of the fundamental resonance frequency of soil sites. The lower-frequency limit was identified from a visual review of the vertical spectra to minimize lower-frequency noise at each site and varies between 0.3 and 0.5 Hz. The higher-frequency limit is defined by the sampling rate of each station.

The ratios compare favorably with the site response spectra obtained for stations that exhibit large amplification (greater than 2). We note that an amplification factor near 2 is observed at a frequency of 0.15 Hz in the spectral response of station WMOK (Figure 3.22); however, this resonance frequency is not visible in the WMOK HVSR curve. A review of the horizontal and vertical S-wave spectra recorded for the 2011 earthquake at station WMOK reveals a spectral peak at around this frequency for both horizontal and vertical components. The similarity in horizontal and vertical spectra in this frequency range indicates that the spectral peaks would cancel out in the HVSR computation. The spectral inversion, on the other hand, would identify response peaks present in the horizontal recordings. This observation points out a possible uncertainty in HVSR calculations caused by amplification on the vertical component. Also, spectral responses (black curves) at many of the stations exhibit a prominent peak at a frequency of about 0.3 Hz. This spectral peak in the ground motion has been observed at sites in Oklahoma and Kansas for several induced earthquakes that have occurred within the last decade (e.g., Rennolet et al., 2017). It would be worthwhile to investigate this feature to see if it reflects general crustal properties across the region.

Also shown in Figure 3.22 are the SH transfer functions (shown in red) for a horizontally-stratified medium (Thomson, 1950) calculated using the velocity profiles obtained from the on-site field measurements completed at or near stations OK001, OK002, OK005, OK009, V35A, W35A, W36A and WMOK. The SH amplification curves are generally flat at frequencies lower than 5 to 10 Hz but are consistent with the theoretical H/V curves calculated for these sites in the previous section (e.g., Figs. 2.2f, 2.3g, 2.4e, 2.7e). The SH transfer functions, however, do not coincide with the resonance peaks suggested by the seismological analysis, including the spectral inversion results and the observed HVSR curves. This result is due to the fact that there is little overlap between the frequency ranges among the different methods. Amplification observations from the spectral analysis thus appear to incorporate velocity variations at depths greater than those sampled by the on-site geophysical surveys, which are most sensitive to the soil structure in the top 30-50 meters. These deeper structures would contribute to the total site response and are important to document for an appropriate recovery of the effective ground motions.

4. SUMMARY

Geophysical field investigations were conducted to obtain robust estimates of Vs-velocity variation down to 30 m depth at selected seismograph station locations near Oklahoma City. Some of these stations also recorded the Mw 5.6 Prague, Oklahoma earthquake of 6 November 2011, allowing an independent derivation of broadband site-response parameters from the earthquake recordings.

The field investigations included targeted active-source geophysical surveys using I-, Y- or K-shaped 3-component sensor arrays deployed at or near the seismic-station locations. Rayleigh-wave dispersion curves were obtained at each site using an Interferometric Multichannel Analysis of Surface Waves (IMASW) approach. The 3-component field recordings from each array sensor were also used to calculate H/V ratios for each site that identify resonant frequencies within a wide 0.25 to 100 Hz frequency range. The fundamental-mode phase velocities obtained from the IMASW analysis and the field-derived H/V ratios were then simultaneously inverted to recover Vs-Depth models, allowing a NEHRP site classification at each site.

Broadband horizontal waveforms recorded within 2° of the 2011 Prague earthquake epicenter were analyzed using a spectral inversion methodology that recovers the source properties, the anelastic attenuation effects, and the site response parameters that contribute to the observed horizontal displacement spectra at each site. This provides estimates of the earthquake size, the wave attenuation properties along the source-station propagation path, and the site amplification based on the weak recorded ground motions. The site-response spectra recovered from this process identify peaks and resonance frequencies that are consistent with horizontal-to-vertical spectral ratios calculated at the same sites using the earthquake recordings. The seismologic analyses include eight of the seismic-station sites where geophysical field measurements were performed. For these sites, there is little overlap between the frequency ranges included in the seismological investigation and those sampled in the field measurements. The spectral analysis incorporates velocity variations at depths greater than 50 m that contribute to the effective ground motion.

5. ACKNOWLEDGEMENTS

This research has been supported by the U.S. Geological Survey (USGS), Department of the Interior, under USGS National Earthquake Hazard Reduction Program (NEHRP) award number G17AP00021. The outcome of this study would not have been possible without the cooperation, generosity, and support from many individuals and organizations. In particular, application of the seismological methodology benefitted from an important collaboration with Steve Hartzell. Thanks to Lincoln Steele for field data collection, landowners across Oklahoma, and Jake Walters for assisting with site access.

6. DISSEMINATION OF RESULTS

The USGS Science Database may host the csv, SEGY, and GIS survey/metadata files. O'Connell and Turner plan to co-author a forthcoming SRL article with Bill Stephenson to present all the recent site-specific Oklahoma Vs and H/V survey data (including data from Cushings, Fairview, etc.) in a single peer-reviewed resource. Mendoza plans to prepare a scientific article in collaboration with Stephen Hartzell to publish the seismological site response study in a peer-reviewed journal.

7. REFERENCES

- Atkinson, G., (2004), Empirical Attenuation of Ground-Motion Spectral Amplitudes in Southeastern Canada and the Northeastern United States , Bull. Seism. Soc. Am. 94, 1079-1095.
- Boore, D. M., (2015), Adjusting Ground-Motion Intensity Measures to a Reference Site for which $V_{s30} = 3000$ m/sec, PEER Report No. 2015/06, May 2015.
- Brune, J. N. (1970), Tectonic stress and the spectra of seismic shear waves from earthquakes, J. Geophys. Res. 75, 4997–5009.
- Brune, J. N. (1971), Correction, J. Geophys. Res. 76, 5002.
- Bensen, G. D., M. H. Ritzwoller, M. P. Barmin, A. L. Levshin, F. Lin, M. P. Moschetti, N. M. Shapiro, Y. Yang, (2007), Processing seismic ambient noise data to obtain reliable broad-band surface wave dispersion measurements, Geophys. J. Int., doi:10.1111/j.1365-246X.2007.03374.x.
- Brocher, T. M., (2005), Empirical Relations between Elastic Wavespeeds and Density in the Earth's Crust, Bull. Seism. Soc. Amer., (2005) 95 (6): 2081-2092.
- Clayton, R. W., and R. A. Wiggins, (1976), Source shape estimation and deconvolution of teleseismic body waves, Geophysical Journal of the Royal Astronomical Society, 47, 151–177.
- Draganov, D., K. Wapenaar, and J. Thorbecke, (2006), Seismic interferometry: Reconstructing the earth's reflection response: Geophysics, 71, no. 4, SI61–SI70.
- Erickson, D., D. E. McNamara and H. M. Benz, (2004), Frequency-Dependent L_g Q within the Continental United States, Bull. Seism. Soc. Am. 94, 1630-1643.
- Halliday, D. and Curtis, A., (2008), Seismic interferometry, surface waves and source distribution, Geophys. J. Int., 175, 1067–1087.
- Haney, M. M. and Nakahara, H., (2016), Erratum to: Surface wave Green's tensors in the near field: Bulletin of the Seismological Society of America, 106, 816-818.
- Haney, M. M., Mikesell, T. D., van Wijk, K., and Nakahara, H., (2012), Extension of the spatial autocorrelation (SPAC) method to mixed-component correlations of surface waves: Geophysical Journal International, 191, 189–206. doi: 10.1111/j.1365-246X.2012.05597.x.
- Hartzell, S. and C. Mendoza, (2011). Source and Site Response Study of the 2008 Mount Carmel, Illinois, Earthquake, Bull. Seism. Soc. Am. 101, 951-963, doi: 10.1785/0120100222.
- Heran, W.D.; Green, G.N., Stoeser, D.B., (2003). A Digital Geologic Map Database for the State of Oklahoma, United States Geological Survey Open File Report 03-247, 2003.
- Kawase, H., F. J. Sánchez-Sesma, and S. Matsushima (2011). The optimal use of horizontal-to-vertical spectral ratios of earthquake motions for velocity inversions based on diffuse-field theory for plane waves, Bull. Seismol. Soc. Am. 101, 2001-2014.
- Kimman, W.P. and Trampert, J., (2010), Approximations in seismic interferometry and their effects on surface waves, Geophys. J. Int., 182, 461–476.
- Liu, P., Hartzell, S., Stephenson, W., (1995). Non-linear multi-parameter inversion using a hybrid global search algorithm: Application in reflection seismology, Geophys. J. Int. 122, 991–1000.

McNamara D. E., L. Gee, H. M. Benz and M. Chapman, (2014), Frequency-Dependent Seismic Attenuation in the Eastern United States as Observed from the 2011 Central Virginia Earthquake and Aftershock Sequence , Bull. Seism. Soc. Am. 104, 55-72.

O'Connell, D.R.H., Turner, J.P., (2011). Interferometric multichannel analysis of surface waves (IMASW), Bulletin Seismological Society of America, Vol. 101, No. 5, pp. 2122-2141, October 2011, doi: 10.1785/0120100230. Rennolet, S.B., M.P. Moschetti, E.M. Thompson, W.L. Yeck, (2017). A flatfile of ground motion intensity measurements from induced earthquakes in Oklahoma and Kansas, Earthquake Spectra, doi: 10.1193/101916EQS175DP.

Stephenson, W.J., (2017). Personal Communication.

Sun, X. and S. Hartzell, (2014), Finite-fault slip model of the 2011 Mw 5.6 Prague, Oklahoma earthquake from regional waveforms, Geophys. Res. Lett. 40, 4207-4213, doi:10.1002/2014GL060410.

Thomson, W. T. (1950). Transmission of elastic waves through a stratified solid medium, J. Appl. Phys. 21, 89-93. Tuan. T. T. (2009), The ellipticity (H/V-ratio) of Rayleigh surface waves, Dissertation in GeoPhysics, Friedrich-Schiller-University Jena, Germany.

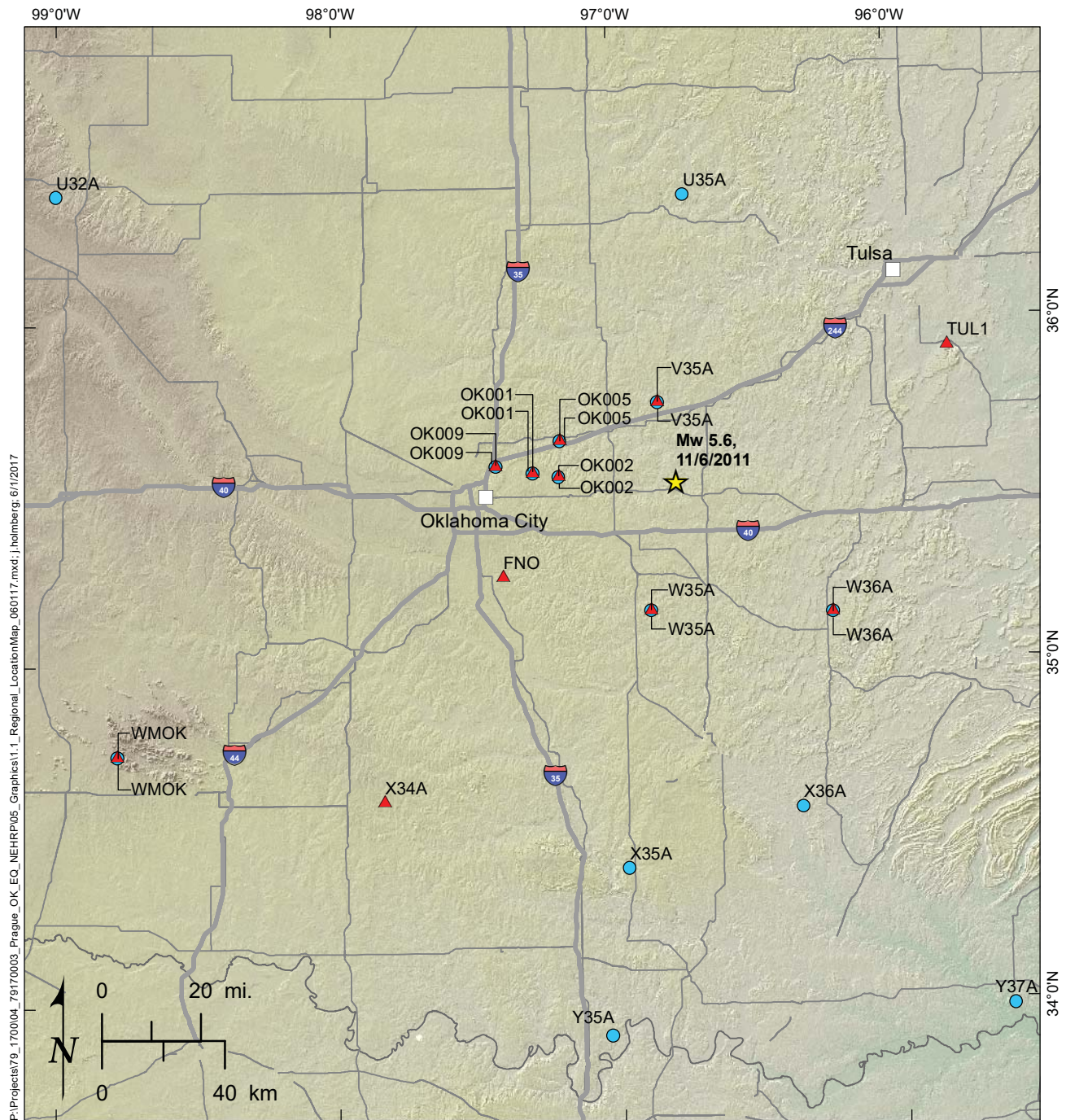
USGS, (2005). National-scale geologic map to support national and regional-level projects, including mineral resource and geo-environmental assessments, USGS Mineral Resources, 2005.

Van der Neut, J., J. Thorbecke, K. Mehta, E. Slob, and K. Wapenaar. (2011), Controlled-source interferometric redatuming by crosscorrelation and multidimensional deconvolution in elastic media, Geophysics, 76(4), SA63-SA76.

Vasconcelos, I. and R. Snieder, (2008), Interferometry by deconvolution: Part 2 - Theory for elastic waves and application to drill-bit seismic imaging, Geophysics, 73, S129-S141.

Wapenaar, K., J. Fokkema, J., (2006), Green's function representations for seismic interferometry, Geophysics, 71(4), P.S133-S146.

Wapenaar, K., J. van der Neut, E. Ruigrok, D. Draganov, J. Hunziker, E. Slob, J. Thorbecke and R. Snieder, (2011), Seismic interferometry by cross-correlation and by mutidimensional deconvolution: a systematic comparison, Geophys. J. Int., 185, 1335-1364.






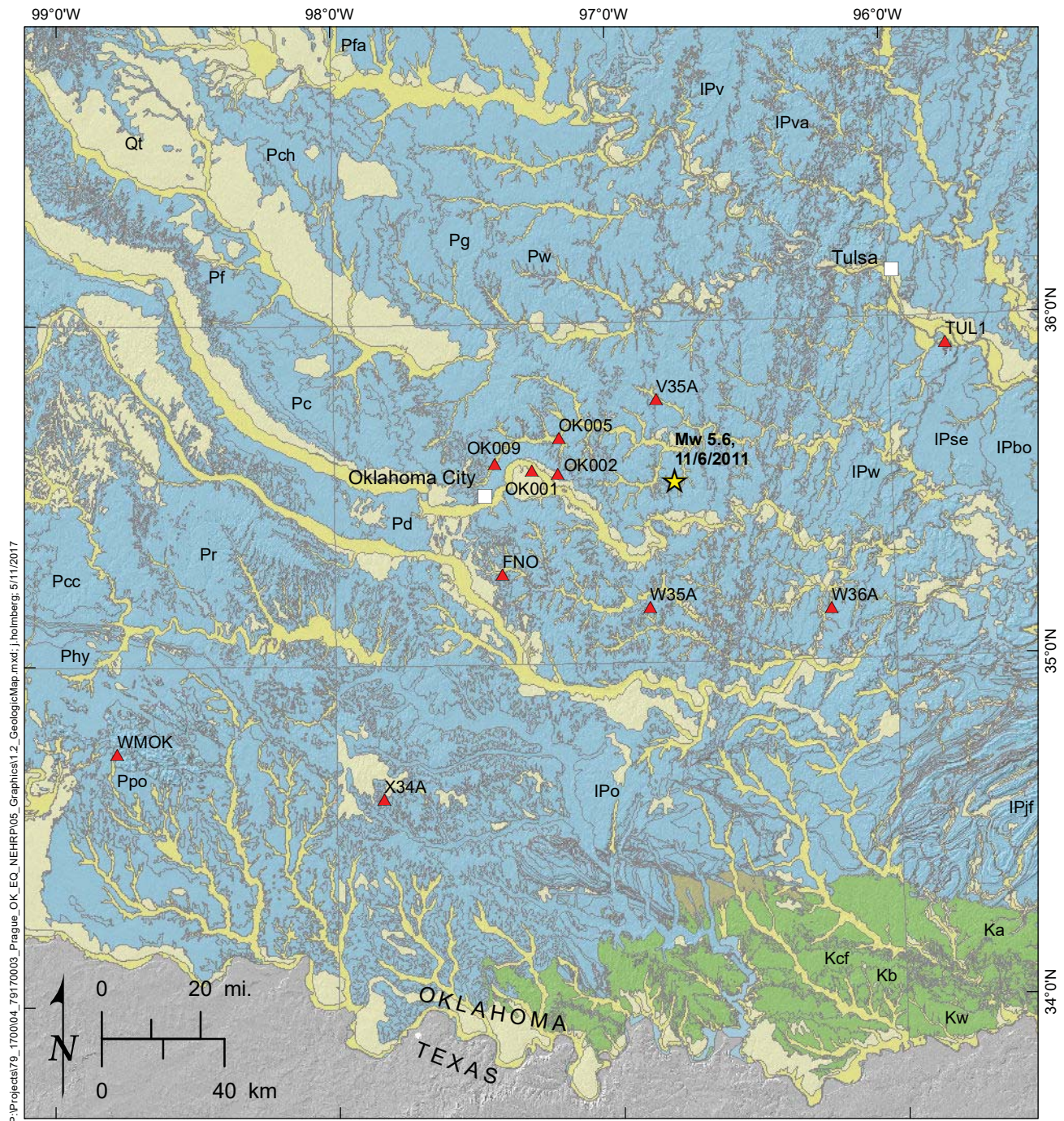
- | | Explanation |
|---|--|
| OK001  | Seismic stations |
|  | Earthquake epicenter, November 6, 2011 |
|  | Stations included in seismological site analysis |

Figure 1.1. Regional location map.



- Explanation**
- OK001 ▲ Seismic stations
- ★ Earthquake epicenter, November 6, 2011

Figure 1.2 Geologic map and station locations.

Explanation

Qt	Terrace Deposits, Pleistocene
Pc	Chickasha Formation, Early Permian
Pfa	Fairmont Shale, Early Permian
Pg	Garber Sandstone, Early Permian
Pw	Wellington Formation, Early Permian
IPv	Vanoss Group, Late Pennsylvanian
IPca	Calvin Sandstone, Middle Pennsylvanian
IPw	Wewoka Formation, Middle Pennsylvanian
Cwg	Wichita Granite Group, Middle Cambrian

Figure 1.3 Explanation of geologic units.

**Explanation**

- Receiver location
- ▲ Seismic station

Figure 2.1a. FNO site location.

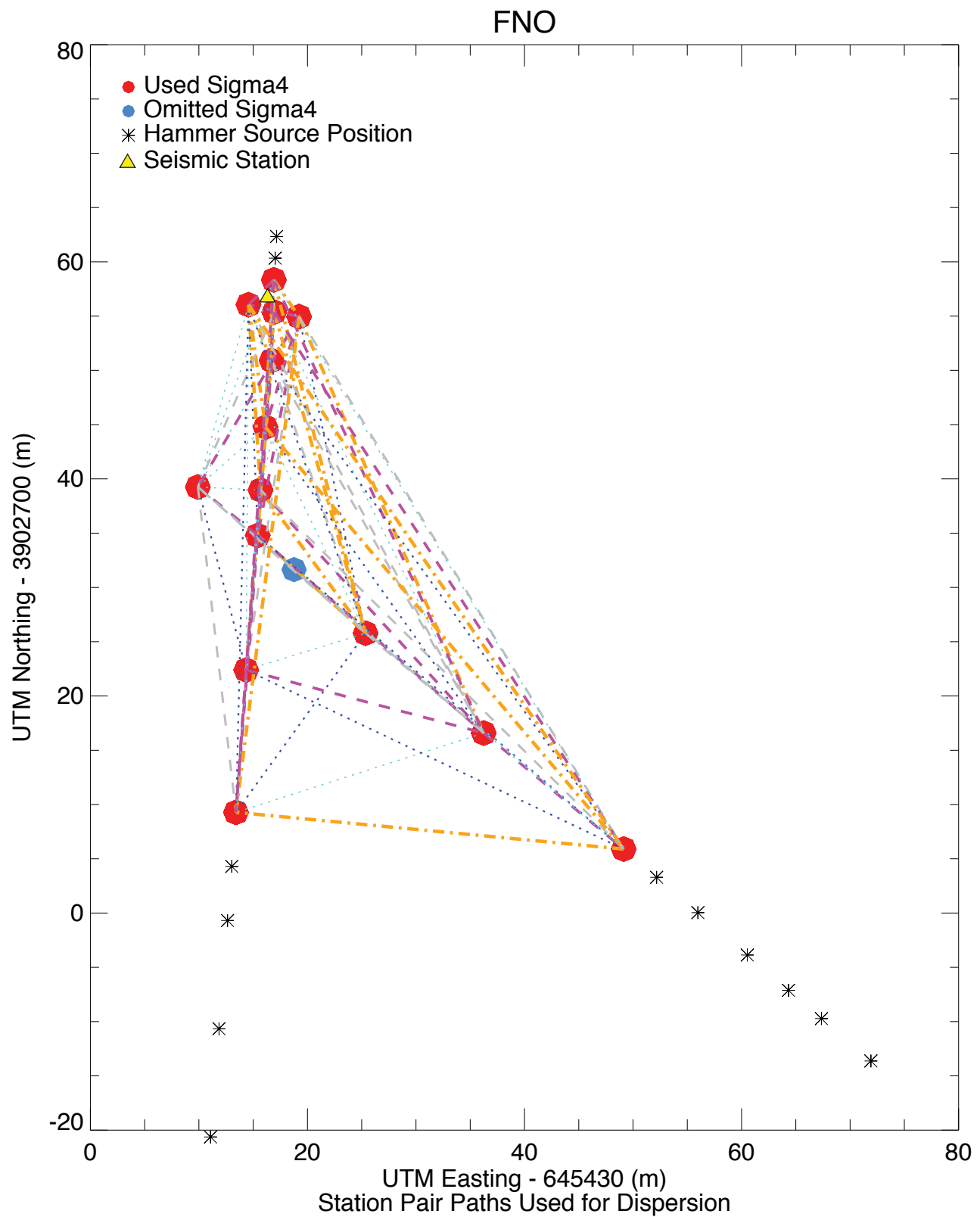


Figure 2.1b FNO station dispersion pathways and source positions.

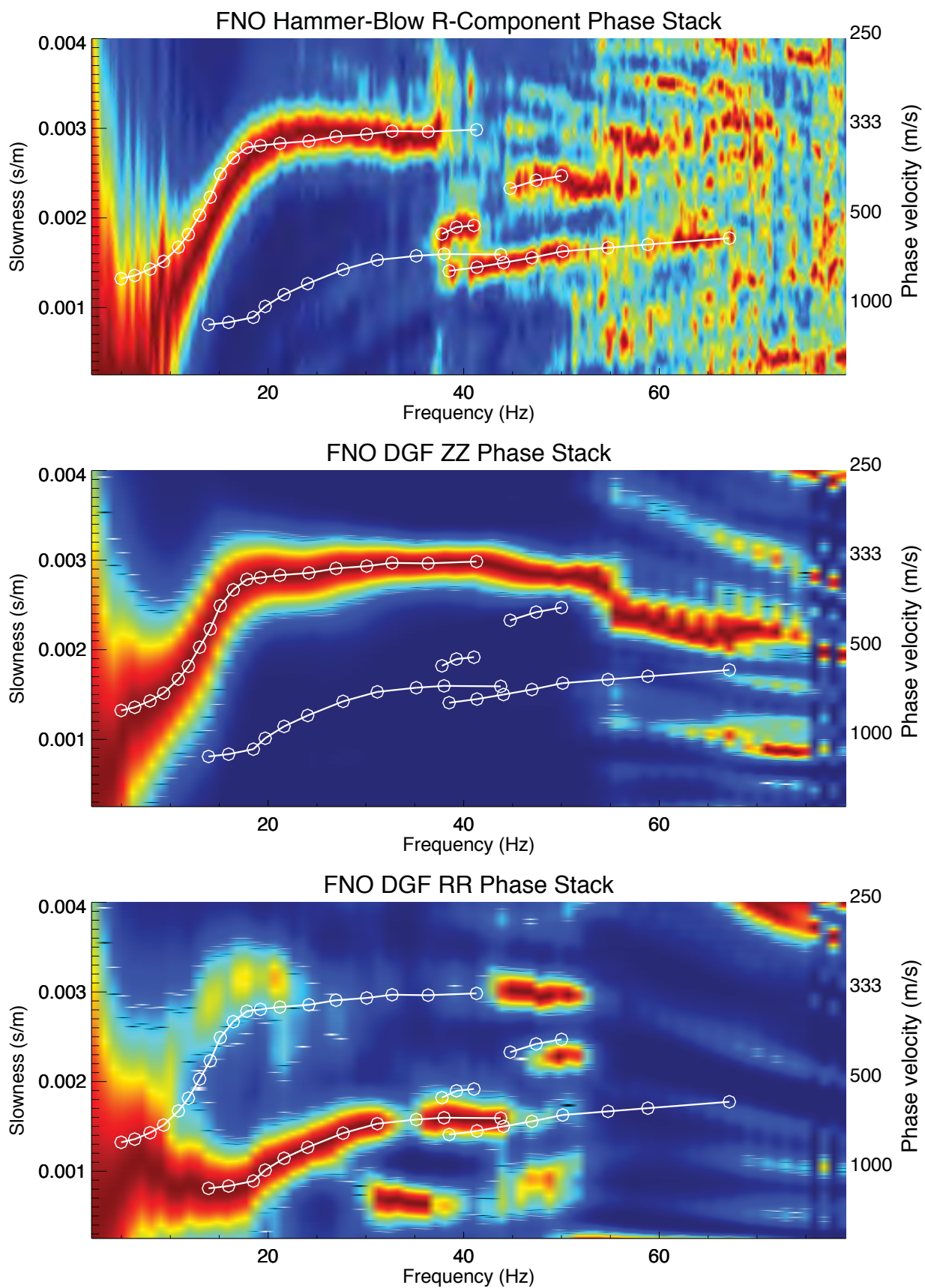


Figure 2.1c. FNO multimodal p-f dispersion images and picks.

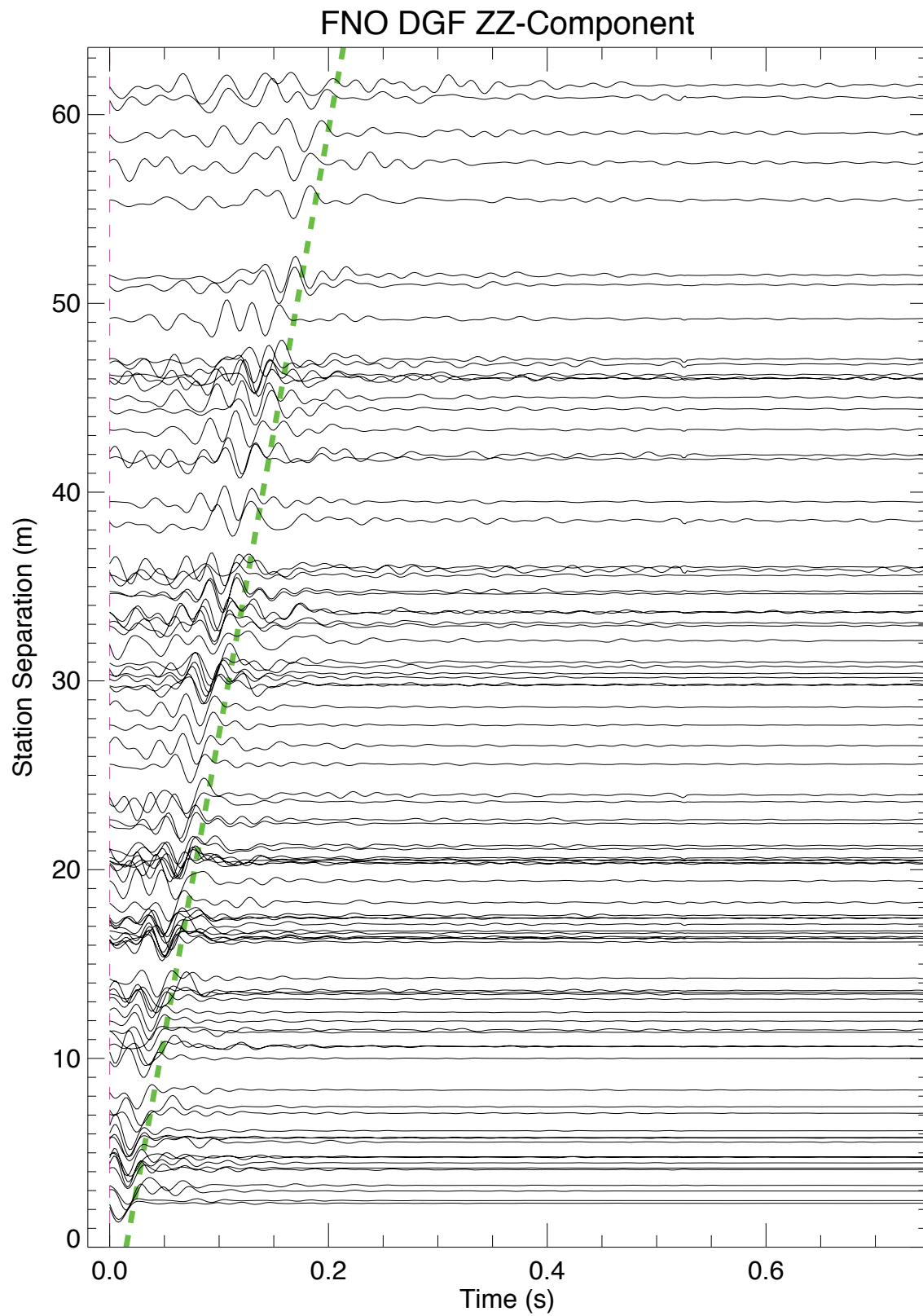


Figure 2.1d. FNO vertical component dispersion green's function.

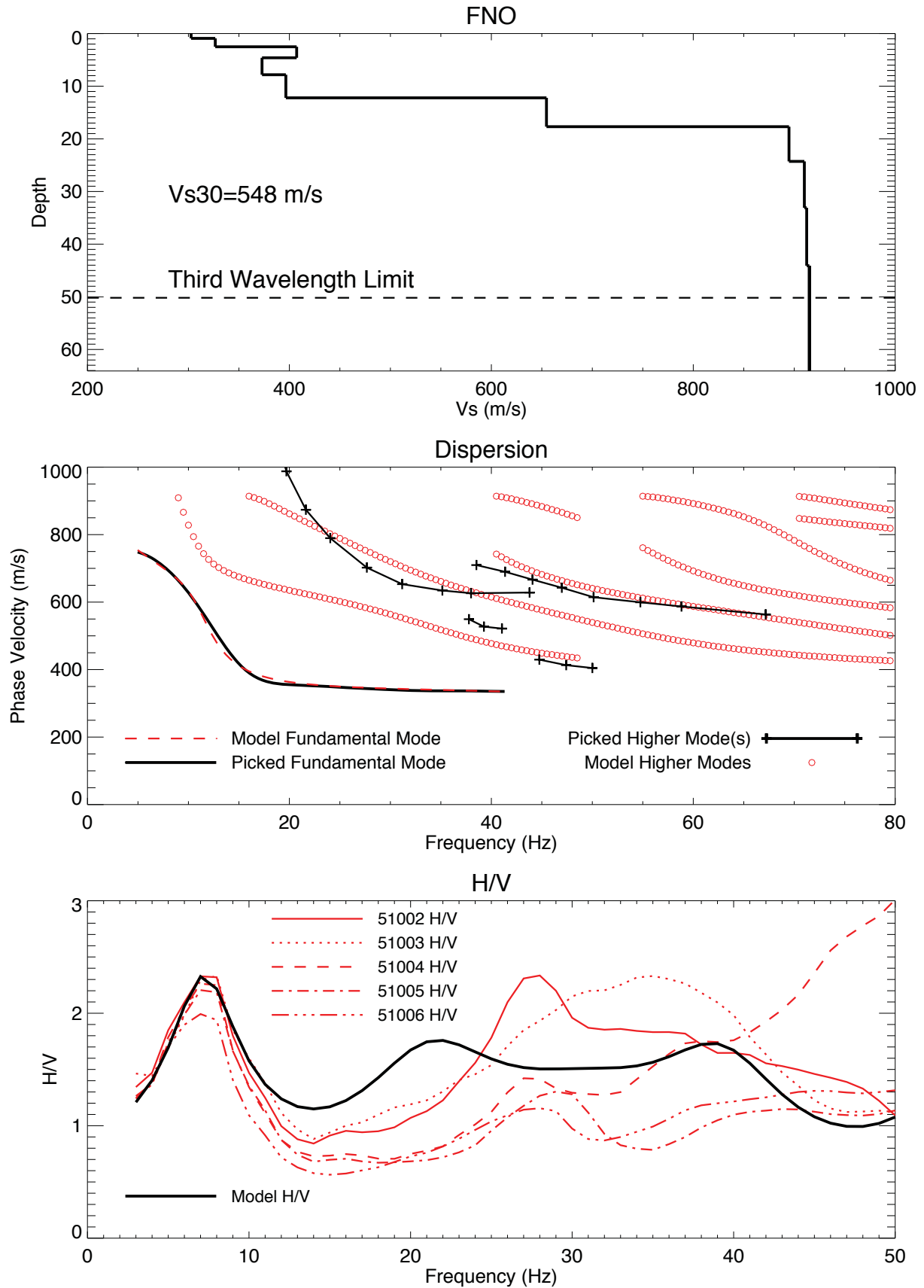


Figure 2.1e. FNO Vs-depth, Vs30, and nearfield H/V model.

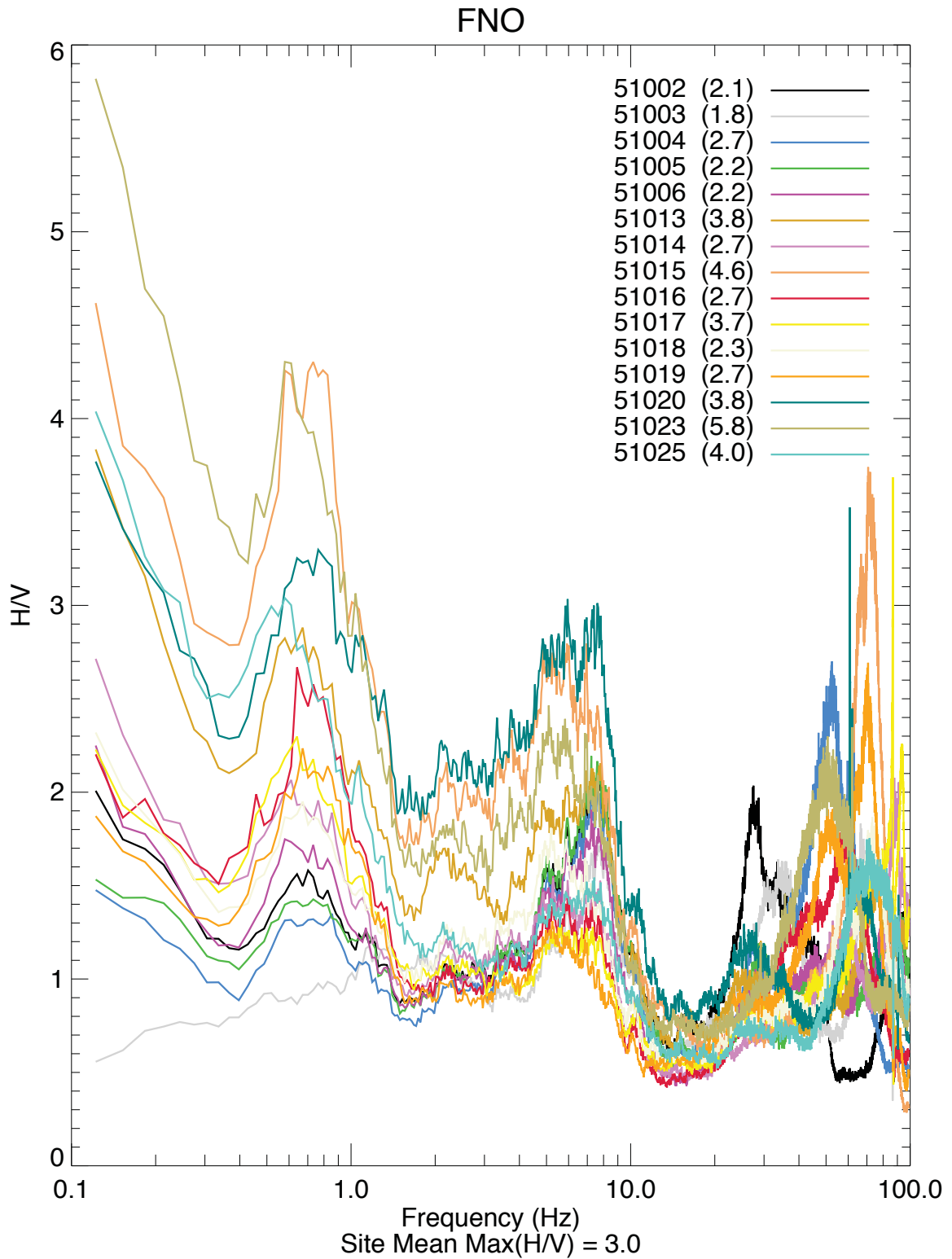


Figure 2.1f. FNO all stations H/V.

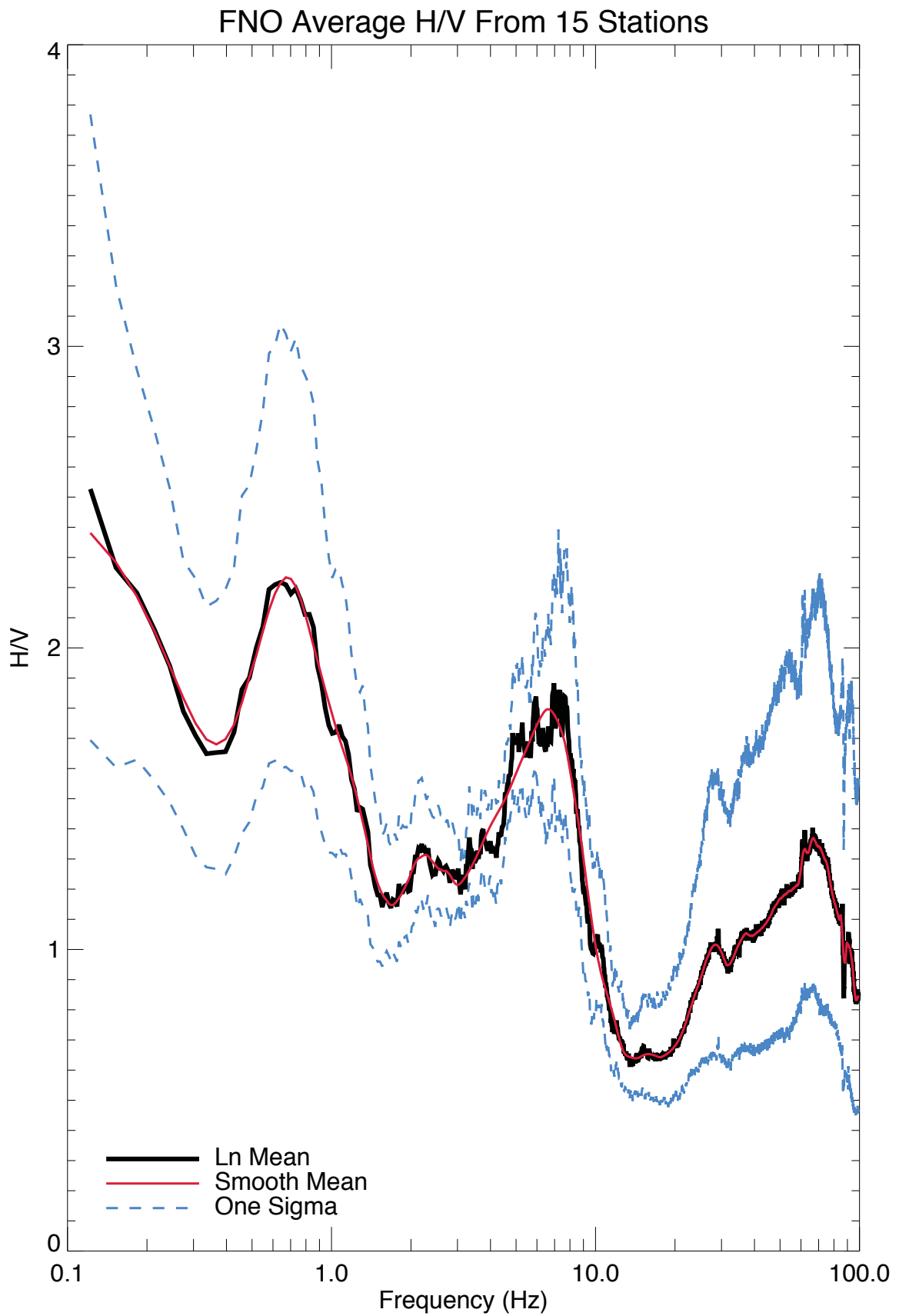
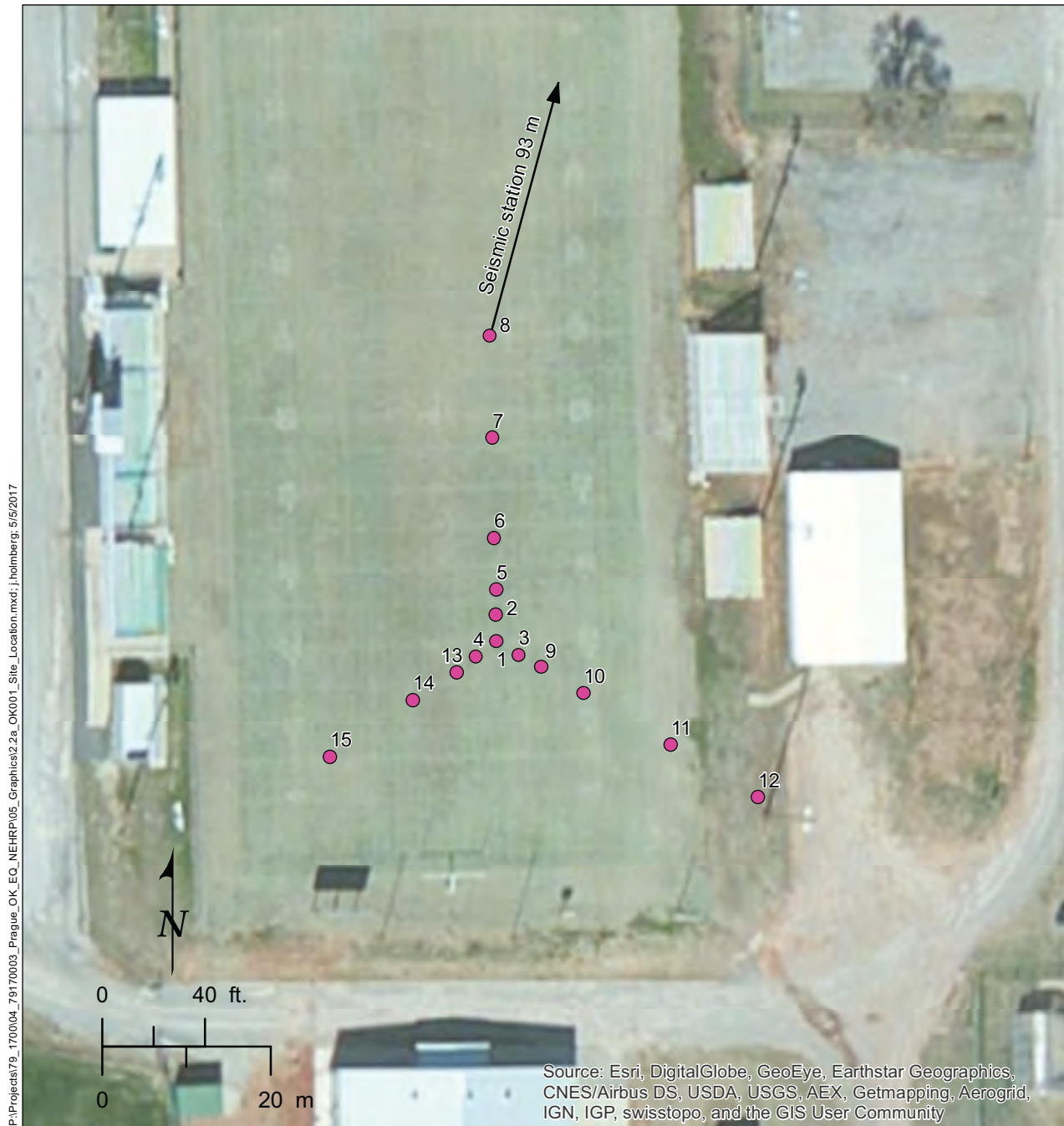


Figure 2.1g. FNO site average H/V.



Explanation

● Receiver location

Figure 2.2a. OK-001 site location.

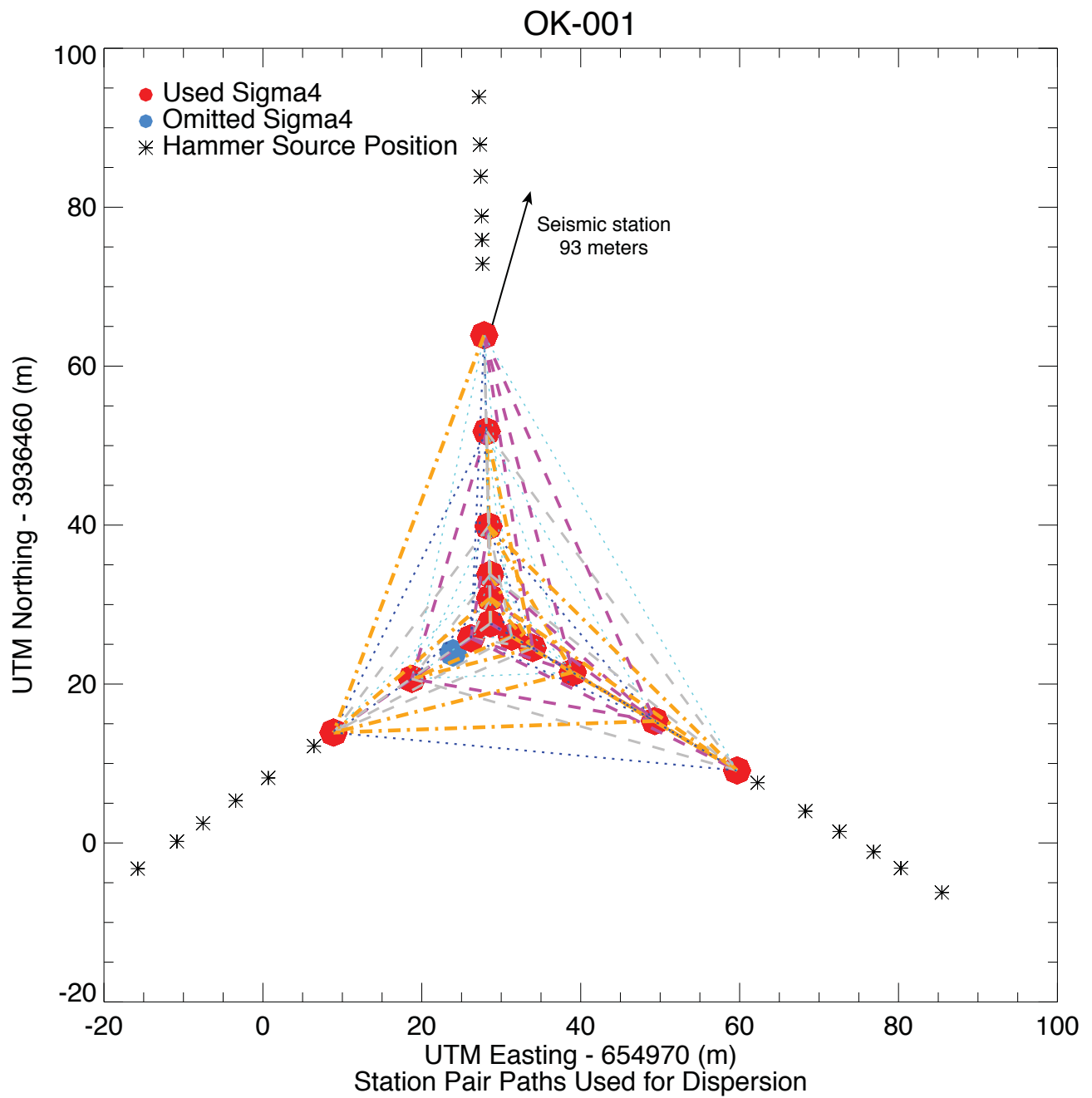


Figure 2.2b. OK-001 station dispersion pathways and source positions.

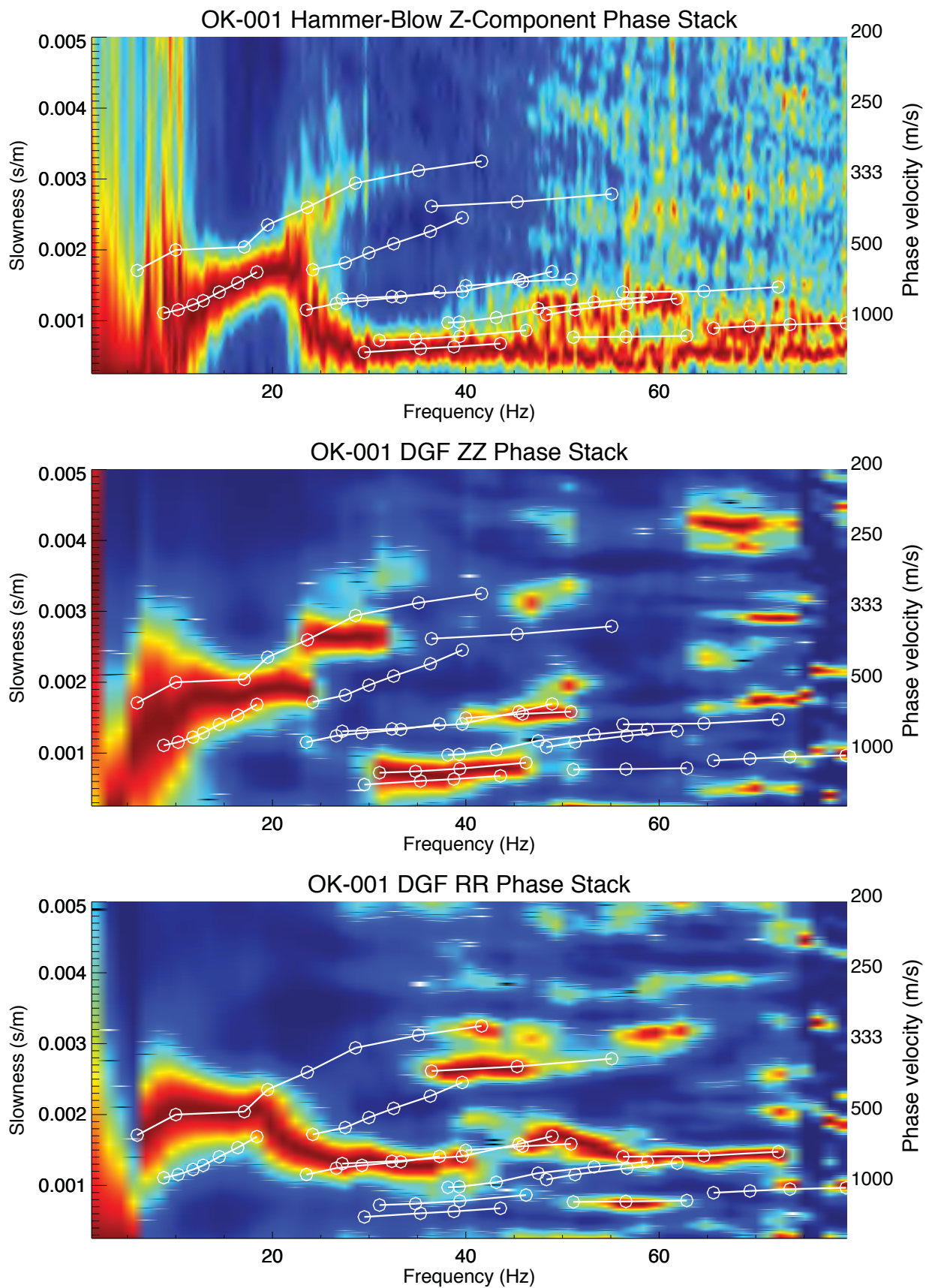


Figure 2.2c. OK-001 multimodal p-f dispersion images and picks.

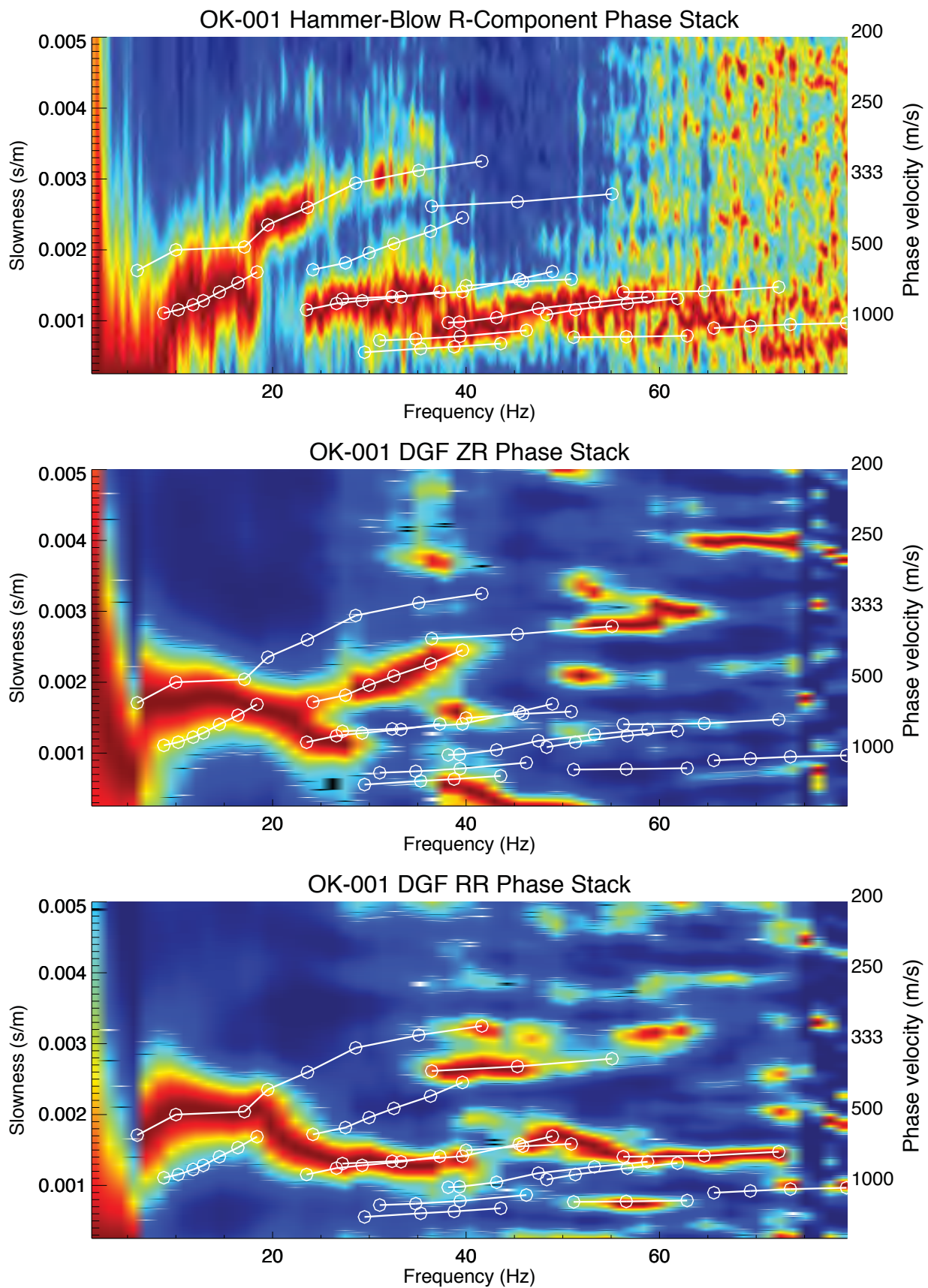


Figure 2.2d. OK-001 additional multimodal p-f dispersion images and picks.

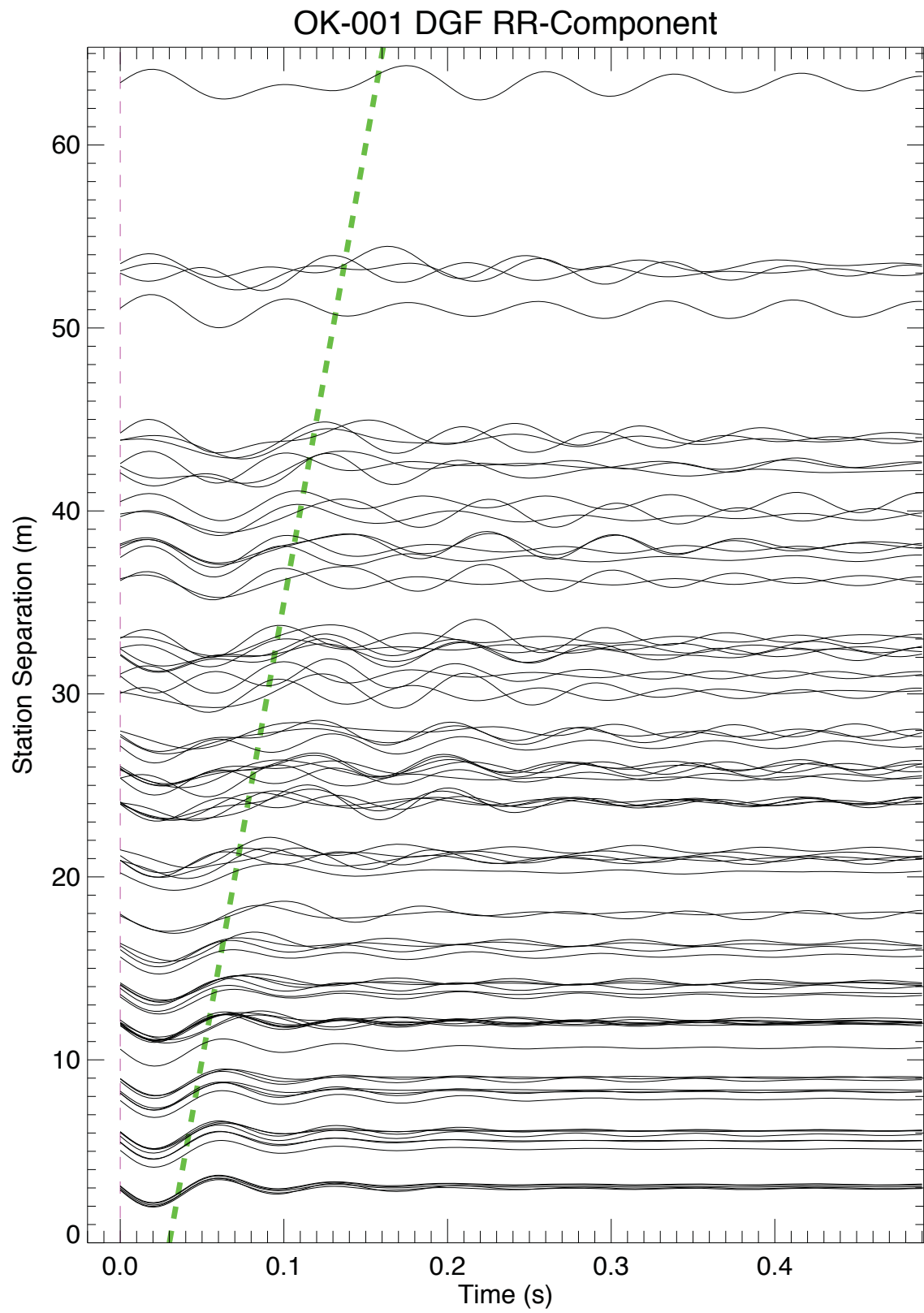


Figure 2.2e. OK-001 radial component dispersion Green's Function.

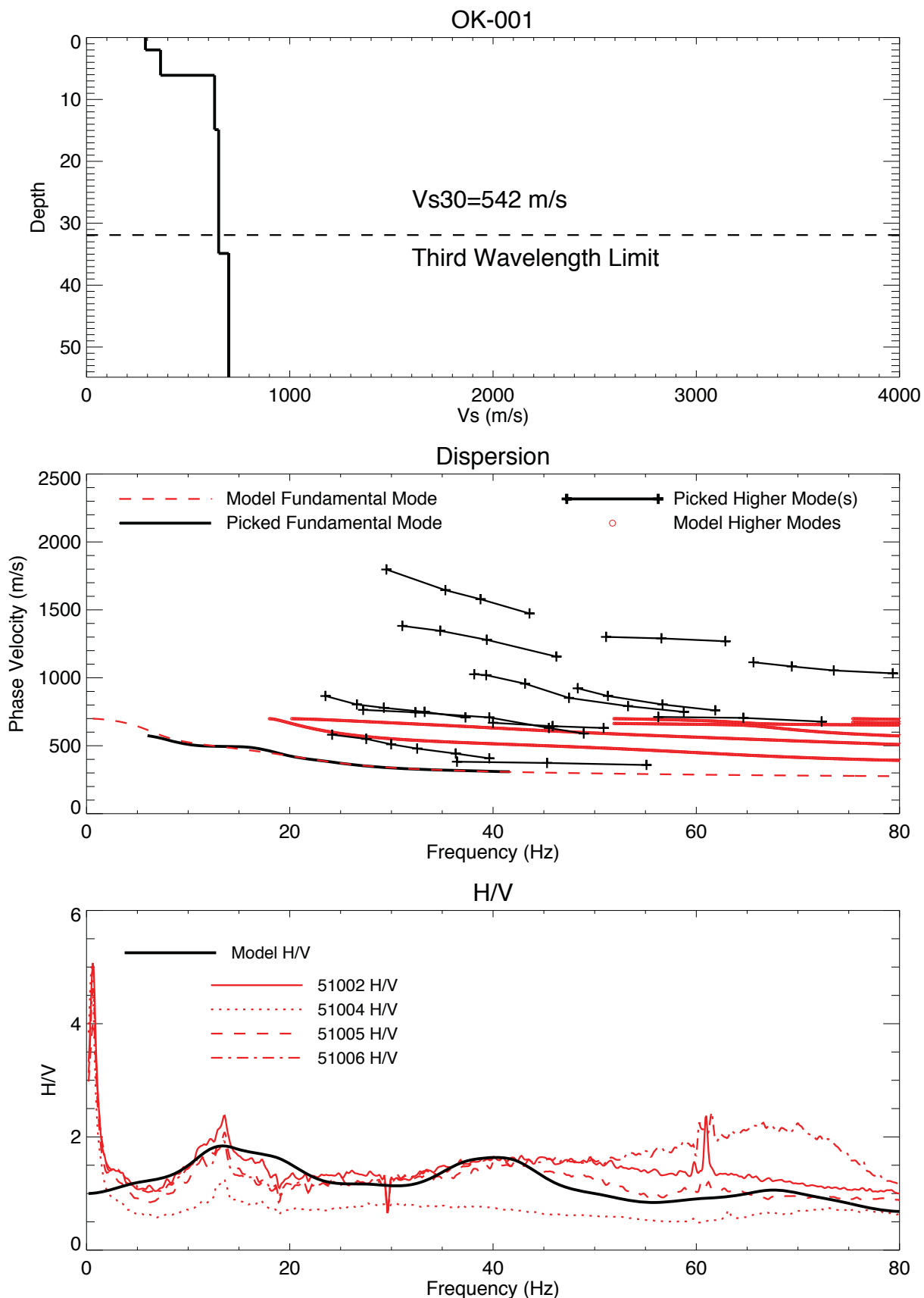


Figure 2.2f. OK-001 Vs-depth, Vs30, and Nearfield H/V Model.

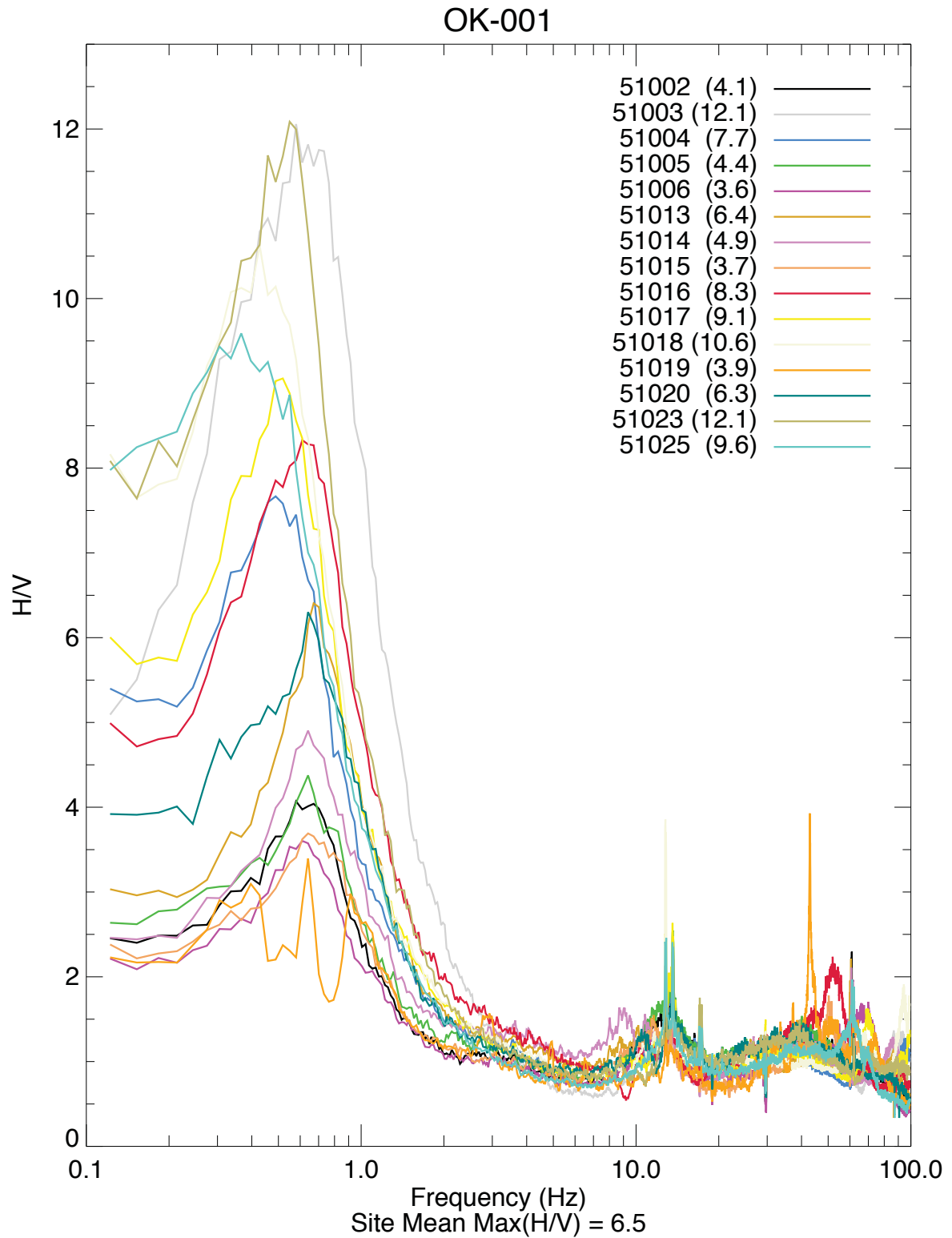


Figure 2.2g. OK-001 all stations H/V.

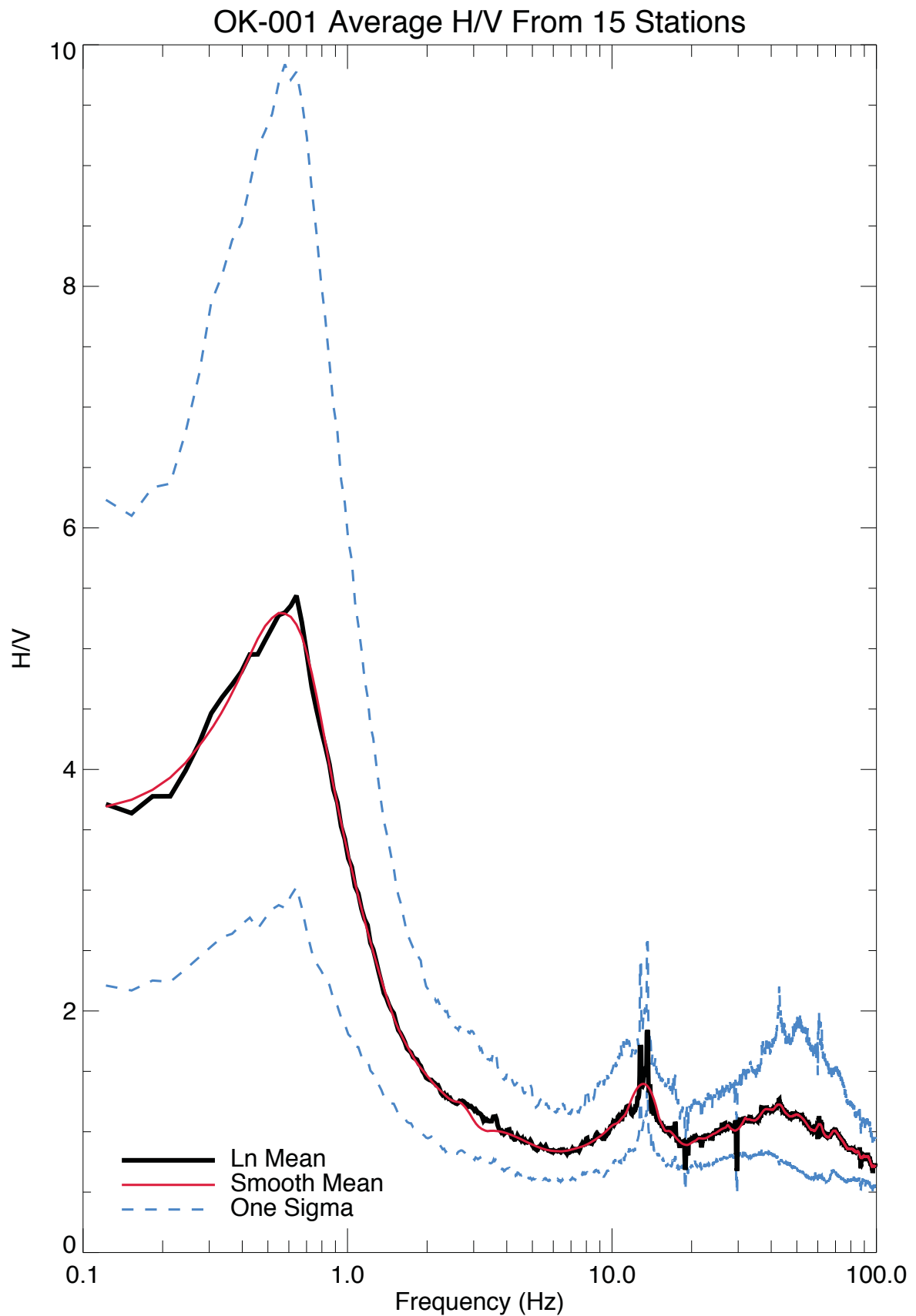


Figure 2.2h. OK-001 site average H/V.



Explanation

- Receiver location

Figure 2.3a. OK-002 site location.

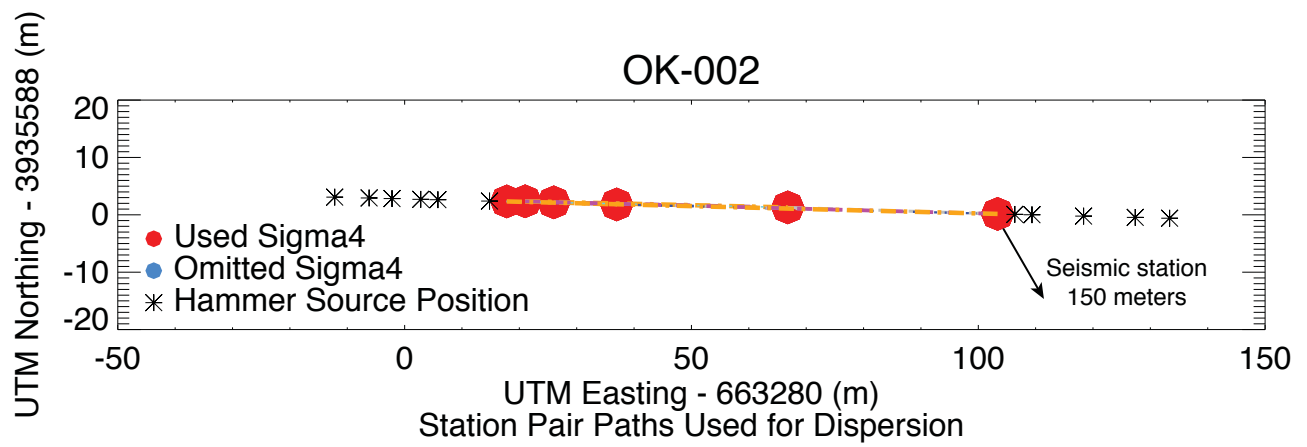


Figure 2.3b. OK-002 station dispersion pathways and source positions.

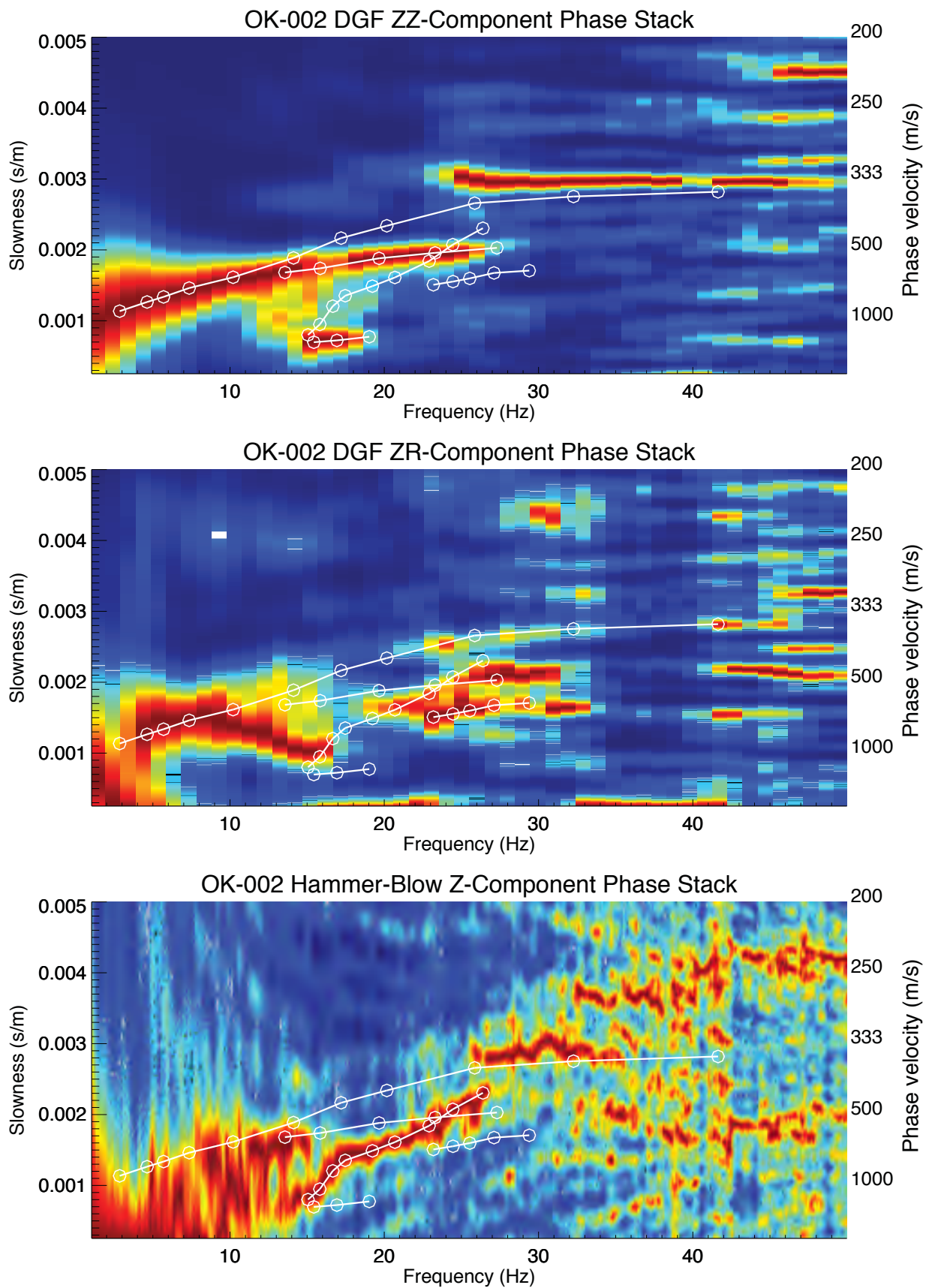


Figure 2.3c. OK-002 dispersion Green's Function ZZ and ZR multimodal p-f dispersion images and picks.

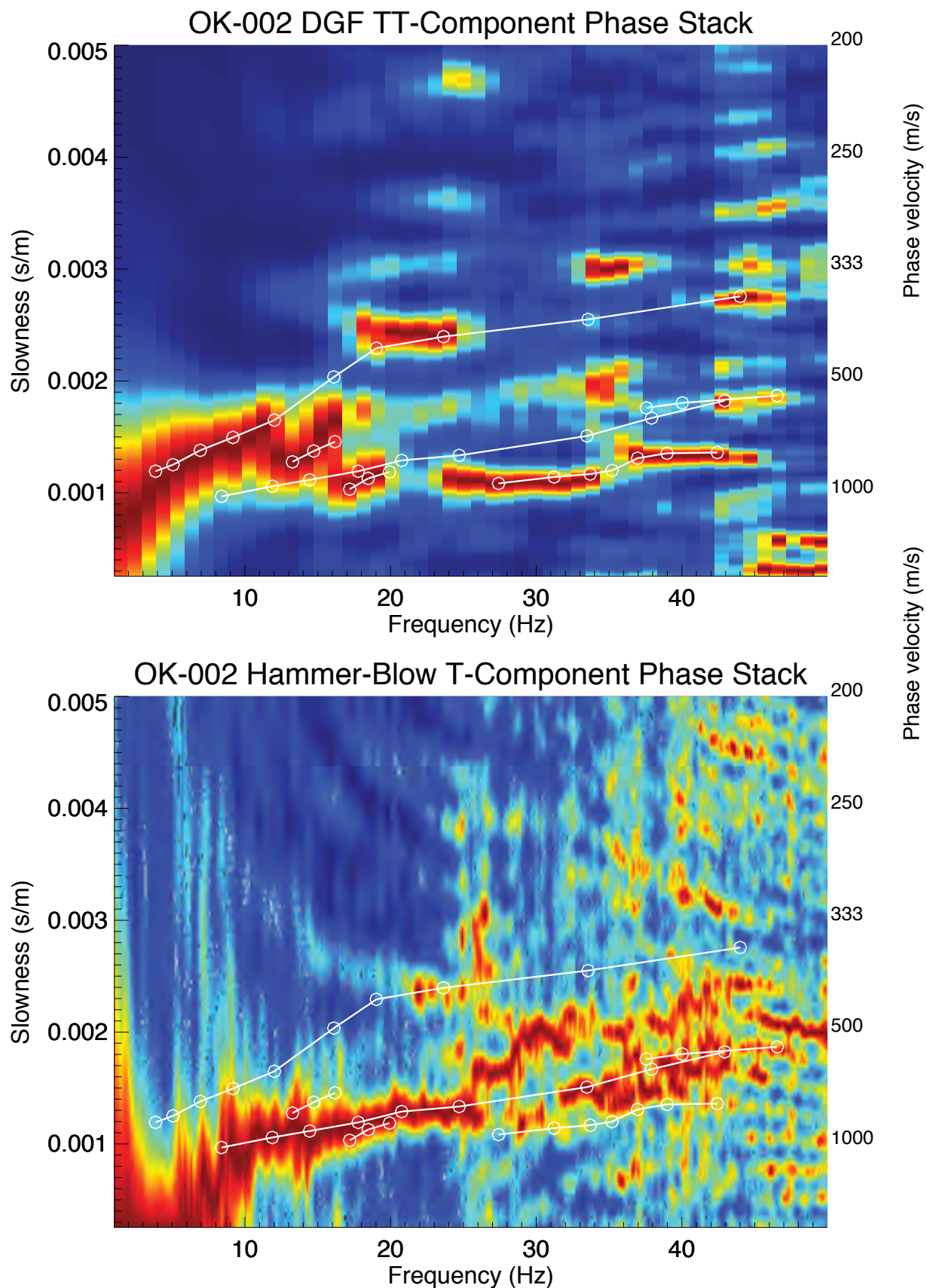


Figure 2.3d. OK-002 dispersion Green's Function TT component multimodal p-f dispersion images and picks.

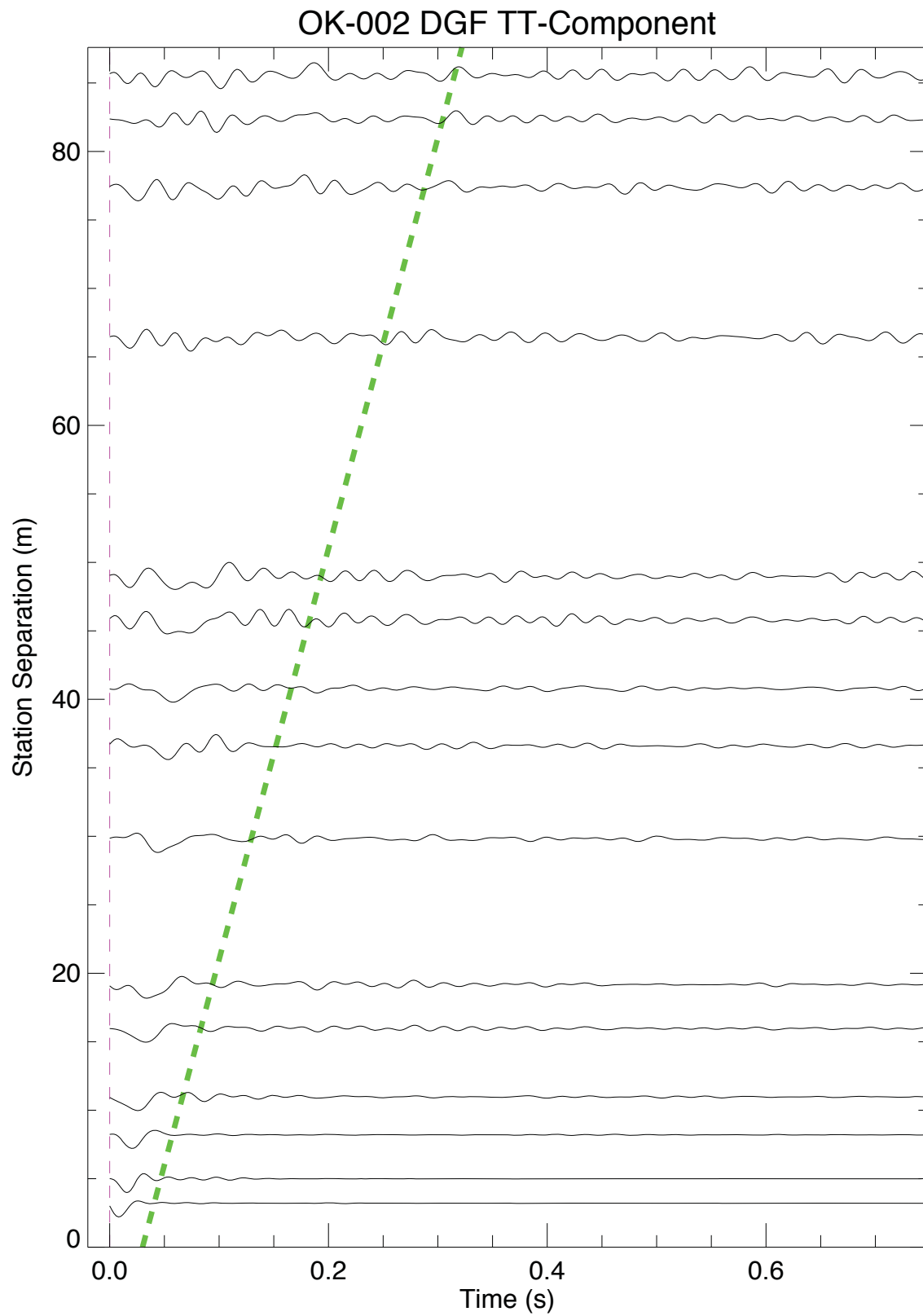


Figure 2.3e. OK-002 TT component dispersion Green's Function.

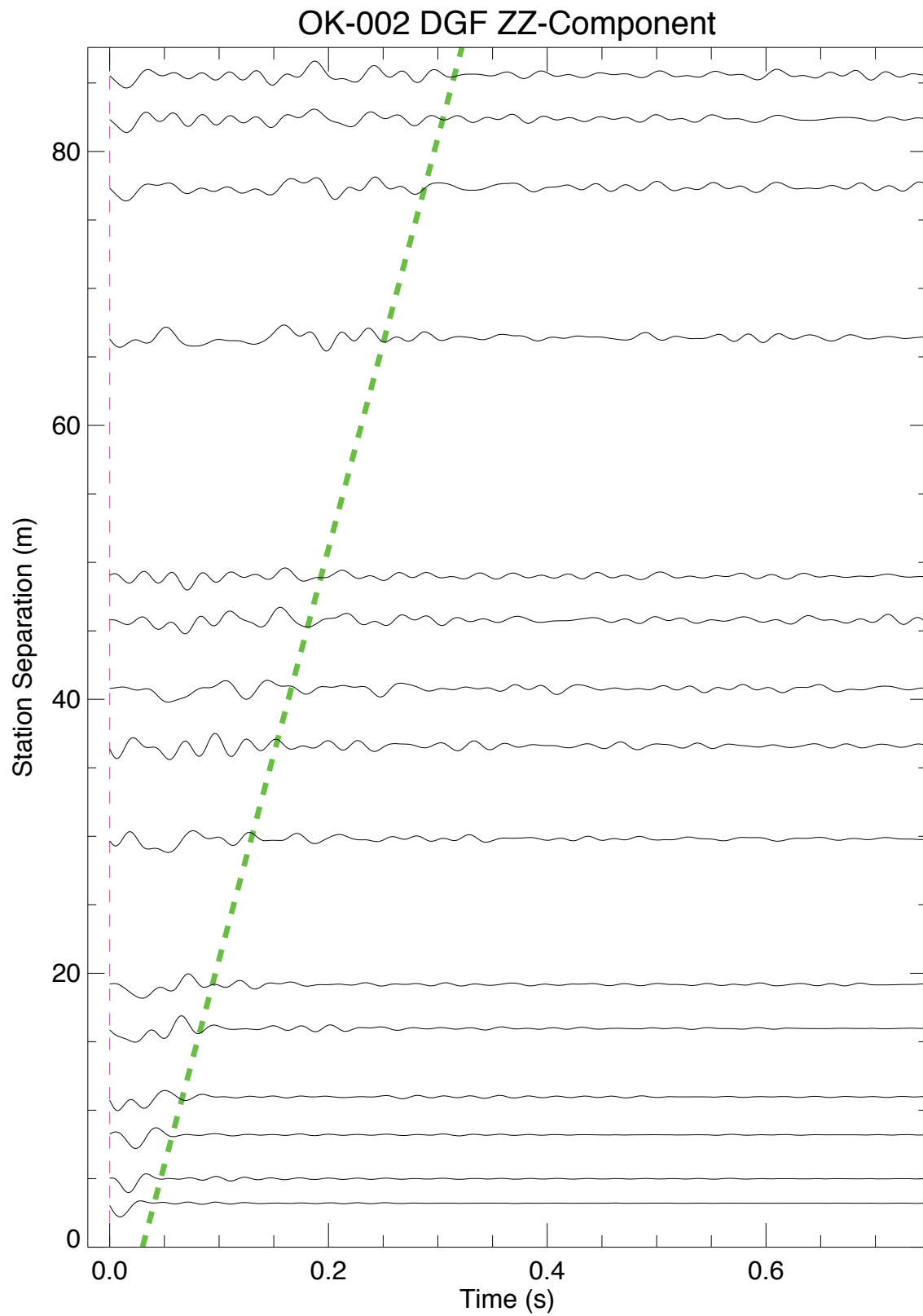


Figure 2.3f. OK-002 ZZ component dispersion Green's Function.

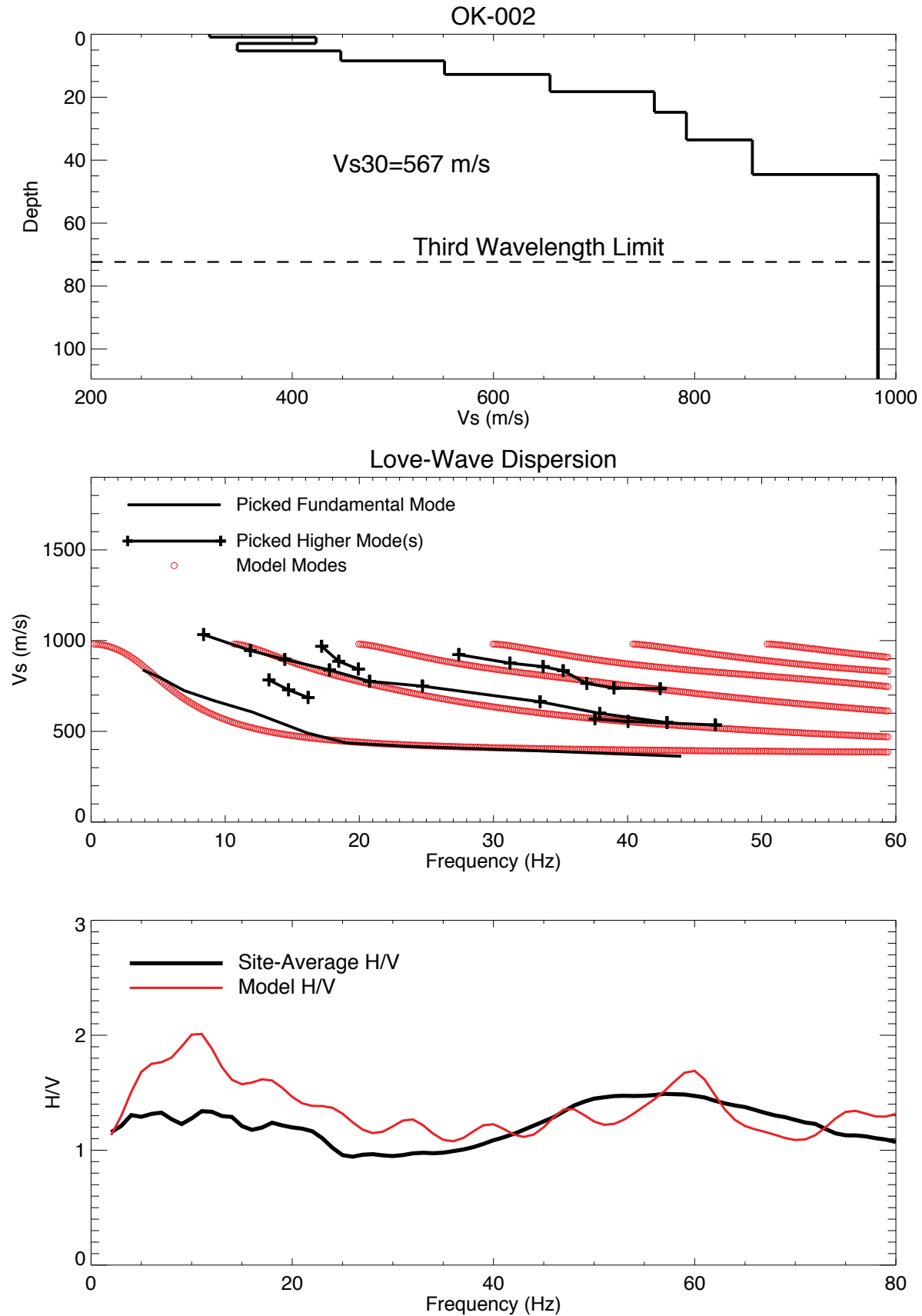


Figure 2.3g. OK-002 Love Wave Vs-Depth, Vs30, and H/V model.

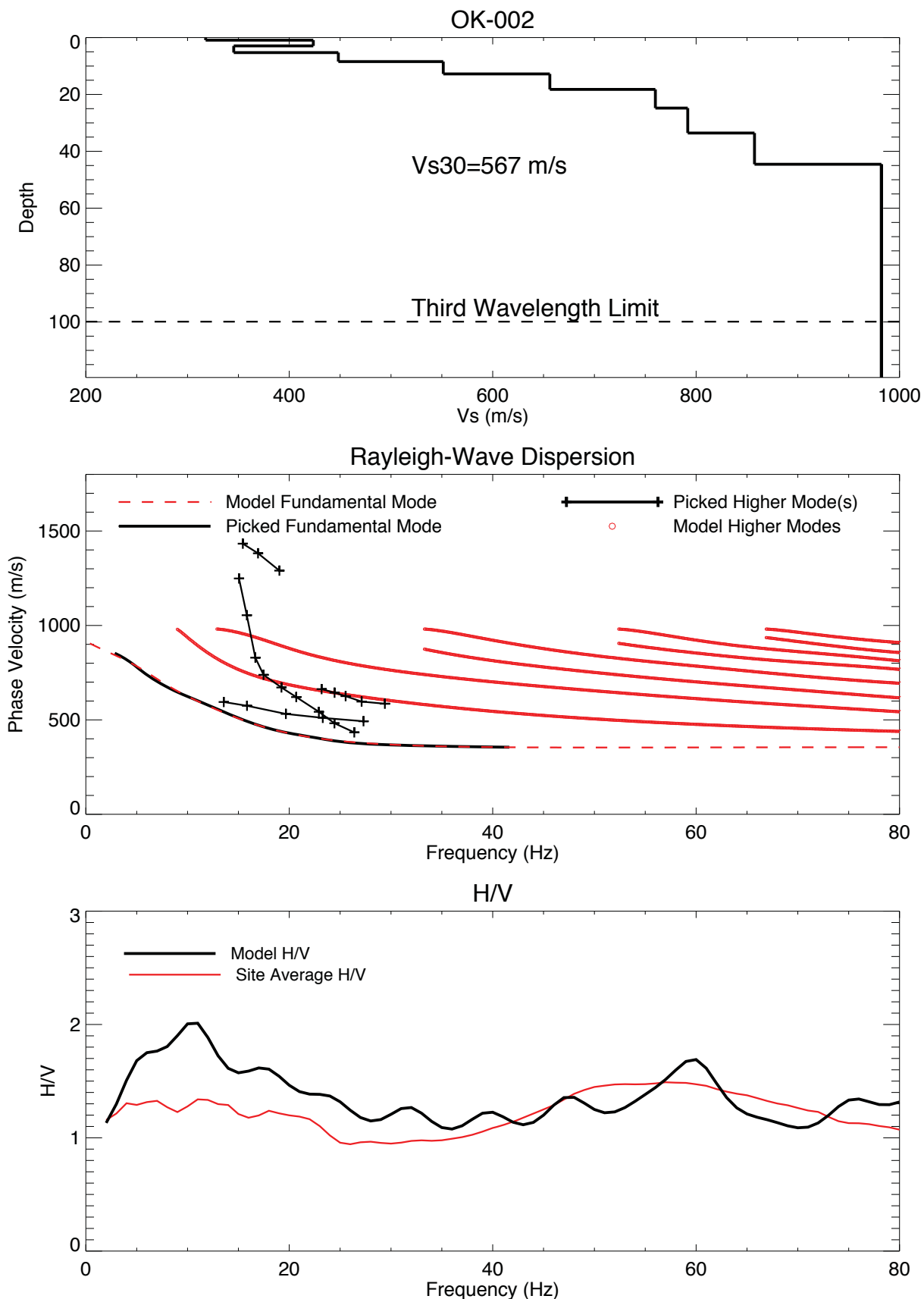


Figure 2.3h. OK-002 Rayleigh Wave Vs-depth, Vs30, and H/V model.

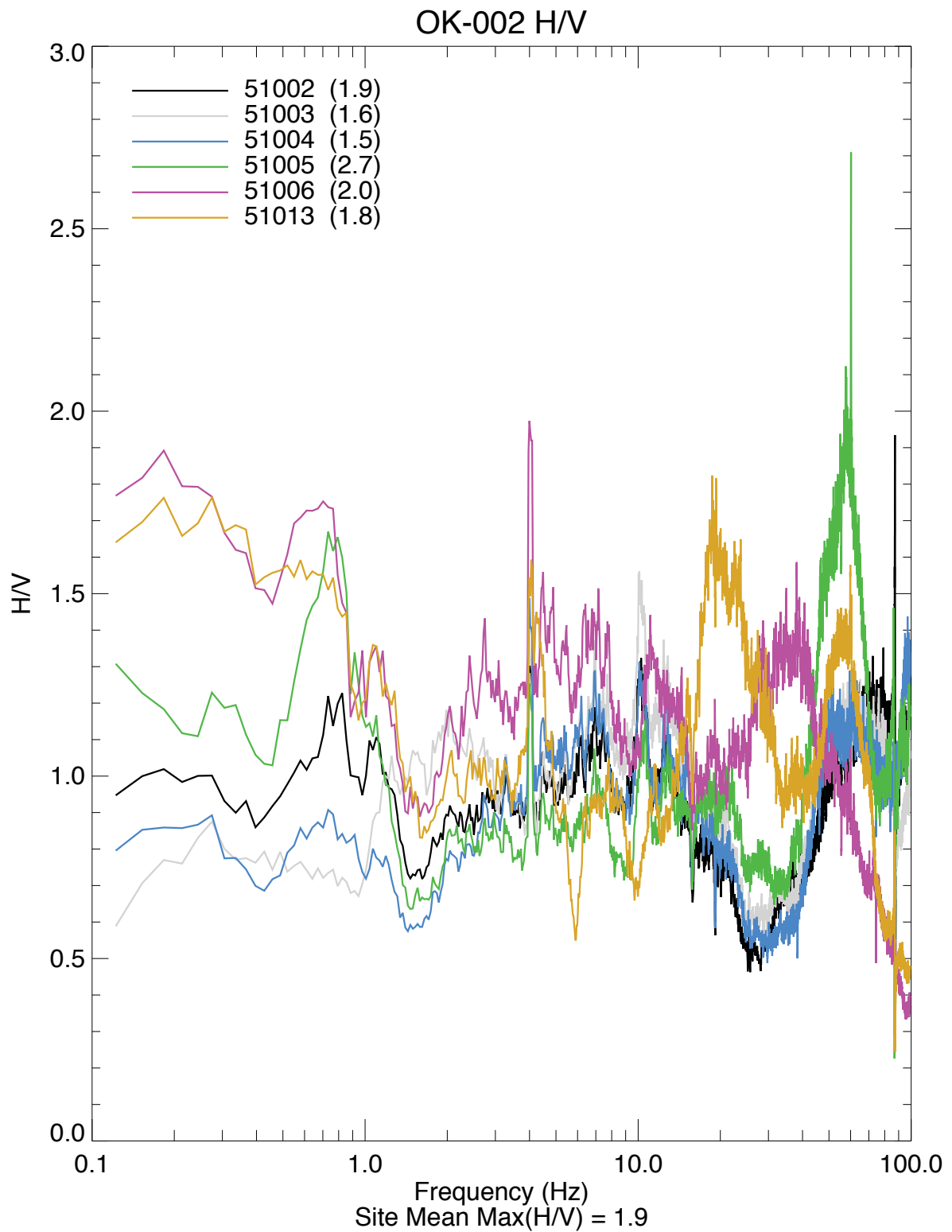


Figure 2.3i. OK-002 all stations H/V.

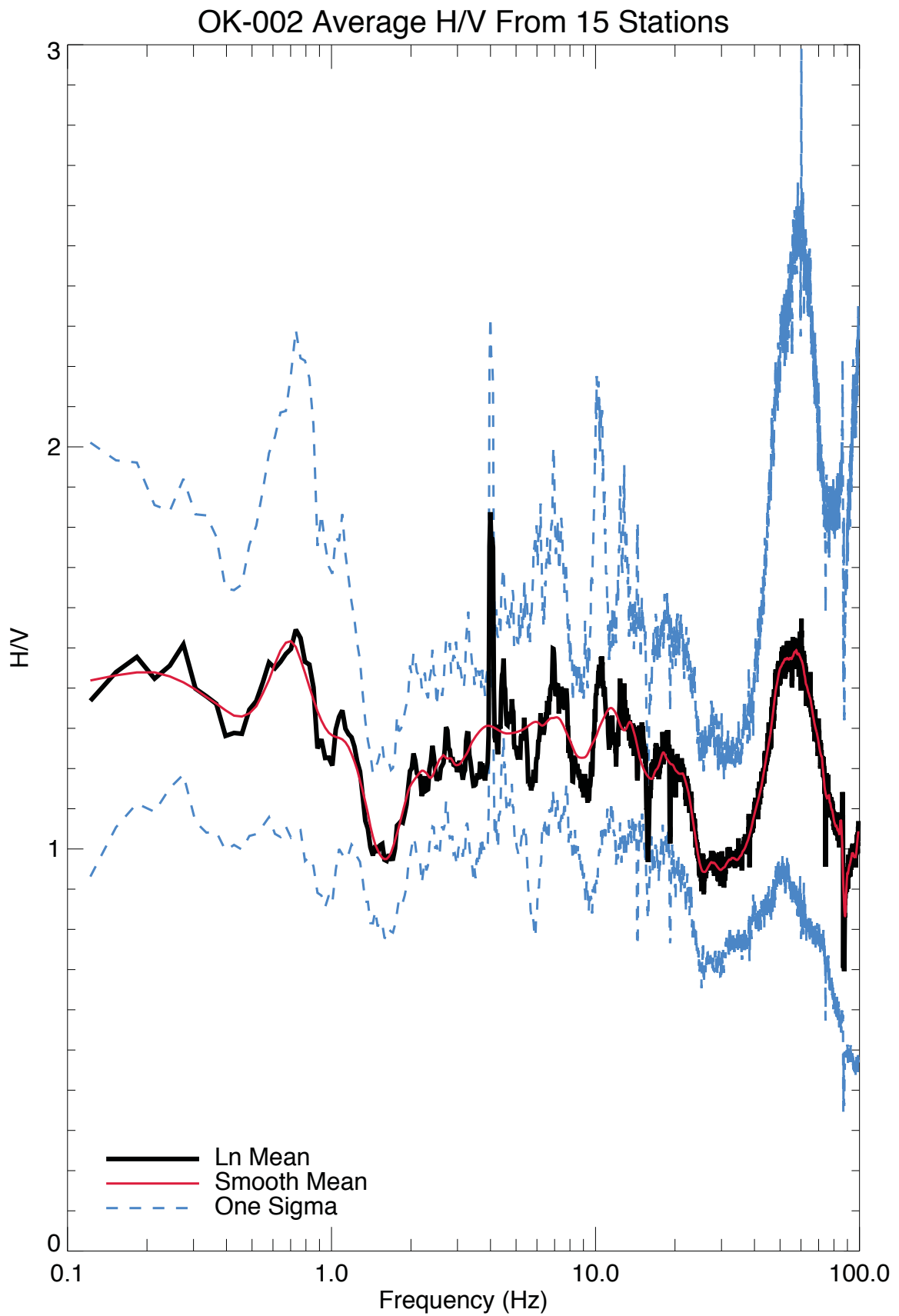


Figure 2.3j. OK-002 site average H/V.



- Explanation**
- Receiver location

Figure 2.4a. OK-005 site location.

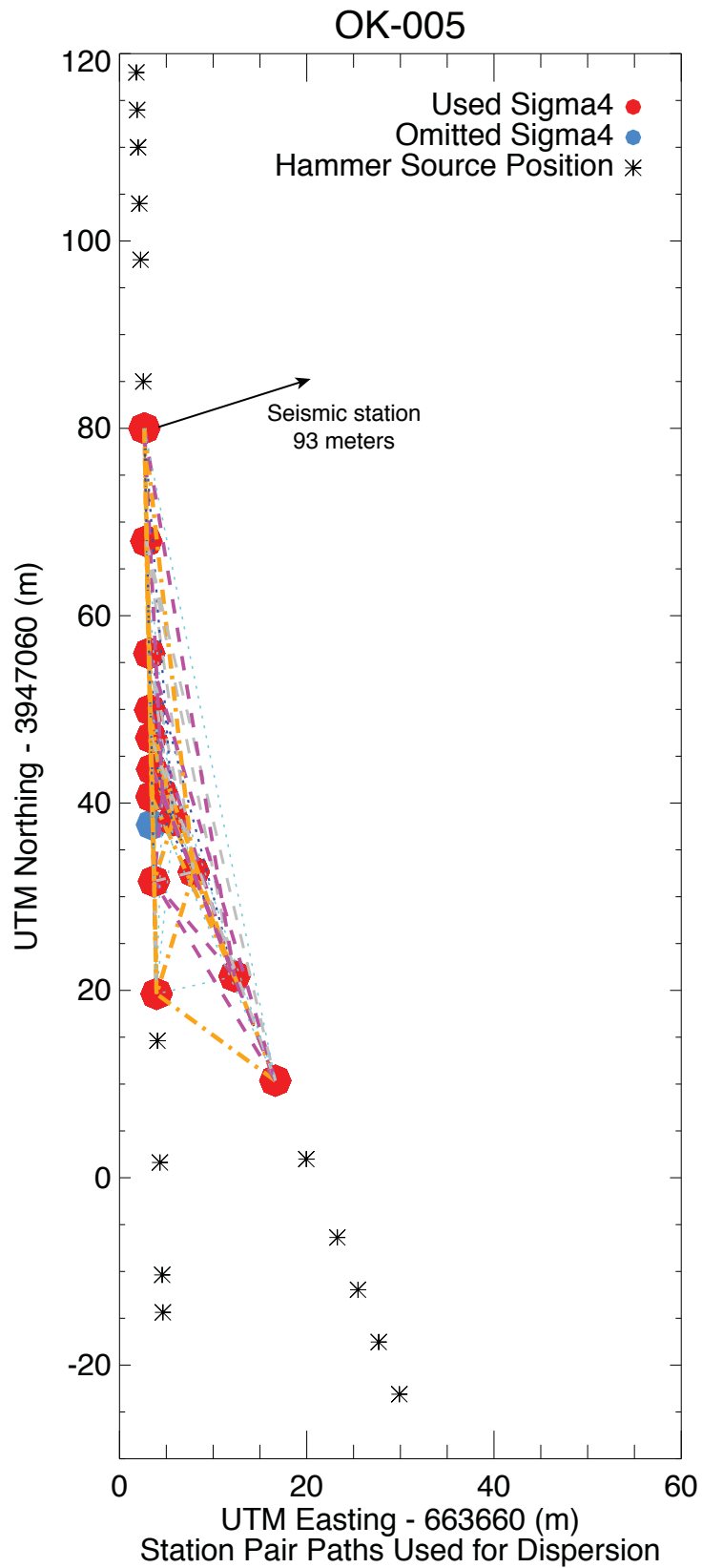


Figure 2.4b OK-005 station dispersion pathways and source positions.

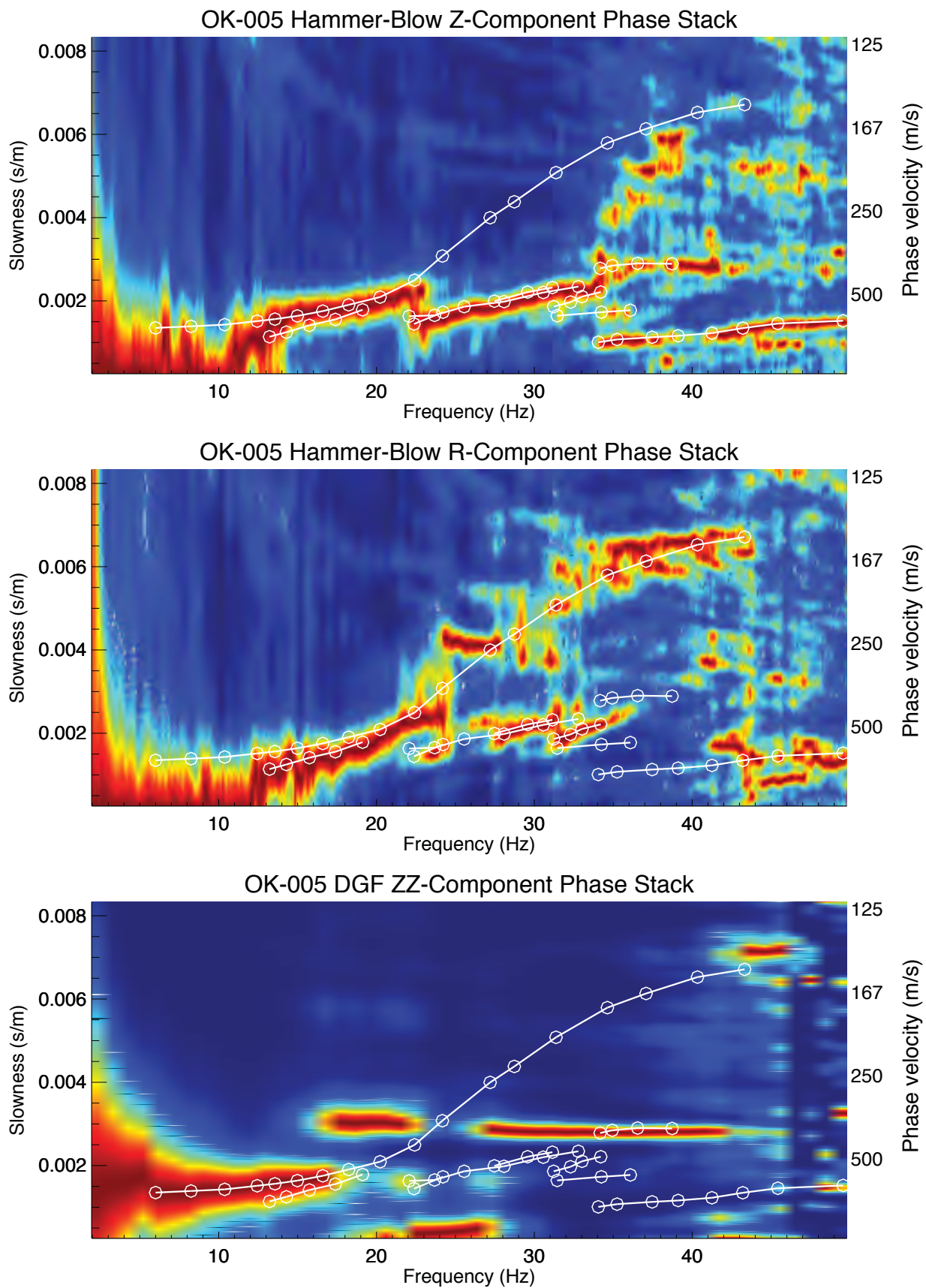


Figure 2.4c. OK-005 multimodal p-f dispersion images and picks.

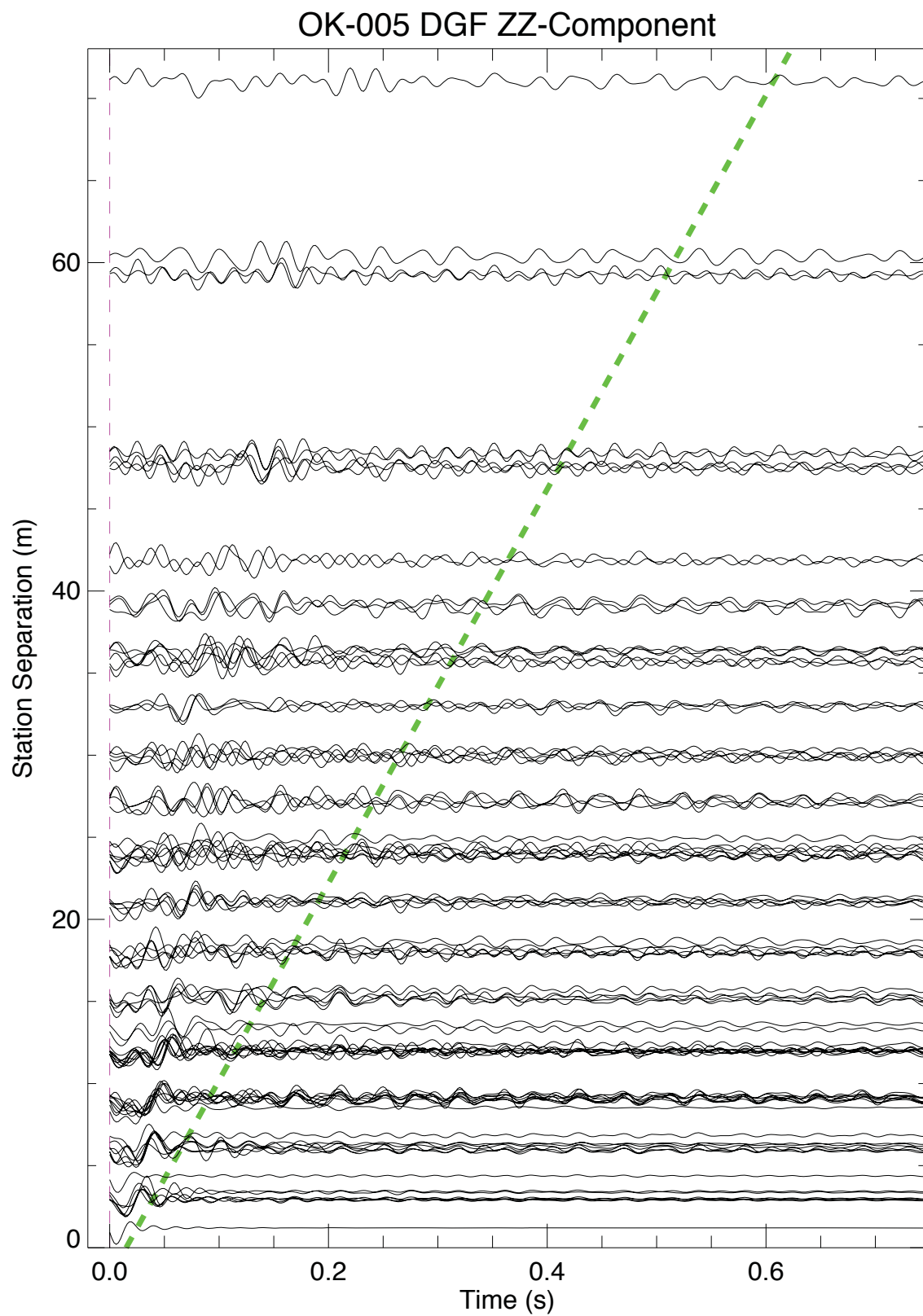


Figure 2.4d. OK-005 vertical component dispersion Green's Function.

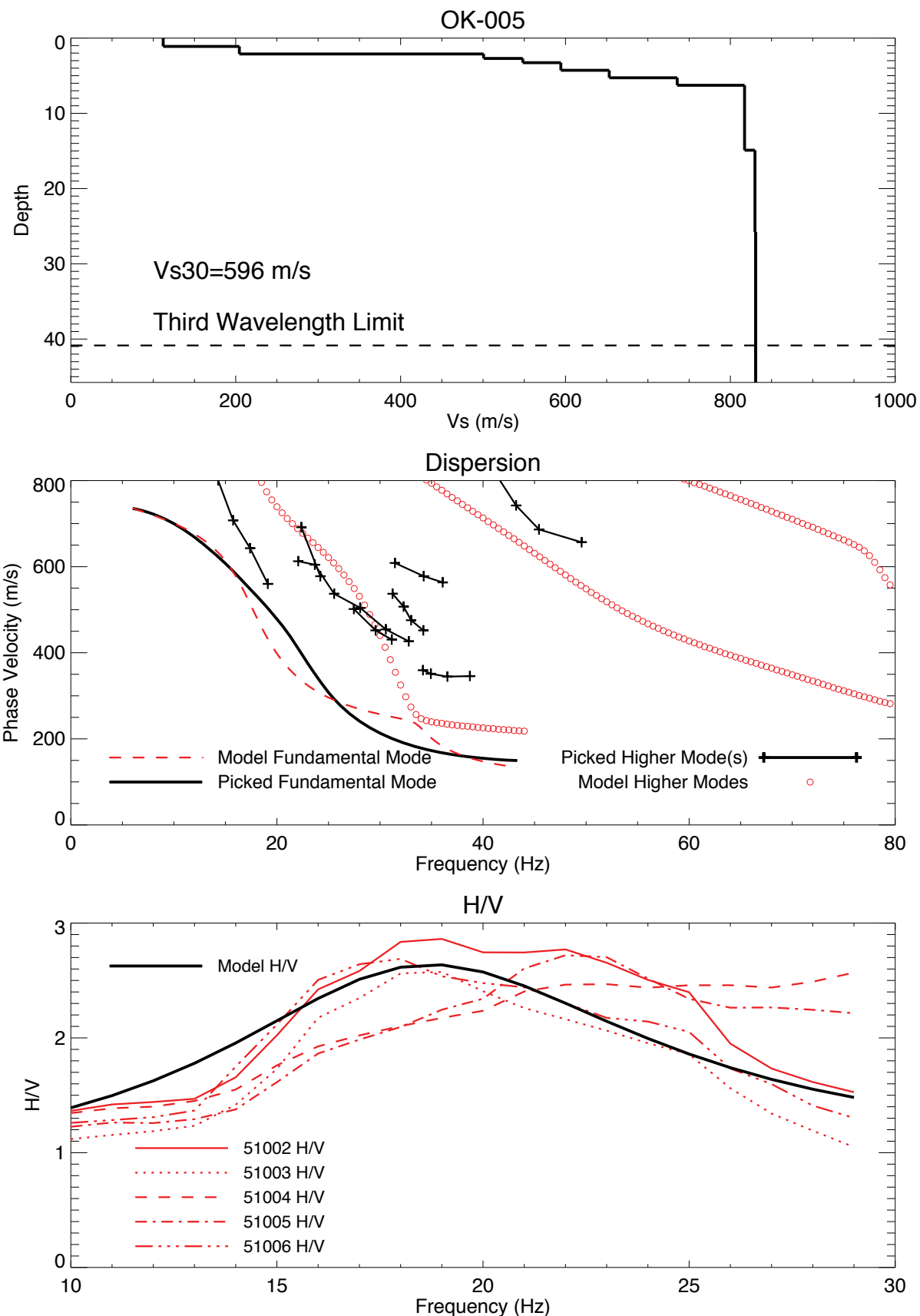


Figure 2.4e. OK-005 Vs-depth, Vs30, and Nearfield H/V Model.

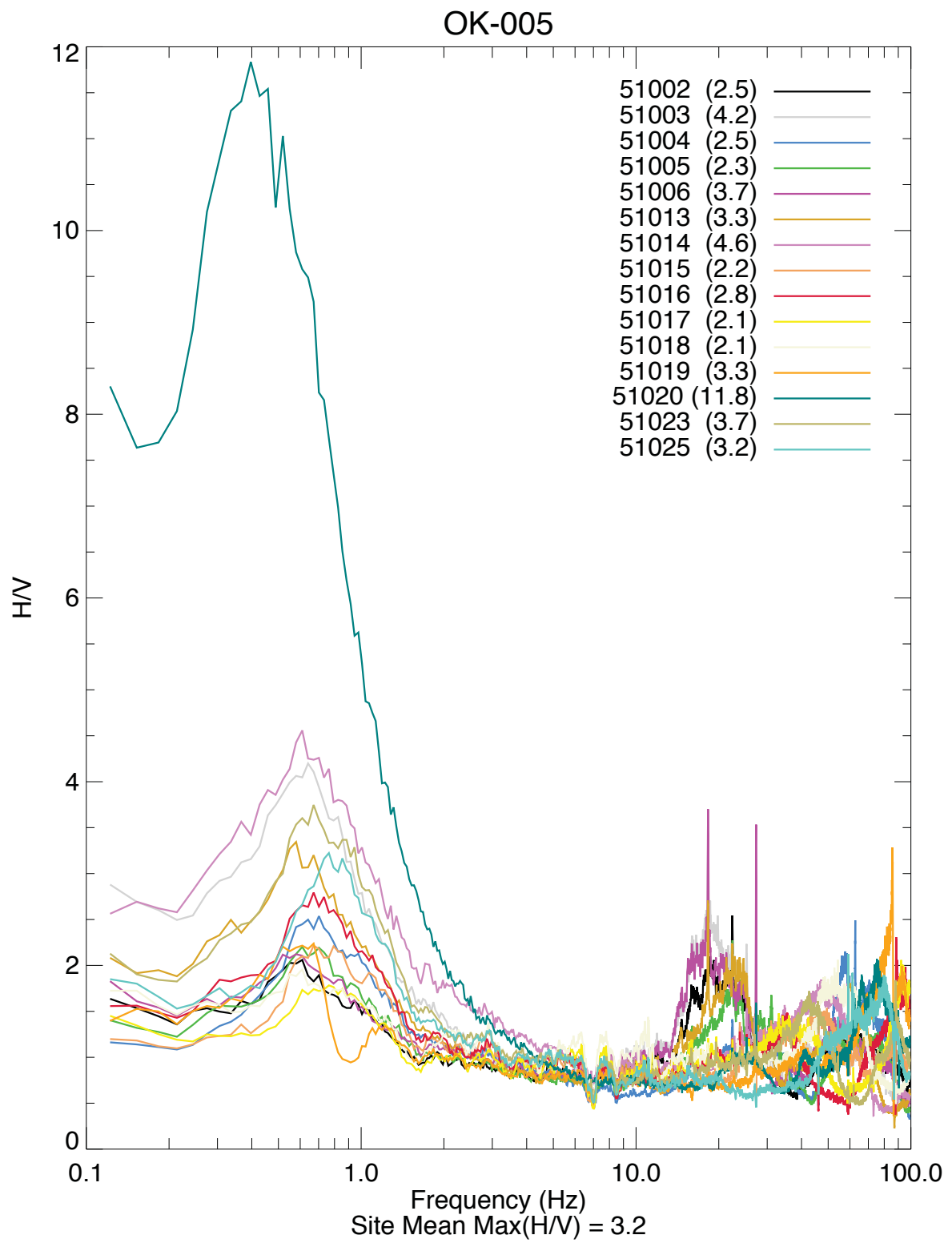


Figure 2.4f. OK-005 all stations H/V.

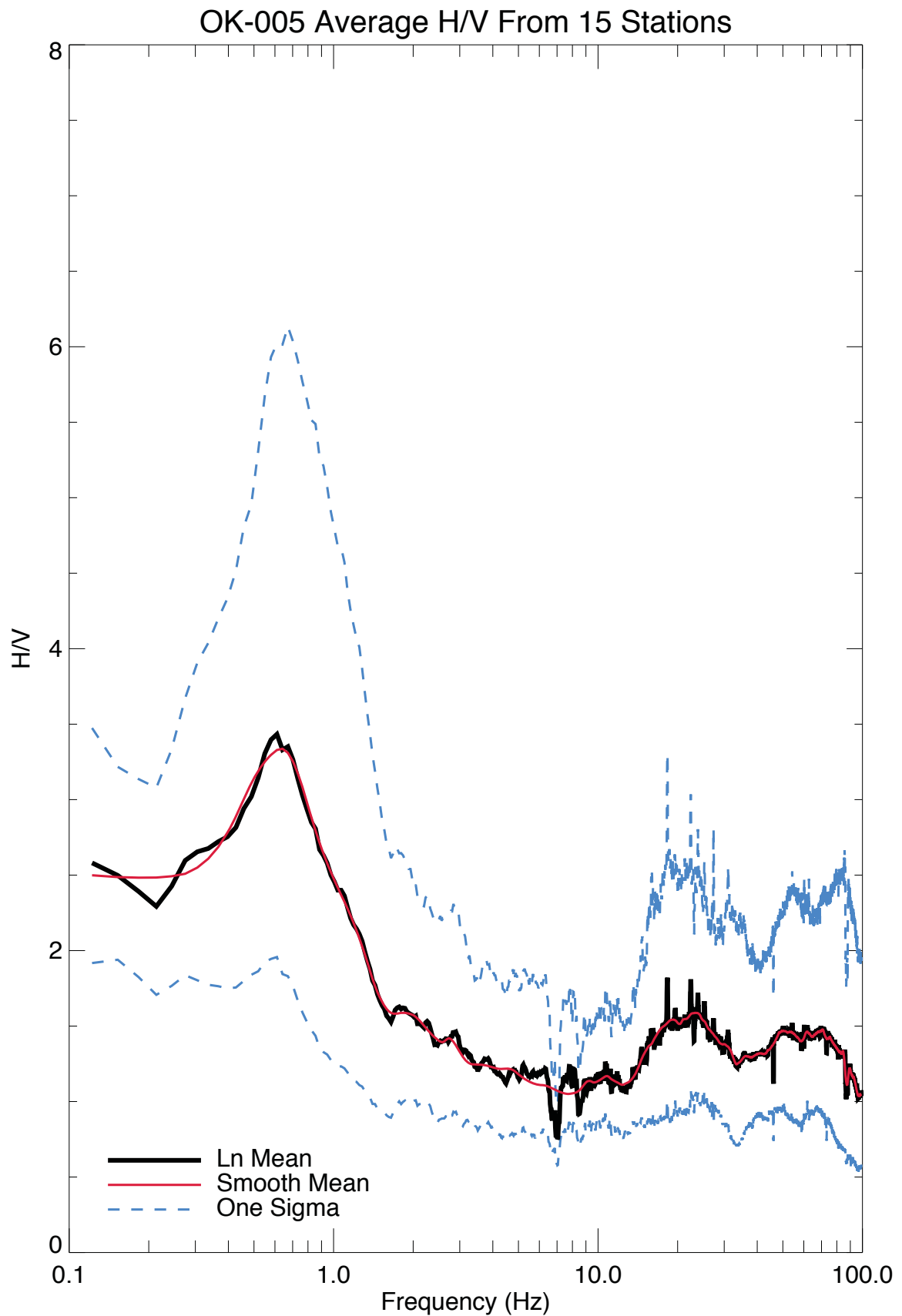
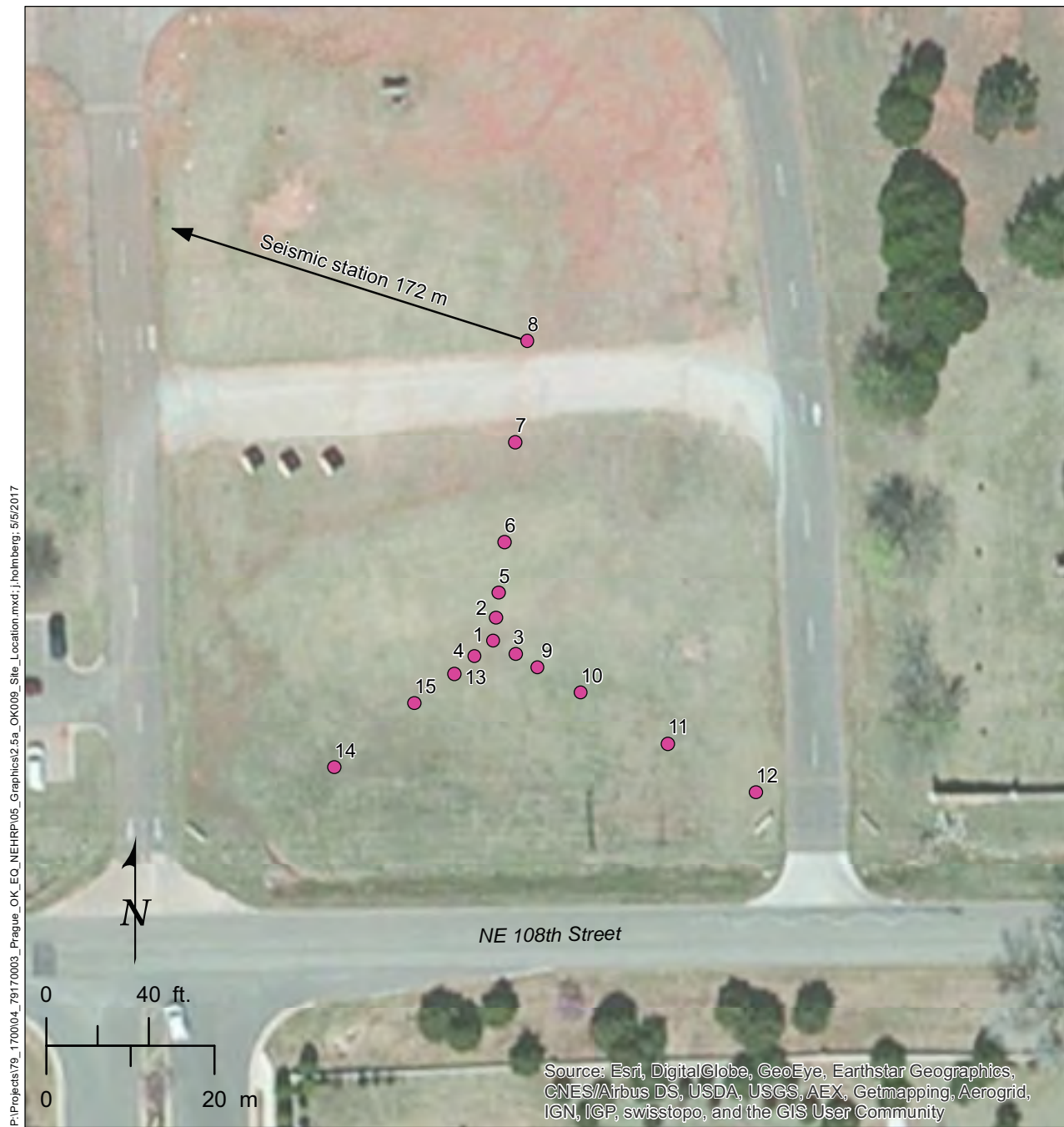


Figure 2.4g. OK-005 site average H/V.



Explanation

- Receiver location

Figure 2.5a. OK-009 site location.

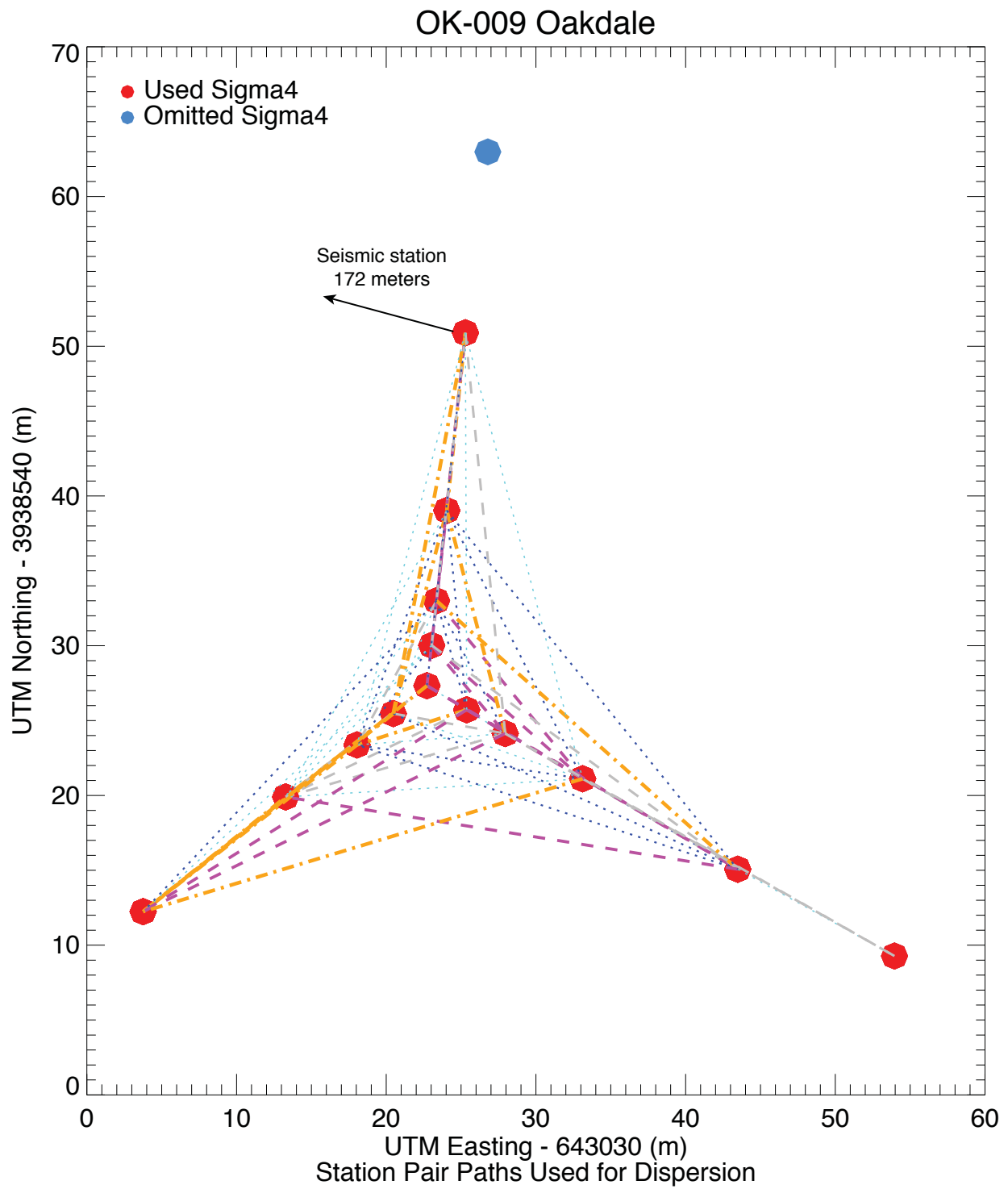


Figure 2.5b OK-009 station dispersion pathways and source positions.

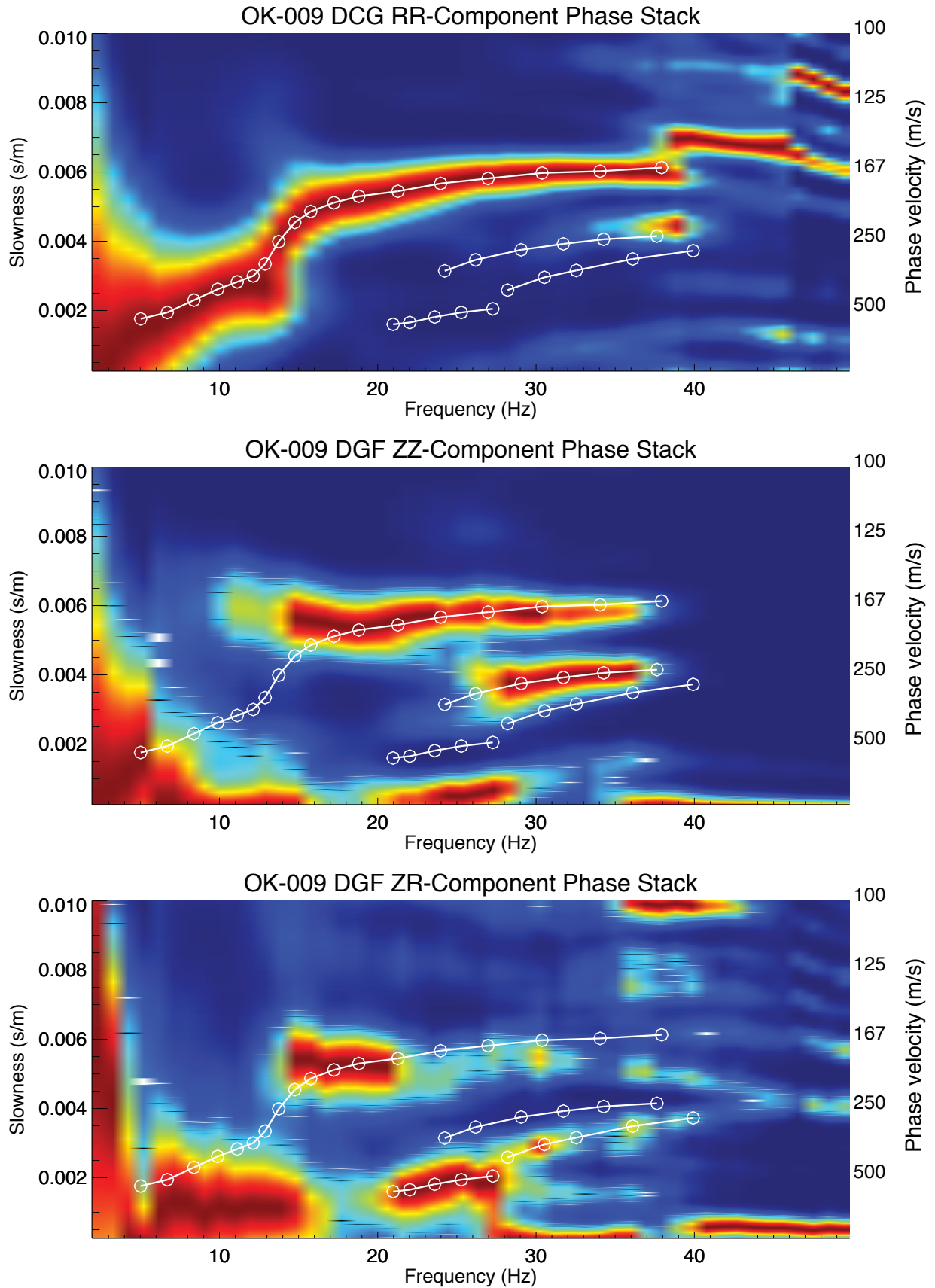


Figure 2.5c. OK-009 multimodal p-f dispersion images and picks.

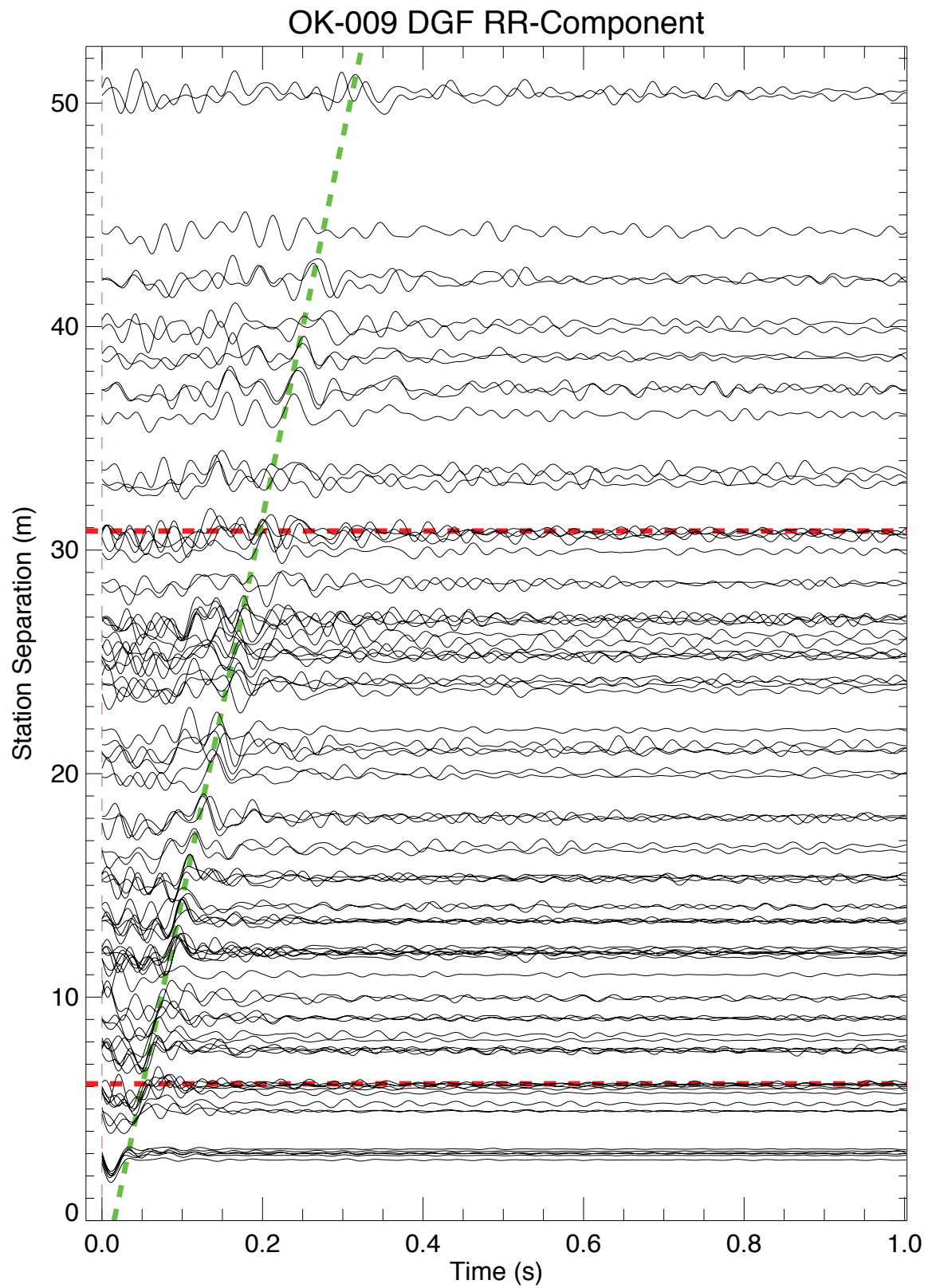


Figure 2.5d. OK-009 radial component dispersion Green's Function.

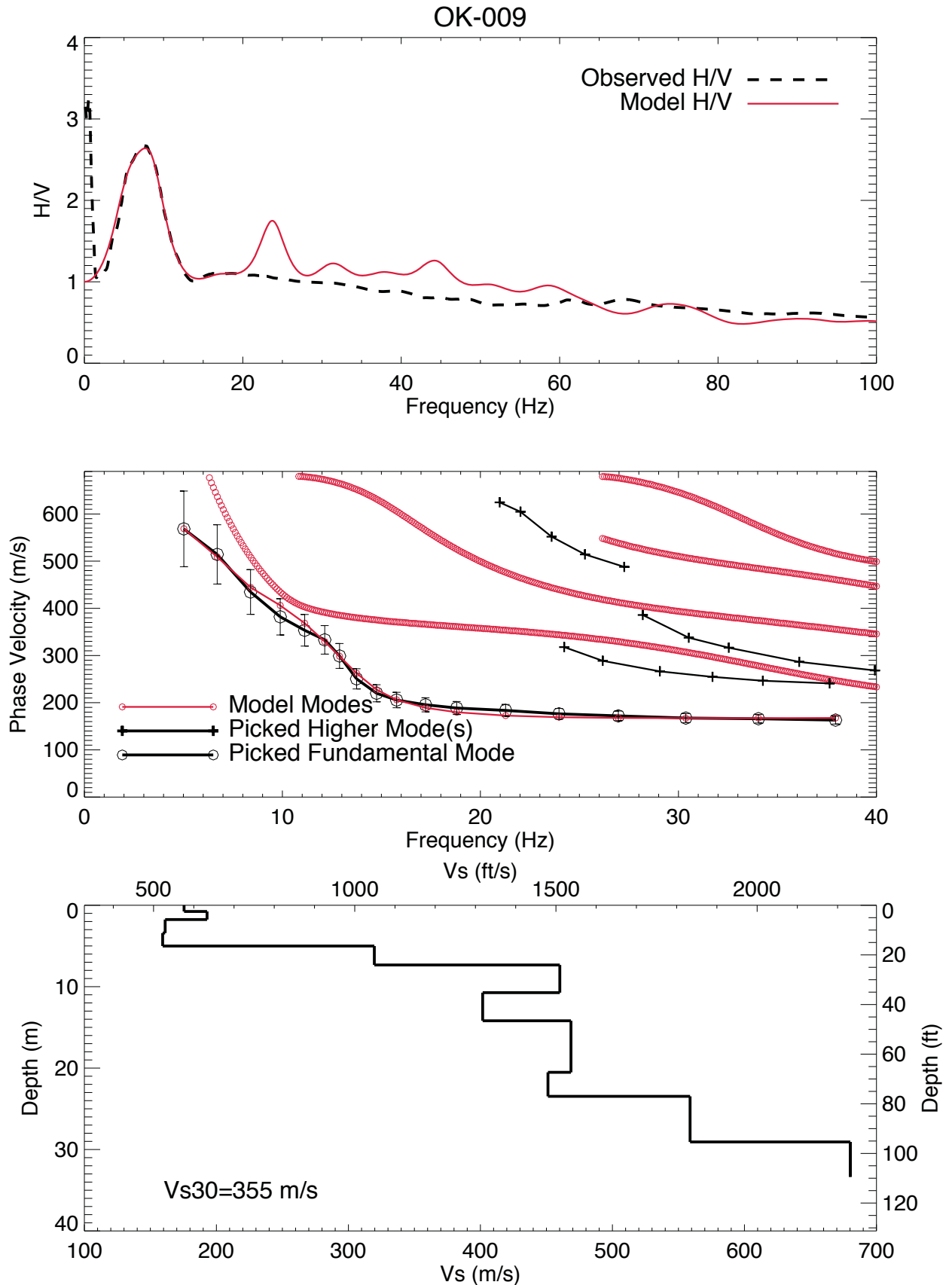


Figure 2.5e. OK-009 Vs-depth, Vs30, and Nearfield H/V Model.

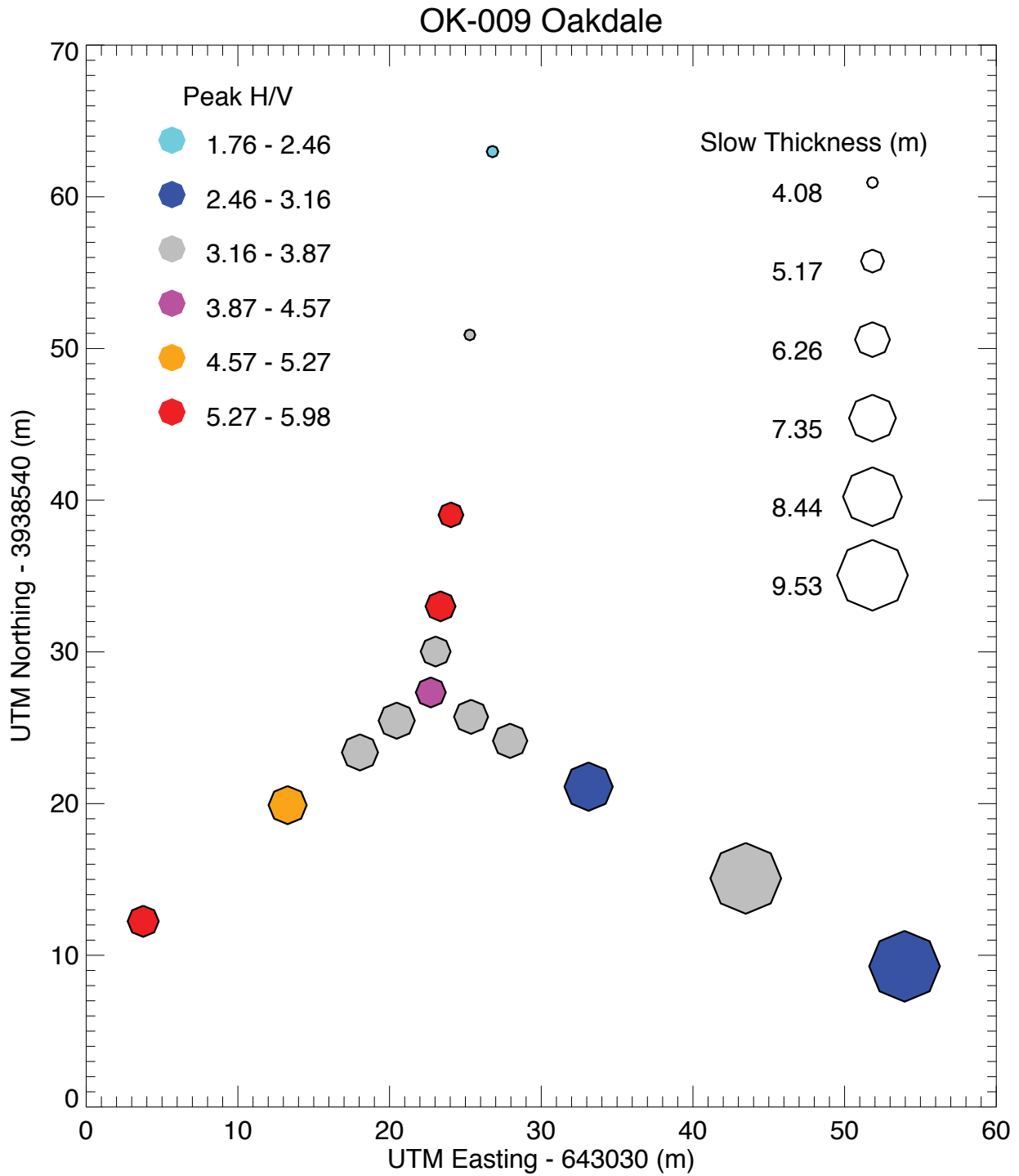


Figure 2.5f. OK-009 map view slow thickness variations and maximum H/V.

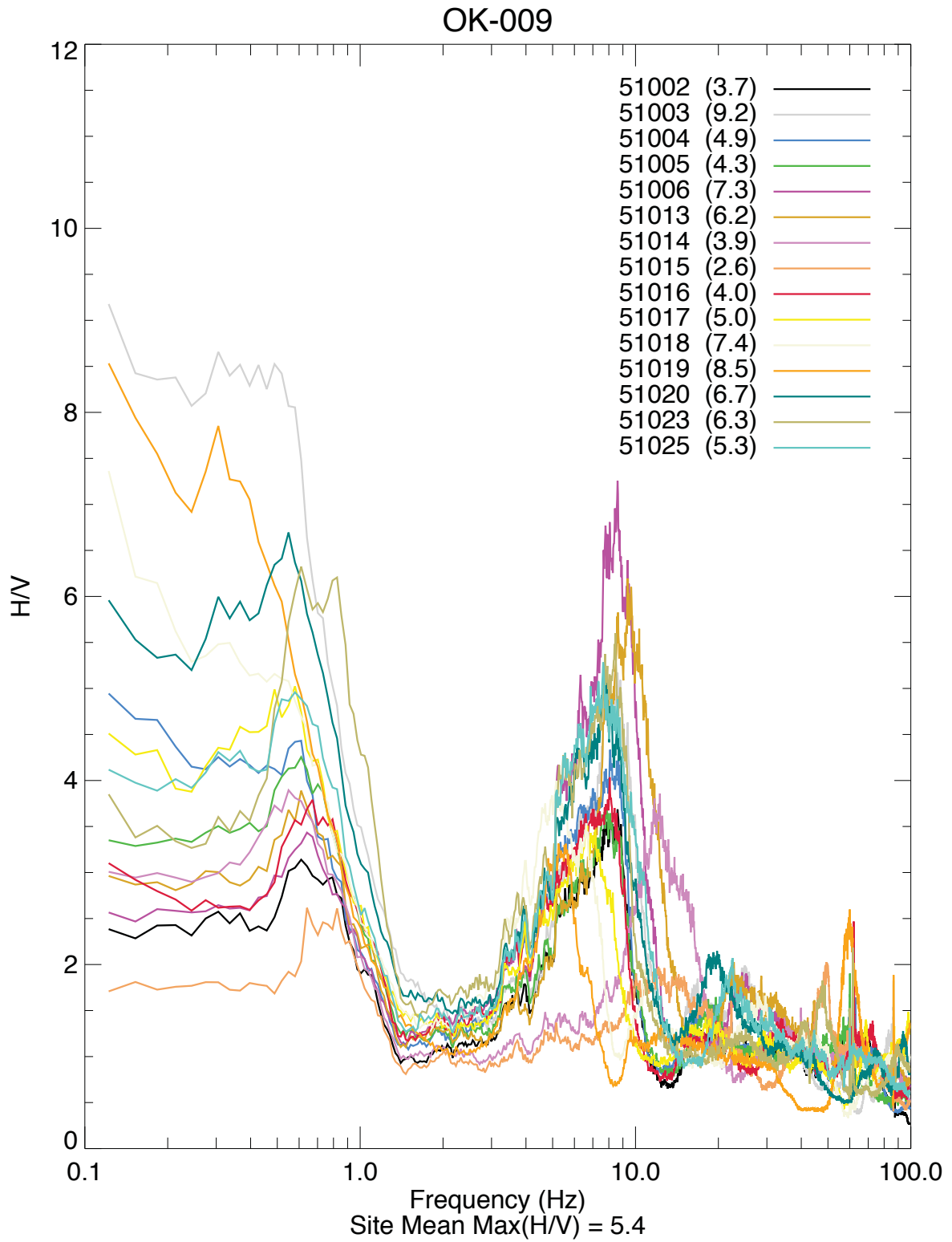


Figure 2.5g. OK-009 all stations H/V.

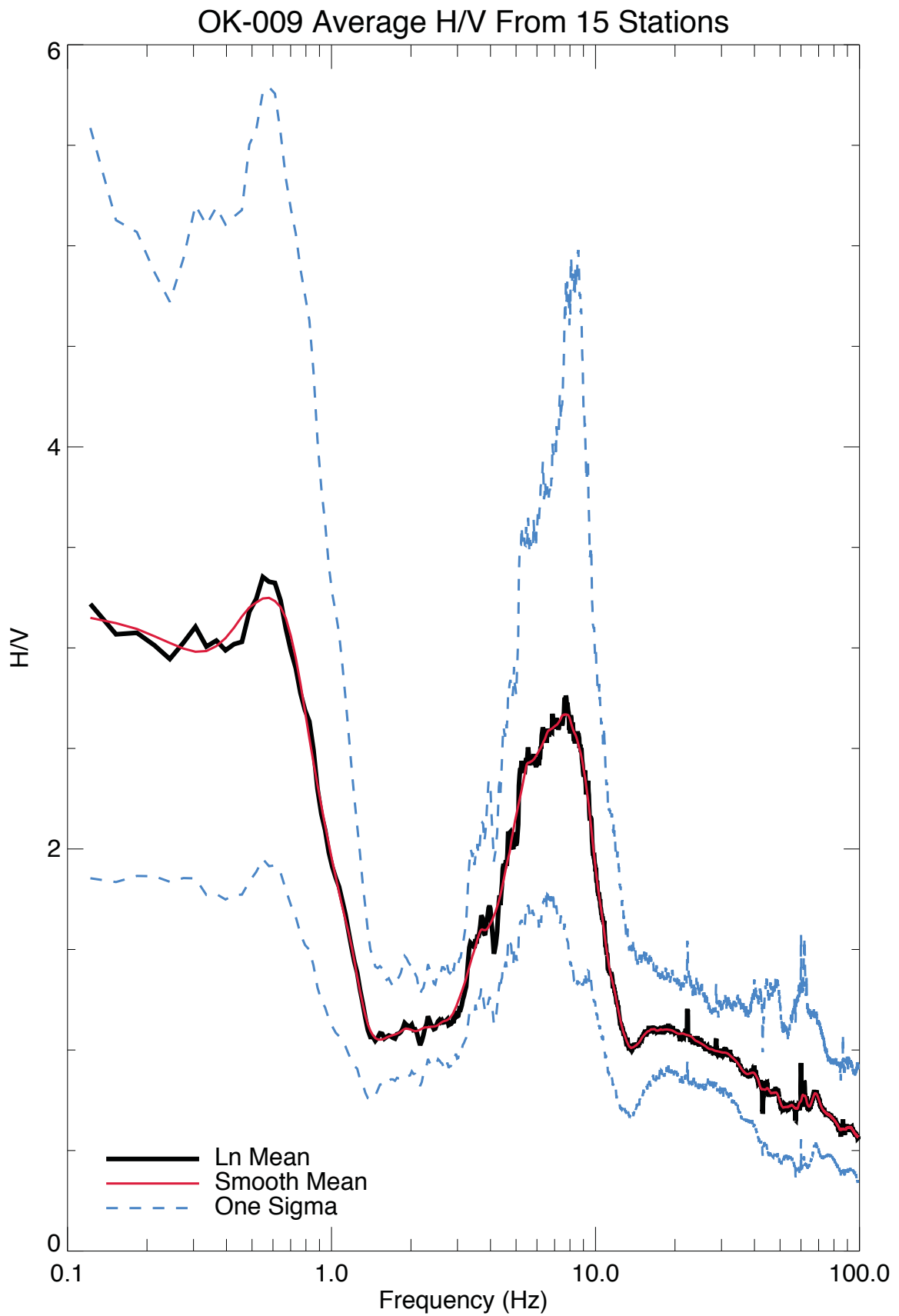


Figure 2.5h. OK-009 site average H/V.



Explanation

- Receiver location
- ▲ Seismic station

Figure 2.6a. TUL-1 site location.

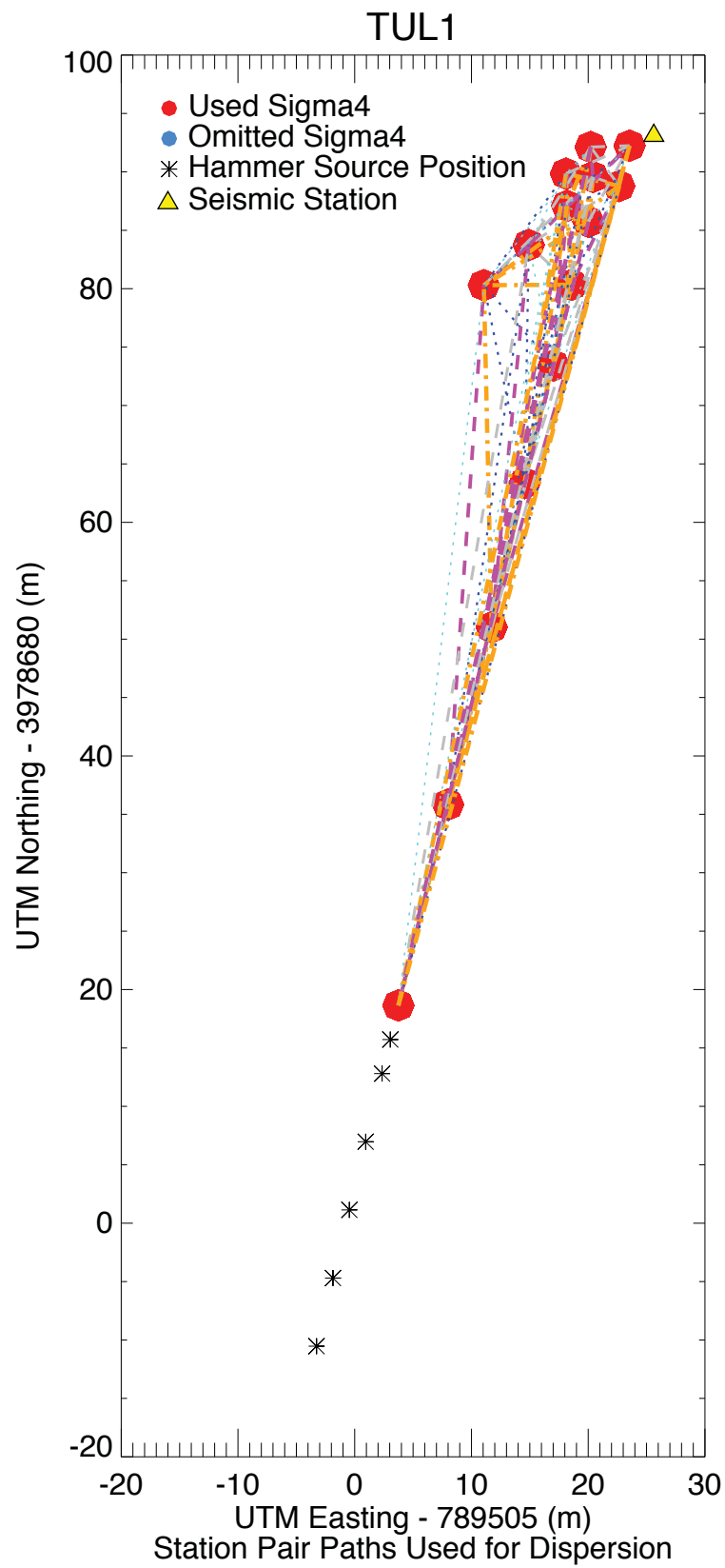


Figure 2.6b. TUL-1 station dispersion pathways and source positions.

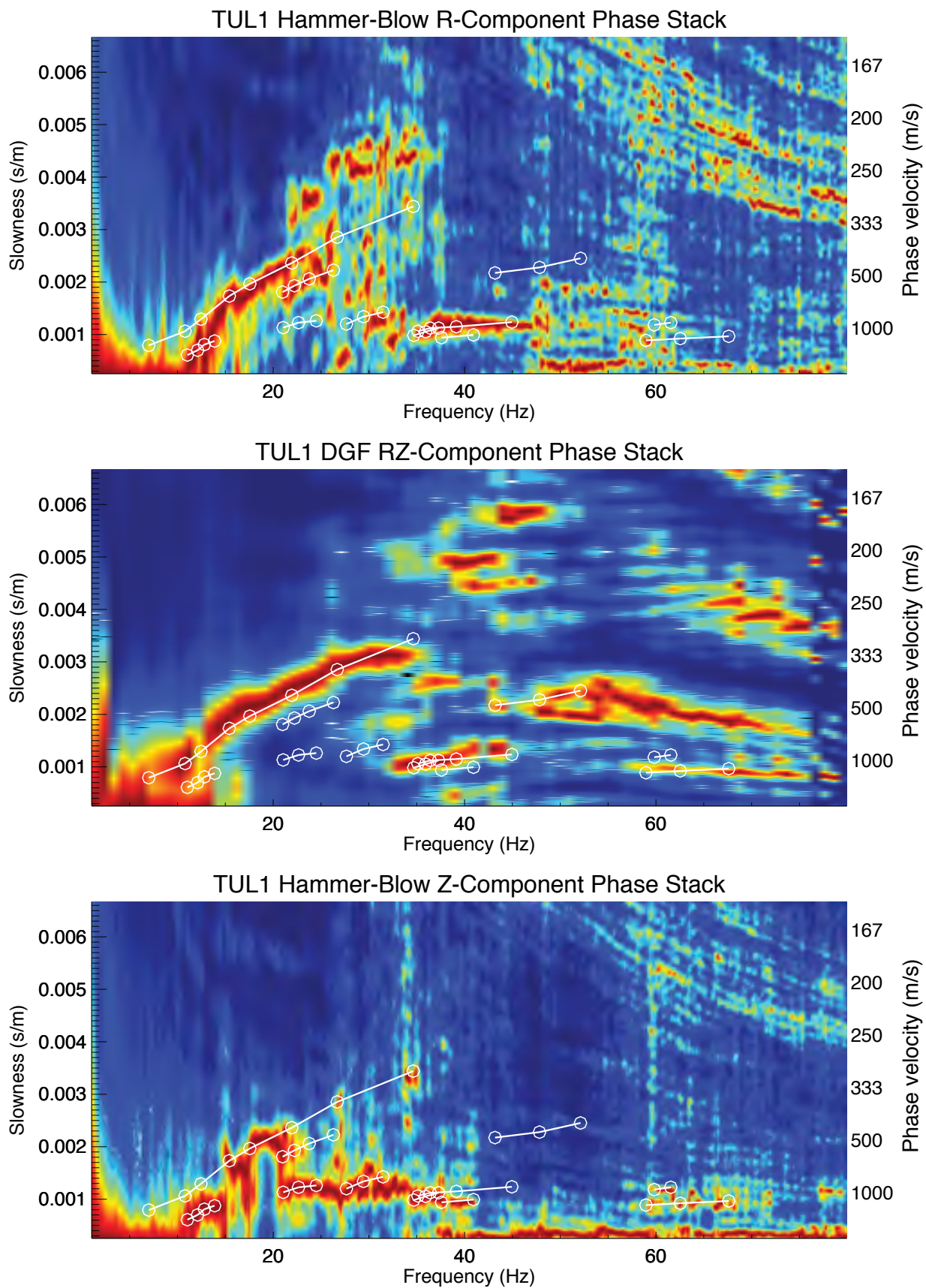


Figure 2.6c. TUL-1 R-, RZ-, and Z-component multimodal p-f dispersion images and picks.

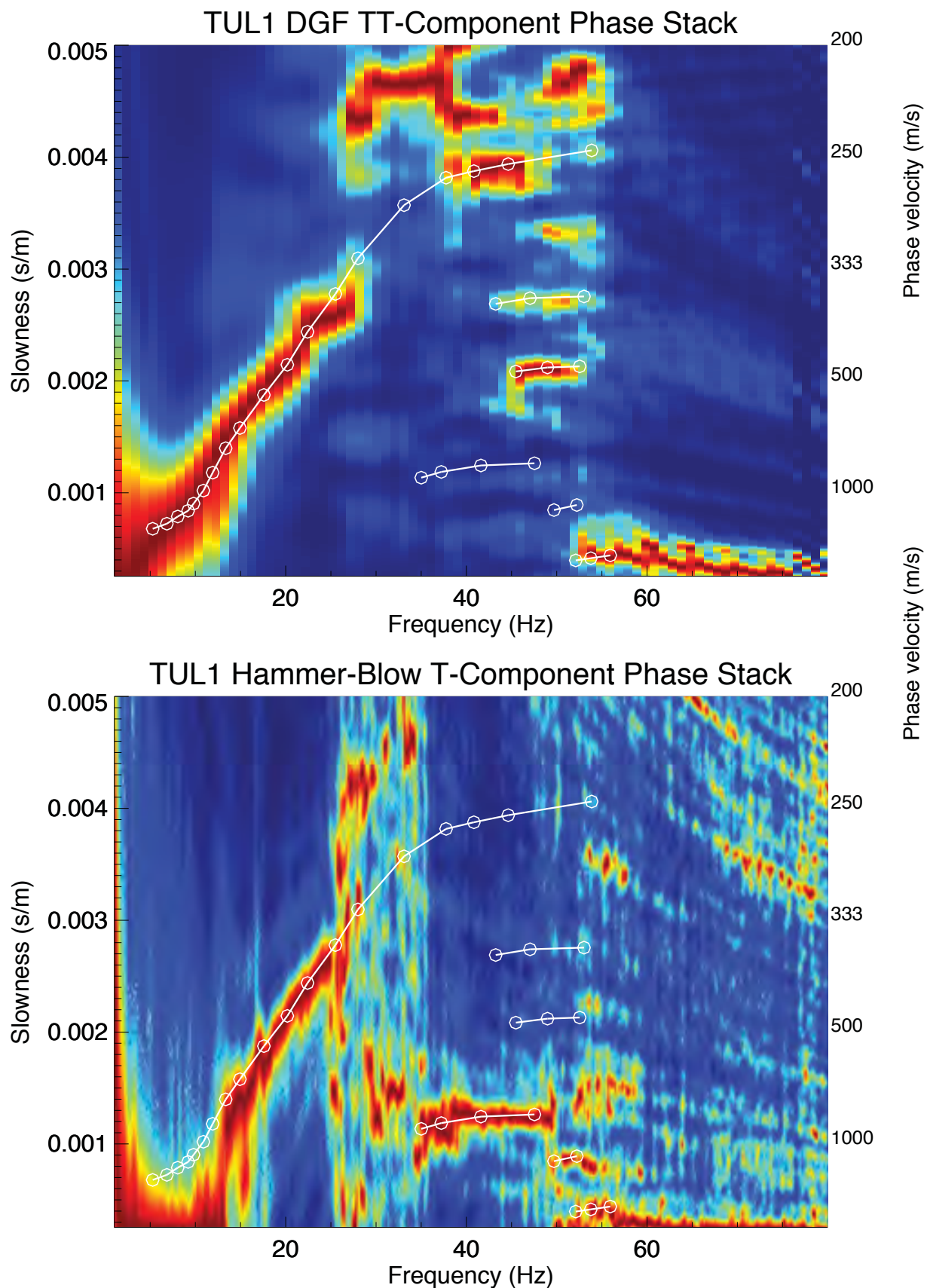


Figure 2.6d. TUL-1 TT- and T-component multimodal p-f dispersion images and picks.

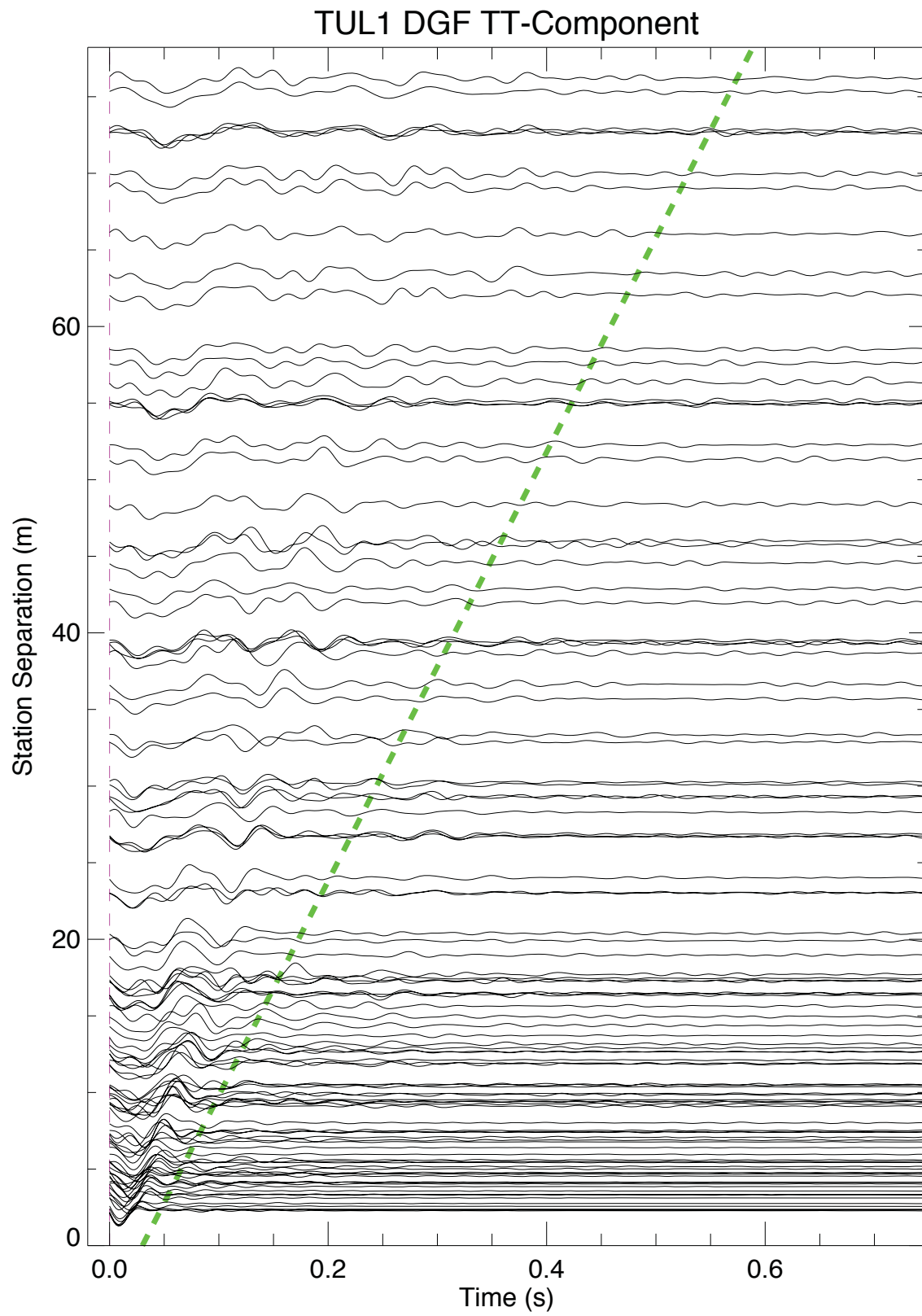


Figure 2.6e. TUL-1 TT component dispersion Green's Function.

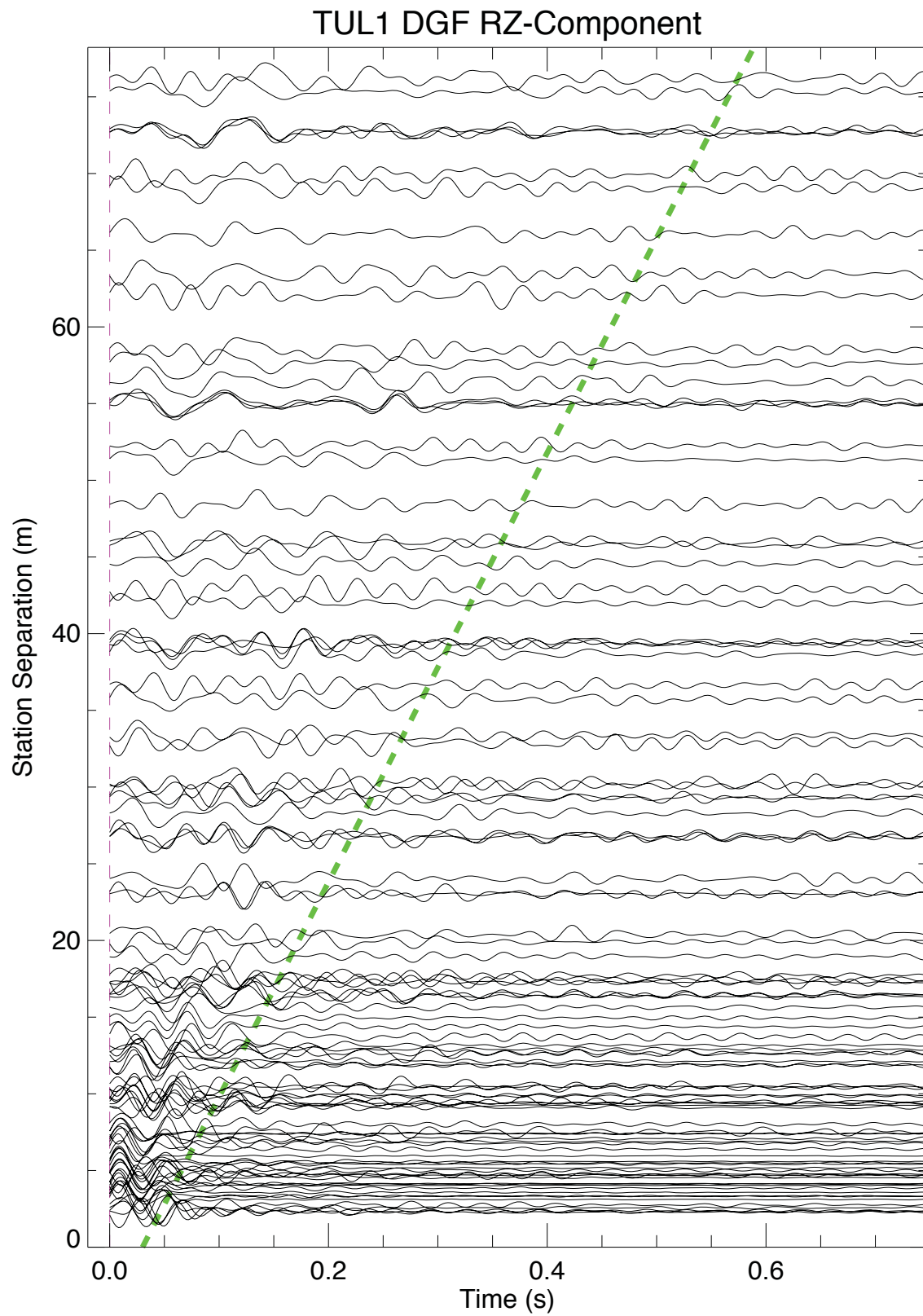


Figure 2.6f. TUL-1 RZ component dispersion Green's Function.

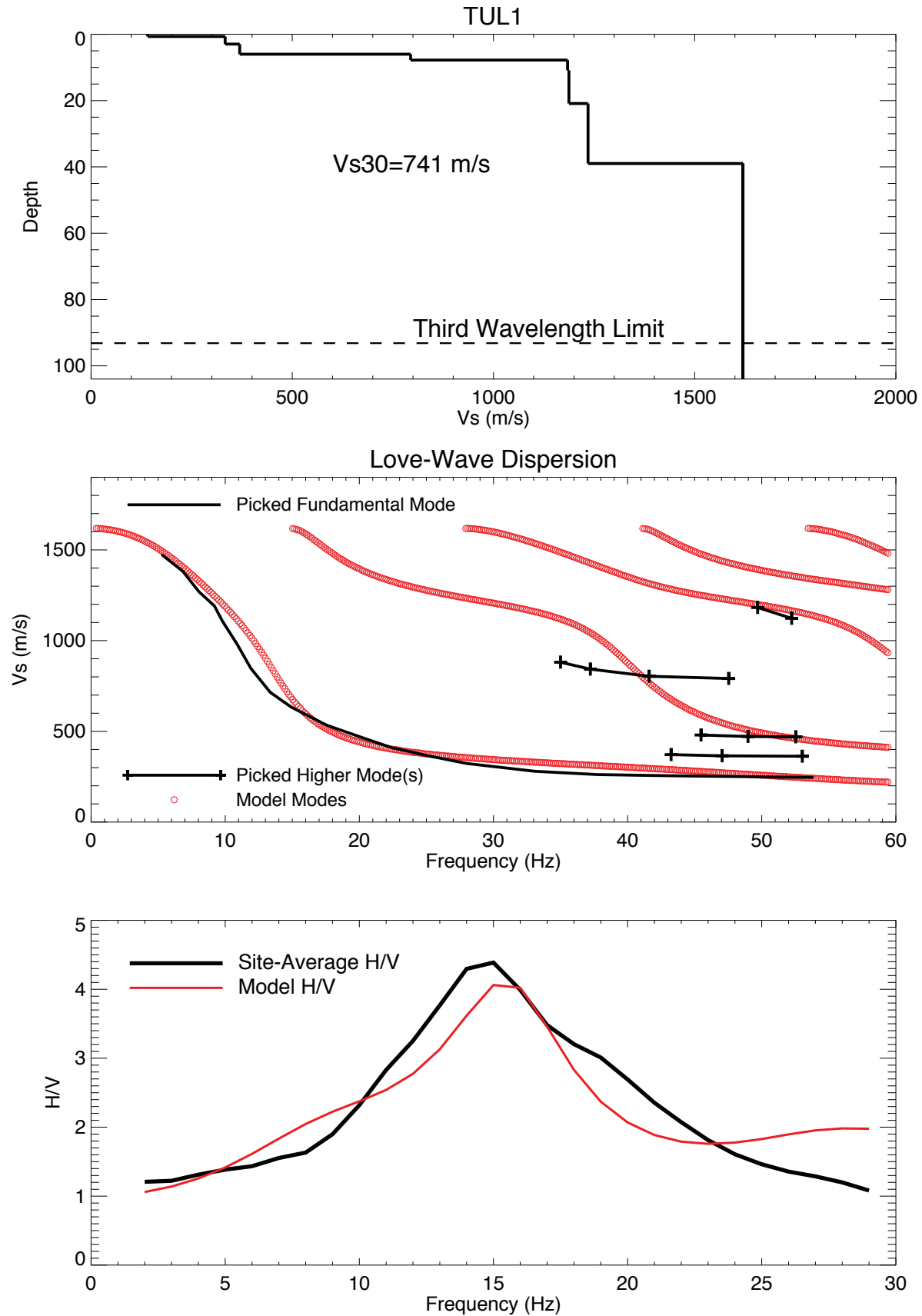


Figure 2.6g. TUL-1 Love Wave Vs-Depth, Vs30, and H/V model.

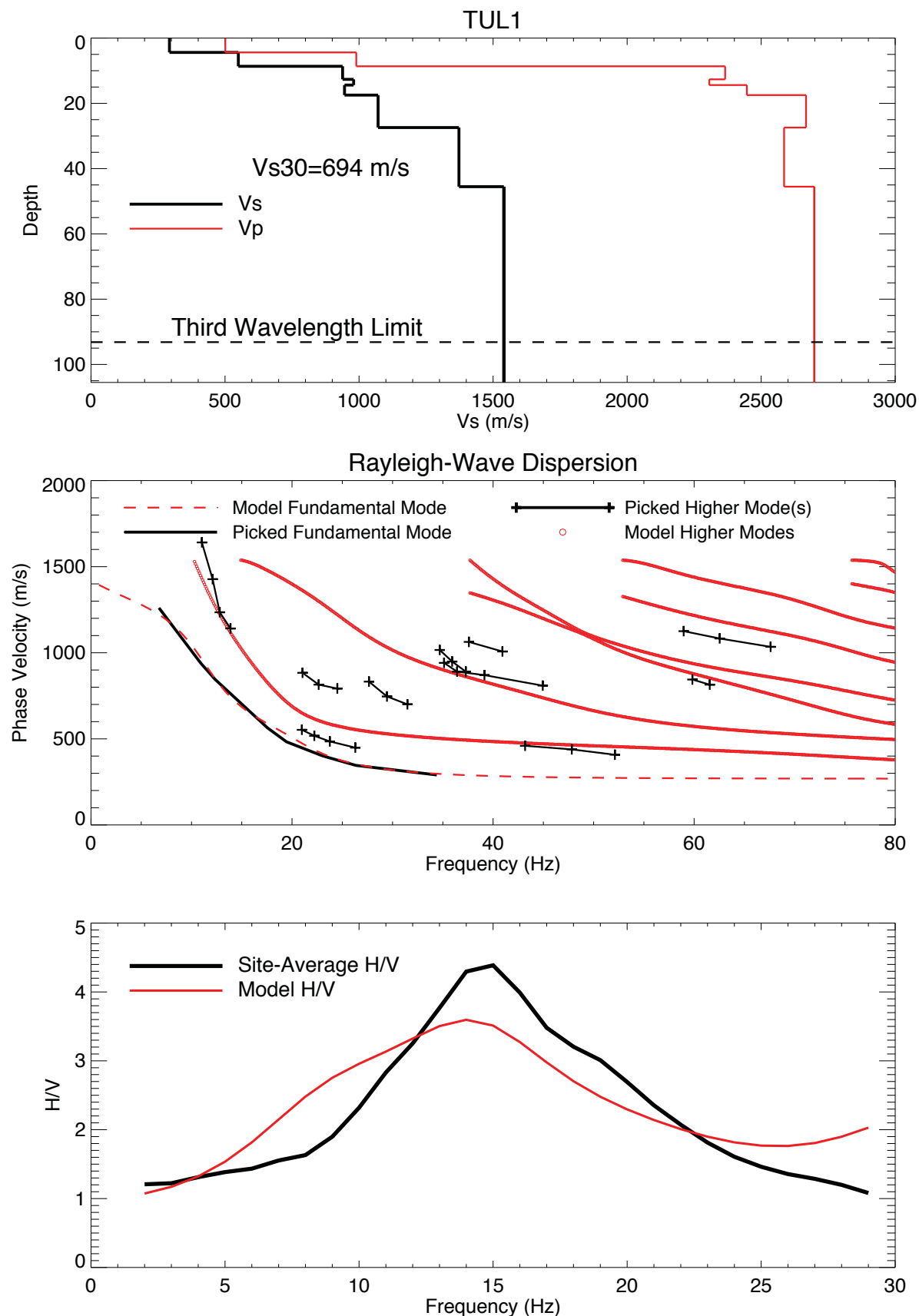


Figure 2.6h. TUL-1 Rayleigh Wave Vs-Depth, Vs30, and H/V model.

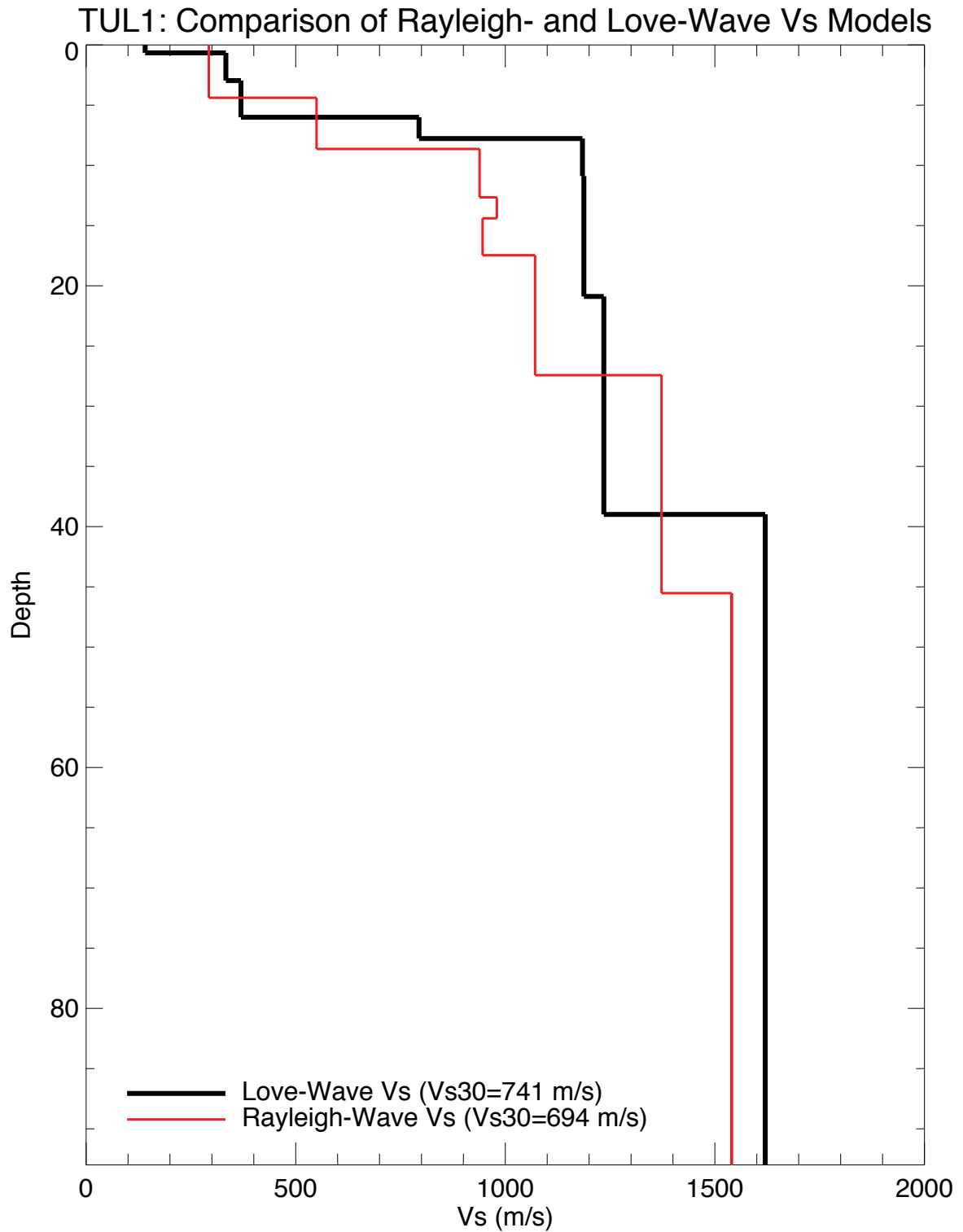


Figure 2.6i. TUL-1 Rayleigh and Love Wave Vs-depth model comparison.

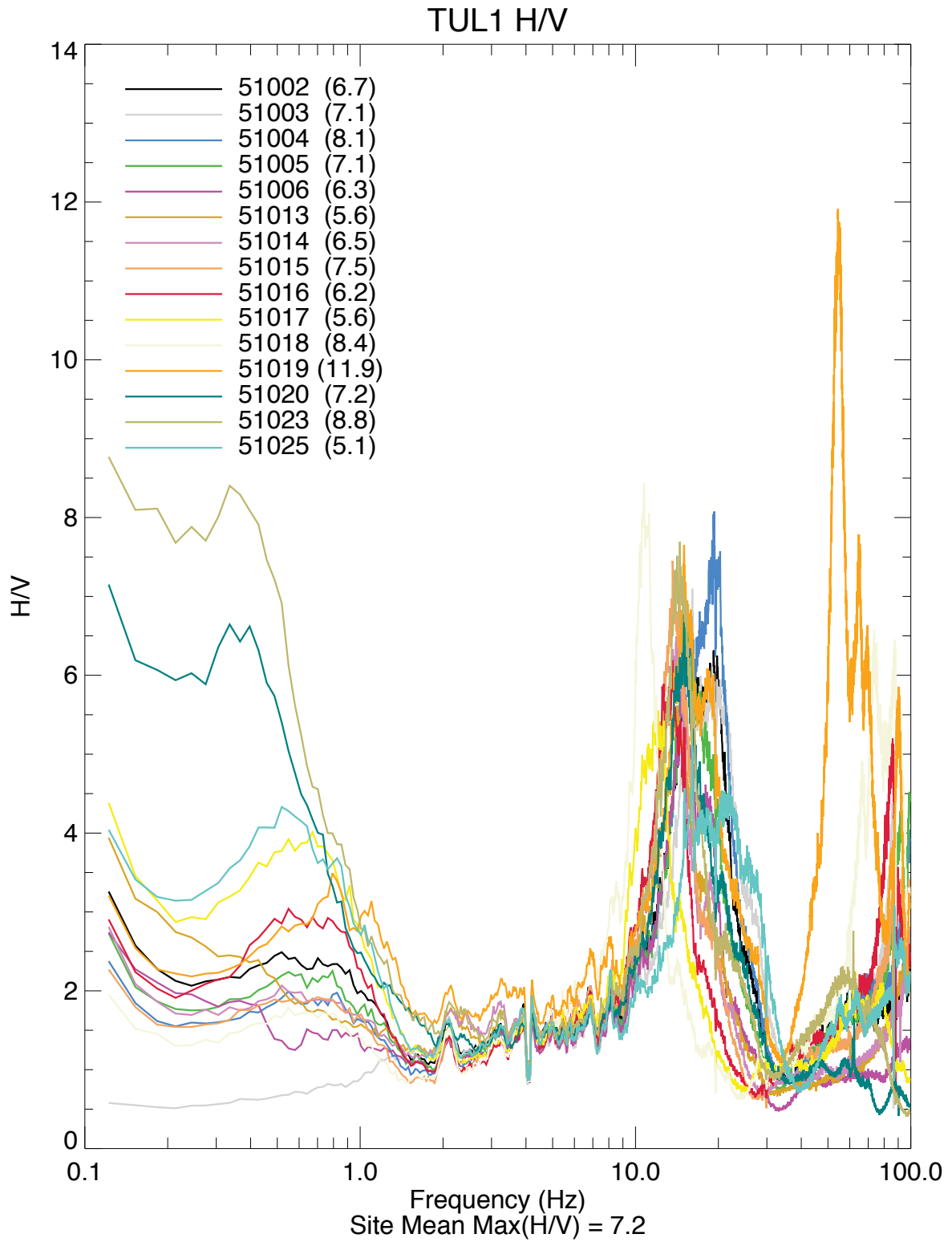


Figure 2.6j. TUL-1 all stations H/V.

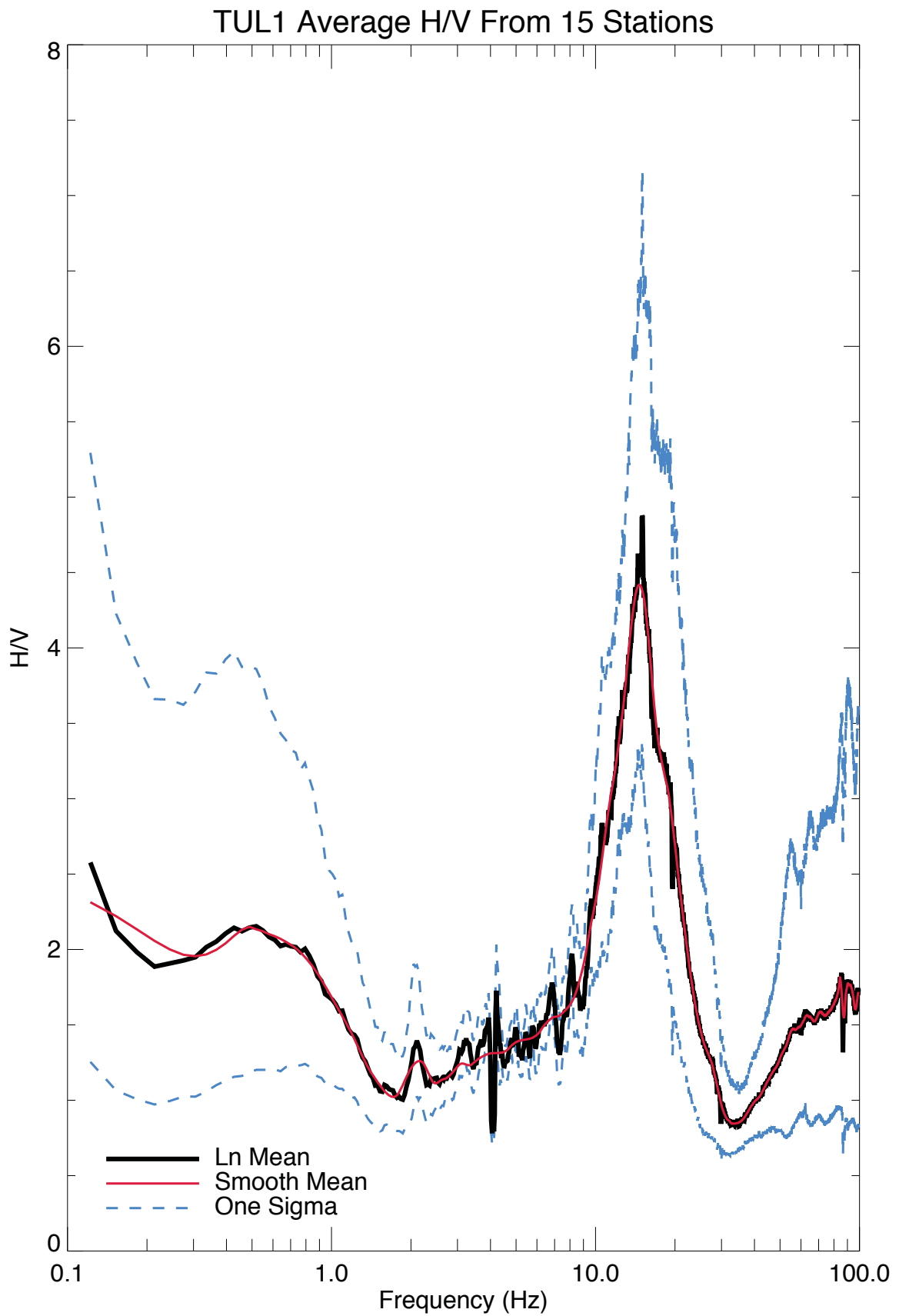


Figure 2.6k. TUL-1 site average H/V.

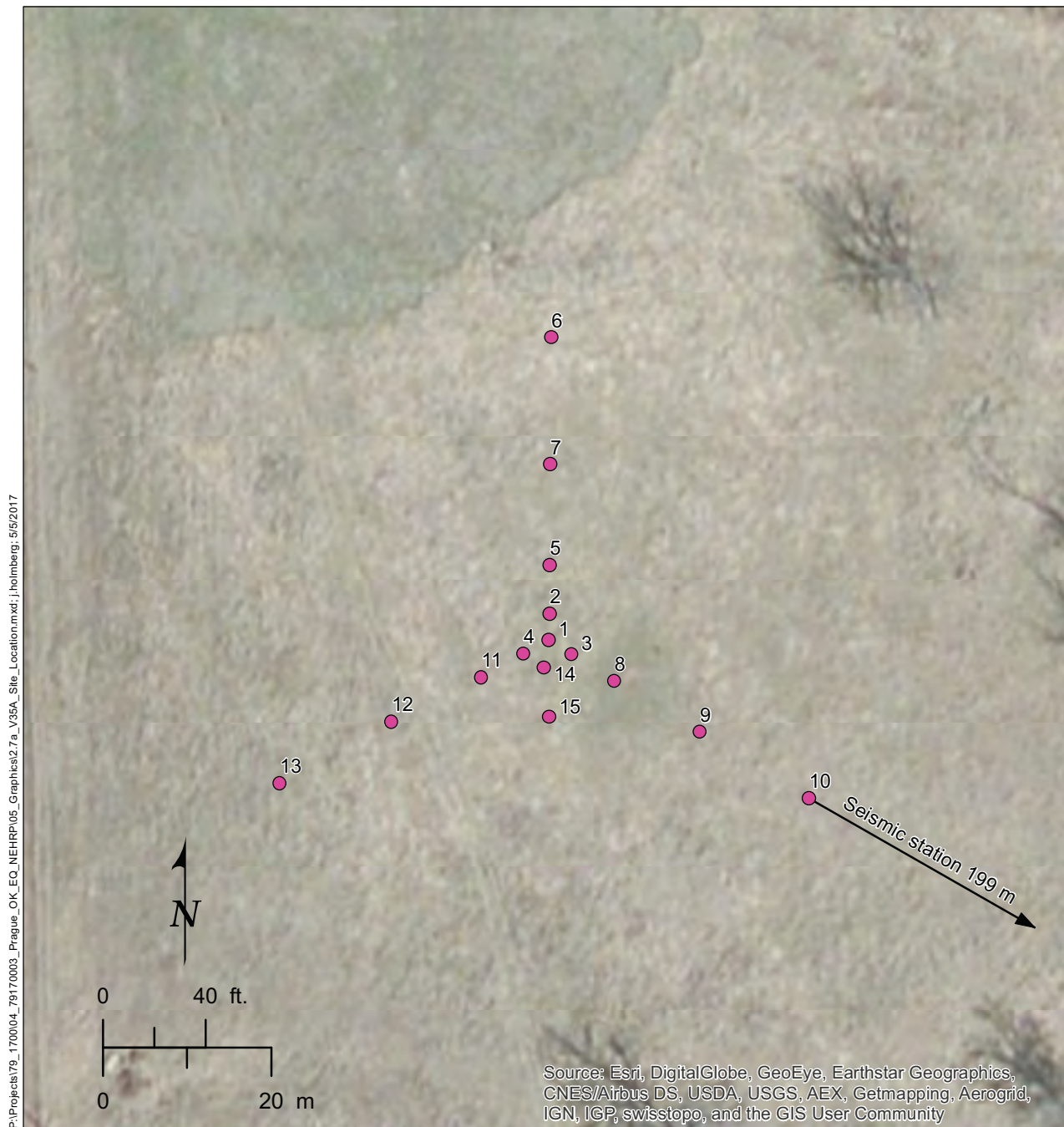


Figure 2.7a. V35A site location.

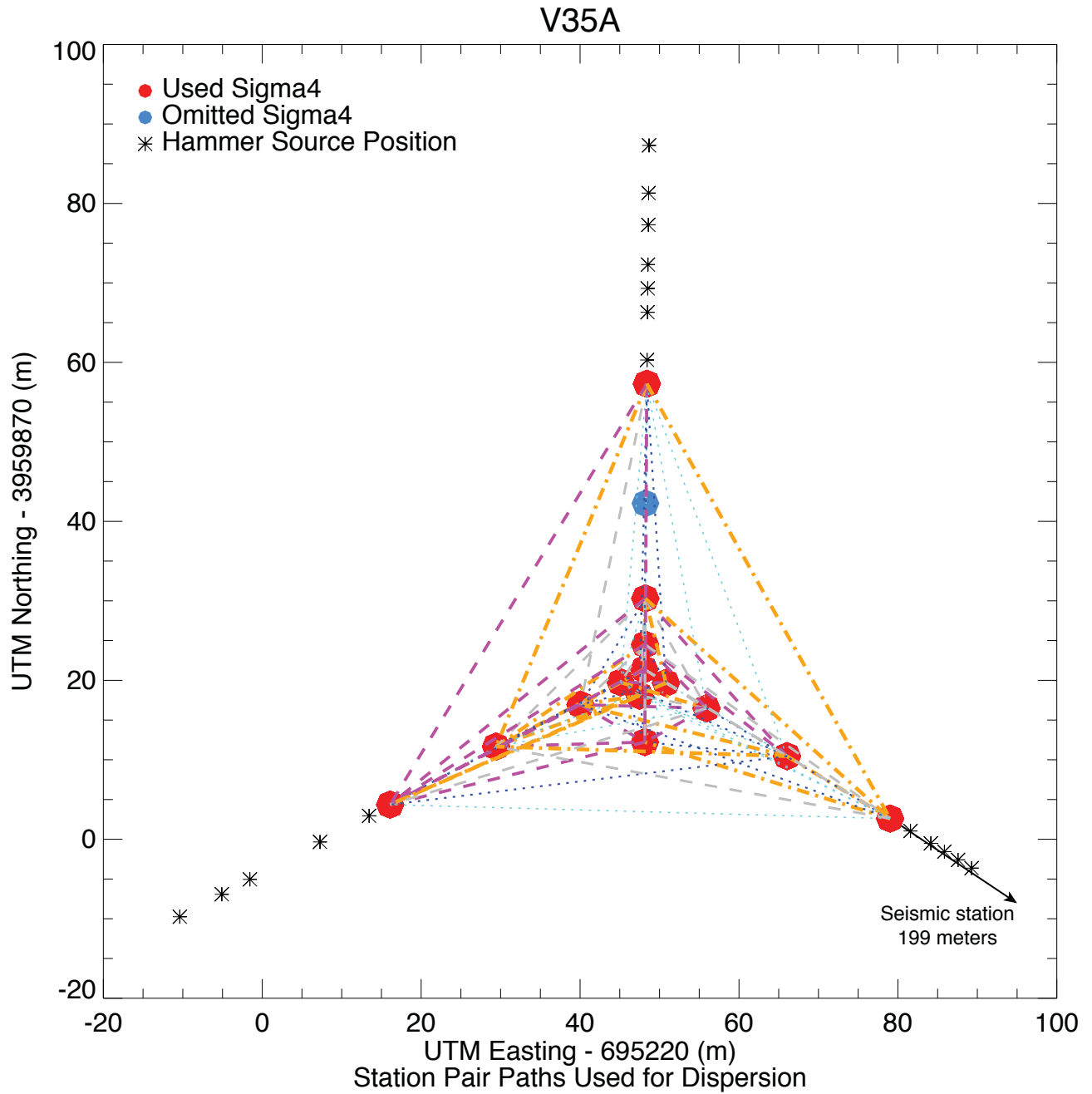


Figure 2.7b. V35A station dispersion pathways and source positions.

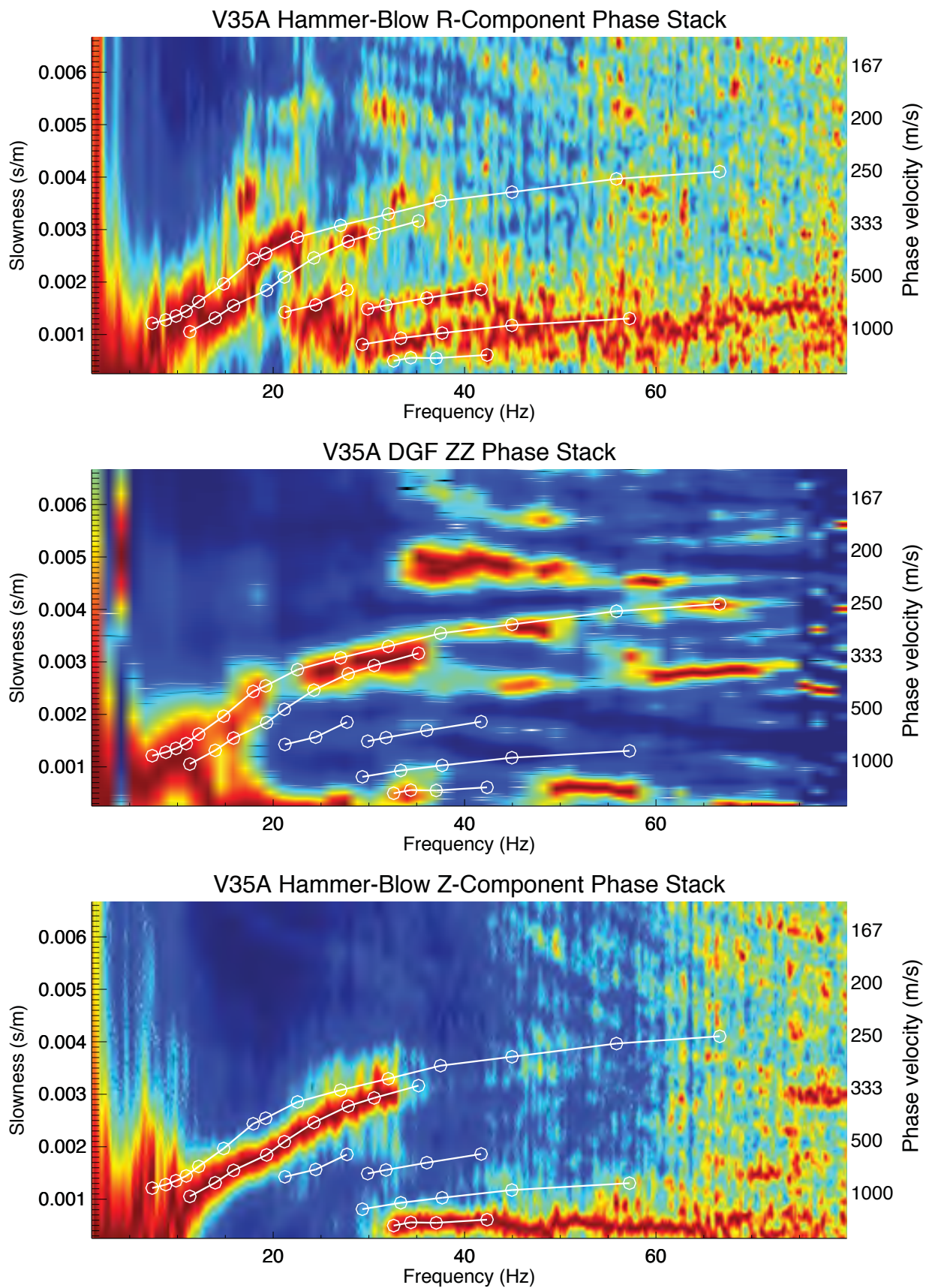


Figure 2.7c. V35A multimodal p-f dispersion images and picks.

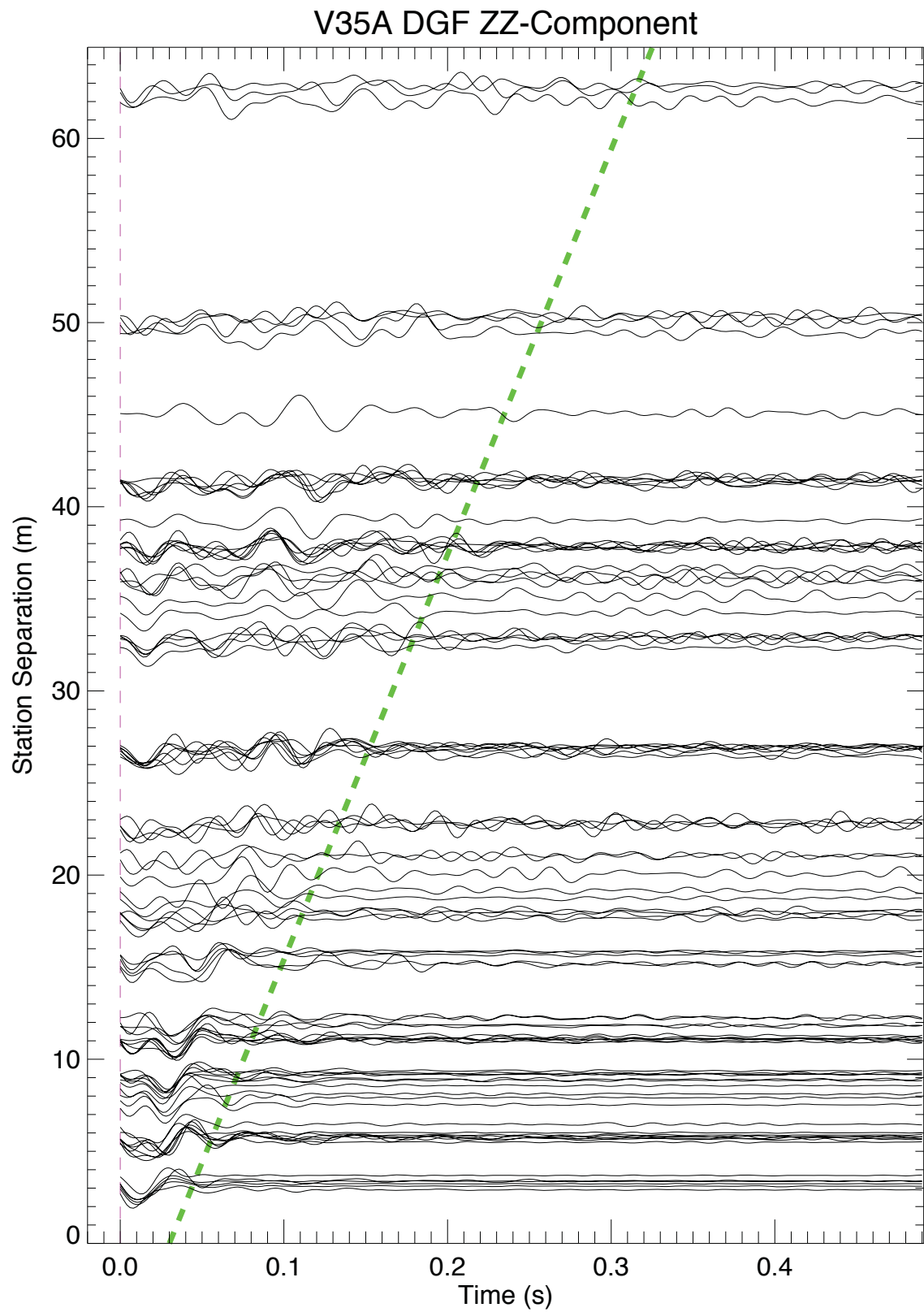


Figure 2.7d. V35A vertical component dispersion Green's Function.

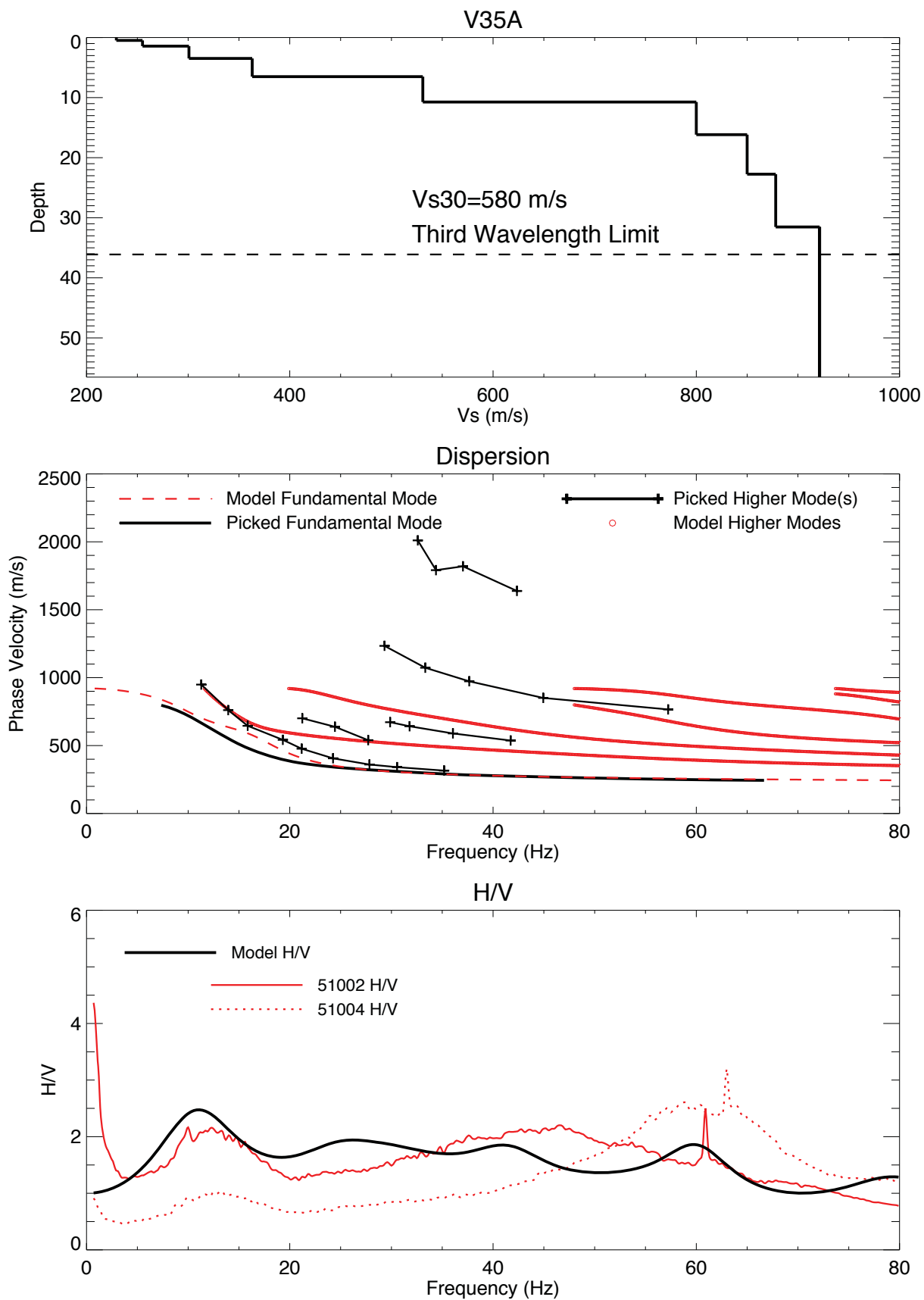


Figure 2.7e. V35A Vs-Depth, Vs30, and Nearfield H/V Model.

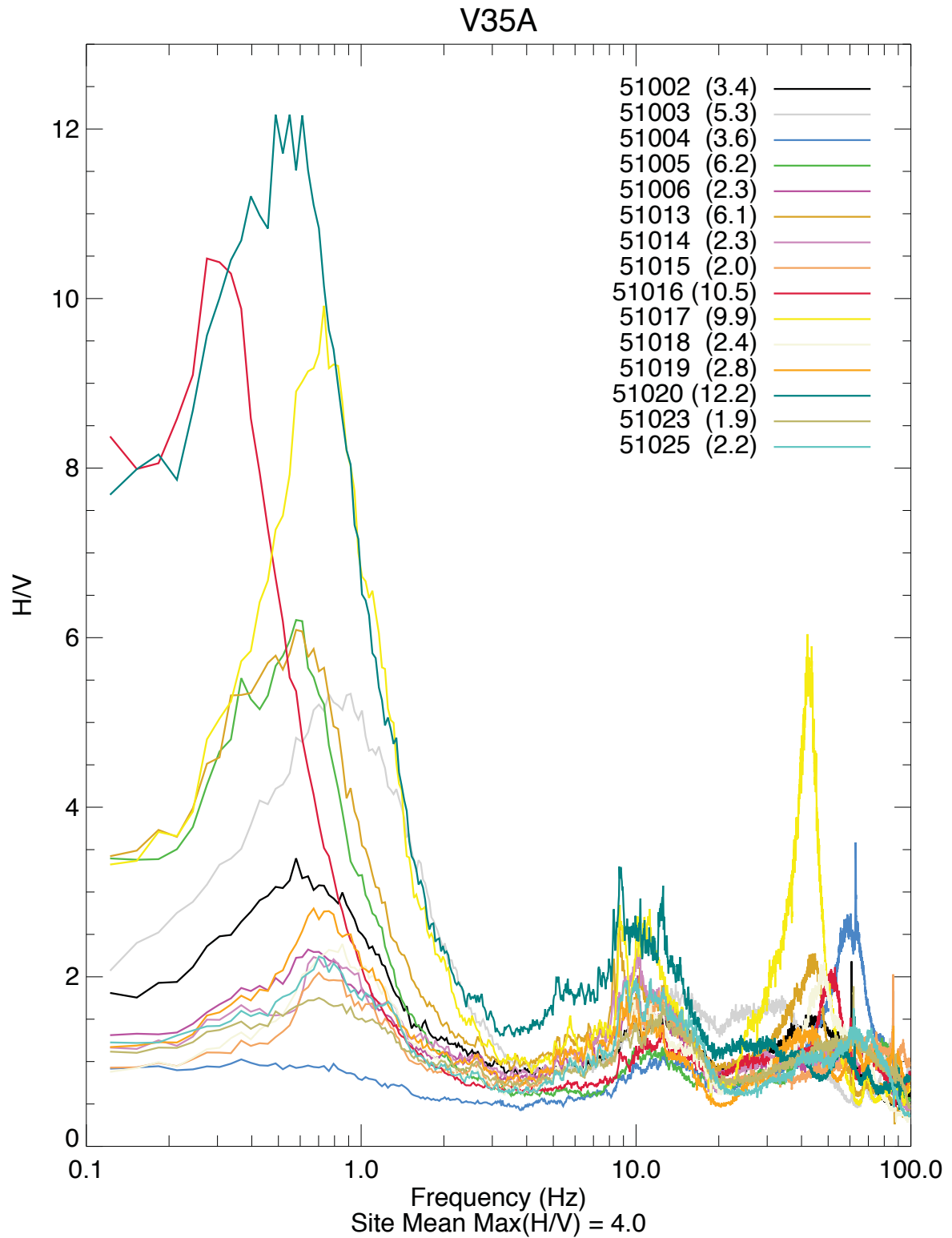


Figure 2.7f. V35A all stations H/V.

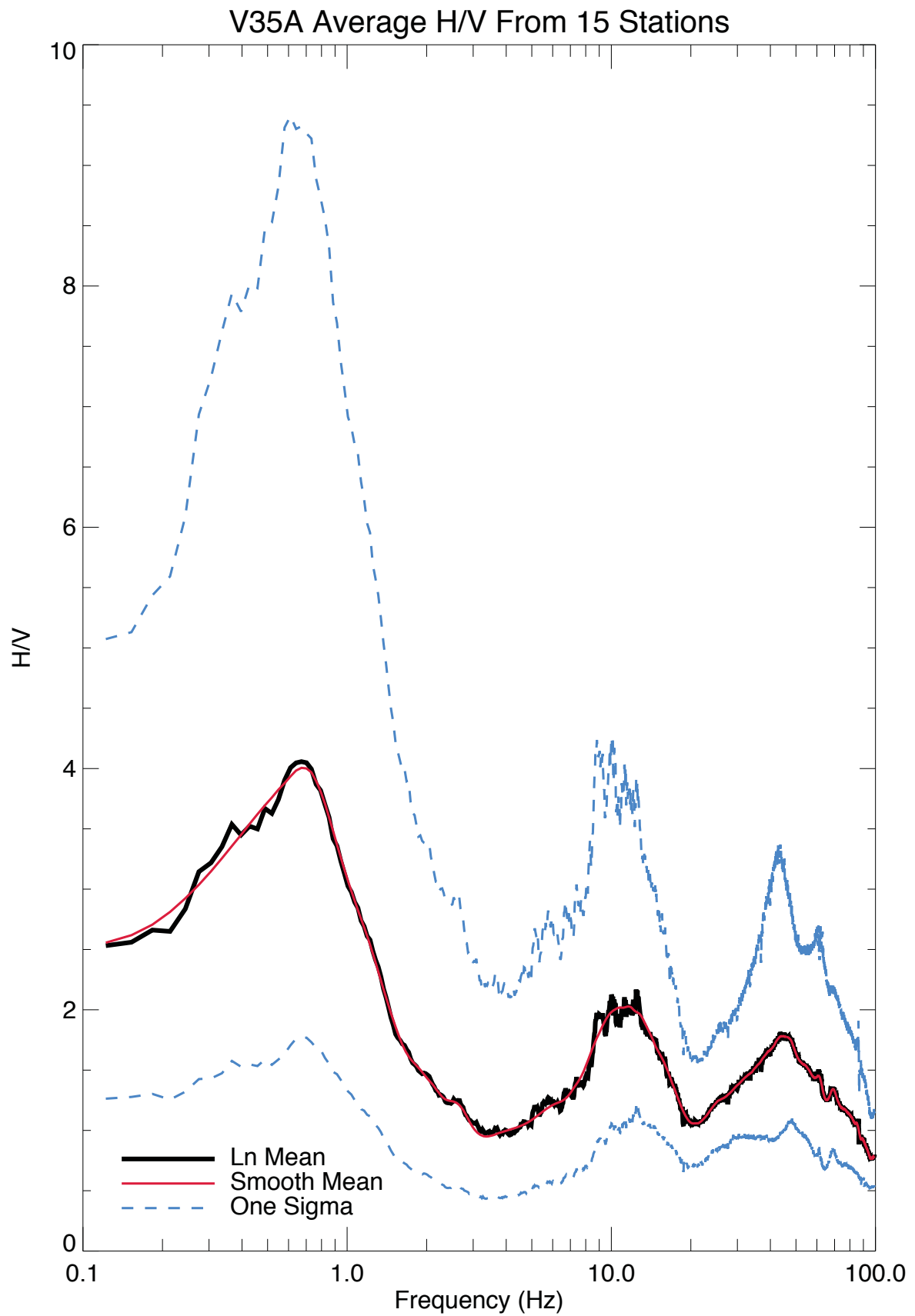
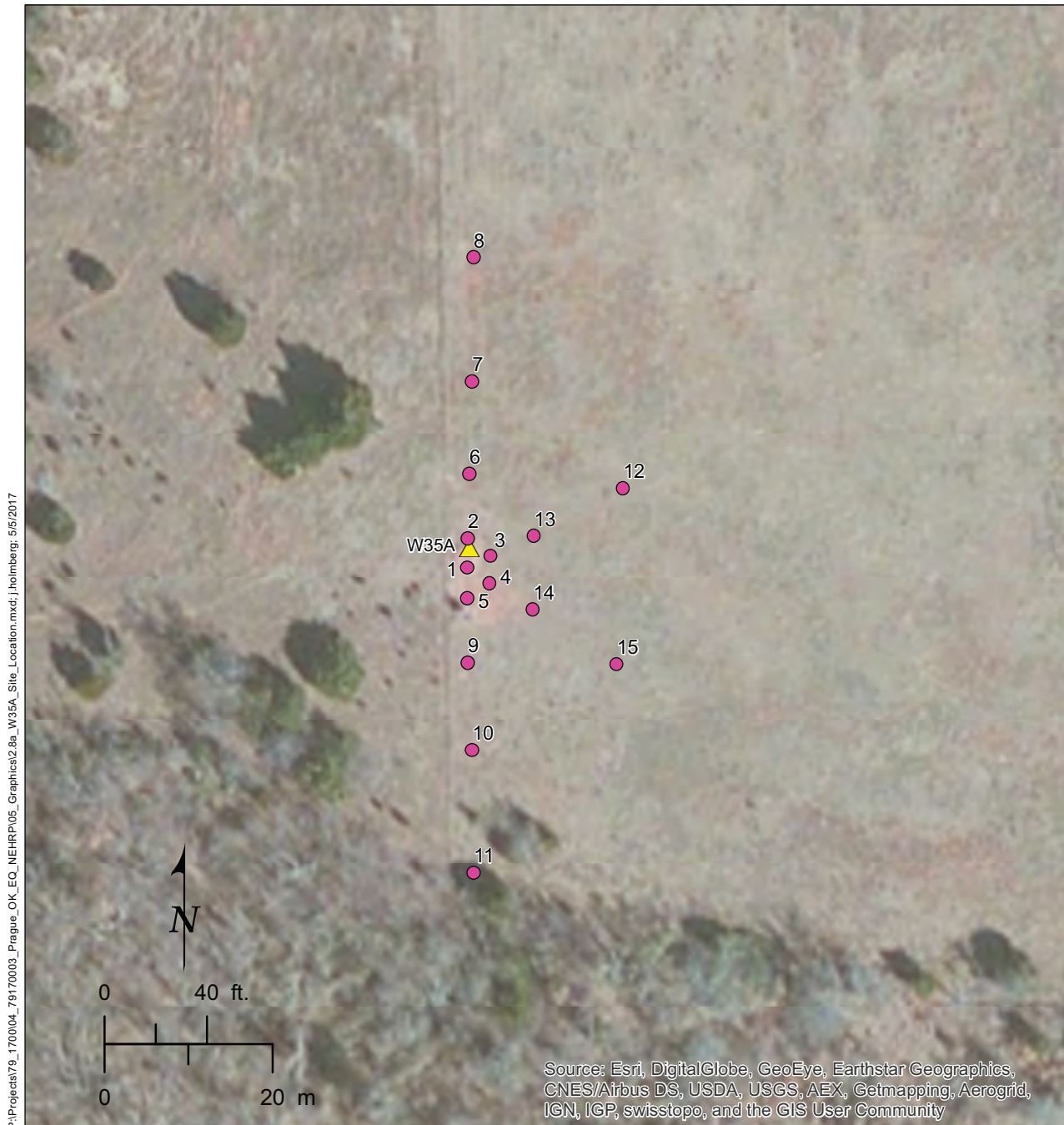


Figure 2.7g. V35A site average H/V.



Explanation

- Receiver location
- ▲ Seismic station

Figure 2.8a. W35A site location.

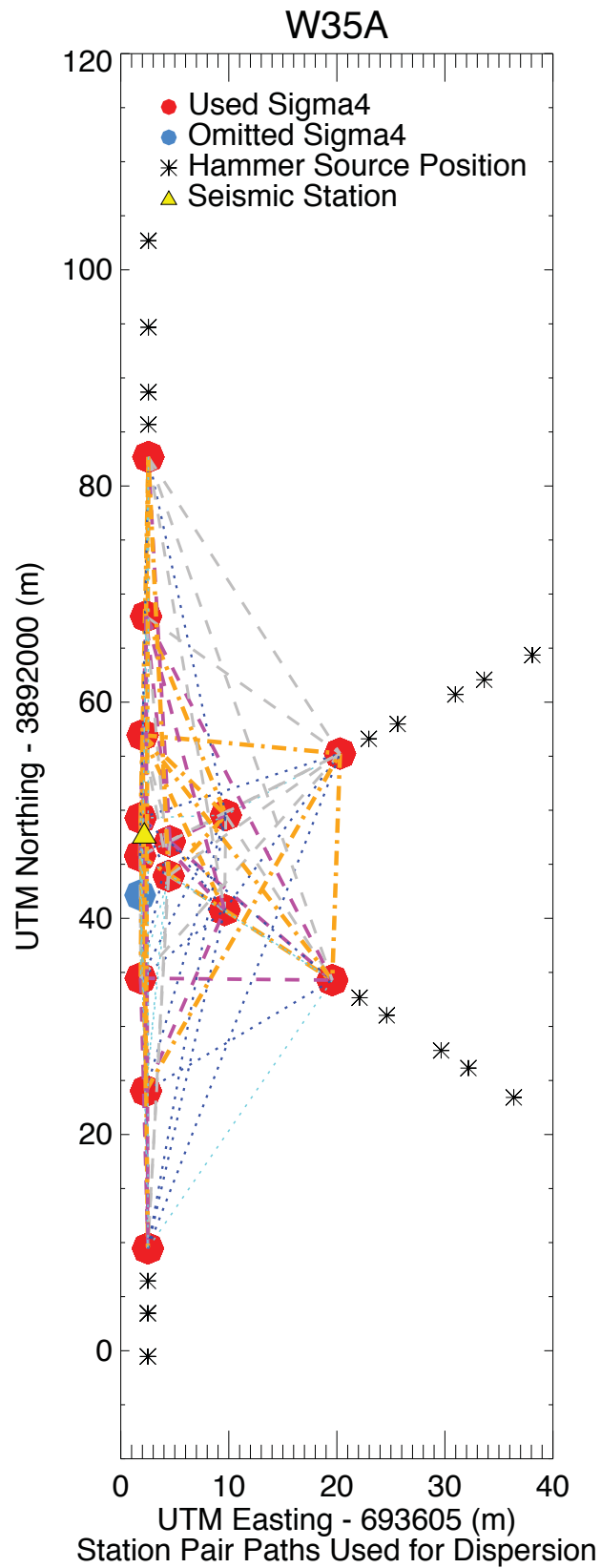


Figure 2.8b. W35A station dispersion pathways and source positions.

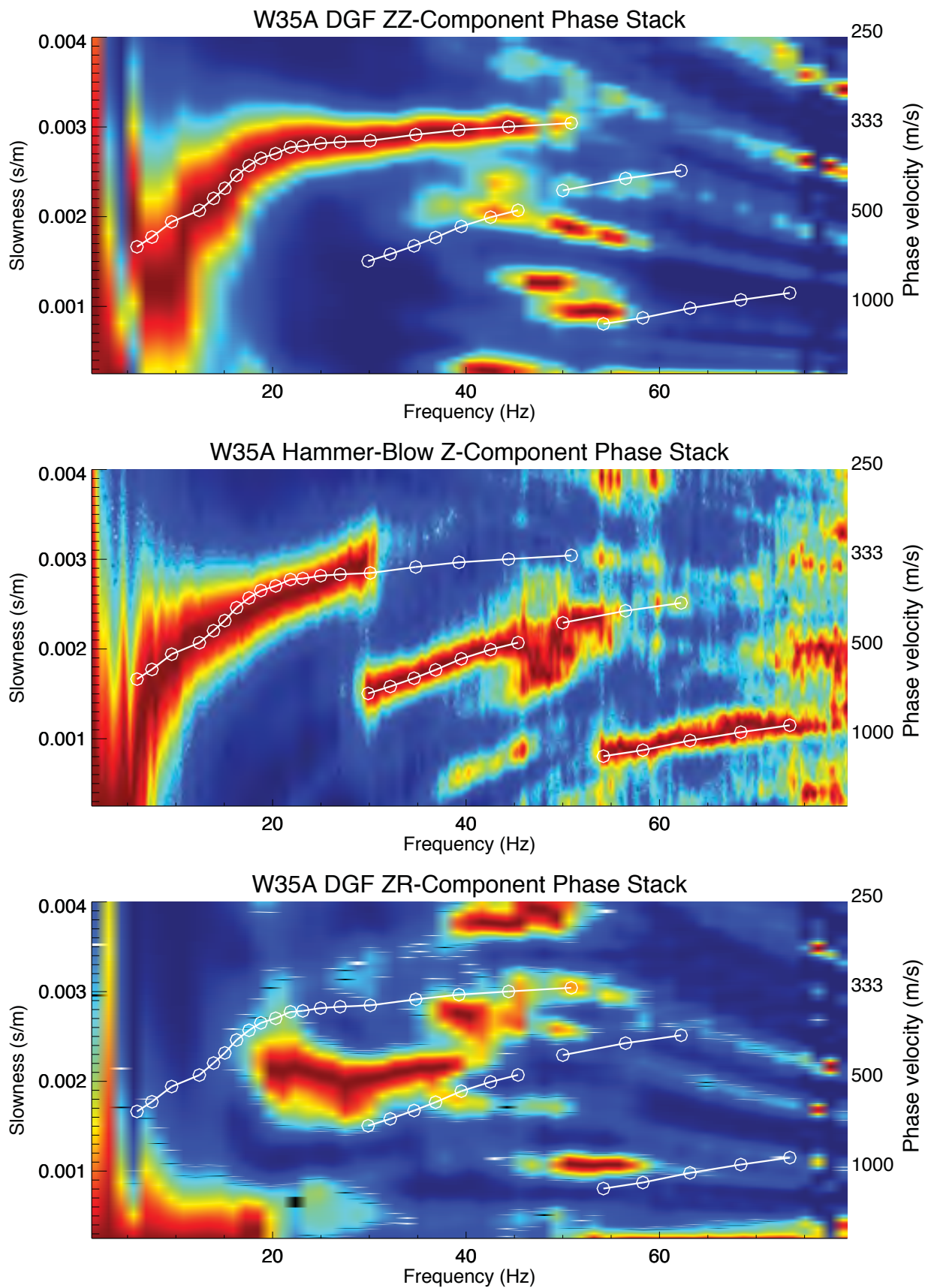


Figure 2.8c. W35A multi-component multimodal p-f dispersion images and picks.

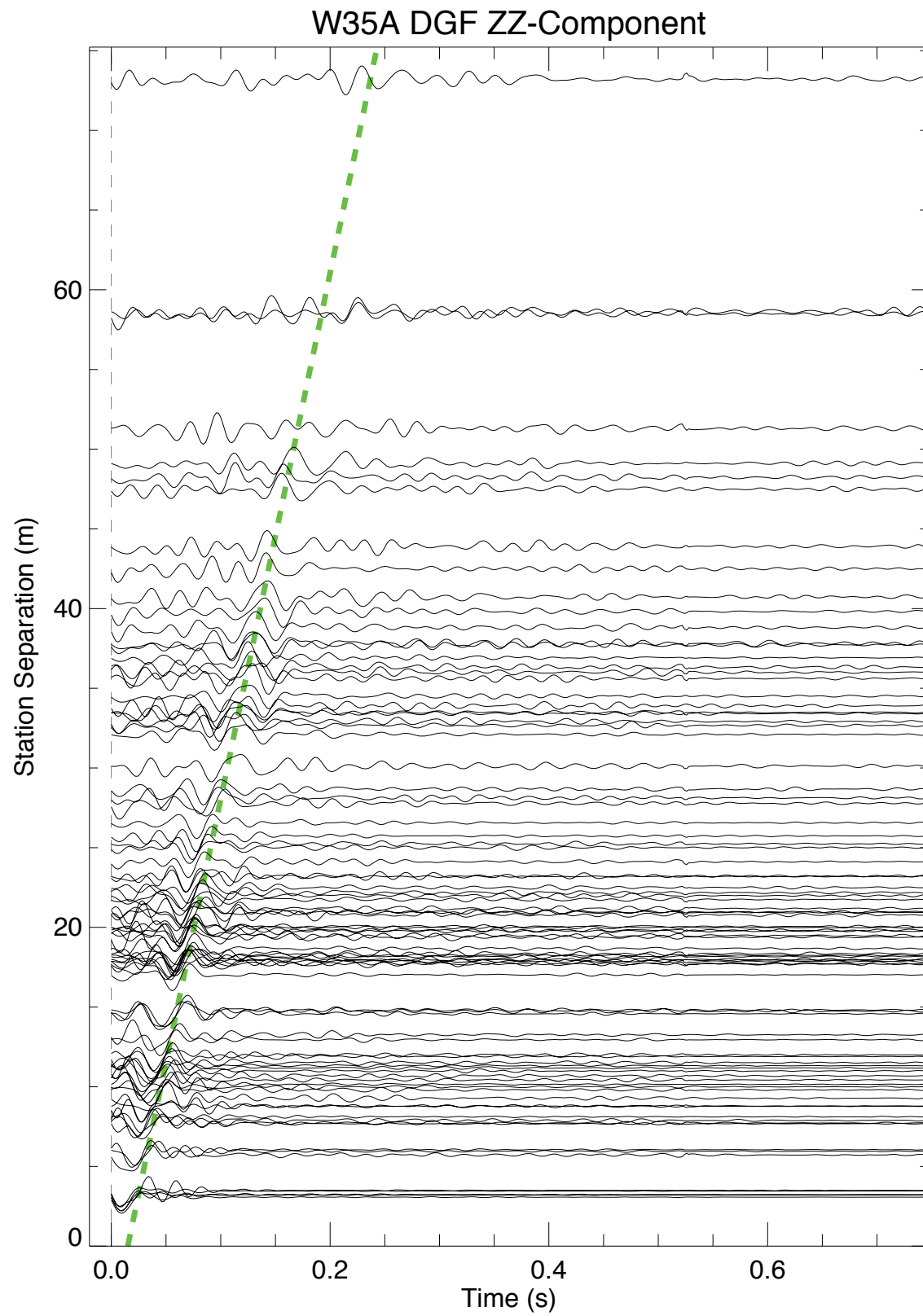


Figure 2.8d. W35A vertical component dispersion Green's Function.

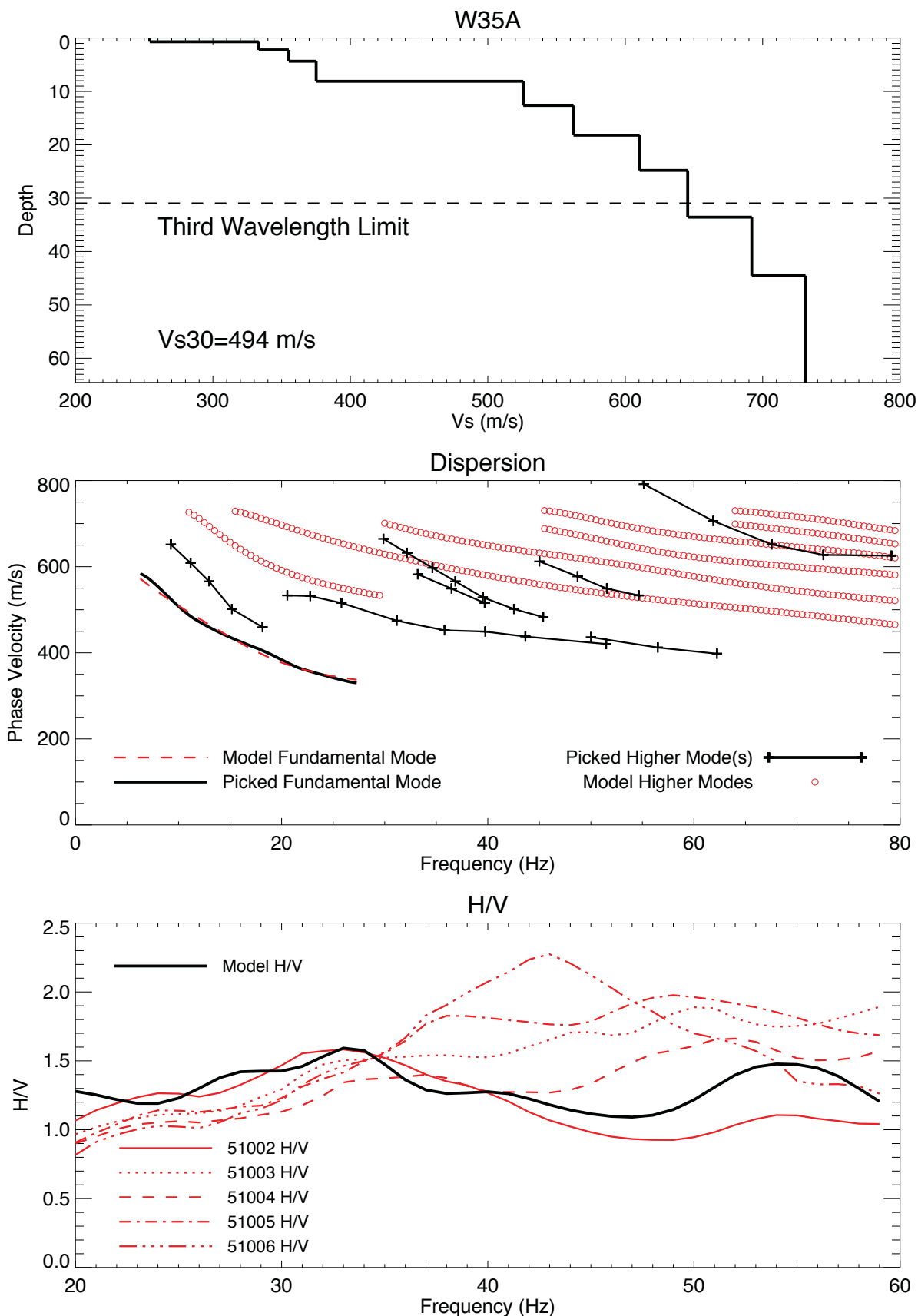


Figure 2.8e. W35A Vs-depth, Vs30, and Nearfield H/V Model.

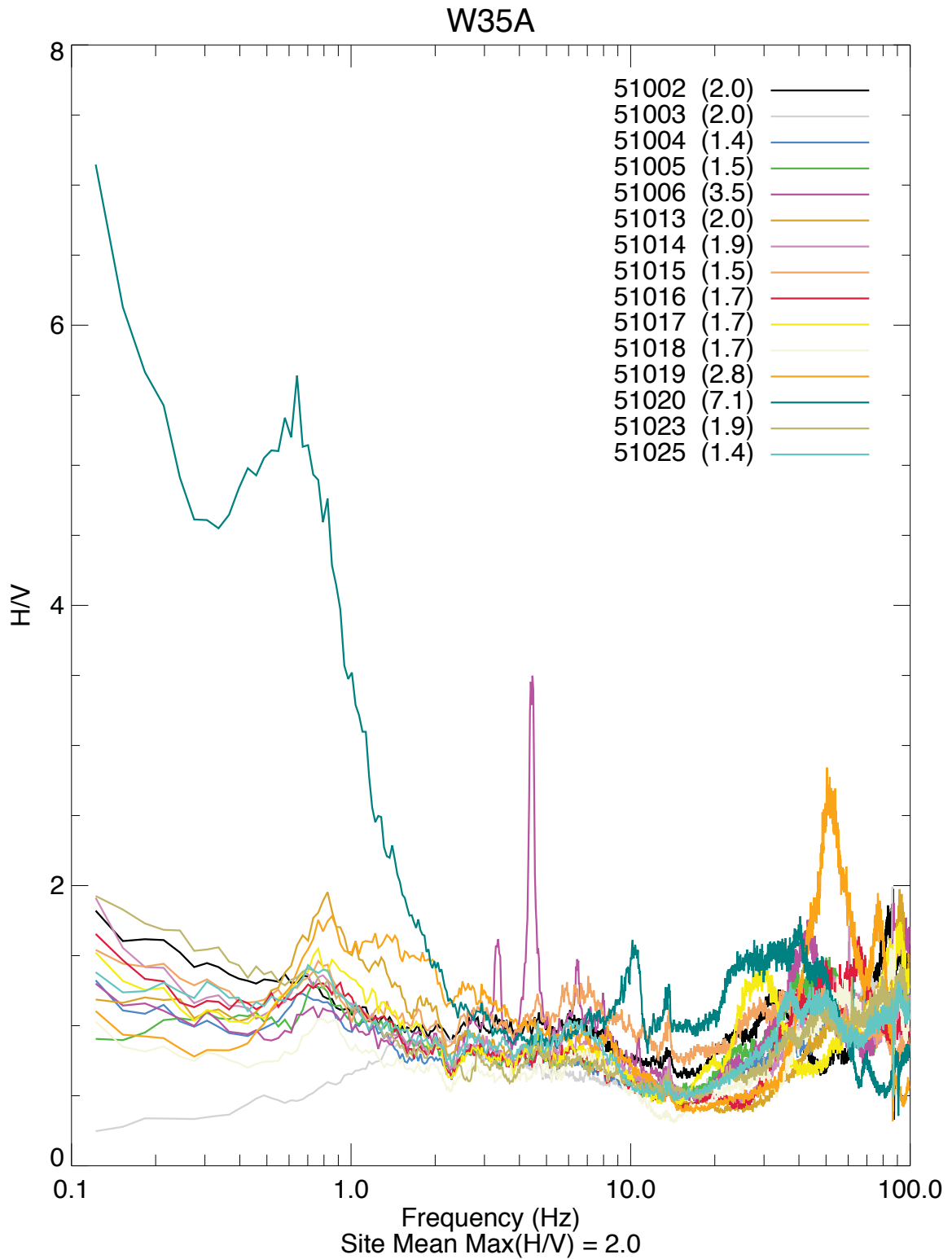


Figure 2.8f. W35A all stations H/V.

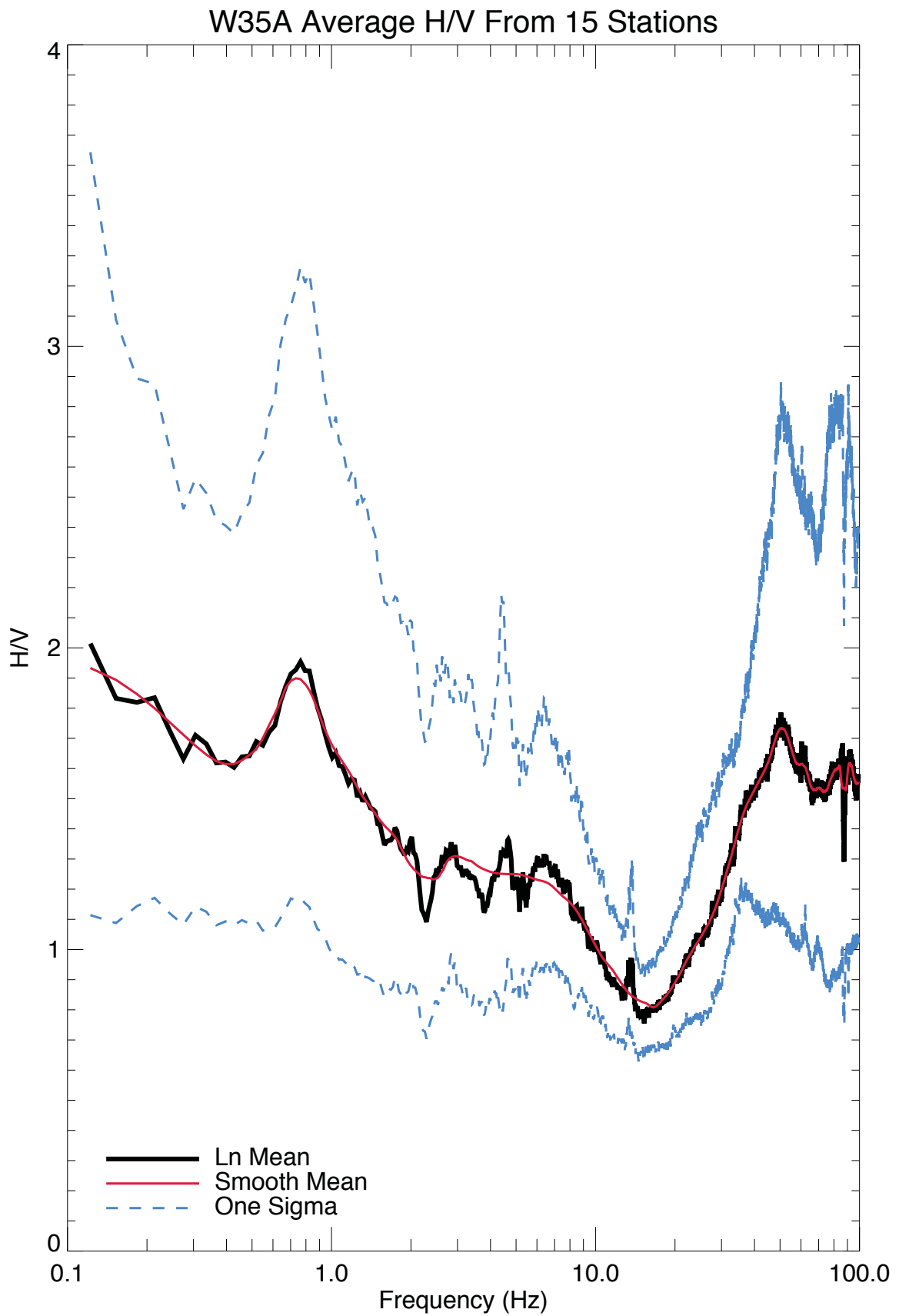
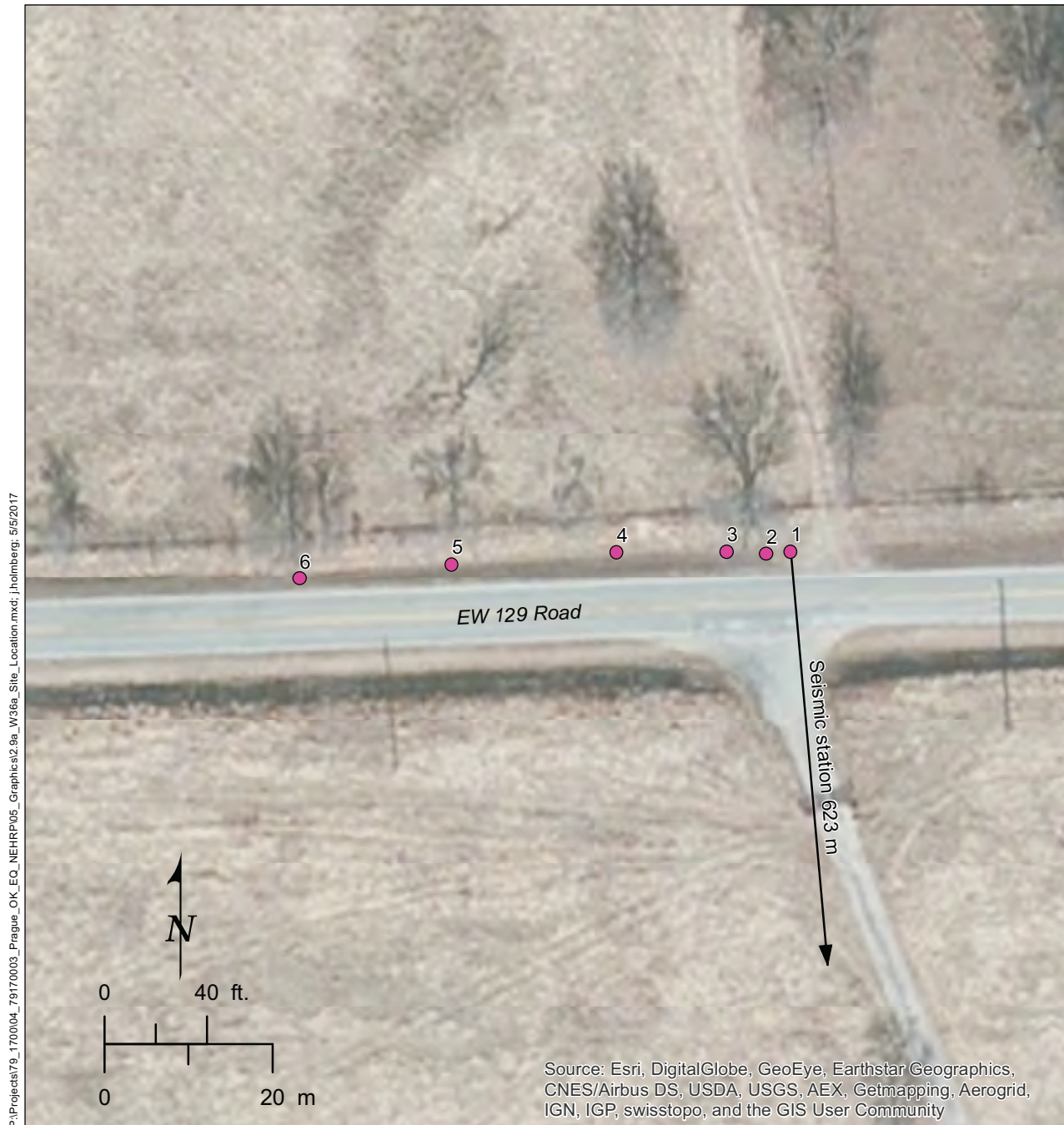


Figure 2.8g. W35A site average H/V.



- Explanation**
- Receiver location

Figure 2.9a. W36A site location.

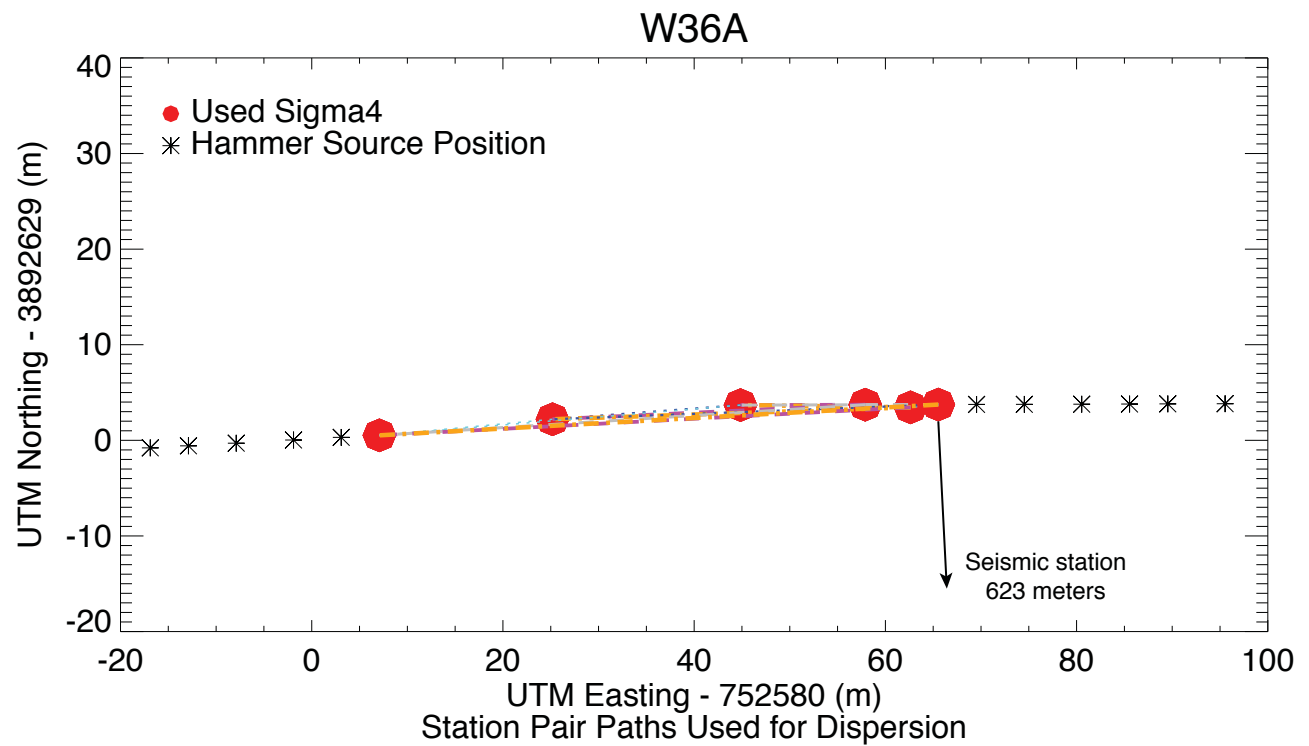


Figure 2.9b. W36A station dispersion pathways and source positions.

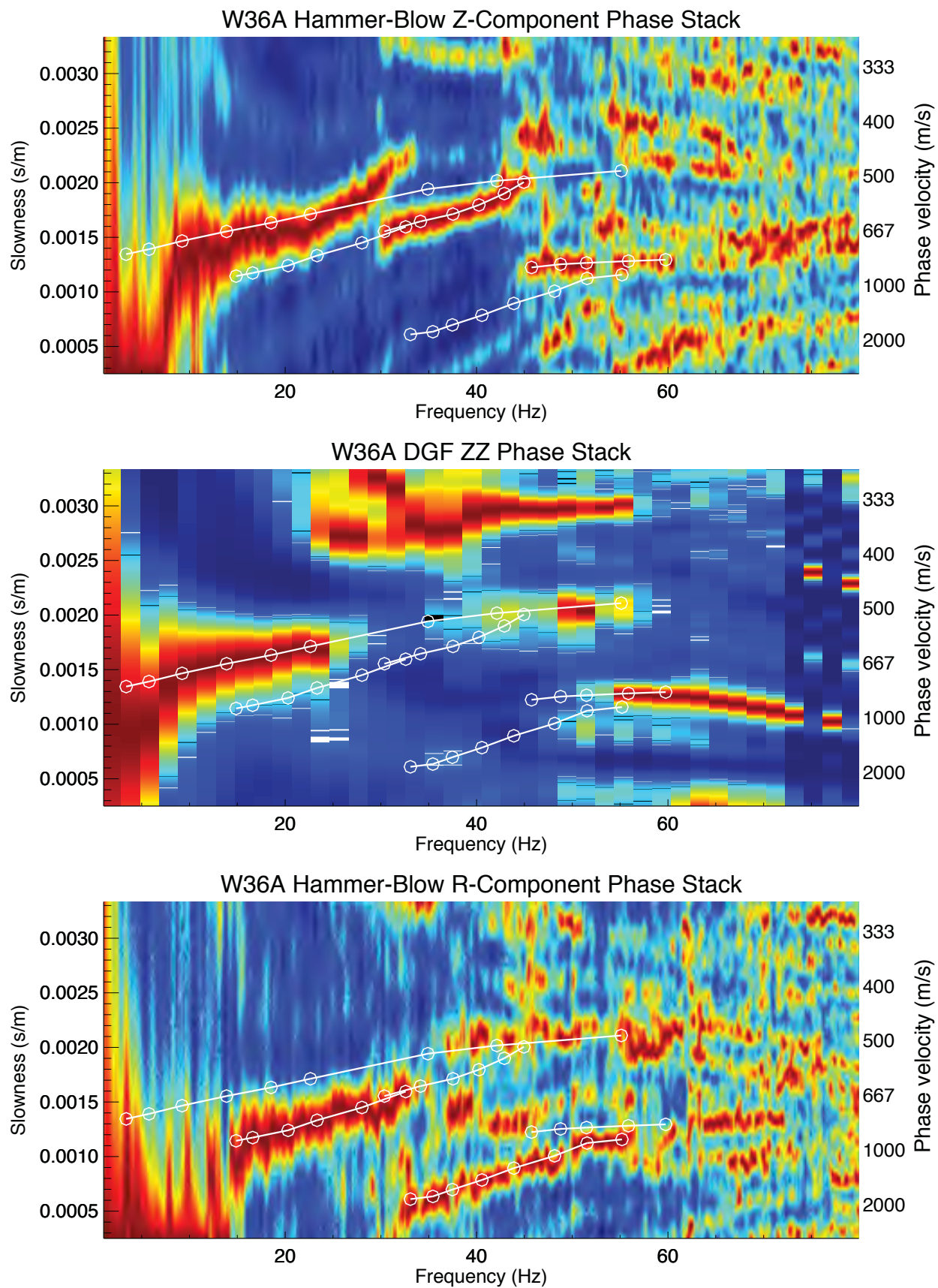


Figure 2.9c. W36A multi-component multimodal p-f dispersion images and picks.

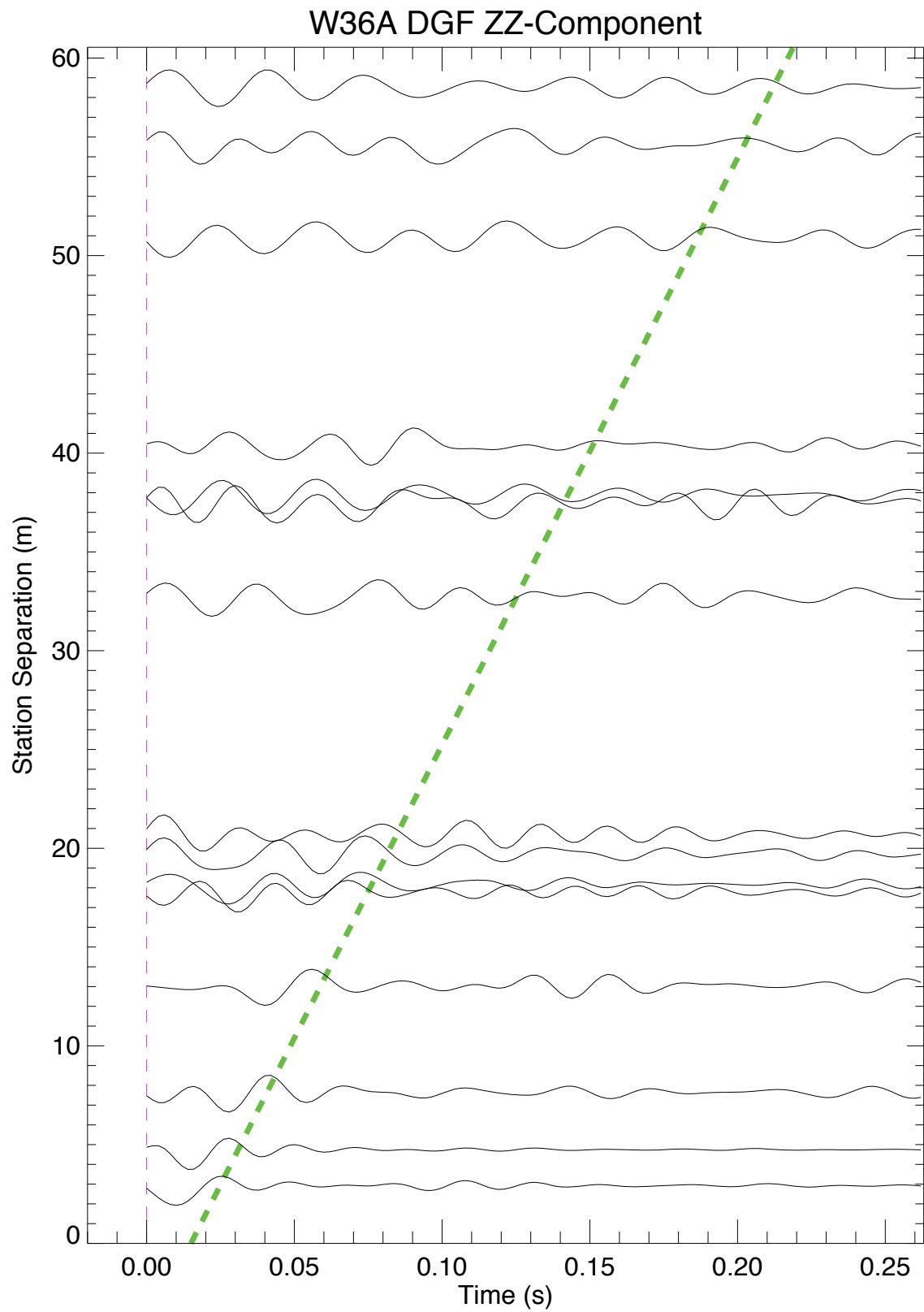


Figure 2.9d. W36A vertical component dispersion Green's Function.

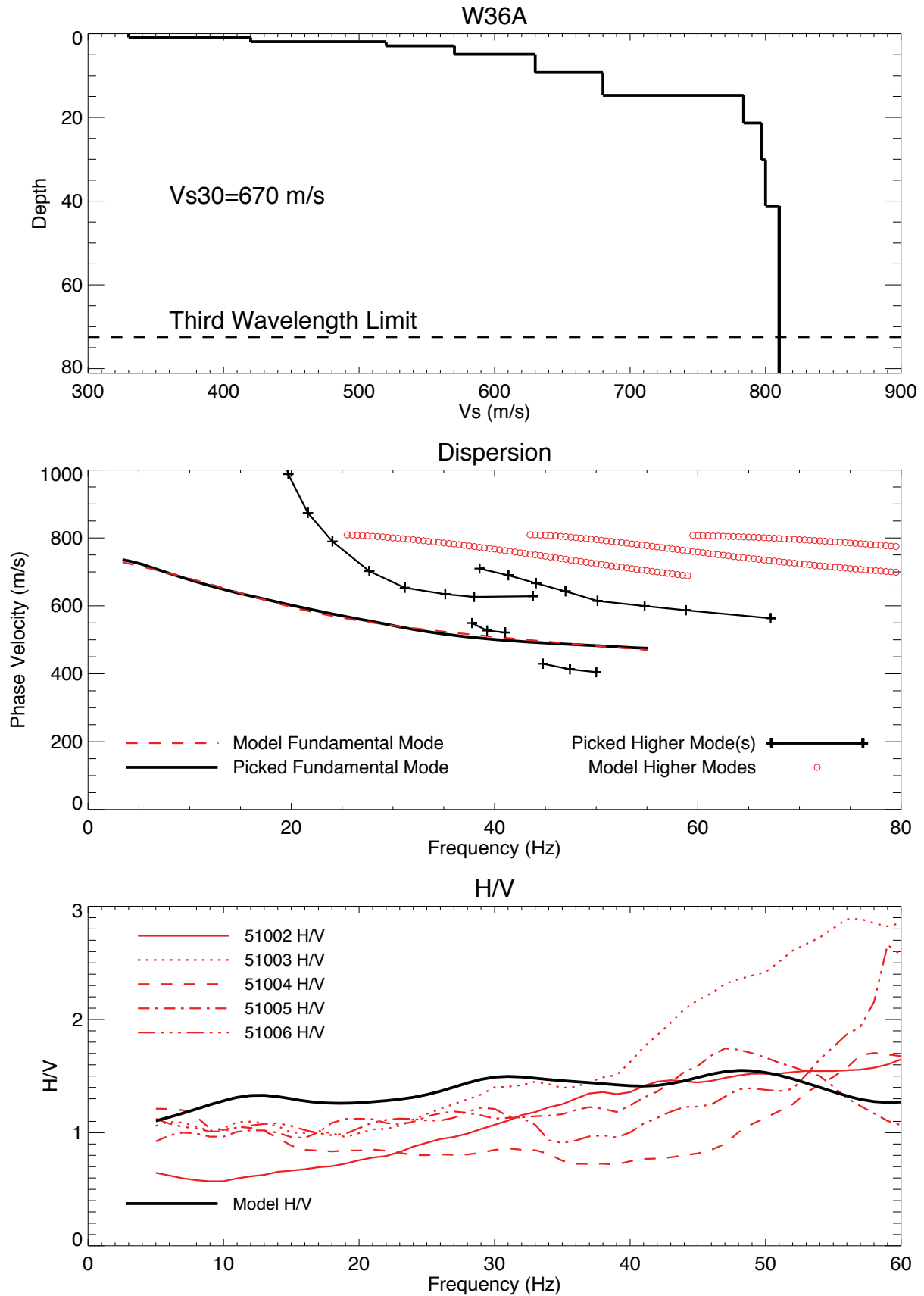


Figure 2.9e. W36A Vs-depth, Vs30, and Nearfield H/V Model.

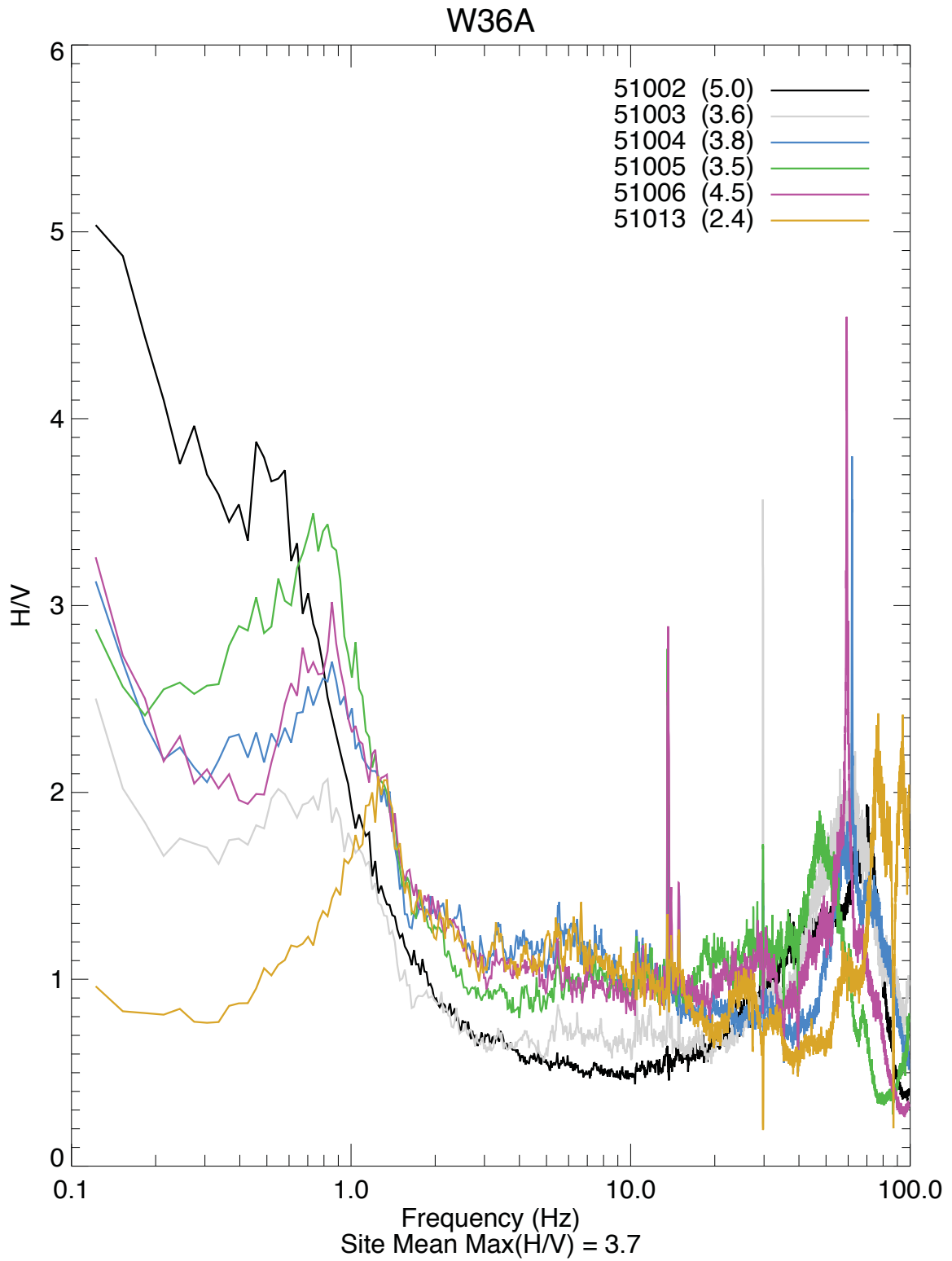


Figure 2.9f. W36A all stations H/V.

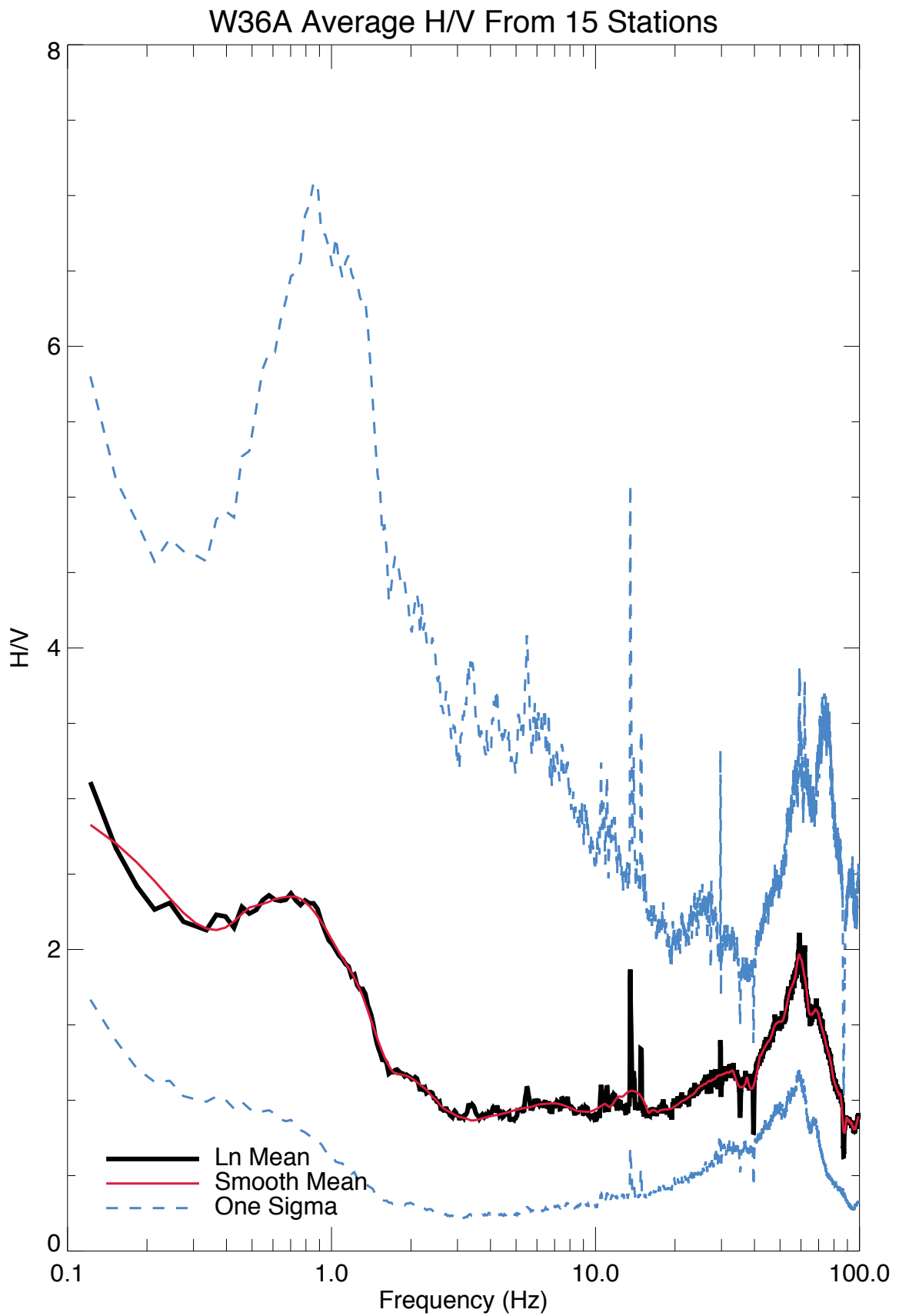


Figure 2.9g. W36A site average H/V.



Explanation

- Receiver location
- ▲ Seismic station

Figure 2.10a. WMOK site location.

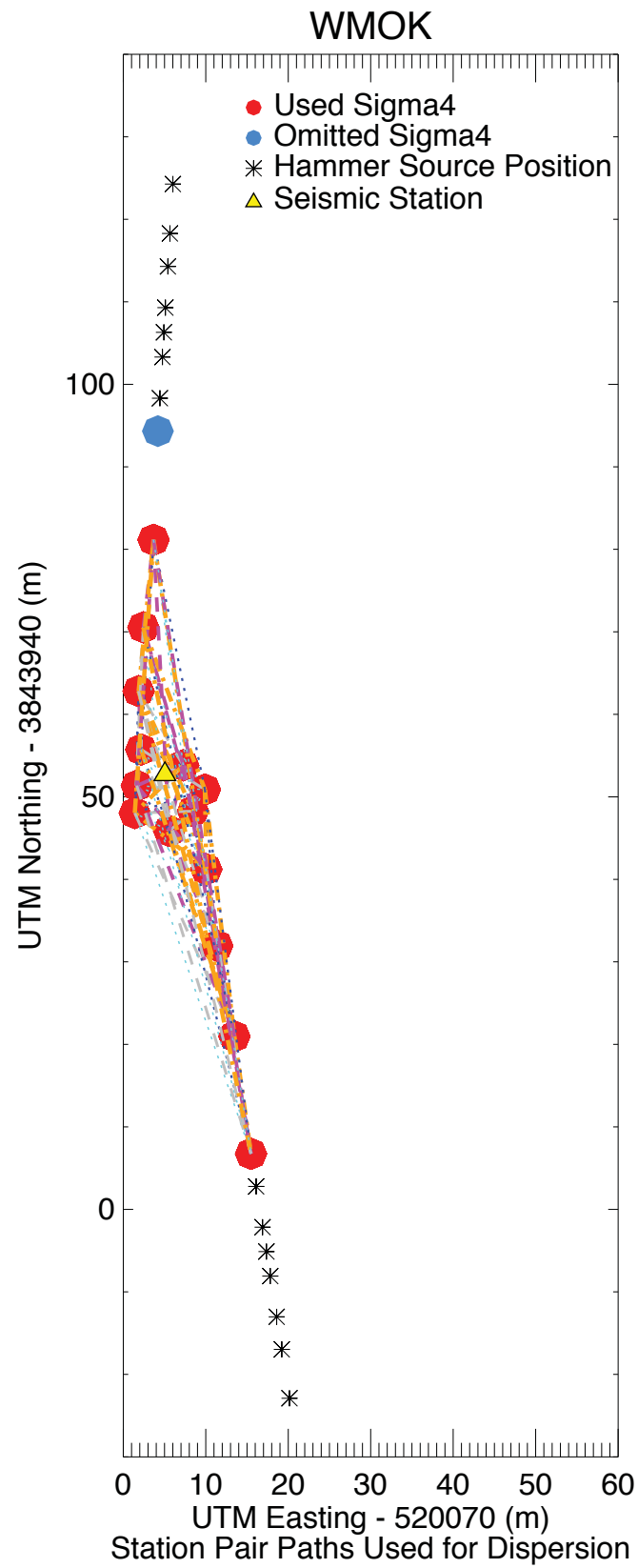


Figure 2.10b. WMOK station dispersion pathways and source positions.

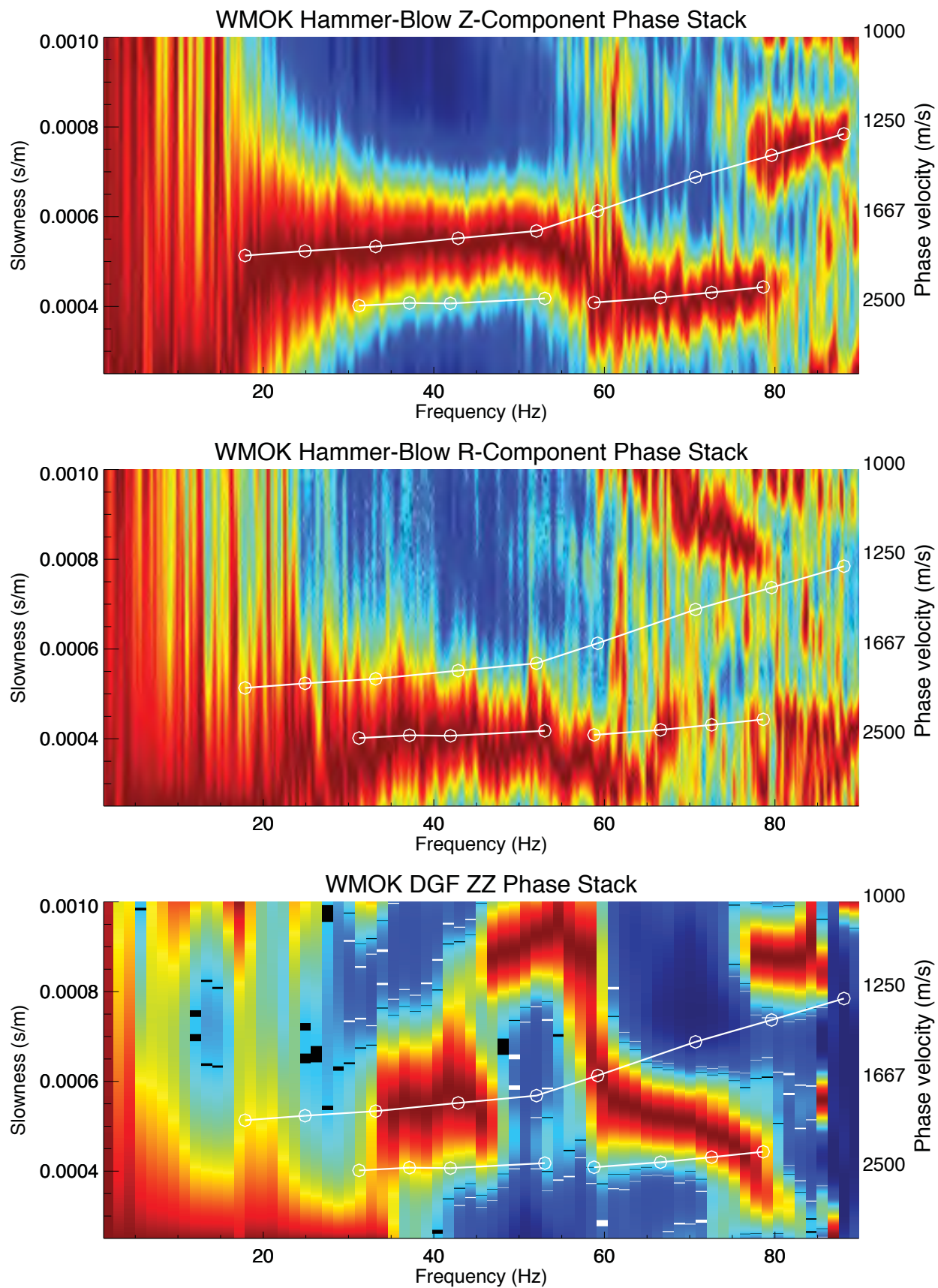


Figure 2.10c. WMOK multi-component multimodal p-f dispersion images and picks.

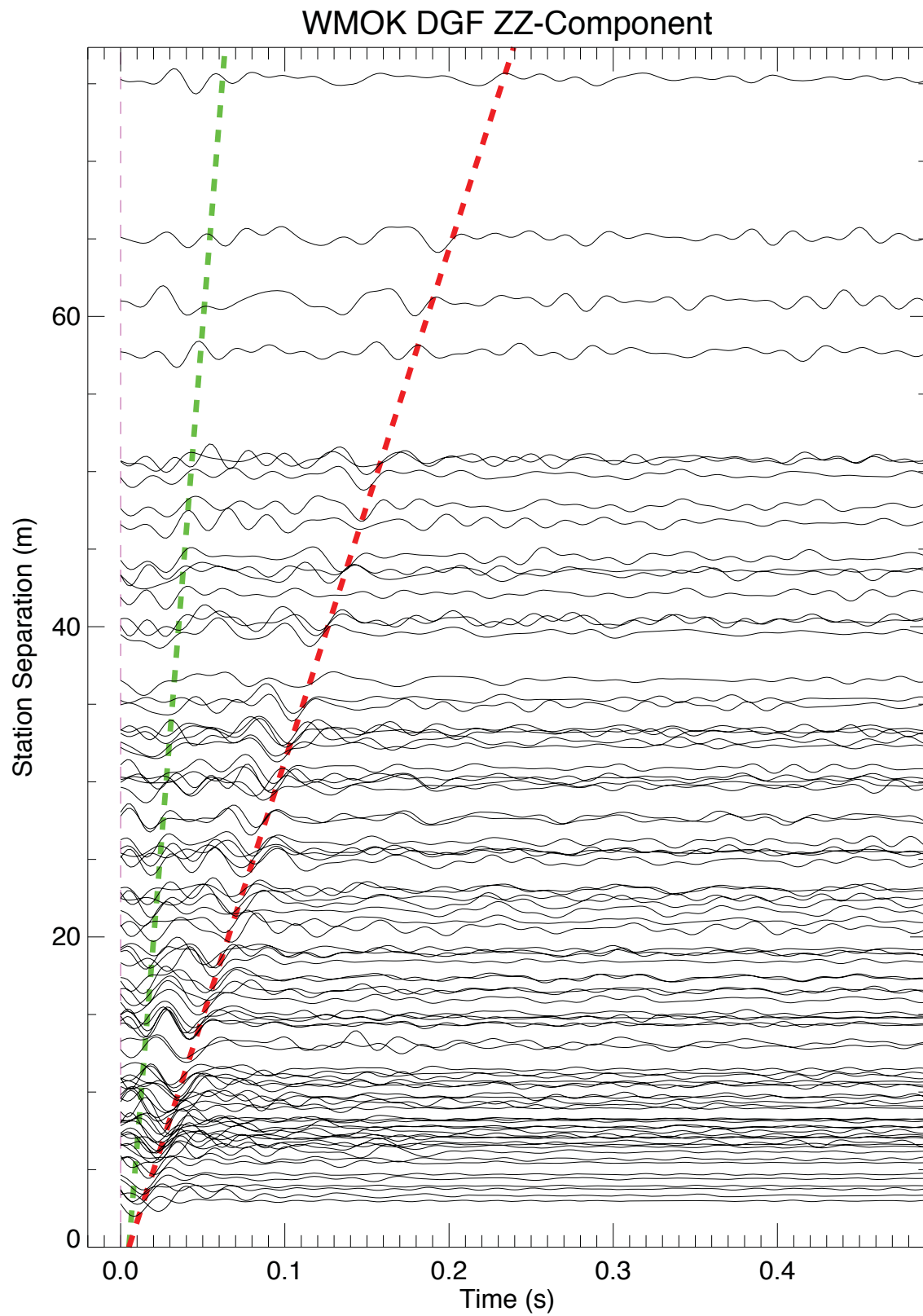


Figure 2.10d. WMOK vertical component dispersion Green's Function.

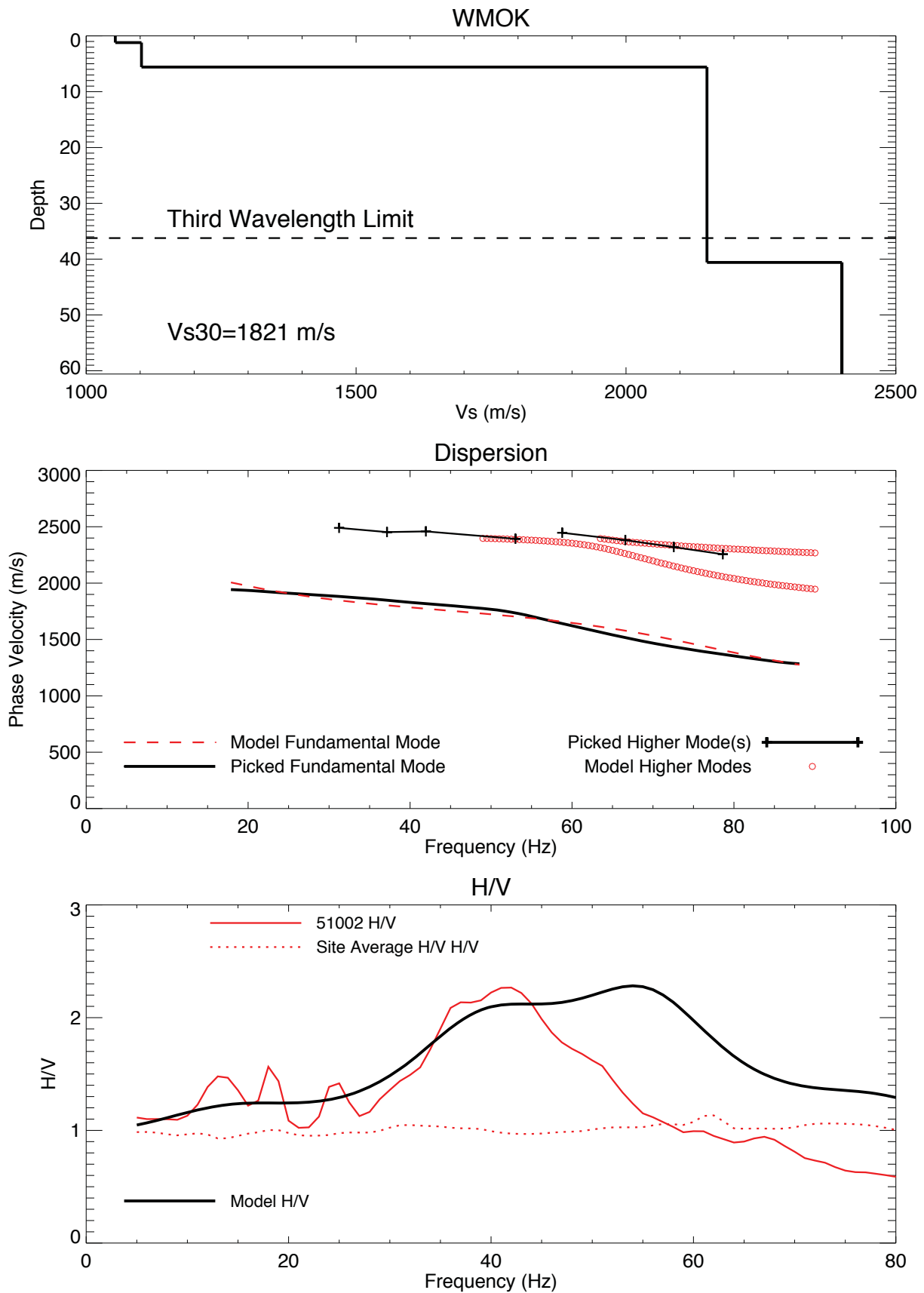


Figure 2.10e. WMOK V_s -depth, V_{s30} , and Nearfield H/V Model.

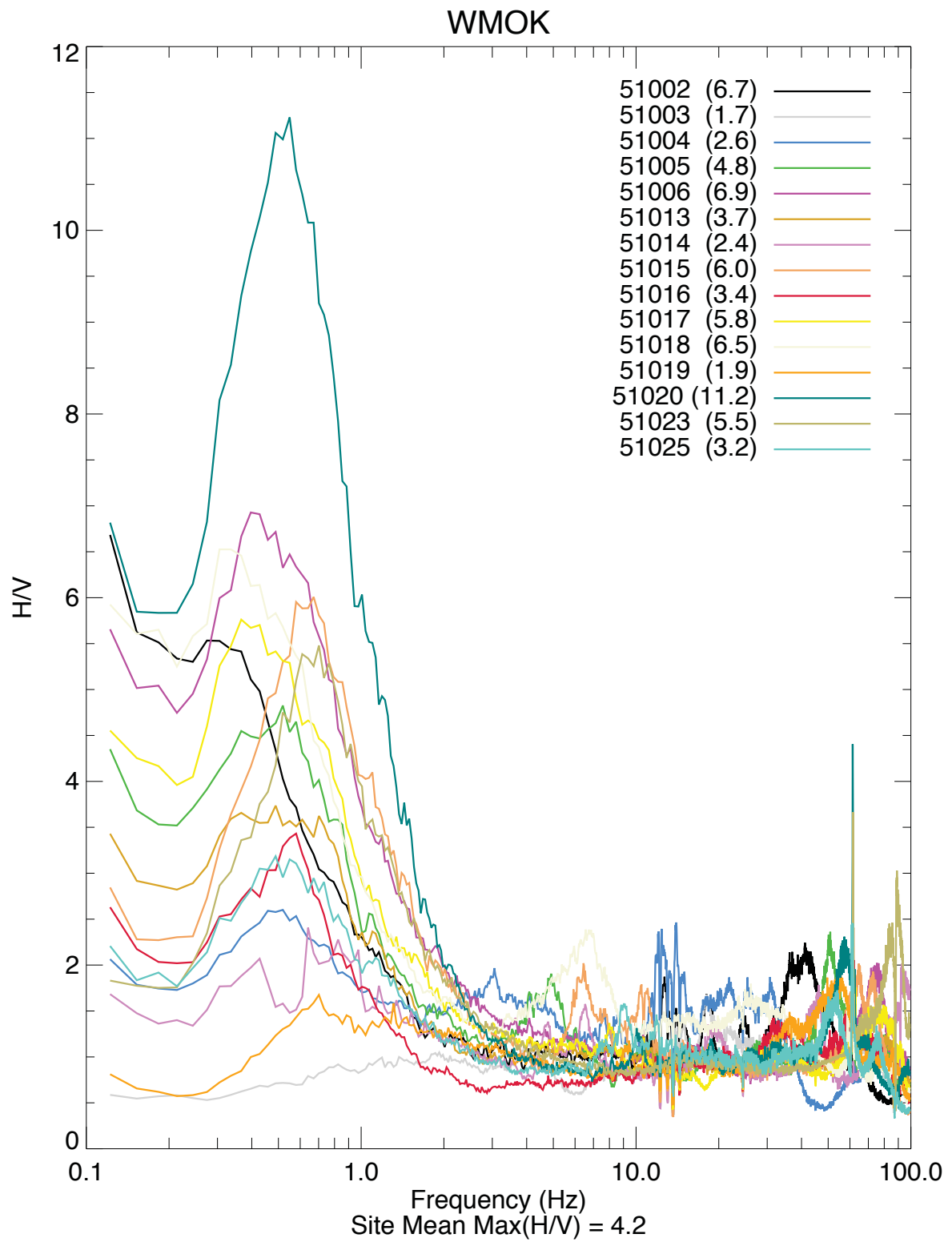


Figure 2.10f. WMOK all stations H/V.

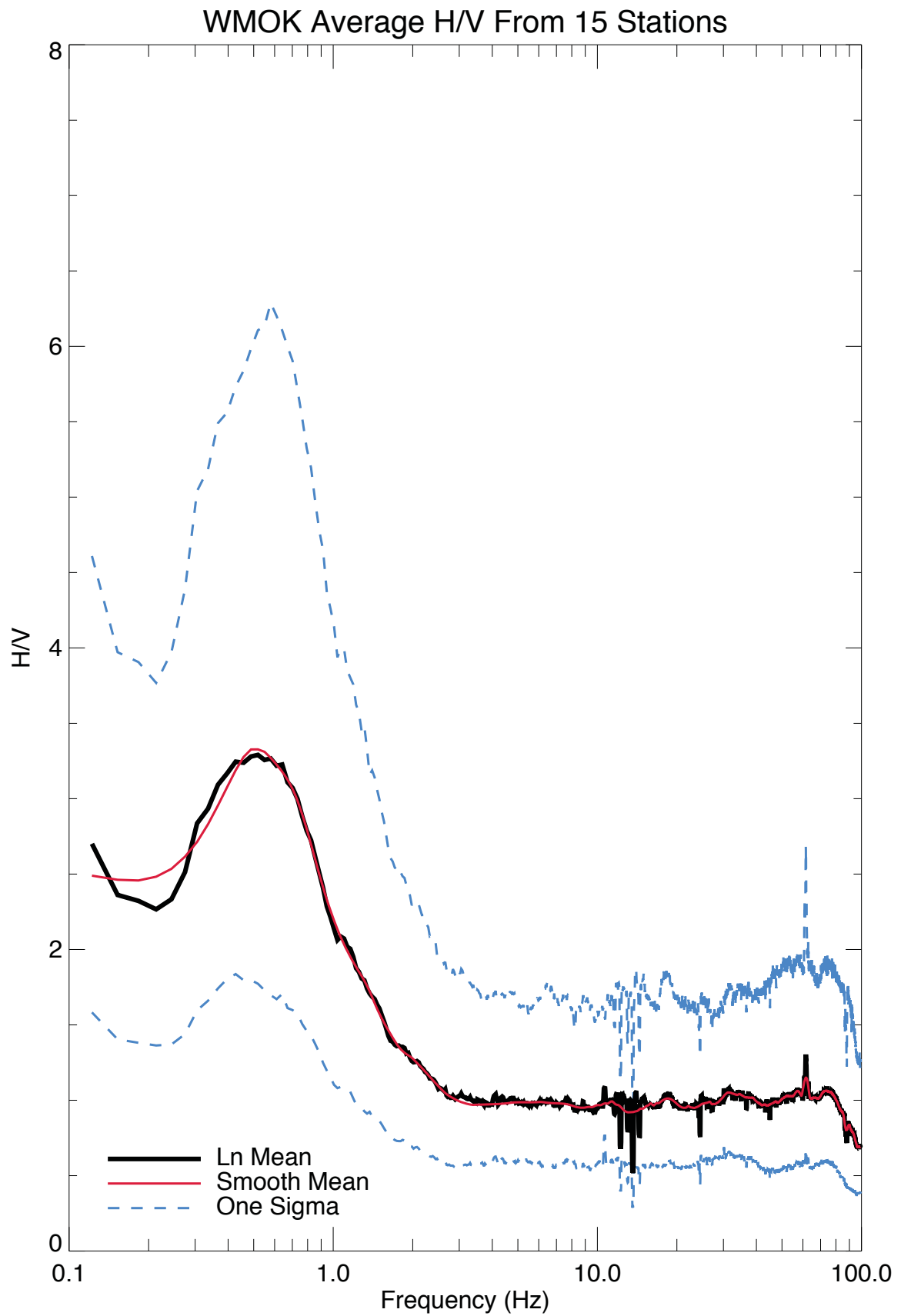
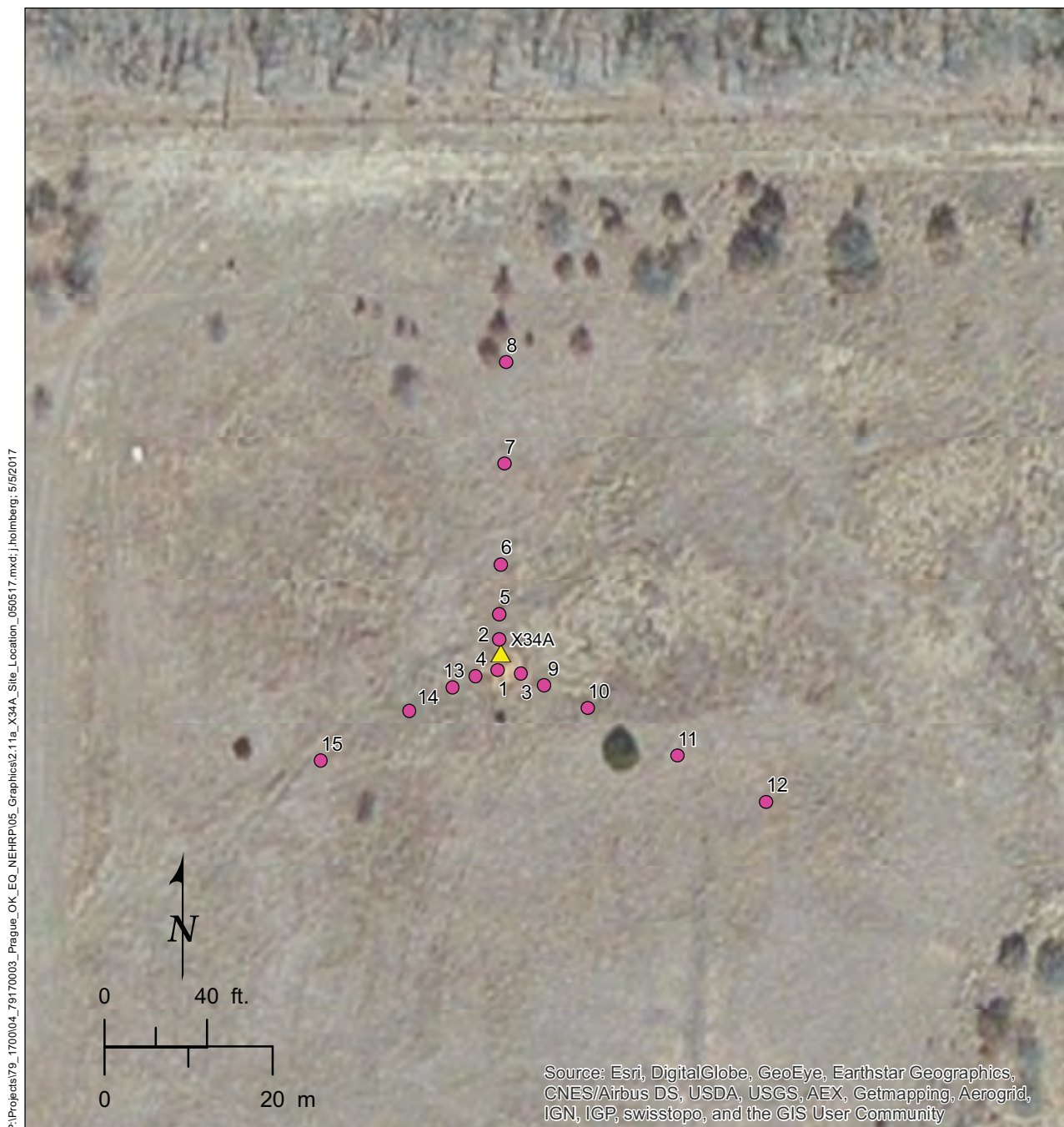


Figure 2.10g. WMOK site average H/V.



Explanation

- Receiver location
- ▲ Seismic station

Figure 2.11a. X34A site location.

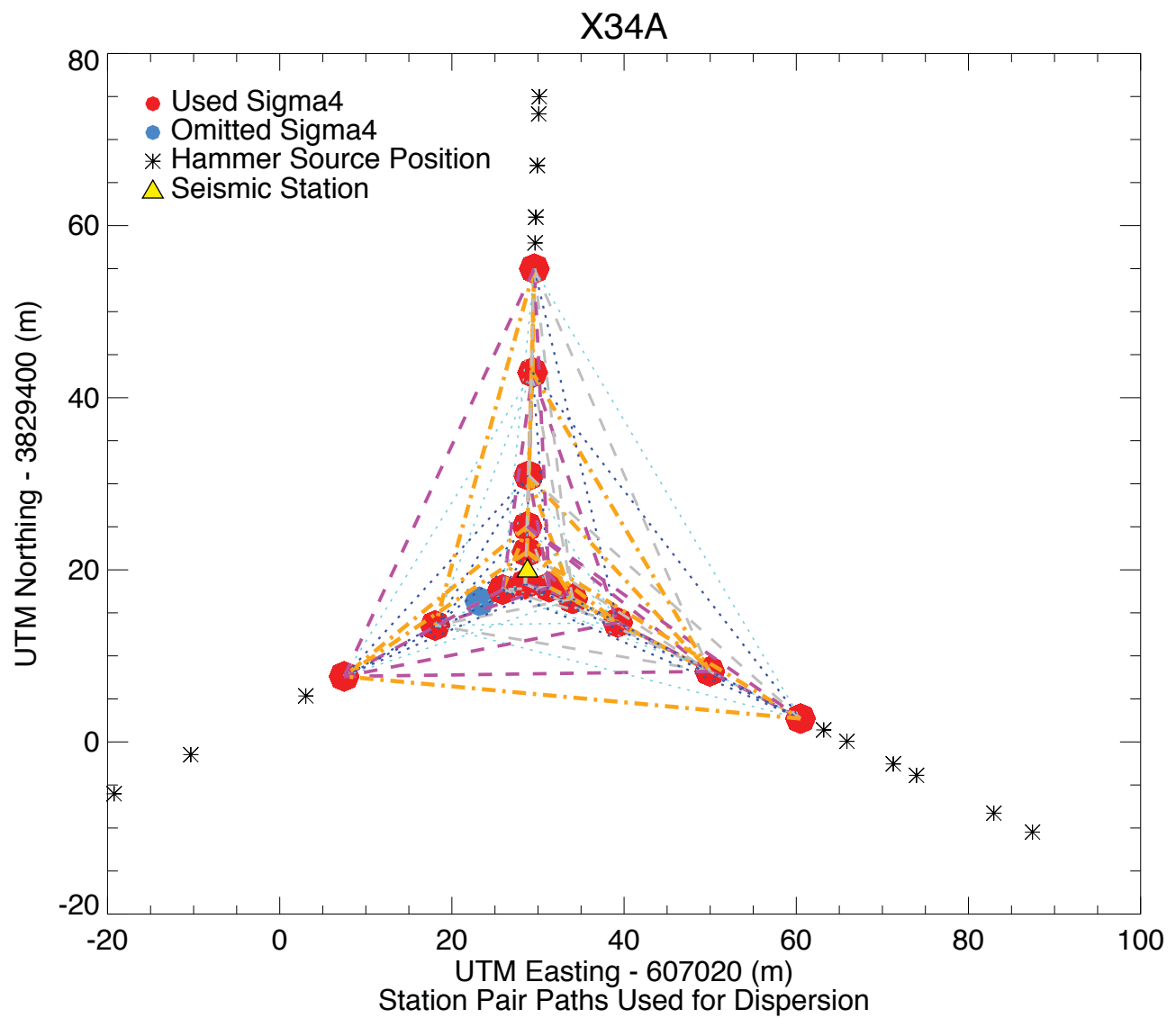


Figure 2.11b. X34A station dispersion pathways and source positions.

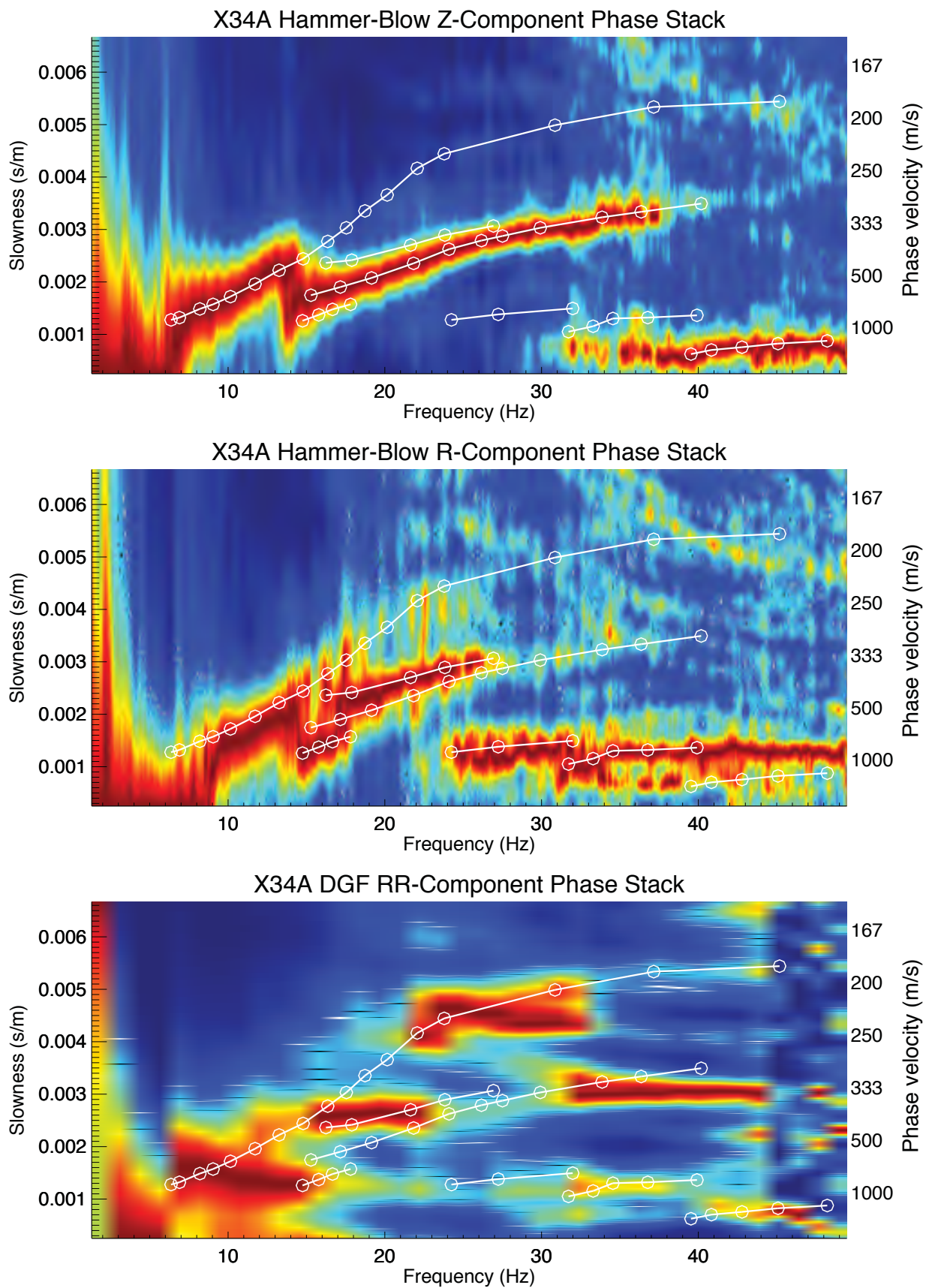


Figure 2.11c. X34A multi-component multimodal p-f dispersion images and picks.

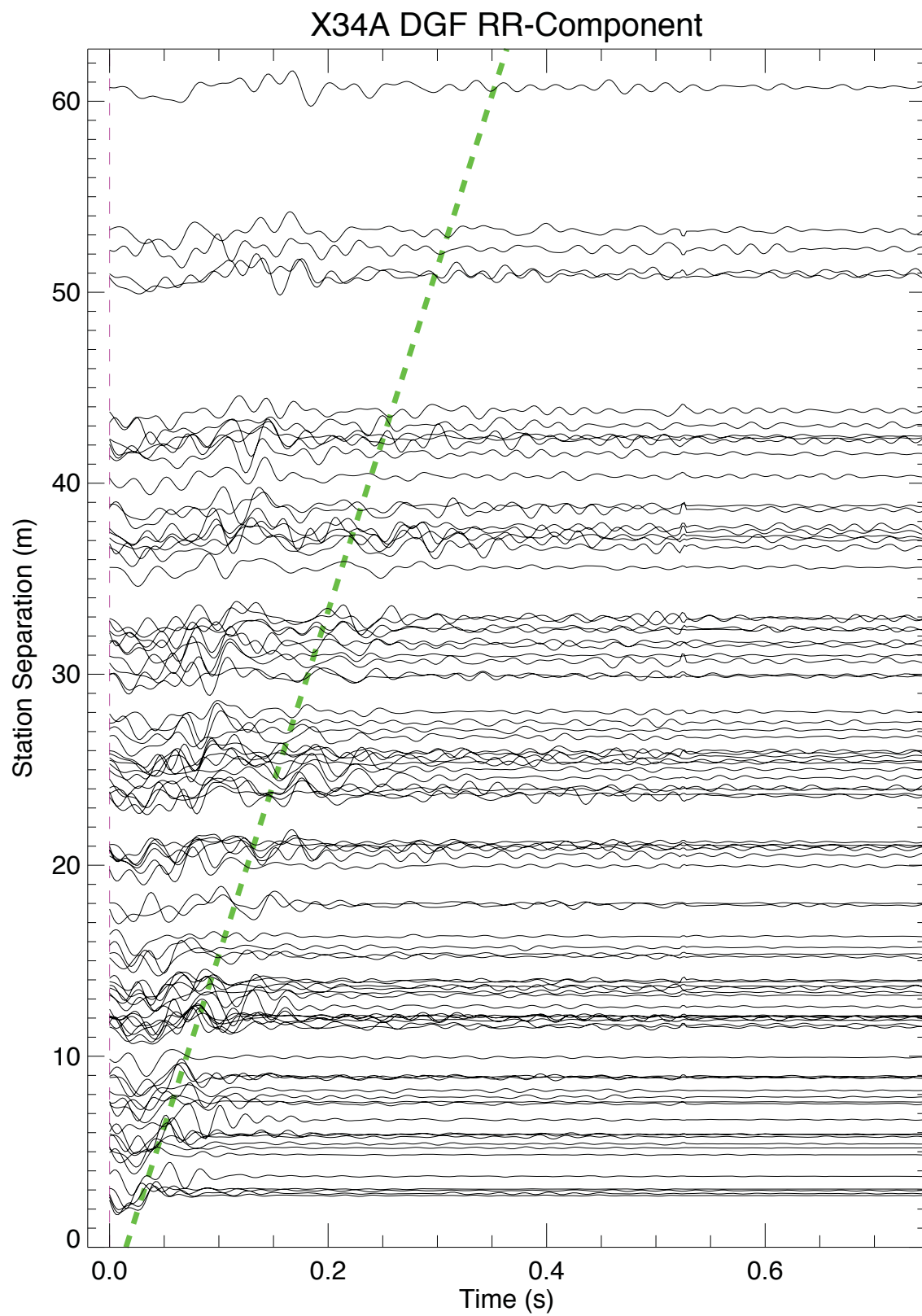
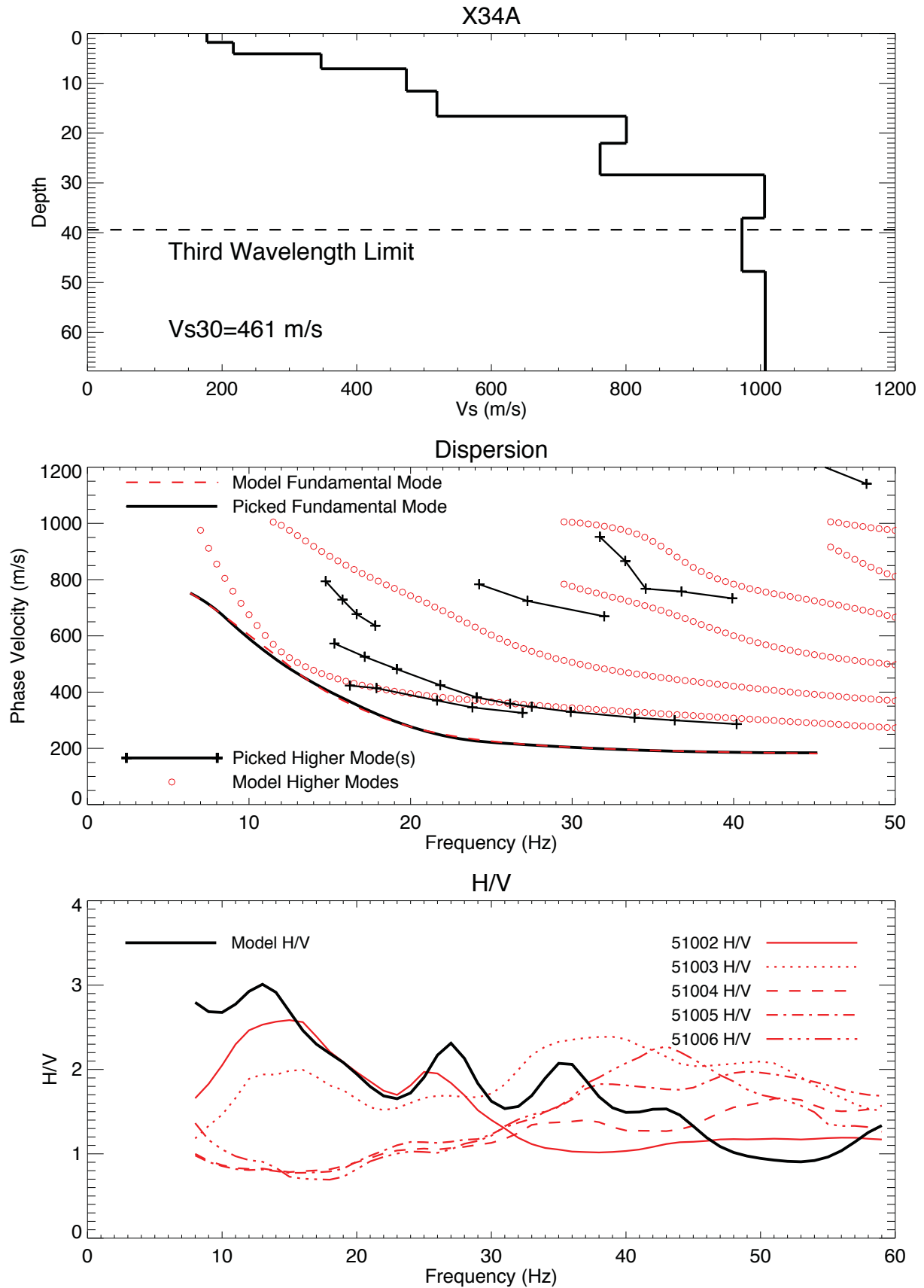


Figure 2.11d. X34A radial component dispersion Green's Function.



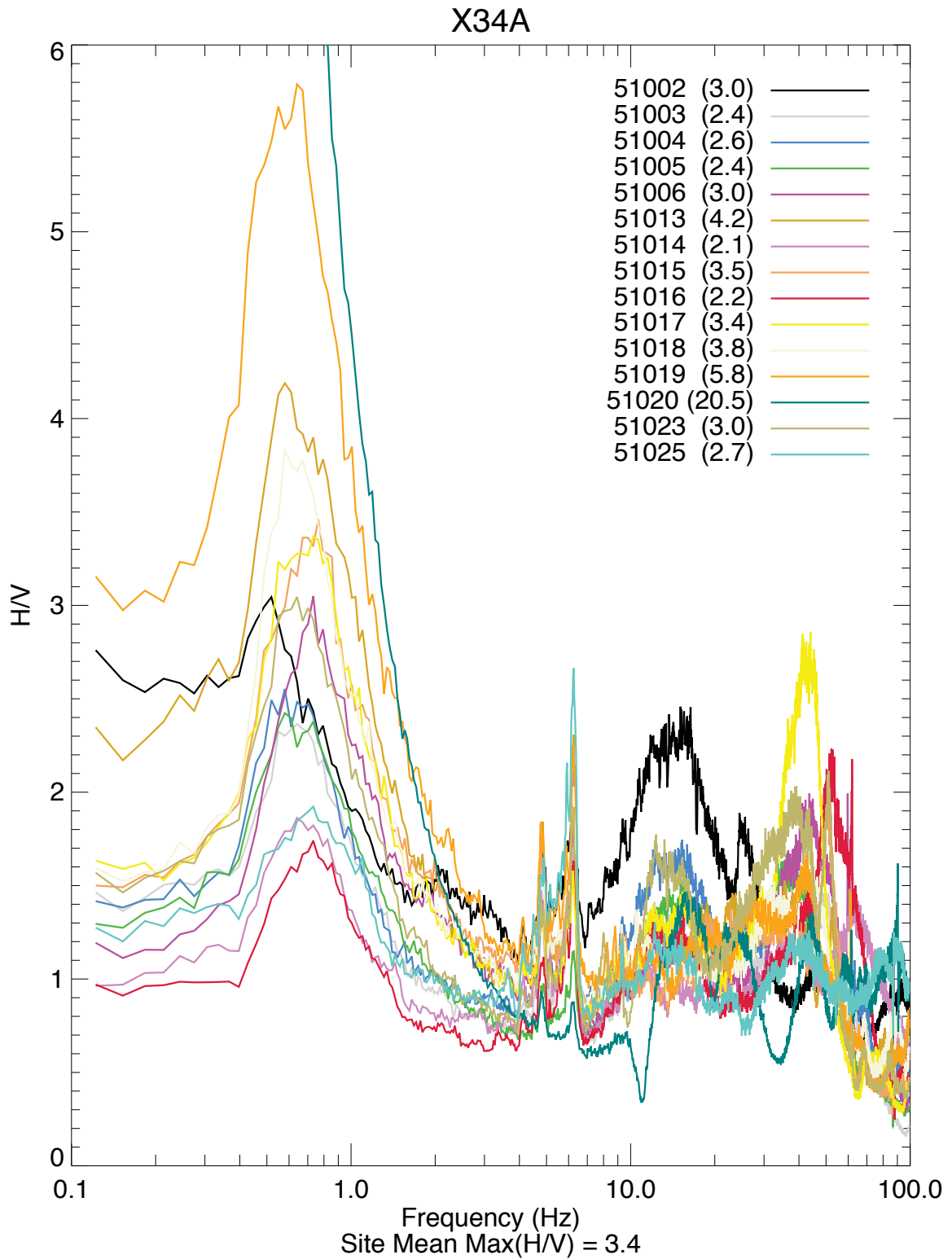


Figure 2.11f. X34A all stations H/V.

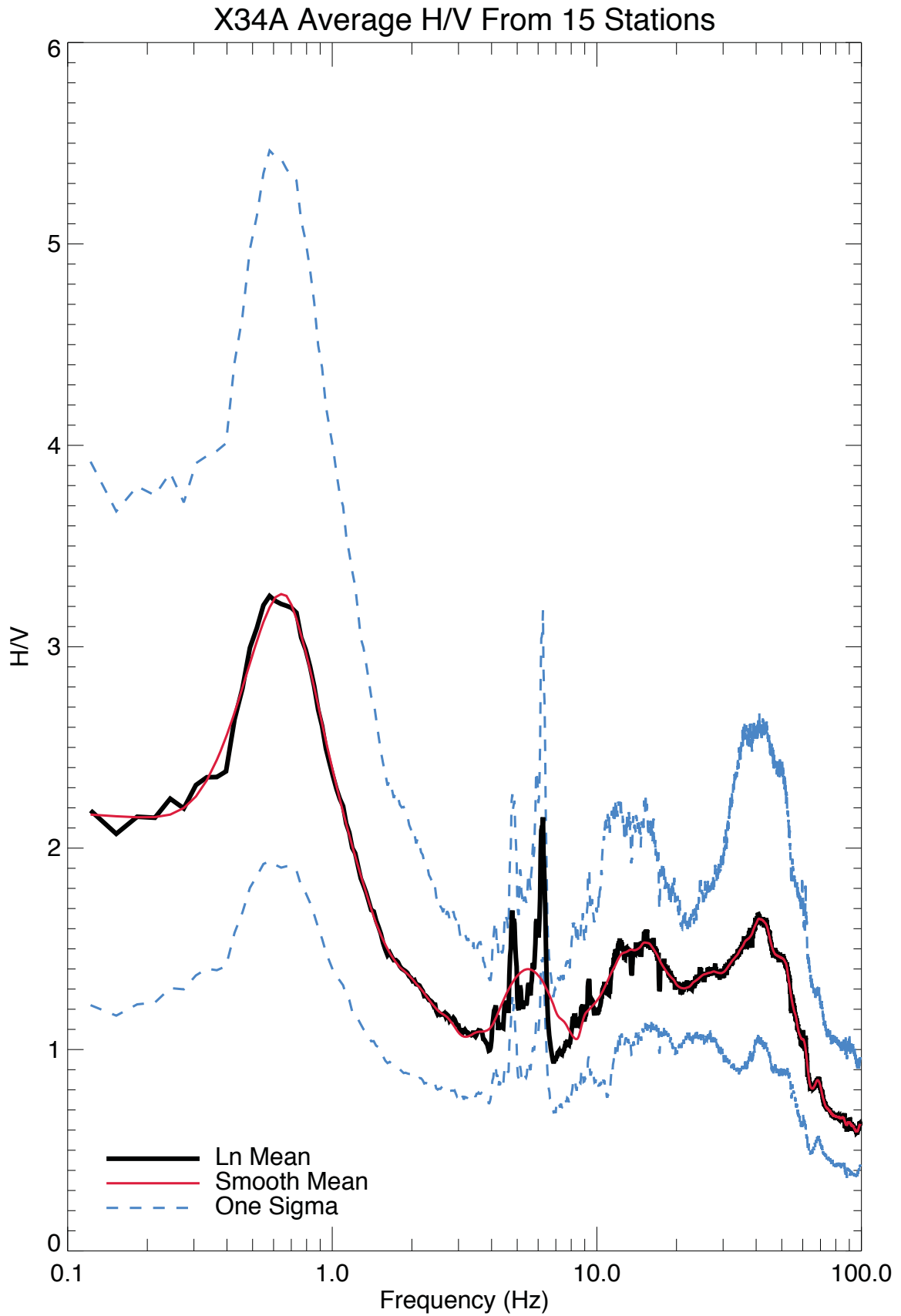


Figure 2.11g. X34A site average H/V.

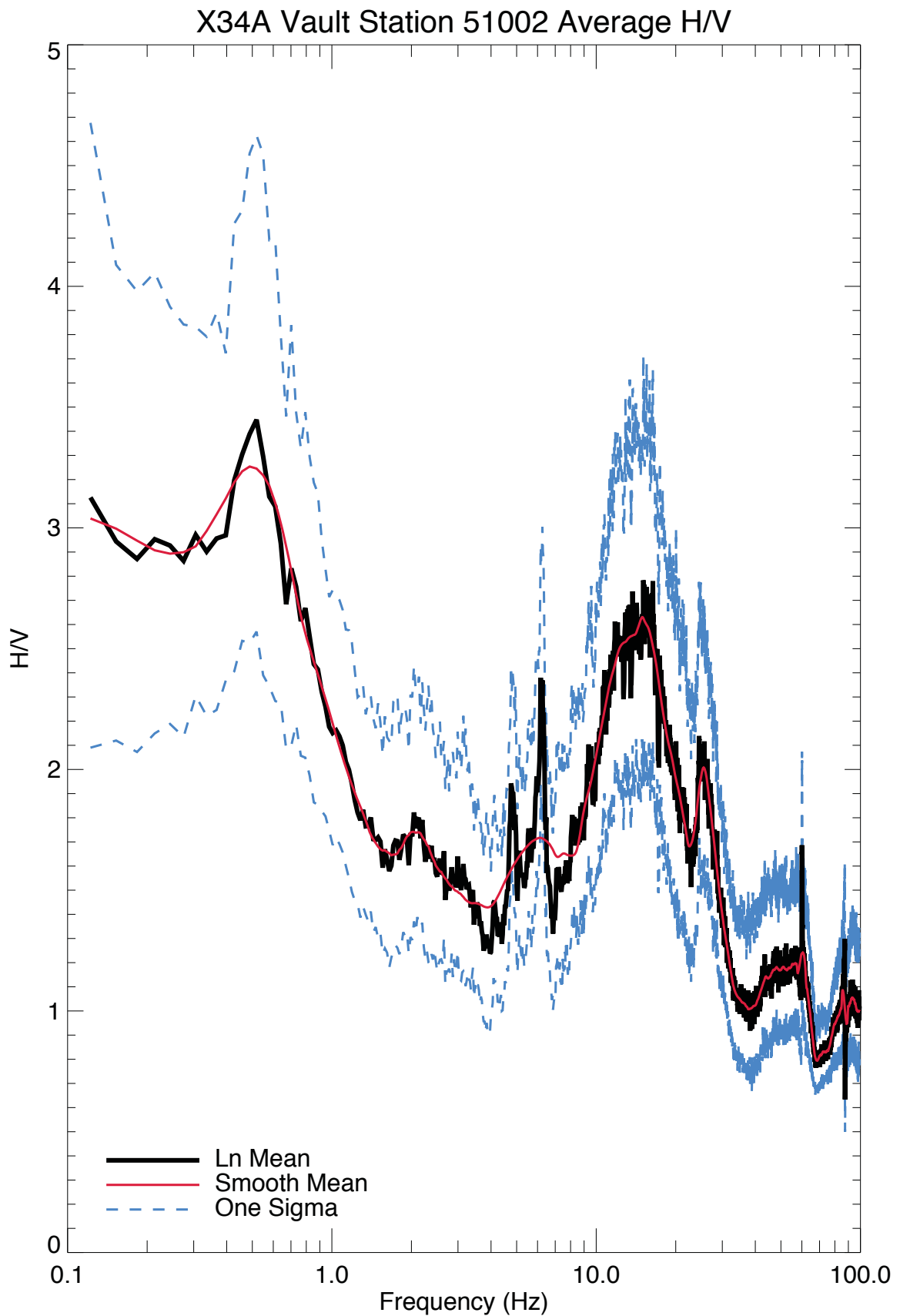


Figure 2.11h. X34A average H/V at the vault.

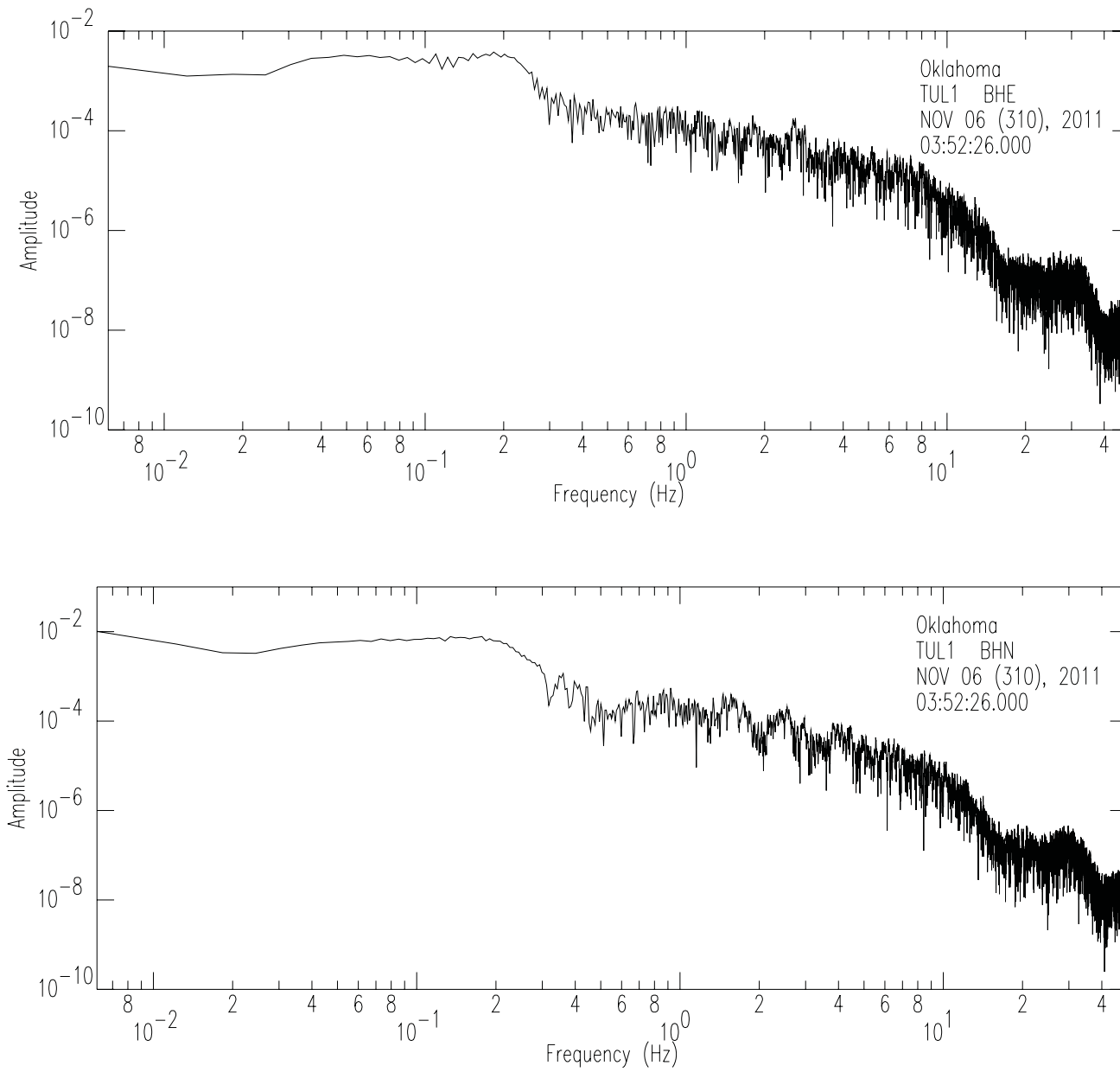


Figure 3.1. TUL1 observed horizontal displacement spectra.

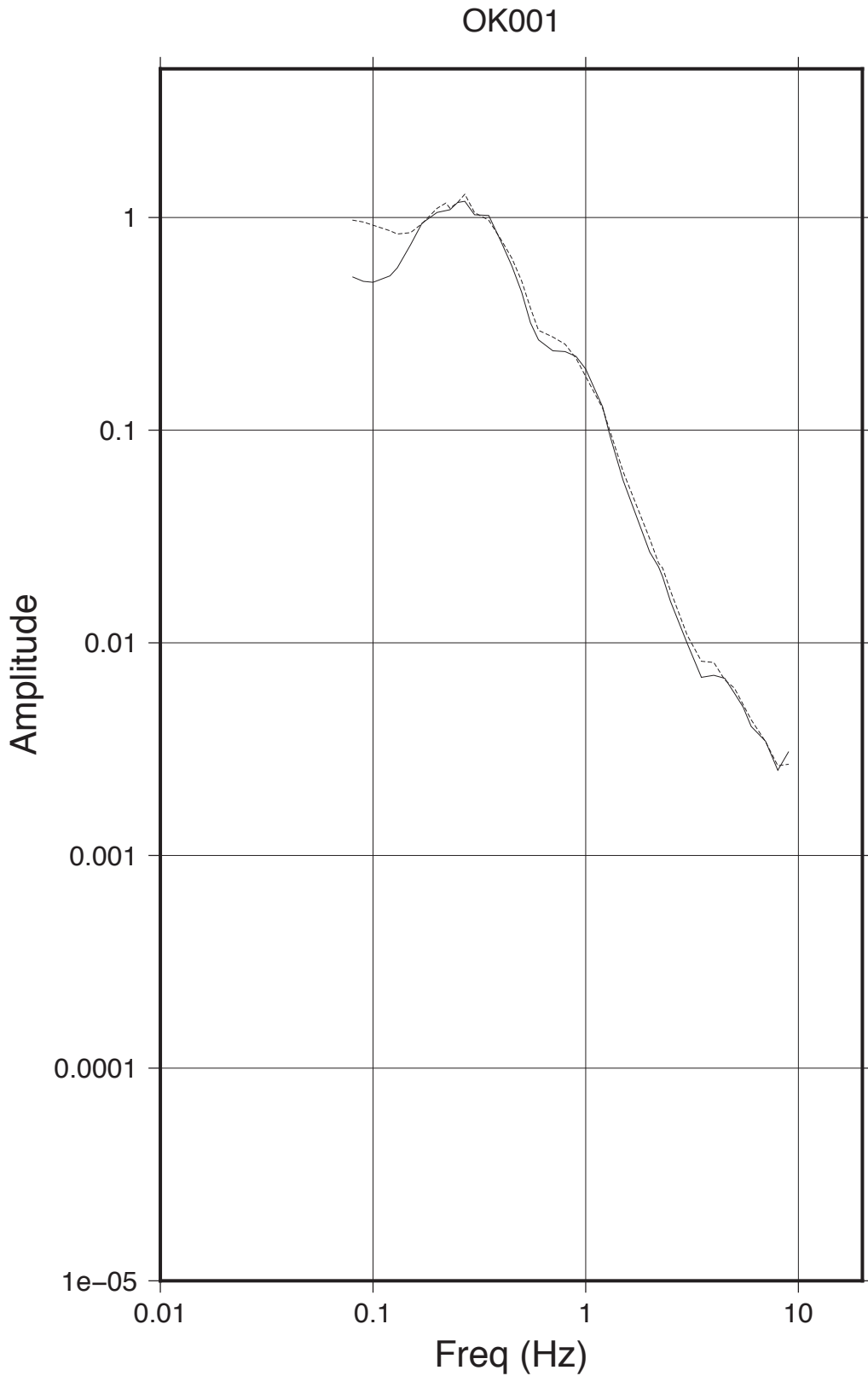


Figure 3.2. OK001 observed and predicted horizontal displacement spectra.

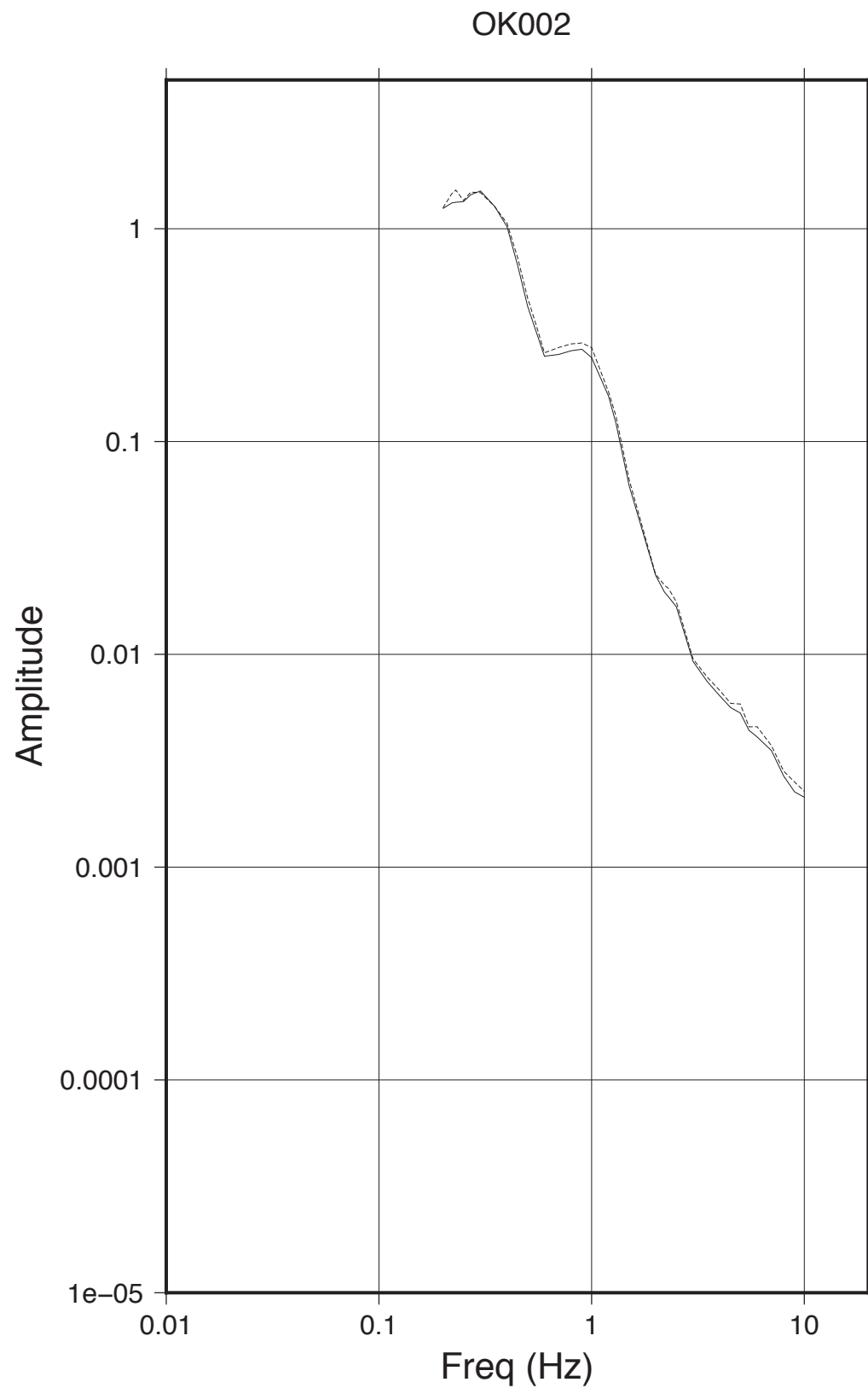


Figure 3.3. OK002 observed and predicted horizontal displacement spectra.

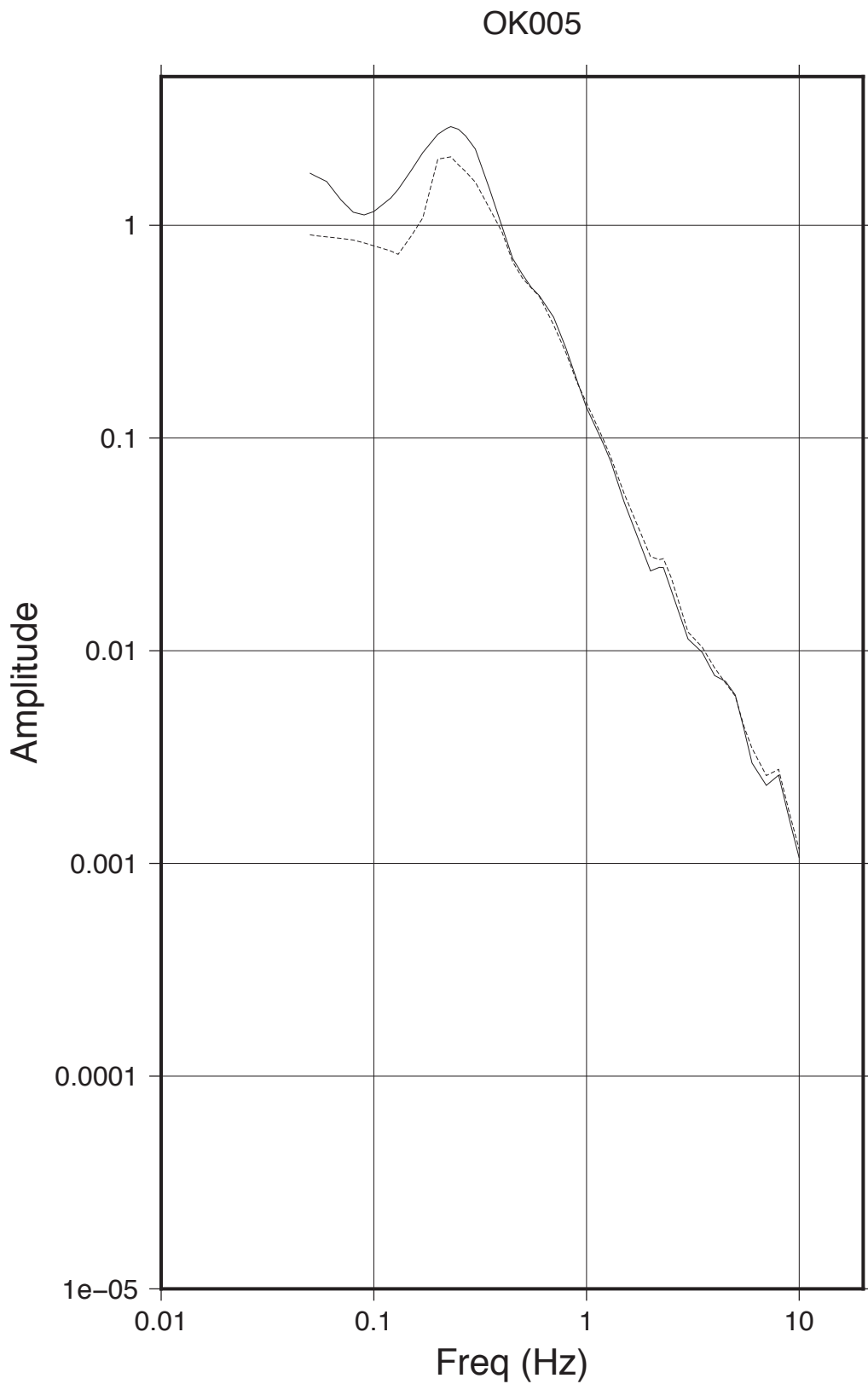


Figure 3.4. OK005 observed and predicted horizontal displacement spectra.

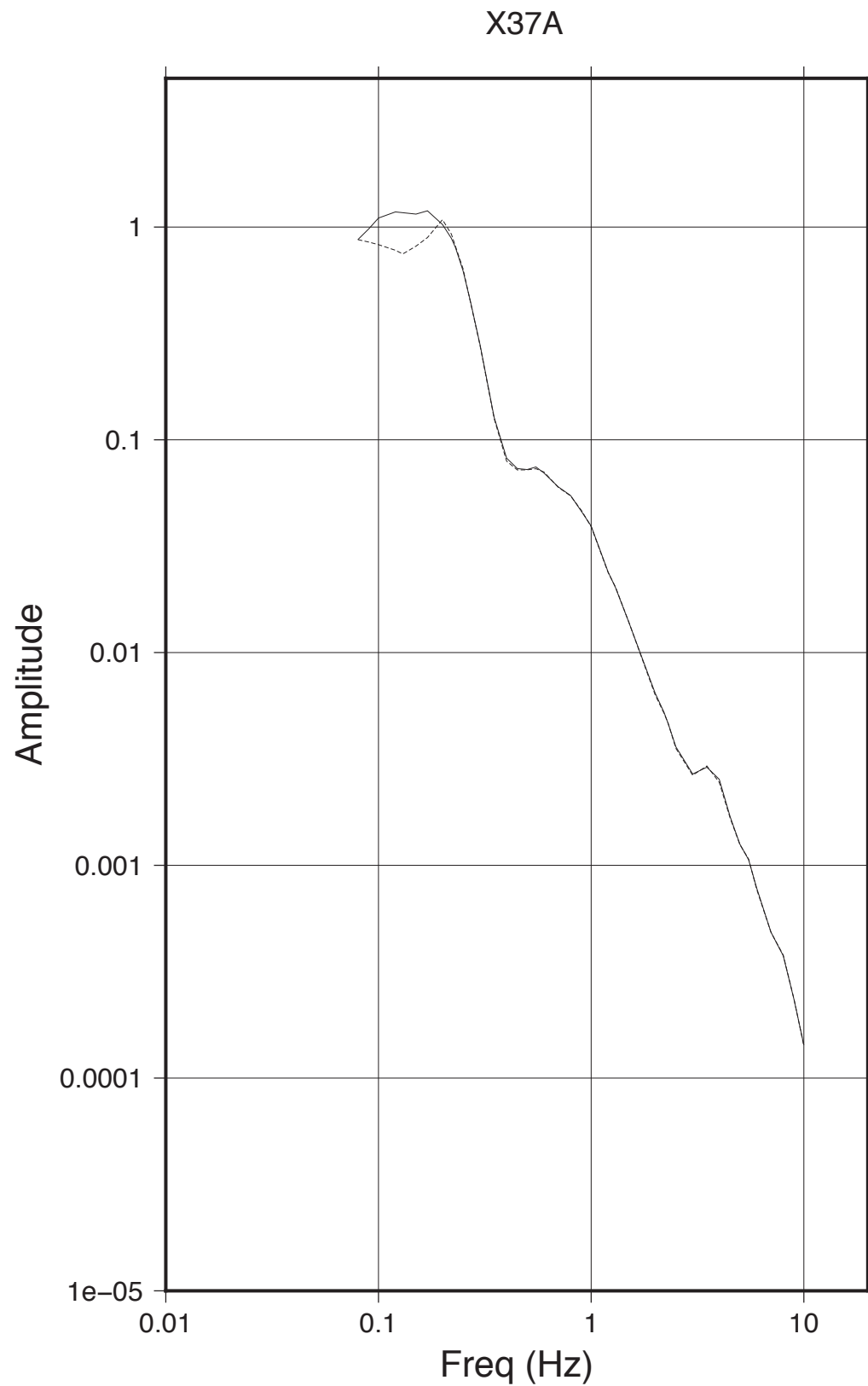


Figure 3.5. OK009 observed and predicted horizontal displacement spectra.

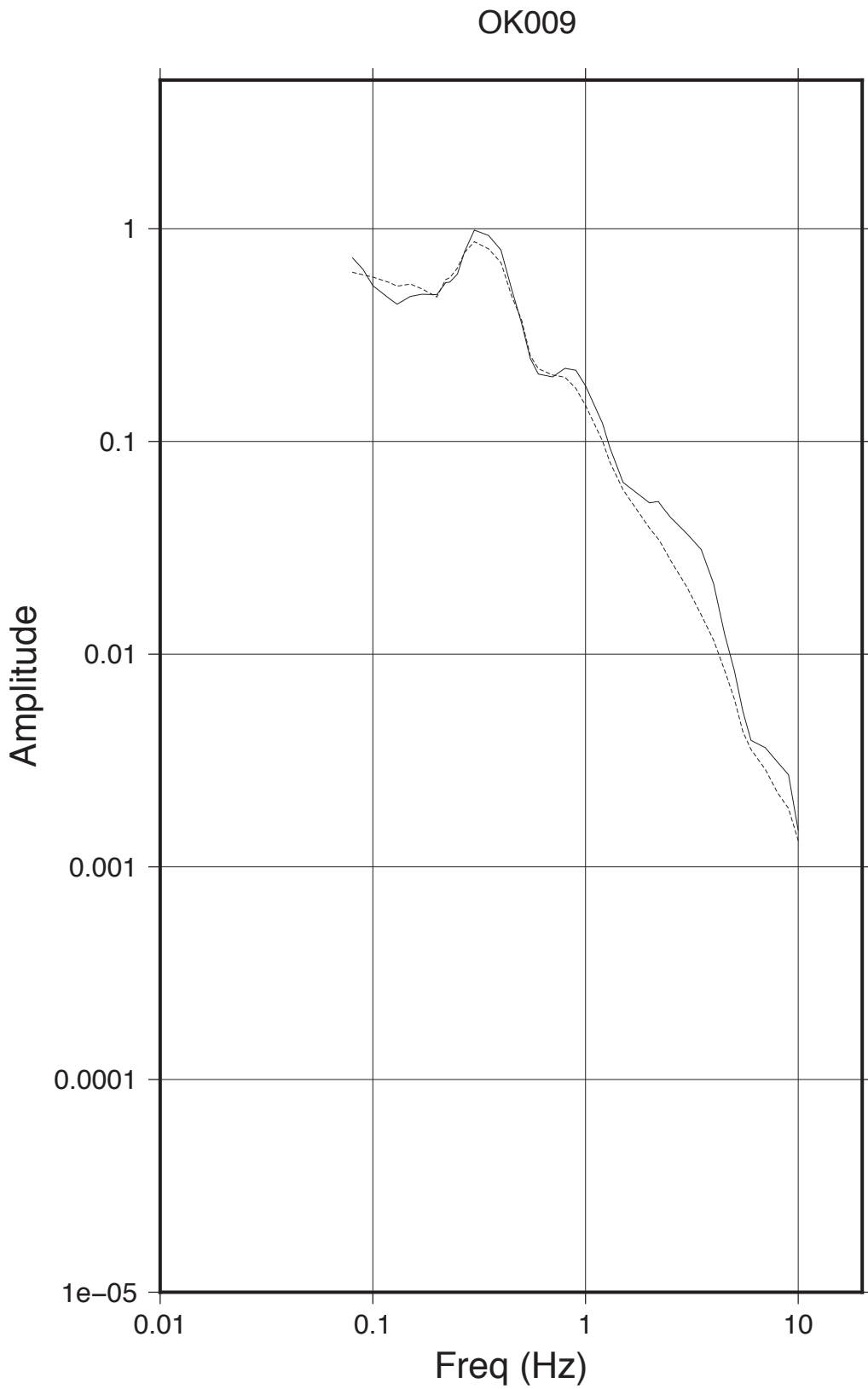


Figure 3.6. T34A observed and predicted horizontal displacement spectra.

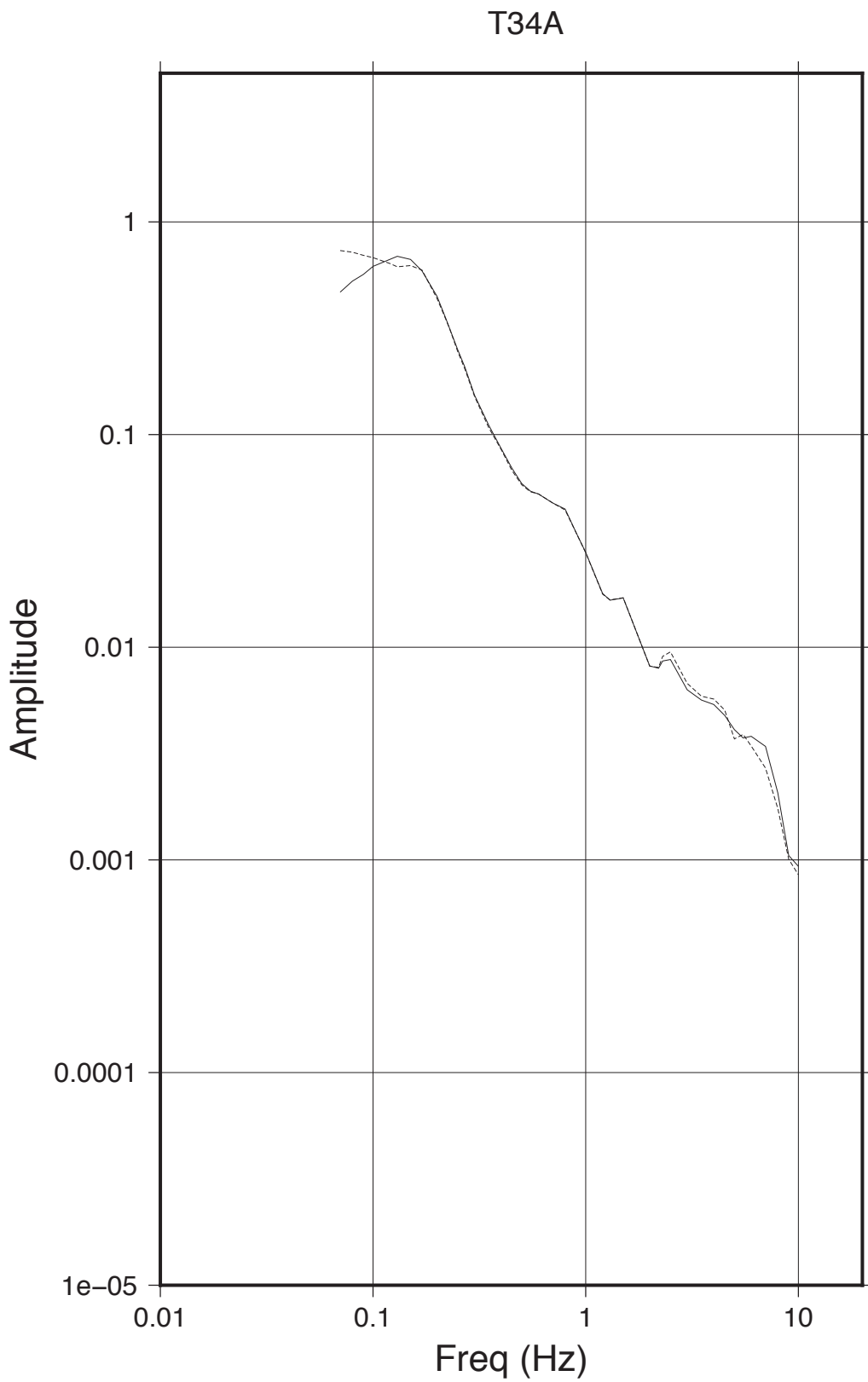


Figure 3.7. U32A observed and predicted horizontal displacement spectra.

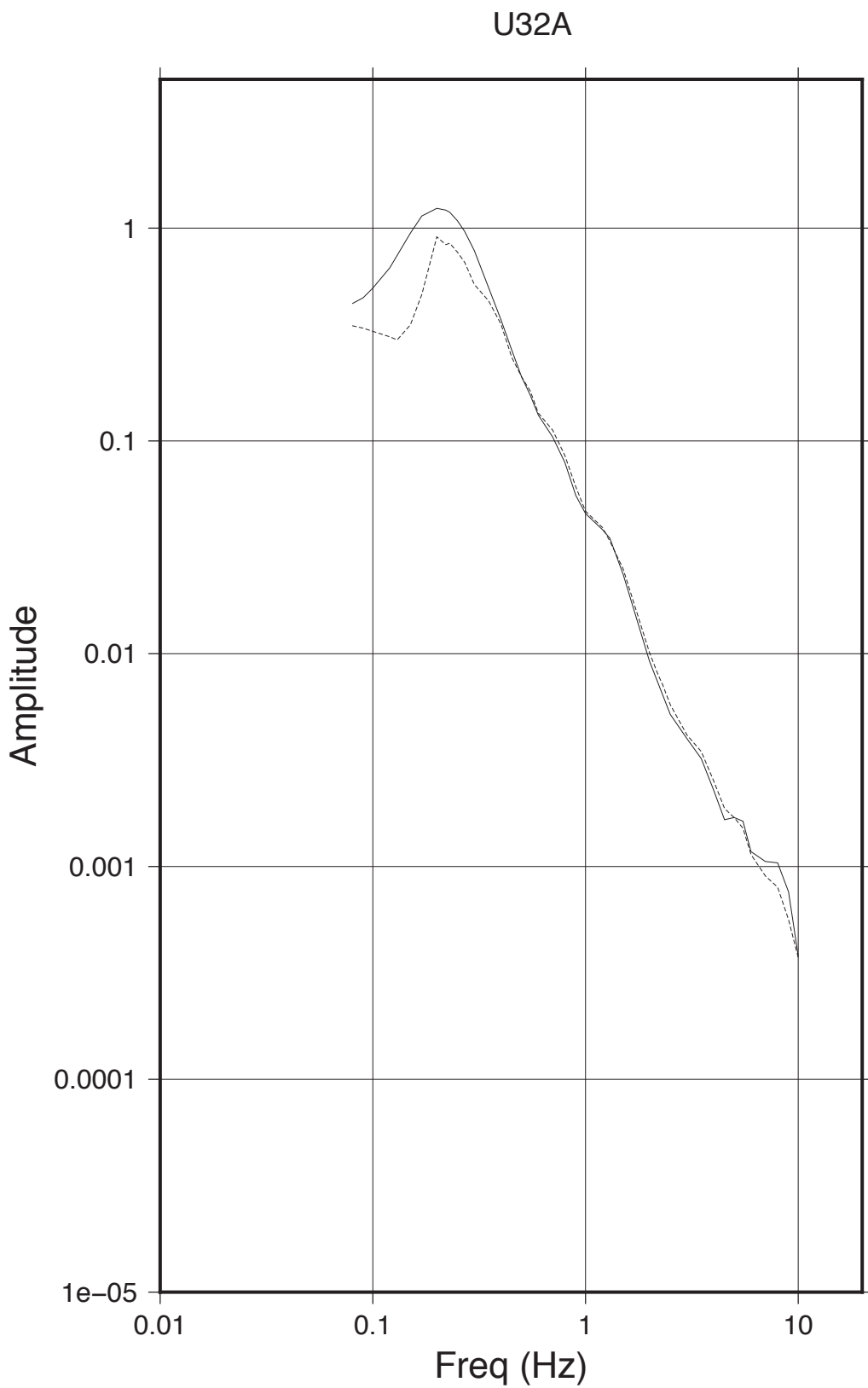


Figure 3.8. U35A observed and predicted horizontal displacement spectra.

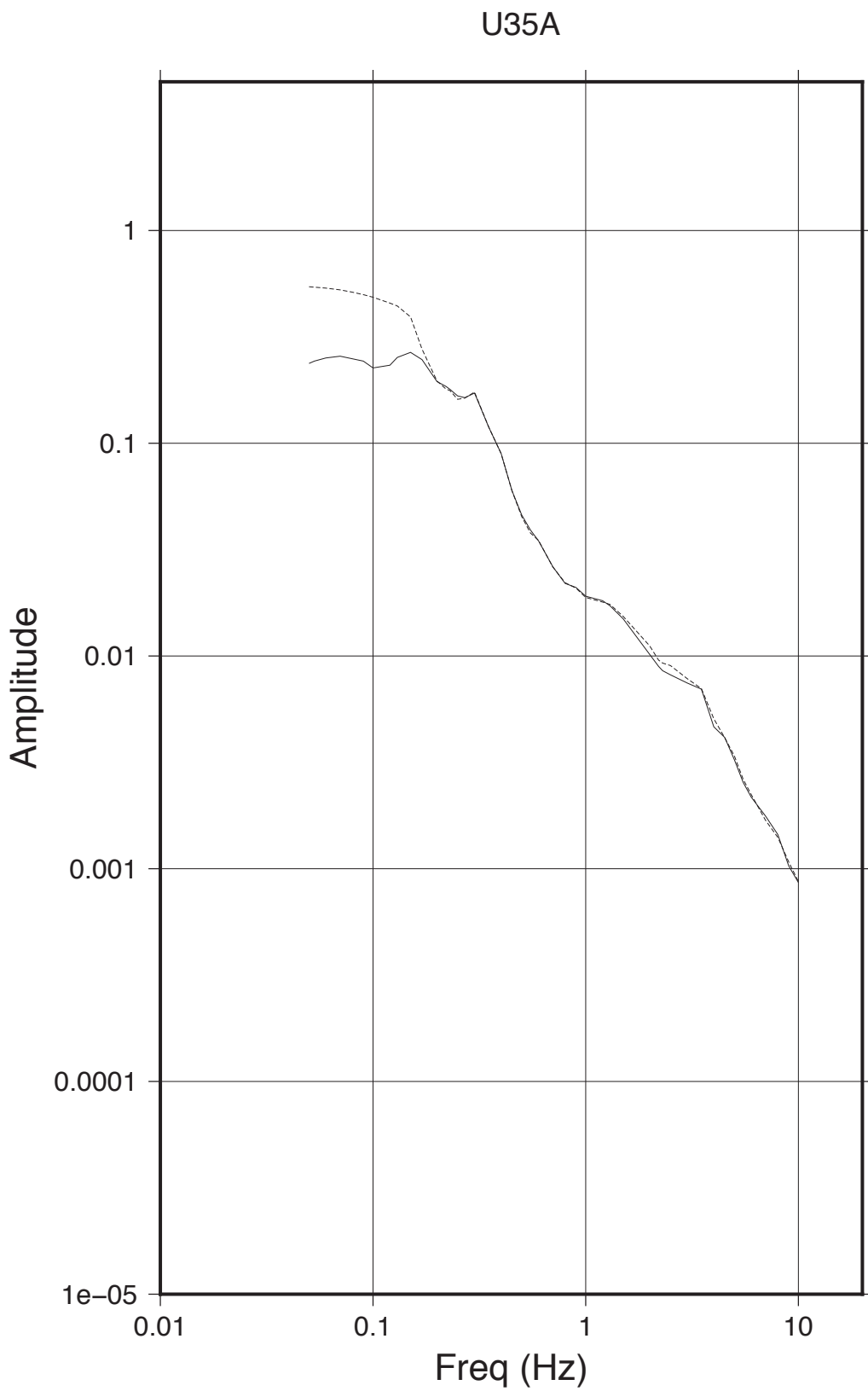


Figure 3.9. V35A observed and predicted horizontal displacement spectra.

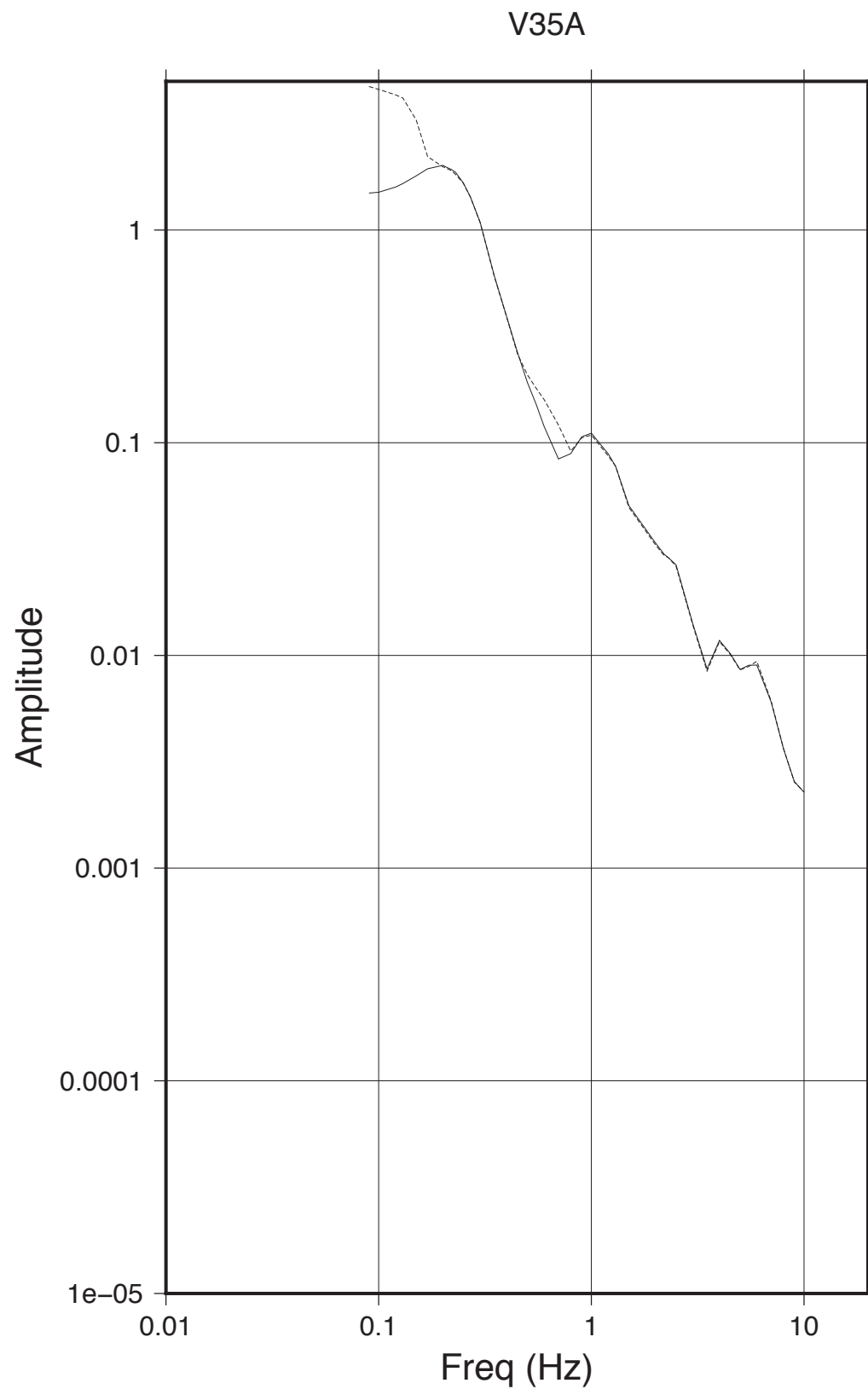


Figure 3.10. W35A observed and predicted horizontal displacement spectra.

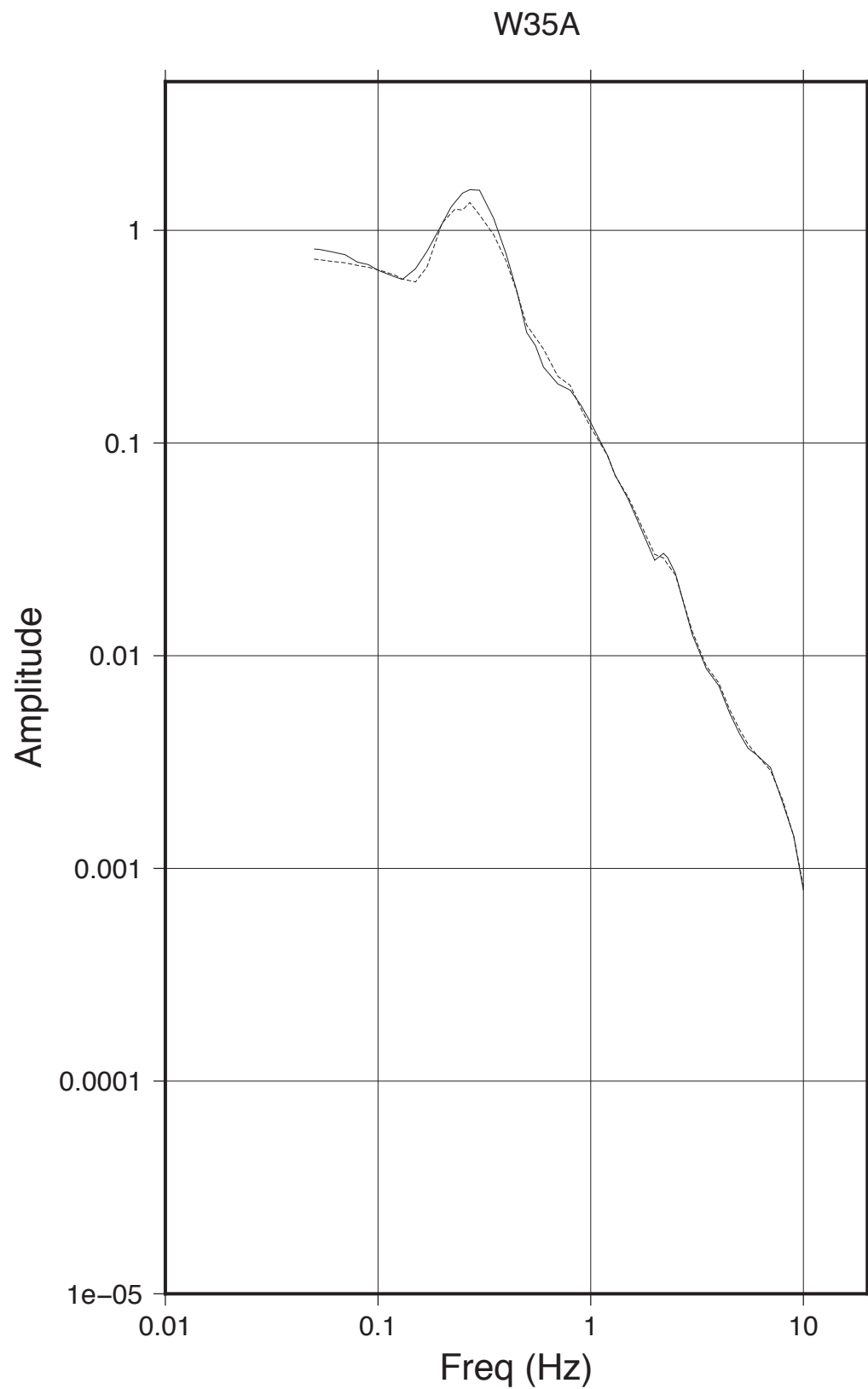


Figure 3.11. W36A observed and predicted horizontal displacement spectra.

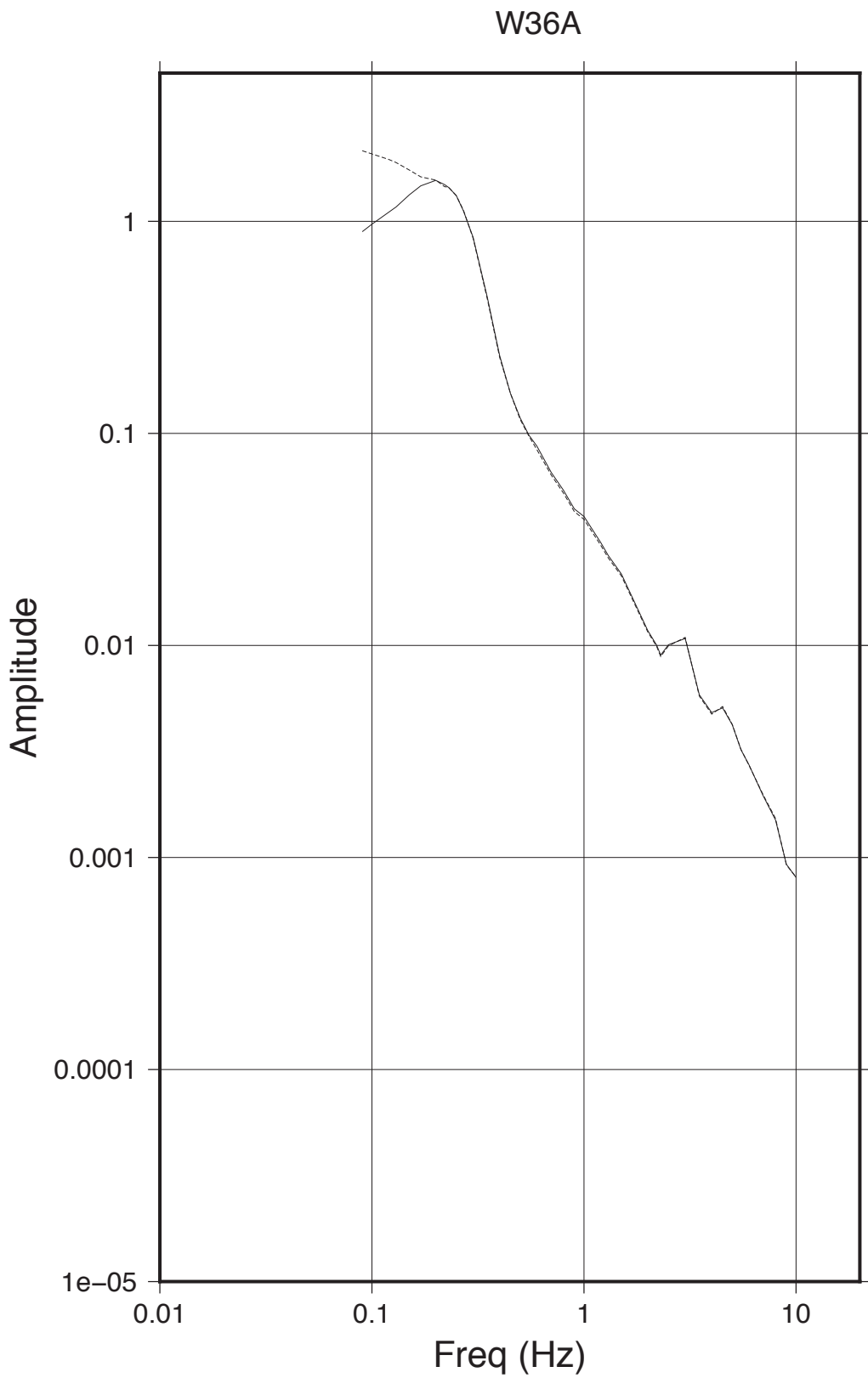


Figure 3.12. W37B observed and predicted horizontal displacement spectra.

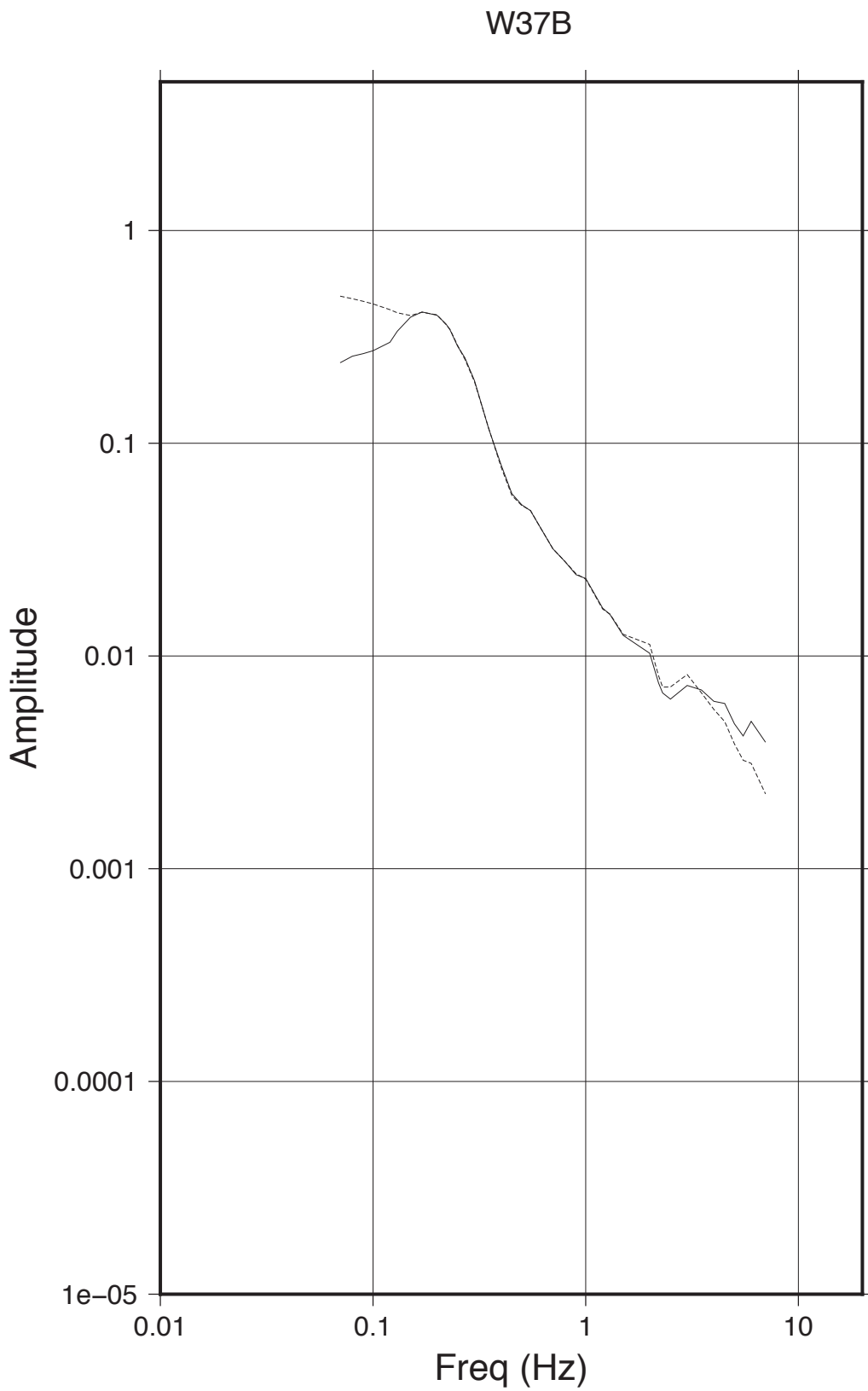


Figure 3.13. W38A observed and predicted horizontal displacement spectra.

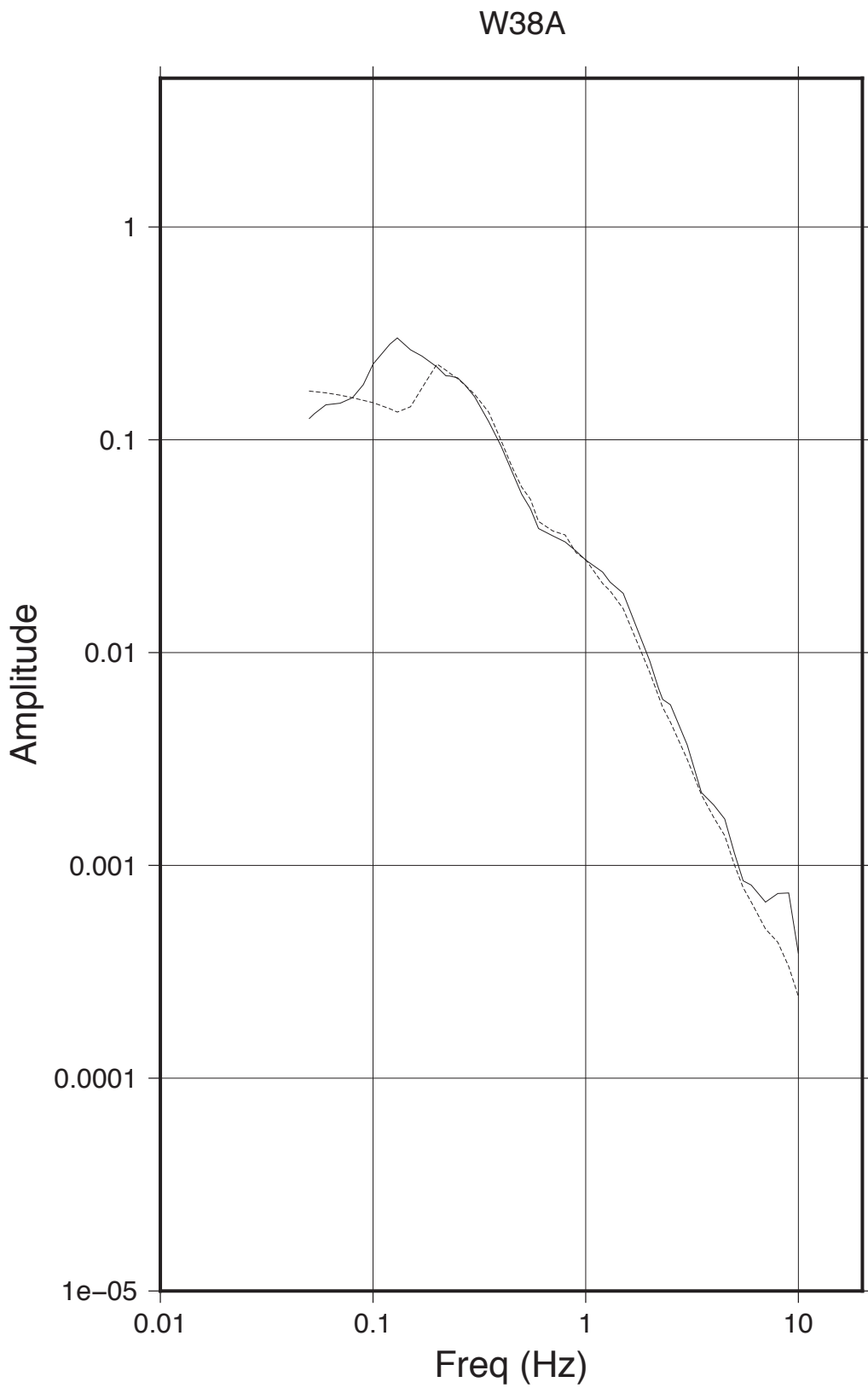


Figure 3.14. X35A observed and predicted horizontal displacement spectra.

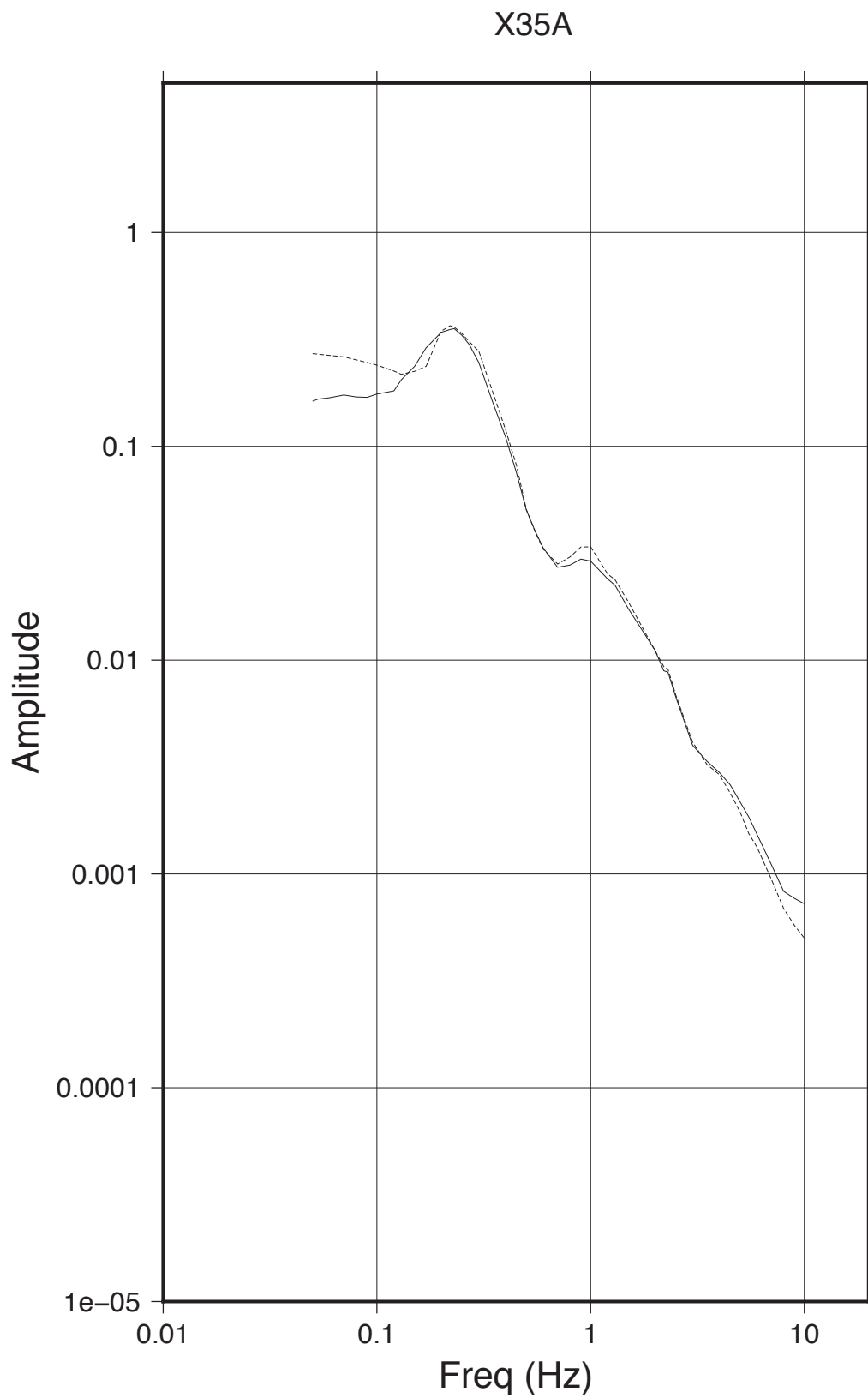


Figure 3.15. X36A observed and predicted horizontal displacement spectra.

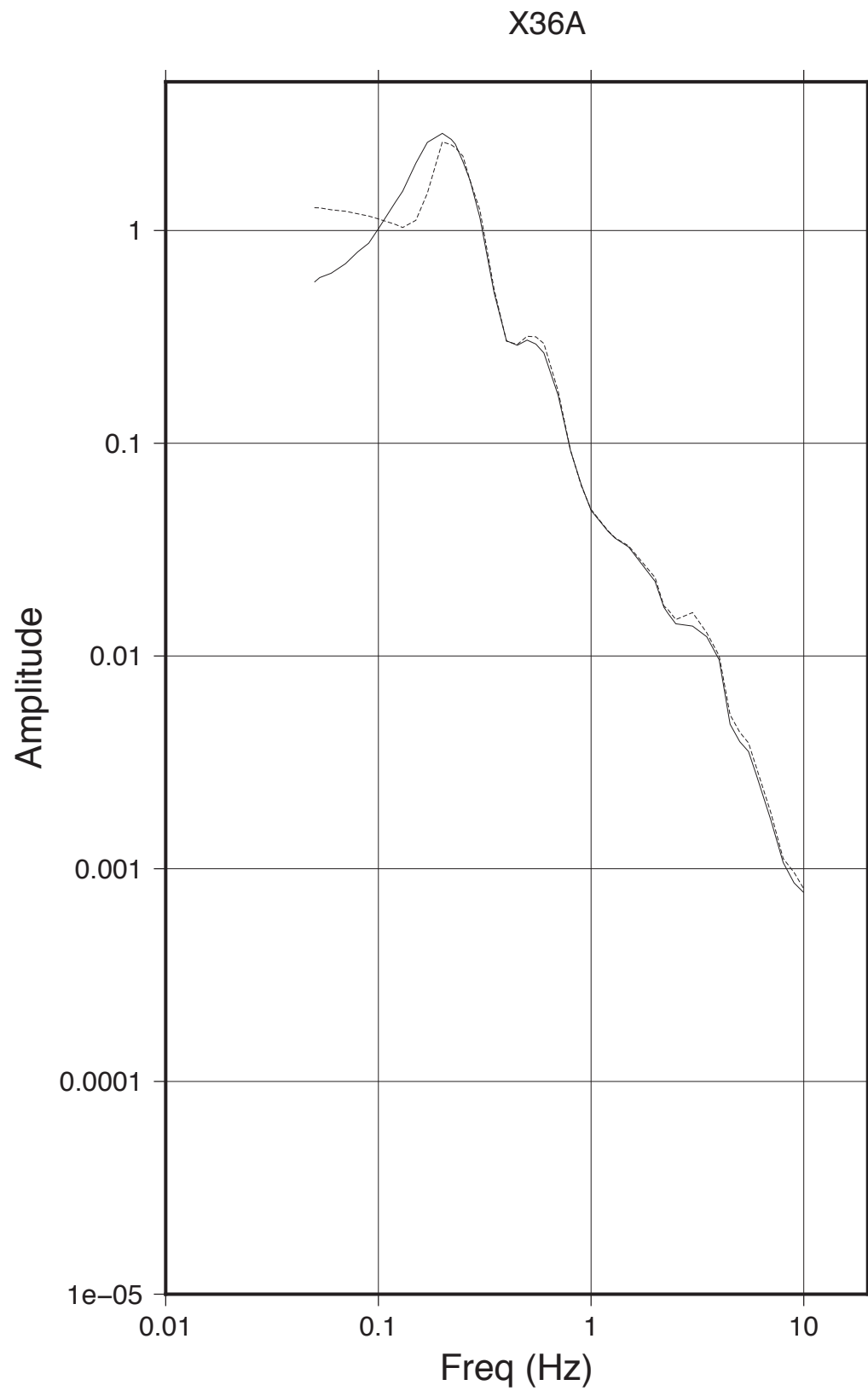


Figure 3.16. X37A observed and predicted horizontal displacement spectra.

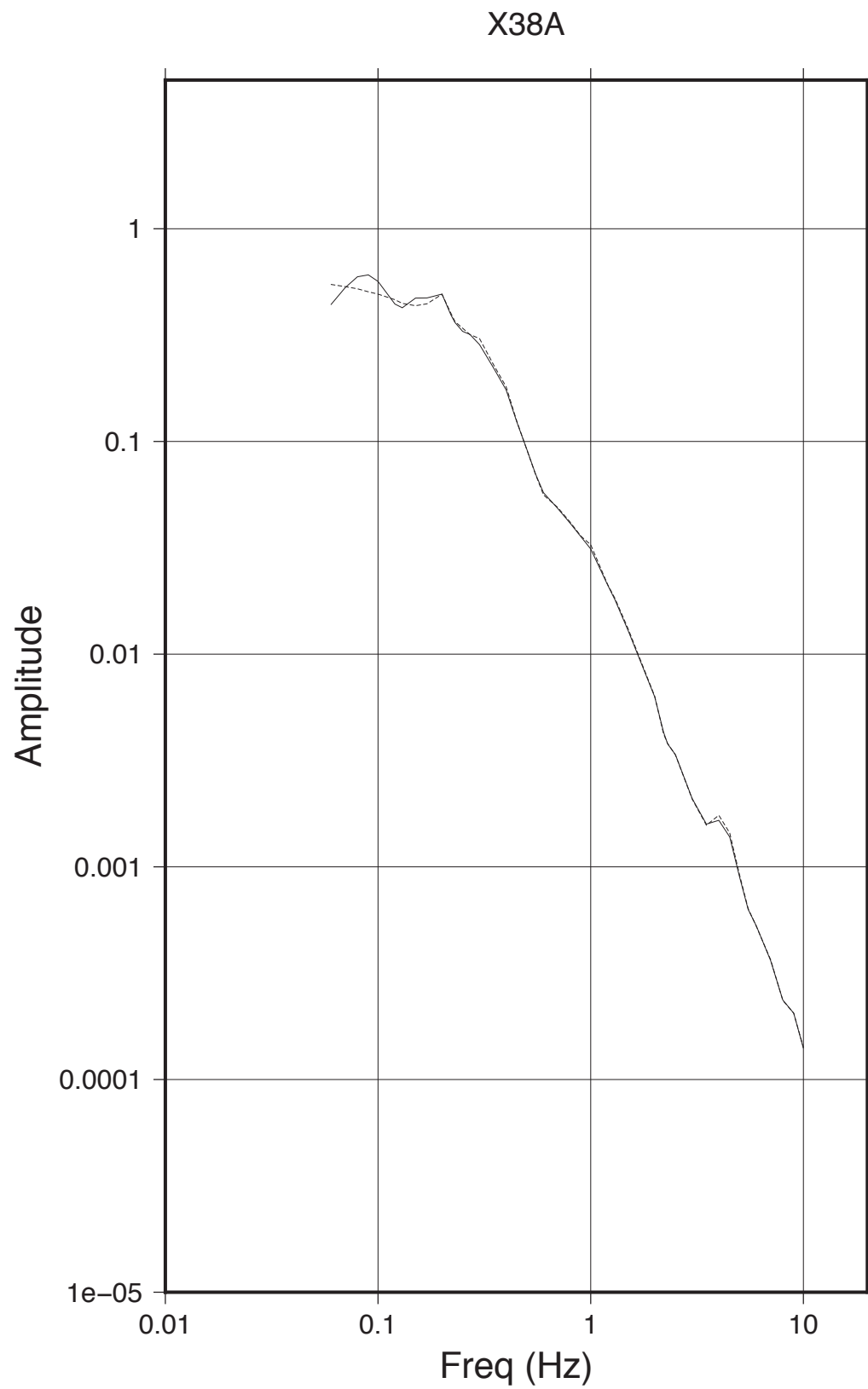


Figure 3.17. X38A observed and predicted horizontal displacement spectra.

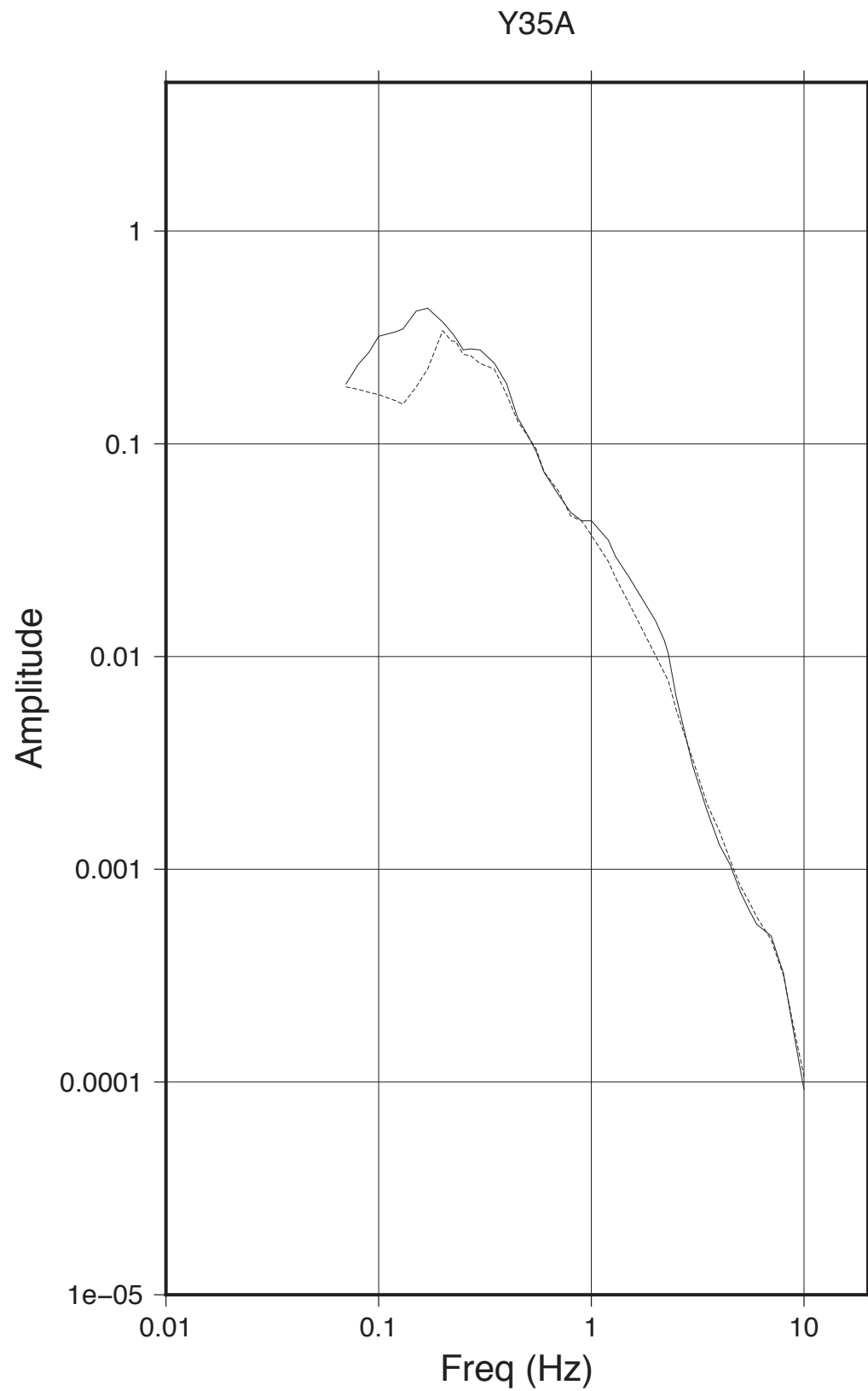


Figure 3.18. Y35A observed and predicted horizontal displacement spectra.

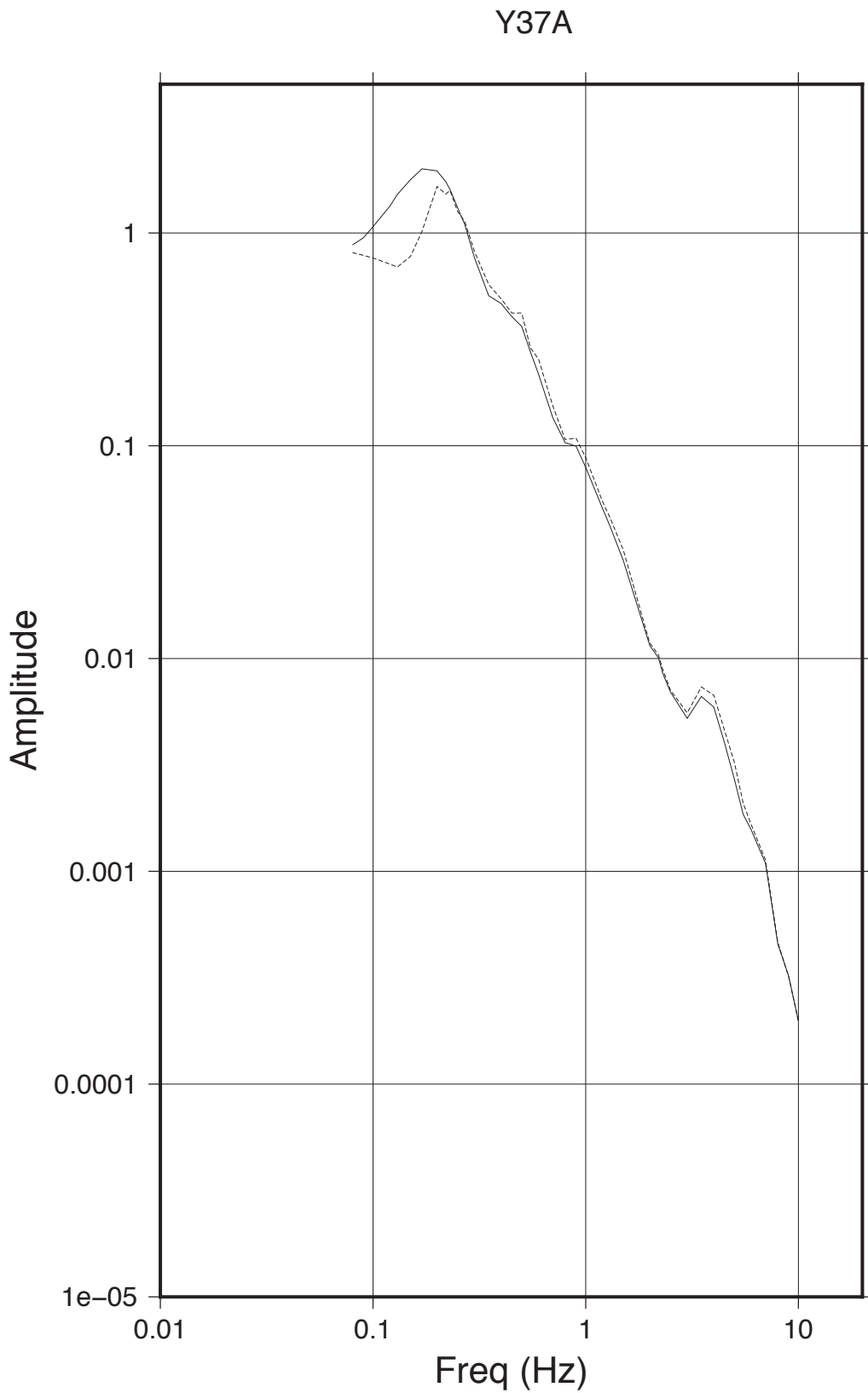


Figure 3.19. Y37A observed and predicted horizontal displacement spectra.

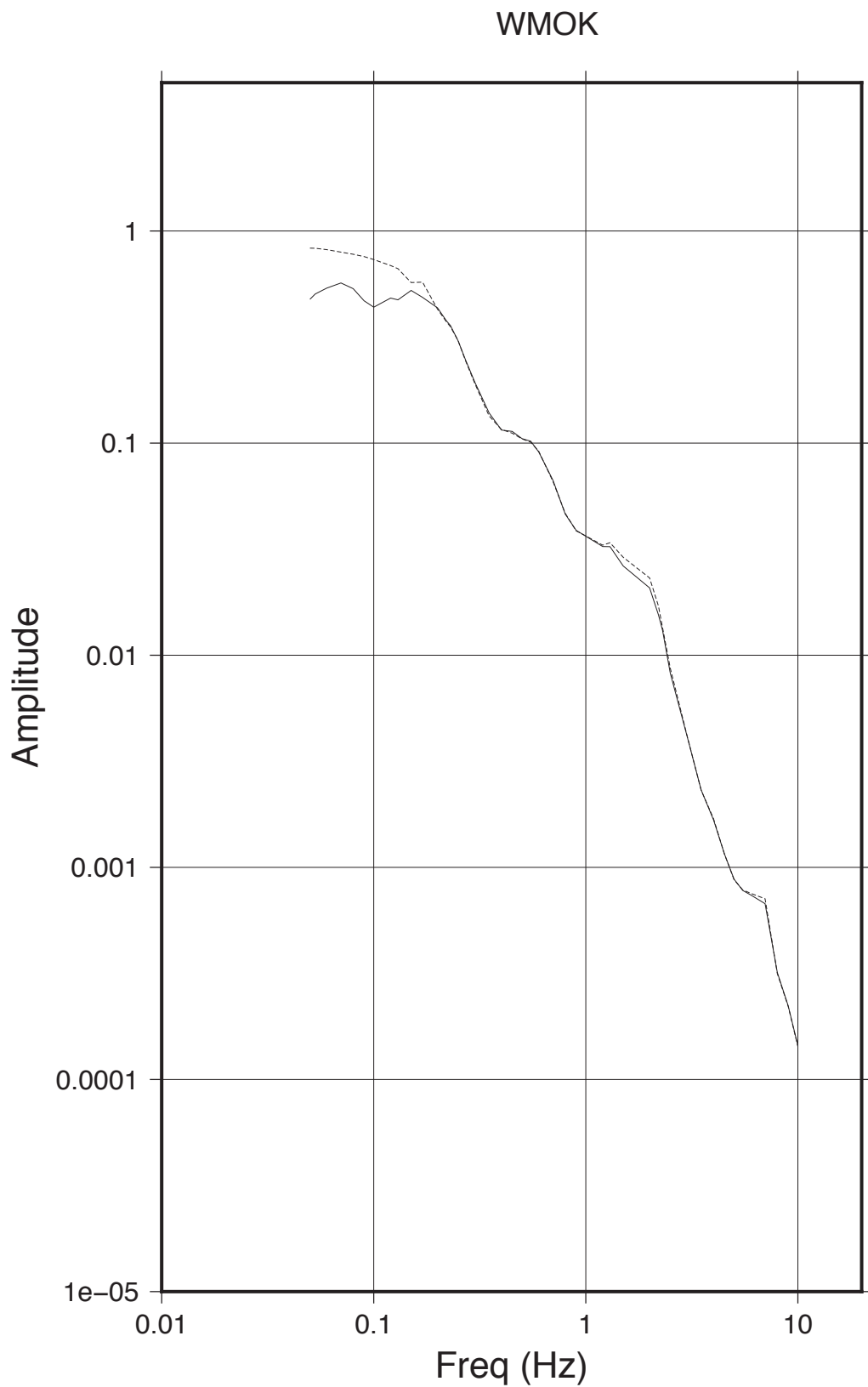


Figure 3.20. WMOK observed and predicted horizontal displacement spectra.

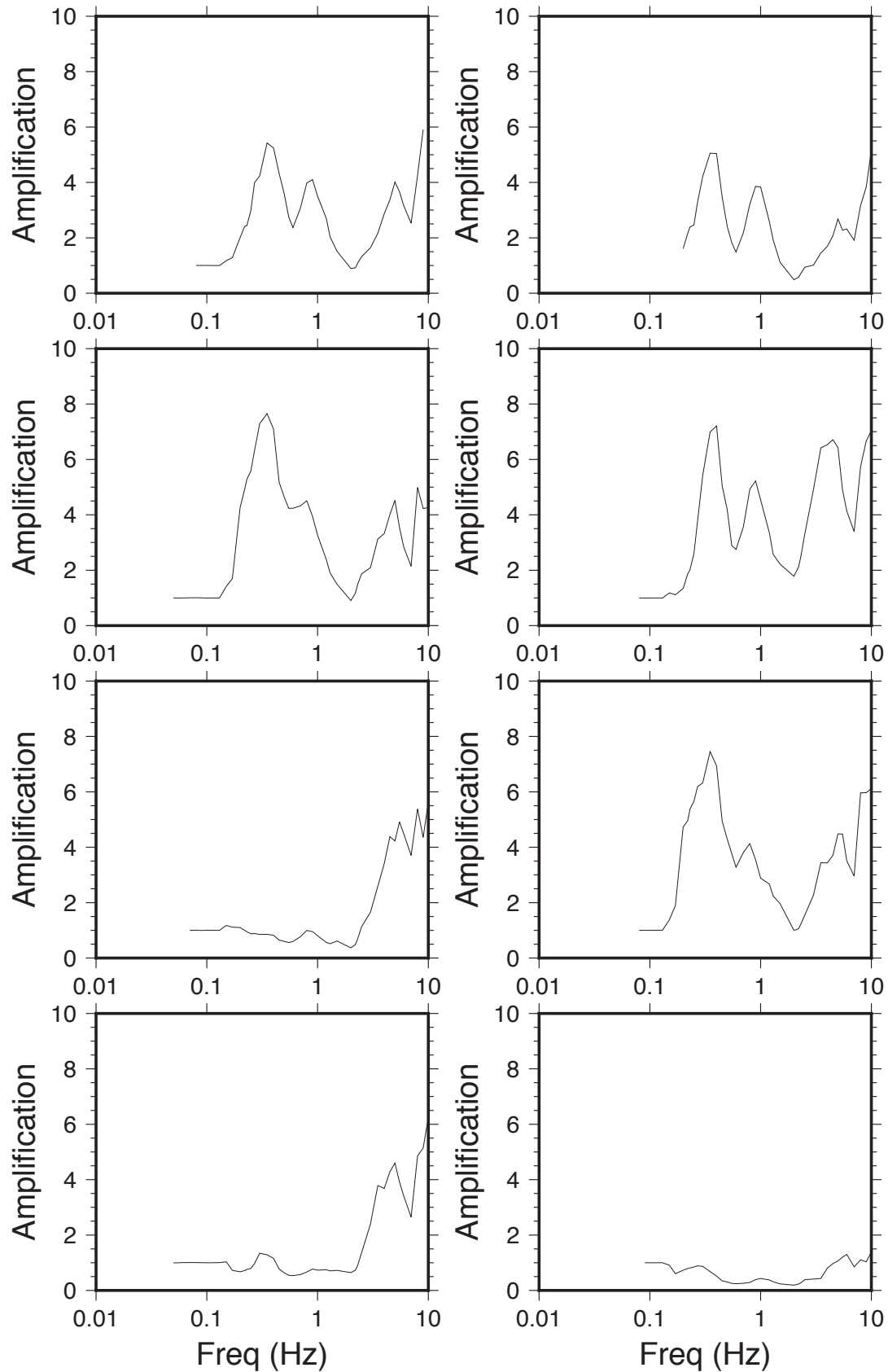


Figure 3.21. OK001, OK002, OK005, OK009, T34A, U32A, U35A and V35A normalized site response obtained by dividing by WMOK response spectrum.

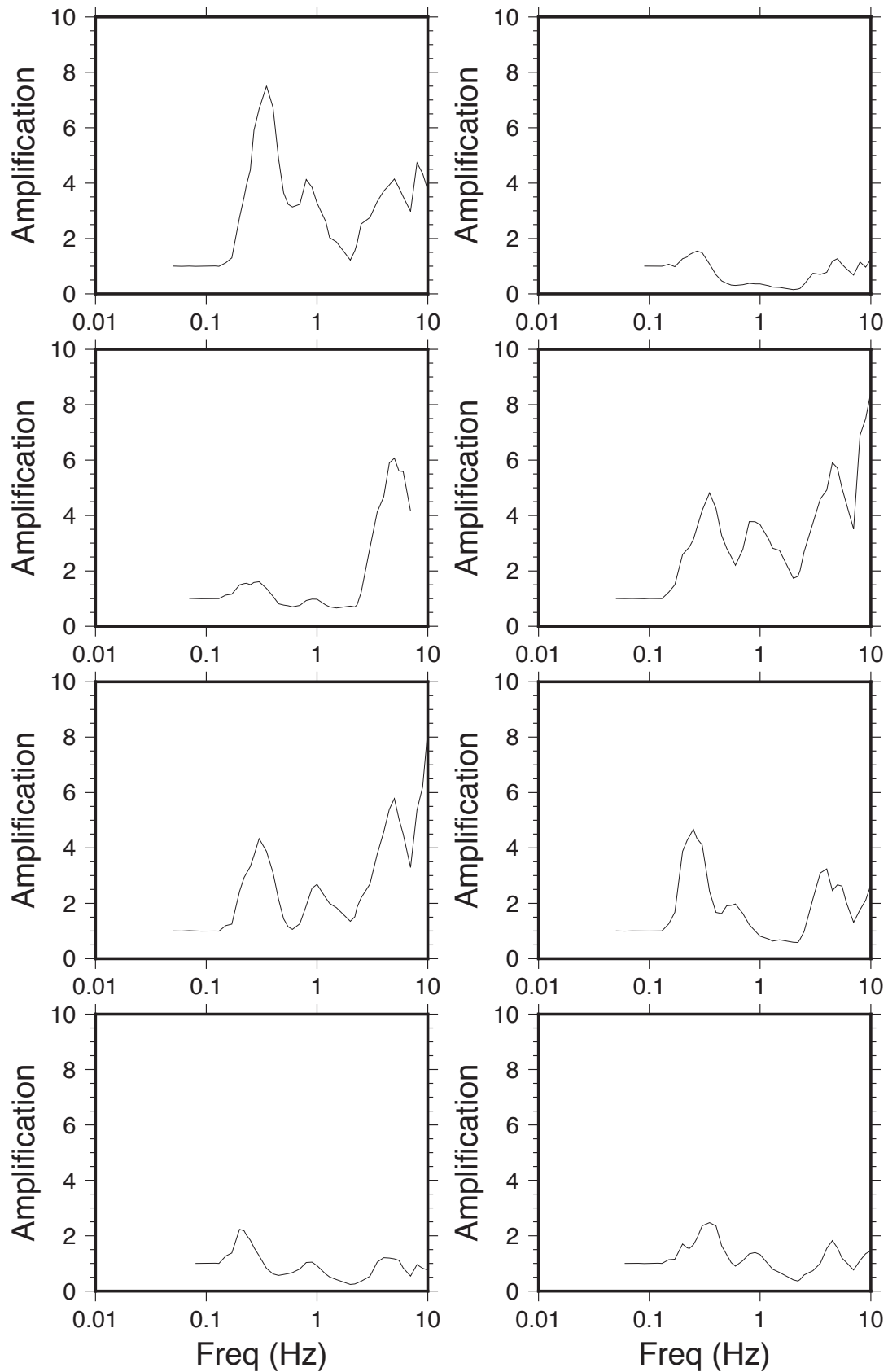


Figure 3.22. OK001, OK002, OK005, OK009, T34A, U32A, U35A and V35A normalized site response obtained by dividing by WMOK response spectrum.

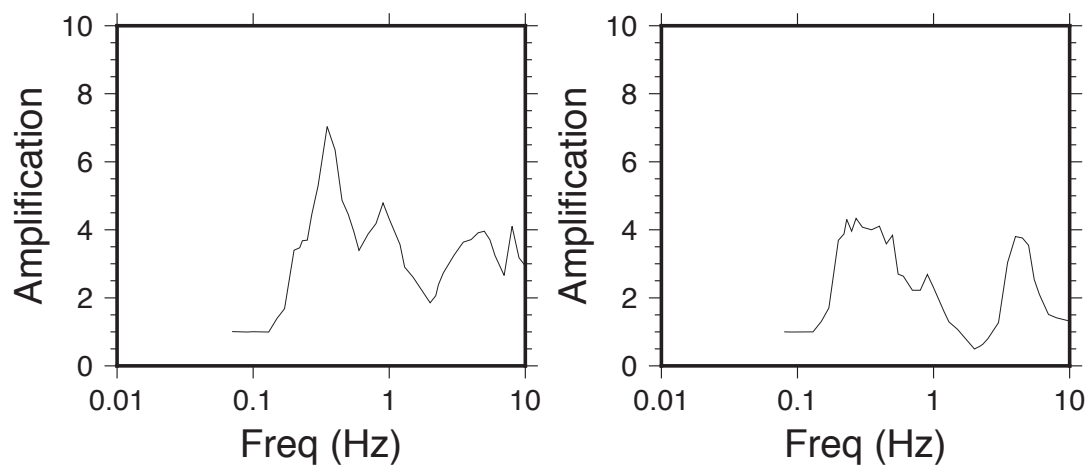


Figure 3.23. OK001, OK002, OK005, OK009, T34A, U32A, U35A and V35A normalized site response obtained by dividing by WMOK response spectrum.